Transonic Dimples

An experimental study of the flow structures formed at transonic speeds over dimpled surfaces

E. Claro Dittrich

Technische Universiteit Delft

TU Delft

Transonic Dimples

An experimental study of the flow structures formed at transonic speeds over dimpled surfaces

by

E. Claro Dittrich

Student number: 4917804

Thesis committee:	Dr. ir. B. W. van Oudheusden,	TU Delft
	Dr. ir. F. F. J. Schrijer,	TU Delft
	Prof. dr. ir. L.L.M. Veldhuis,	TU Delft
	Drs. ir. O. W. G. van Campenhout,	Dimple Aerospace B.V.

TU Delft

Preface

É também um pouco de uma raça,
Que não tem medo de fumaça,
E não se entrega não.

Ary Barroso

This thesis is the final product of an exciting research conducted in the Aerodynamics Department at TU Delft. Its development did not follow the most orthodox path intended for the thesis completion, and considerable parts were done in parallel with courses and internship work. It therefore taught me to effectively alternate between simultaneous tasks, to work remotely (a precious skill during pandemic times), to make precise plans, and also to be flexible about them. In this process, I learned a lot about myself and to be confident in my own capabilities.

Nevertheless, I most certainly did not walk this path alone, and would like to deeply thank those which helped me on the way. First of all, I am extremely grateful to Olaf van Campenhout for his tireless energy and motivation, even in the more adverse moments during the experimental campaigns. I want to extend my graditude to my academic supervisors, dr. Bas van Oudheusden and dr. Ferry Schrijer. Bas' seemingly unending knowledge of flow mechanics and Ferry's deep understanding understanding of gas dynamics and measurement techniques heavily supported this work. I would also like to thank Prof. Leo Veldhuis for encouraging me during the break of a fatidical lecture to contact Dimple Technologies for a Master's thesis in this exciting topic of drag reduction.

I am also grateful for all technicians that work in the lab, Dennis Bruikman, Peter Duyndam and Frits Donker Duyvis. They constantly displayed a positive attitude towards my work and posses a creative mindset which helped me during the setup manufacturing and assembly stages. All of this while coping with my constant demands for extra wind tunnel runs at the end of the day. I also feel indebted to my classmate Giulio Dacome, a great companion during my measurement campaigns and my closest ally in taming the ST-15 wind tunnel, affectionately nicknamed by us as 'Katharina'.

I am also indebted to the amazing classmates I had during this Master's programme. Their dedication motivated me to pursue the best possible quality in my work, and they surely had a large footprint in my learning experience. On a daily basis, I enjoyed the companionship of incredible friends in Netherlands and Brazil, especially from Laura Jou Ferrer, Matheus Pestana and Raphael Nassar. Finally, I must thank my parents. None of this would have been possible without you.

I shall always cherish my years in Delft, as I am sure they were fundamental in my formation as a professional, as well as a human being. As I look back at the end, it still seems unthinkable that I was given the opportunity of studying in this outstanding institution.

E. Claro Dittrich
Delft, February 2021

Abstract

Dimples are shallow surface indentations that have been recently considered as a passive viscous drag reducing technique for turbulent boundary layers. Studies so far were limited to incompressible low Reynolds number flows, and display little consensus on whether dimples are able to actually produce net improvements in total drag. When analysing the device's potential from another perspective, its shape can be regarded as the inverse of a transonic bump, a matured technique applied in compressible flows to achieve wave drag reduction. In light of this, this thesis sets off to provide an initial assessment of the wave drag reducing potential of dimples by analysing the flow structures that arise over them at transonic speeds.

An asymmetric nozzle was re-designed by means of CFD simulations to reproduce the conditions of interest. The resulting flow is characterised by a supersonic pocket terminated by a normal shock and followed by a subsonic adverse pressure gradient. Five test plates were manufactured to evaluate the performance of dimples against the criteria adopted for transonic bumps. Two wave drag reduction approaches are proposed. The first consists of placing the devices underneath the shock interaction, similarly as done for consolidated wave drag reduction techniques which reportedly produce improvements at on-design operation. The second entails a more indirect control by positioning the apparatus upstream of the shock, and strives to reduce the method's sensitivity to shock displacement.

Measurements aimed at analysing the resulting flow structures formed over the indentations. Techniques included Schlieren, surface pressure measurement and 2C-2D Particle Image Velocimetry. By applying isentropic and normal shock relations to velocimetry data, the momentum flow ratio across the shock was computed, allowing an objective comparison between the designs investigated. Results reveal that expansion fans formed at the edges of elongated dents offset the benefits achieved by flow compression promoted within them, what ultimately deteriorates the shock structure and decreases the downstream momentum flow when compared to an uncontrolled interaction. On the other hand, small spherical dimples placed upstream of the shock seem to produce spanwise excitations that subdue the detrimental effects of antagonistic mechanisms, and ultimately allow for a higher momentum retention.

This work provides a preliminary assessment of surface indentations in transonic flows, and focuses on understanding the flow mechanics of a shock interaction controlled by dimples. It serves as a stepping stone for future works aimed at drawing more definite conclusions on their capability of reducing drag in transonic flows. In this context, the spherical dents displayed the highest potential of delivering wave drag decrements for a broader range of conditions such as found in the flight envelope of a commercial aircraft. In general, dimples are strong candidates for applications in the wings and fuselage, given their low maintainability requirements and small impact on airframe design.

Contents

List of Figures

List of Tables

Nomenclature

Abbreviations and Acronyms

BL	Boundary Layer
CFD	Computational Fluid Dynamics
DNS	Direct Numerical Simulation
DUT	Delft University of Technology
e-VTOL	Electric Vertical Take-Off and Landing
FOV	Field of View
ICAO	International Civil Aviation Organization
LDA	Laser Doppler Anemometry
NASA	National Aeronautics and Space Administration
PISFV	Particle Image Surface Flow Velocimetry
PIV	Particle Image Velocimetry
RANS	Reynolds-Averaged Navier Stokes
SWBLI	Shock Wave-Boundary Layer Interaction
SWO	Spanwise Wall Oscillation
TRL	Technology Readiness Level
USD	United States Dollar

English Symbols

Δt	Light pulse separation	[μs]
Δz	PIV laser sheet thickness	[mm]
$\overline{M}$	Mass-averaged normalised momentum flow	[-]
$\overline{p_0}$	Mass-averaged total pressure	[Pa]
c_p	Specific heat capacity at constant pressure	[J/kg.K]
D	Dimple diameter	[mm]
d	Dimple depth	[mm]
h_B	Height of the shock control bump	[mm]
L_x	Center-to-center streamwise dimple spacing	[mm]
L_W	Dimple width	[mm]
p	Static pressure	[Pa]
p_0	Total pressure	[Pa]

R	Distance between leading edge and bottom of a surface dent	[mm]
r	Dimple edge curvature radius	[mm]
s_D	Lateral spacing between three-dimensional flow control devices	[mm]
T	Static temperature	[K]
T_0	Total temperature	[K]
u, v, w	Velocity components in the x, y and z coordinates	[m/s]
u^+	Dimensionless streamwise velocity scaled by u_τ	[-]
U_∞	Free-stream flow velocity	[m/s]
u_τ	Friction velocity	[m/s]
x^+, y^+, z^+	Dimensionless x, y and z coordinates scaled by u_τ and ν	[-]
x_S	Shock location in the streamwise direction	[mm]
a	Local speed of sound	[m/s]
c	Light speed in a specific medium	[m/s]
c_0	Light speed in vacuum	[m/s]
d_τ	Particle image diameter	[pixels]
d_i, d_o	Image and object distances	[mm]
d_p	Tracer particles diameter	[μm]
f	Focal length	[mm]
$f\#$	Camera aperture	[-]
H	Boundary layer shape factor	[-]
h	Static enthalpy	[J/kg]
h_0	Total enthalpy	[J/kg]
K	Gladston-Dale constant	[m^3/kg]
k	Adiabatic index/heat capacity ratio	[-]
M	Magnification factor	[-]
n	Refractive index	[-]
V	Local velocity magnitude	[m/s]
B	Turbulent wall law intercept constant	[-]

Greek Symbols

α	Angle of attack	[°]
δ	Boundary layer thickness	[mm]
δ_1	Boundary layer displacement thickness	[mm]
δ_2	Boundary layer momentum thickness	[mm]
κ	Kármán constant	[-]

λ	Laser wavelength	[nm]
ν	Kinematic viscosity	[m^2/s]
ν_w	Kinematic viscosity at the wall	[m^2/s]
ρ	Static density	[kg/m^3]
ρ_0	Total density	[kg/m^3]
ρ_r	Relative density normalised with stagnation value	[-]
ρ_w	Density at the wall	[kg/m^3]
τ_w	Friction at the wall	[N/m^2]
θ	Flow deflection angle	[°]
θ_1	Ascending angle of surface deformation	[°]
θ_2	Descending angle of surface deformation	[°]
φ	Flow direction angle	[°]

Dimensionless Groups

Ma	Local Mach number	[-]
Ma_∞	Incoming flow Mach number	[-]
Re	Reynolds number	[-]

1 Introduction

The aviation industry is facing the most challenging times since its creation. In a matter of weeks, a virus just 0.1 microns wide was capable of achieving something environmentalists and protesters never dreamed would be possible. Five months after its first identification, Covid-19 was responsible for cutting global passenger numbers in April 2020 by 94%, returning to 1974 levels [6]. This took place when the sector was rehearsing a renaissance, searching for ways of meeting bold sustainability goals while maintaining its steep expansion rate. The pressure to curb flight emissions is still very present, but now the challenge is even greater for aircraft manufacturers, who have to invest in new technologies while attempting to recover from the financial losses accumulated during the pandemic.

1.1. Challenges and solutions of modern flying

In the very beginning of 2020, the scenario of civil aerospace is very different, if not the complete opposite, of what it was fifty years ago. Flying used to be the luxury of a small elite class and the technological flagship of superpowers. In those times, civil supersonic aircraft with inefficient fuel consumption and dismaying noise levels would regularly cross the Atlantic, not as much to supply a real market demand, but more to display new engineering capabilities. Nowadays, the sector is a main driver of a globalised economy and saw its number of annual passengers double to more than 8 billion, in the nine years period between 2009 and 2018 [4]. And a maturing awareness of the environmental costs of widespread flying has taken a central stage, persuading companies to develop greener solutions.

Although not an easy task, the industry accepted the new challenges and started working on a myriad of innovative solutions for the short and long term future. Airlines and manufacturers have pledged on a collective effort to achieve a 50% reduction in net CO2 emissions by 2050 [46]. As a result, demand for more efficient aircraft grew considerably. Airports are encouraging airlines to renew their fleet [3], and innovative materials and manufacturing techniques are deployed in next-generation engines for a reduced fuel burn and emissions of noise and pollutants [56].

The technological advancements from the past five decades in aerodynamics and propulsion resulted in a 100% improvement of commercial aircraft performance [71]. However, the dominant tube-and-wing configuration powered by jet engines remained largely unaltered [13] [89], and modern designs show signs of reaching an asymptotic behaviour in terms of efficiency [72]. There is only so much that can still be refined in the current aircraft design, and it might not be enough to deliver the performance set for the future.

Hence, an effort is being placed on longer-term approaches, which promise to completely disrupt the way we fly. A major trend is the electrification of propulsion, which aims at reducing CO2 emissions and operating costs through the replacement of jet fuel [17]. In this context, hybrid and fully-electric projects are being developed by major players of the sector [27], while multiple startups have sprouted around the new segment of e-VTOL aircraft [82]. Another idea is the adoption of aviation biofuel on commercial flights, produced either from plant crops or waste gas and lumber [34].

There are also strong bets being placed on hydrogen. It can either be used directly as the propellant burned in jet engines or indirectly in fuel cells to generate power for propellers turned by electric motors [7]. Its storage is still a major issue, and could drive manufacturers to explore the feasibility of unconventional airplane architectures. Among the three design concepts of zero-emission hydrogen-powered aircraft recently disclosed by Airbus, the most suitable for hydrogen storage is a blended wing-body configuration. Another strong contestant is the Flying-V, developed at Delft University of Technology, whose design predicts fuel reductions of 20% when compared to an Airbus A350 [15] [35].

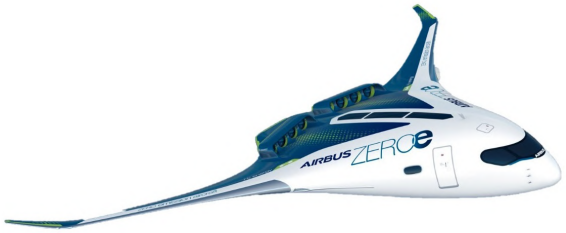

(a) Hydrogen-powered blended wing body by Airbus [5]

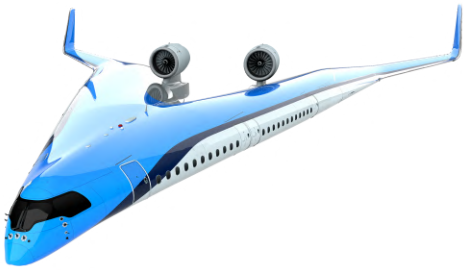

(b) V-shaped blended wing body envisioned at DUT [1]

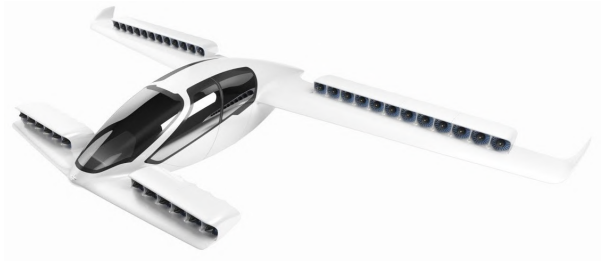

(c) e-VTOL aircraft from the German startup Lilium [2]

Figure 1.1: Disruptive aircraft designs being currently developed in the aerospace sector.

However, in the midst of this revolutionary effort, the aerospace sector abruptly suffered a severe blow. And it was ironically caused, in part, by itself. The industry responsible for interconnecting the world helped a mutated virus from the interior of China to spread worldwide and cause a pandemic. To fight this healthcare crisis, drastic mobility and travel restrictions were imposed, strongly affecting the aviation sector. Recent estimates from ICAO for 2020 indicate an overall reduction of 40-53% of seats offered by airlines and a gross operating revenue loss of USD 300-400 billion [8]. The report also states that damages have by far surpassed previous crisis, and a quick recovery is an unlikely scenario.

Some go as far as predicting that air travel will never recover from Covid-19. The pandemic quickly shifted most social interaction to the digital environment, and companies realised that business travel could be easily replaced by virtual meetings. Regional flying is also in danger, with environmentally-conscious young travellers being more prone to sit a while longer in a train instead of feeling responsible for accelerating climate change [7]. Nonetheless, optimists can still argue that the night is the darkest before the dawn. Although devastating, this crisis might also present opportunities to implement new technologies for flying. With the reduction of flights, airlines are anticipating the retirement of older (and less efficient) airplane models, such as the B747, B757 and A340 [69]. It will indeed take some years for orders of new aircraft to pick up again, but so will the development of new game-changing solutions, and manufacturers could potentially use this low demand period to accelerate their design and certification.

Out of the different possible areas of improvement, one in particular transcends all other innovation approaches and would deliver a substantial impact in achieving the goal of greener flying. This solution consists of reducing drag, the opposing force which is inherent to airborne motion.

1.2. Aircraft drag decomposition

Before diving into the effort of drag reduction, a clear theoretical definition of this force must be provided. The total aerodynamic force perceived by an immersed body is the integral of the fluid stresses acting on it by the flow [14]. This force can be decomposed in two components: one normal to the free-stream velocity vector and another parallel to it. The latter is referred to as the drag force [23]. Drag is directly linked to the momentum transfer between a body and a fluid flow, which causes a deficit of this quantity in one or the other [44]. From the experimental reference frame of a moving stream over a motionless body, the fluid has a momentum deficit, whereas a flying airplane passes on momentum to the surrounding air medium. This momentum transfer takes place at the interface between the fluid and structure, where for viscous flows the boundary layer is formed. Indeed, it is a phenomenon directly linked to the presence of viscosity, and is virtually inexistant in theoretical inviscid irrotational flows.

Total drag can be further subdivided in three main sources: induced, viscous and wave drag.

Induced drag is inseparable to the generation of lift. It is related to the shedding of vorticity over the span of a finite lifting wing [43]. This is more prominent at the wing-tip region, where the pressure side flow has the freedom to swirl to the suction side, following the vertical pressure gradient.

Viscous drag is associated to the movement of any body immersed in a fluid medium, and can be subdivided in two components [44]. Fluid viscosity imposes a no-slip condition on flow particles at the body surface, forming the boundary layer, a region with a wall-normal velocity gradient between the zero relative motion at the wall and free-stream speed away from it. The resulting distribution of tangential forces characterises skin-friction drag. Conversely, pressure drag is a product of normal stresses acting on the body. These normal forces are triggered by a pressure differential between the front and the back of the body, originated from the displacement effect that boundary-layer growth has on the streamlines, which effectively perceive a thicker body.

Wave drag is a by-product of the rapid compression of a supersonic flow, which forms mechanical waves of finite amplitude, commonly known as shocks [39]. These regions are characterised by steep pressure and temperature gradients, and their equilibrium thickness is determined by viscous stresses and thermal conductivity of the gas [99]. The dominance of viscous effects renders this process a highly non-isentropic nature, leading to pressure losses that produce normal stresses on the body. As a result, wave drag can be quantified by the momentum deficiency over the shock wave.

Shock waves can be found over civil aircraft that operate at high subsonic speeds. Flow accelerates over the wings, forming a supersonic region which is terminated by a normal shock. Pressure rise over the shock is followed by an adverse pressure gradient towards the trailing edge, a combination that might lead to flow separation. In order to better cope with these operating conditions, super-critical airfoils were designed to reduce shock strength by means of eliminating flow acceleration over its suction side, achieved through a reduced curvature over the mid-chord region [42]. As a result, the contribution of wave drag to the total resistance suffered by the aircraft is kept small. For high-subsonic aircraft, shock-induced drag delivers only a limited contribution to total drag, as seen in Figure 1.2.

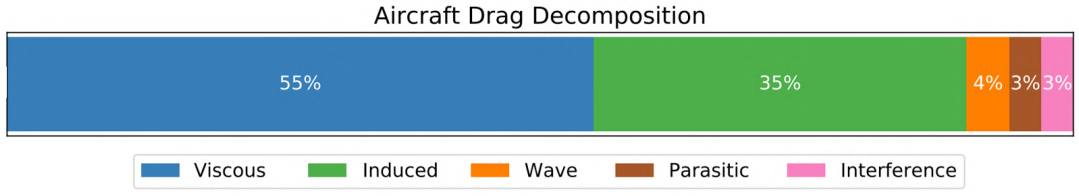

Figure 1.2: Drag breakdown of a commercial aircraft, adapted from [41].

Although wave drag plays a smaller role in the total drag decomposition, future wing designs could take advantage from matured wave drag reduction techniques to develop more efficient aircraft [19]. A direct consequence of the reduced camber of super-critical airfoils is the limitation of the negative pressure level achieved on the suction side of the wing and consequently of its lift production. The presence of wave drag reduction devices would enable shapes with more camber which could produce more lift for a similar drag penalty. The goals set for future aircraft performance are substantial, and, in order to meet them, a whole set of solutions contemplating all aspects of drag will have to be implemented.

1.3. Drag reduction: from research to airworthiness

The effort of researching drag reducing techniques is paramount for increasing the efficiency of most means of transportation. Drag is inherent to motion in any fluid medium, and solutions developed for one application can be re-scaled and transferred to others. Also, advancements in the field of drag reduction are hardly compromised by the adoption of other technologies: it is equally desirable to decrease the drag acting on an electric, hydrogen-powered or V-shaped airplane as it is for the current tube-and-wing configuration that dominated the past five decades [13].

Flow control techniques can be divided in two groups: active and passive [33]. In one side, active flow control promises greater potential of gross drag decrease and larger adaptability to different operation regimes. However, it usually introduces weight, has a higher cost and the necessary energy expenditure substantially lowers the net benefits achieved. Passive methods, on the other hand, are lighter and more reliable solutions. Notwithstanding, reductions in flow resistance are more limited, their performance can rapidly deteriorate in off-design conditions and they usually involve delicate structures.

Although many different techniques are being currently investigated, one claiming to be better than the other, very few are actually implemented in civil aircraft. Spalart and McLean [79] argue that multiple factors beyond local effects have to be considered when translating measured drag coefficient reductions to actual in-flight improvements. Using riblets as an example, Reynolds effects and partial coverage of the aircraft might shrink the drag reduction from 10% to 3%. On the other hand, there are also indirect benefits to be reaped: a plane that produces less drag can fly with less fuel, and therefore needs to generate less lift. This leads to additional decrements in drag production which ultimately enhance the overall performance of the control technique.

A successful flow control method must strike a good balance between all practical aspects of its implementation and at the same time prove to work robustly within a given flight envelope. The emissions reduction targets set on aviation for the next decades demand the adoption of different technologies, and drag-reducing devices will be necessary to reach this goal. Passive methods seem to be very strong contestants, given their inherent simplicity, light weight and low costs.

1.4. Passive wave drag reduction

Wave drag reduction devices aim at reducing the shock wave strength, leading to a smeared pressure rise over the interaction. This is achieved by compressing the flow upstream of the shock, what usually leads to the formation of a lambda shock system.

One of the first passive devices that targeted wave drag were perforated plates, extensively researched in the EUROSHOCK I project [30]. They consist of replacing a smooth solid surface by a porous plate covering a cavity. With the plate located at the shock region, a natural re-circulation flow pattern is formed through the cavity, from the downstream high-pressure part of the interaction to the low-pressure flow upstream of the shock [84]. This blowing mechanism provokes an upward streamlines deflection, which in turn induces a leading oblique wave. The resulting lambda shock system is capable of increasing pressure recovery across the shock, thus effectively decreasing wave drag. However, it also causes a more rapid thickening of the boundary layer and a larger viscous drag downstream of the interaction, which largely offsets the net benefits achieved [70].

Another thoroughly researched method are transonic bumps, which aim at improving the SWBLI by simply introducing a deformation in the surface contour. While for perforated plates an upwards deflection is caused indirectly by the blowing effect of recirculating air from the cavity, for bumps the change of flow direction is explicitly promoted by a modification of the surface in the location of the shock [25]. This technique has a smaller influence on the downstream boundary layer, and is reported to produce decrements in wave drag without negatively affecting the viscous component [49]. Despite having proved to work under experimental conditions, the shortcomings of both techniques, related to poor performance at off-design conditions, prevented them from being incorporated in actual aircraft.

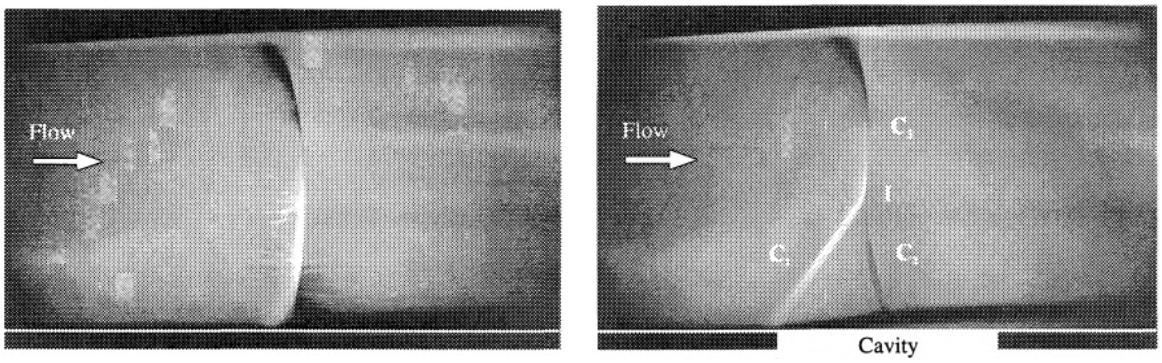

(a) Uncontrolled shock wave (reference case)

(b) Controlled shock wave by perforated plate

Figure 1.3: Schlieren images of uncontrolled and controlled SWBLI's using perforated plate [70].

1.5. Dimple drag reduction

The potential of dimples to reduce viscous drag was found by chance in 1977, when scientists attempted to increase the heat transfer efficiency of heat exchangers by fitting their surface with spherical dimples. These results were published by Kiknadze in 1984 [40], and it sparked the research on the aerodynamic applications of this device.

At Delft University of Technology, the topic gained momentum with the Master's theses from Vervoort [97], van Nesselrooij [93], van Campenhout [91], and Weersch [101]. These works aimed at understanding the flow mechanics and quantifying the drag reduction of large arrays of indentations applied to flat surfaces. Their main conclusion was that shallow surface indentations would be capable of reducing the viscous drag component by inducing spanwise oscillations in the flow, what was experimentally confirmed for incompressible low-Re flows. However, recent Direct Numerical Simulations from Spalart et al. [80] of the TU Delft dimples predicted a drag increase of at least 1%, shedding doubts on the potential of dimples delivering viscous drag reduction.

Notwithstanding, dimples have not yet been investigated under transonic conditions, found at the fuselage of a flying vehicle, their main use case. It can also be argued that the shape of a dimple is the opposite of transonic bumps, and thus they could also have the potential of controlling the shock. Motivated by this, the current work aims at broadening the range of applications of dimpled surfaces by studying the flow structures that arise when it interacts with a shock, which could give indication of potentially using them as a wave drag reduction technique.

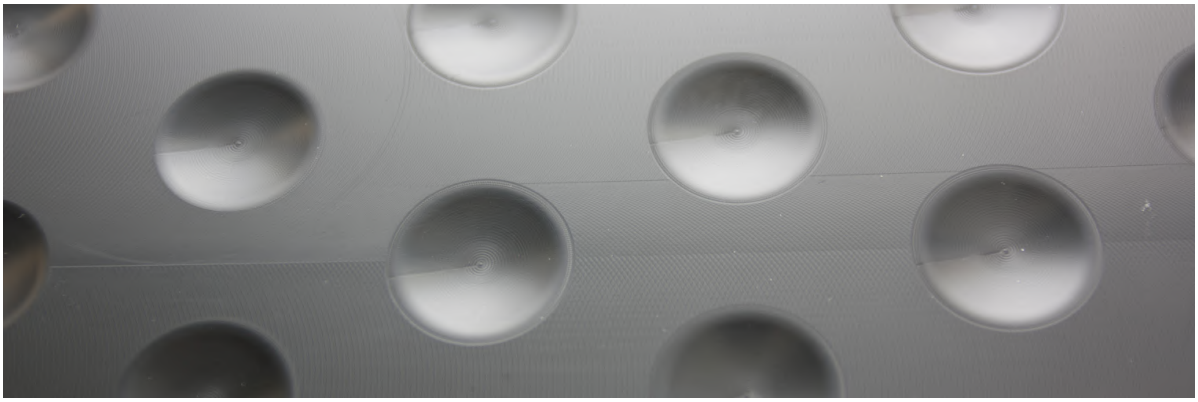

Figure 1.4: Example of a dimpled surface used to reduce viscous drag [93].

1.6. Scope

Research objectives. Dimples can be considered a potential candidate for reducing flow resistance in real-life applications. The shallow indentations have low maintainability requirements, small impact on airframe design and can be retrofitted on existing aircraft [90]. So far research has mainly focused on viscous drag reduction of incompressible low Reynolds number flows. However, results don't display a clear agreement on their drag reducing capability, with recent DNS indicating a slight increase of viscous drag [80]. Conversely, there is a lack of study at high-speed flows of these indentations, whose shape is equivalent to an inverted transonic bump, a matured but never implemented wave drag reducing device. In the meantime, the aviation sector is rehearsing a technological revolution, in the attempt of meeting the challenging sustainability requirements set for the upcoming years. New concepts and aircraft architecture are proposed, a fertile ground for introducing a next generation of wings that take advantage of shock control devices to increase their aerodynamic efficiency.

In light of the geometric similarities between dimples and bumps, and the need for new means of reducing drag of high-subsonic planes, this work proposes an investigation of dimples in transonic flow. Given the absence of similar works, the current analysis is dedicated to understanding the physics of the flow, characterised by a shock wave-boundary layer interaction over a dented surface. Results would then serve as a stepping stone for future works aimed at directly quantifying their potential for wave drag reduction. Since for subsonic aircraft this component originates from normal shock waves found over the wings, a similar structure shall be investigated.

In summary, this research has the following main objective:

To experimentally investigate the flow mechanics of a transonic flow over a dimpled surface.

This main objective can be subdivided three-fold:

1. **Reproduce the desired flow regime in a wind tunnel.** The conditions of interest are those found over the suction side of a transonic airfoil, namely a supersonic region, terminated by a normal shock and followed by an adverse pressure gradient at subsonic speeds. It is desired to perform this over the wind tunnel wall, so that resulting flow structures are more accurately resolved by measurement techniques.
2. **Measure the flow field around a dimple-controlled SWBLI.** It is expected that dimples will produce a flow compression upstream of the shock, thus reducing its strength. By measuring the flow structures that arise from the controlled interaction, conclusions can be draw on that indicate the potential of dimples to reduce wave drag.
3. **Determine the geometry of effective shock control dimples.** The dimple shape is analogous to that of an inverted bump, a matured wave drag reducing device. By critically analysing flow characteristics over bumps and their performance, it should be possible to design dimples that can successfully control a normal shock.

Research questions. From the research objectives, three research questions have been set:

1. Can the transonic flow conditions found over wings be experimentally reproduced over an asymmetric nozzle while avoiding flow separation?
2. How is a transonic flow field modified by a dimpled surface?
3. Which shape should a surface indentation assume in order to effectively control the shock wave?

Thesis structure. Following the introductory chapter, chapter 2 will cover the relevant literature on shock control devices and dimpled surfaces, laying the theoretical foundations of the current work. Chapter 3 will describe the preliminary simulations conducted to design a test section that produced the desired flow conditions. Then, Chapter 4 describes the design of the experiment, covering the setup components and test plates design, while Chapter 5 gives an overview of the measurement techniques deployed. Subsequently, the results are presented, being grouped according to the measurement campaigns. First, in Chapter 6, the outcome of Schlieren and pressure measurements is displayed, and afterwards in Chapter 7 the Particle Image Velocitmetry results are discussed. Finally, Chapter 8 consolidates all observations from the experimental analysis and draws conclusions to the research questions posed. Additional results from simulations and preliminary measurement campaigns are found in the appendices, as well as information on the assembly and manufacturing of the setup.

2

Literature review

This chapter outlines the theory and literature that supports the present work. It will first cover the theoretical background of compressible flows and boundary layer, presenting the expressions used later throughout the report. Then, it will characterise the shock wave-boundary layer interaction, a flow structure intrinsic to transonic flows and responsible for the wave drag component. Next, the methods to control the SWBLI are reviewed, with a focus on transonic bumps given their geometric similarity with dimples. The chapter is concluded by outlining the literature on dimples themselves, including a prognosis on the potential benefits achieved by this method in transonic speeds.

2.1. Compressible flow relations

In this section, the isentropic flow relations and normal shock equations are presented. For the purposes of this work, the fluid is always air, which is assumed to be a calorically perfect gas, meaning that its specific heat capacity does not change with temperature.

Isentropic flow relations

A flow can be considered isentropic when changes occur gradually, in a reversible way, and without heat exchange (adiabatic). As a result, equations that arise from the constant entropy assumption are no longer valid in regions where viscous dissipative phenomena are dominant, such as inside boundary layers and over shock waves [99]. The main isentropic relations are presented in Equation 2.1. Here, the denominator of the fraction is the stagnation quantity of the thermodynamic property (i.e., total pressure, density and temperature), which is used as a reference for the flow field.

A main non-dimensional number of compressible flows is the Mach number, defined as being the ratio between the local flow velocity and the local speed of sound. The local speed of sound for a perfect gas is determined solely by the local static temperature (Equation 2.2).

$$\frac{p}{p_0} = \left(\frac{\rho}{\rho_0}\right)^k = \left(\frac{T}{T_0}\right)^{\frac{k}{k-1}} \tag{2.1}$$

$$Ma = \frac{V}{a}, \quad a = \sqrt{k\,R\,T} \tag{2.2}$$

From the adiabatic assumption, it can be concluded that flow total enthalpy is constant. Total temperature is defined in the stagnation point, where flow velocity equals zero (Equation 2.3). The specific heat capacity results from thermodynamic properties of the gas. By substituting c_p, it is possible to introduce the local speed of sound in the equation, which in turn allows the temperature ratio to be written as a function of the local Mach number. Combining this result with the isentropic relations from Equation 2.1, the expressions of an isentropic compression to zero velocity are derived for the other quantities (Equation 2.4).

$$h_0 = h + \frac{V^2}{2} = \text{const.}, \quad h = c_p\,T, \quad c_p\,T + \frac{V^2}{2} = c_p\,T_0, \quad c_p = \frac{k}{k-1}\,R \tag{2.3}$$

$$\frac{T}{T_0} = \left(1 + \frac{k-1}{2}\,Ma^2\right)^{-1}, \quad \frac{p}{p_0} = \left(1 + \frac{k-1}{2}\,Ma^2\right)^{-\frac{k}{k-1}}, \quad \frac{\rho}{\rho_0} = \left(1 + \frac{k-1}{2}\,Ma^2\right)^{-\frac{1}{k-1}} \tag{2.4}$$

Finally, the constant total enthalpy equation can be used to express the static temperature in terms of the local velocity magnitude. A reference point is taken, referred by the indent 'ref'. From there, the local speed of sound of the reference point is brought up in the equation. This relation is particularly useful when flow properties are known in a specific point of the flow field and it is desired to compute them in other locations where only the velocity is known. It will be later used to compute the isentropic density and Mach number distributions from PIV data.

$$c_p\,T + \frac{V^2}{2} = c_p\,T_{\text{ref}} + \frac{V_{\text{ref}}^2}{2} \tag{2.5}$$

$$\frac{T}{T_{\text{ref}}} = 1 + \frac{k-1}{2}\,Ma_{\text{ref}}^2\left(1 - \frac{V^2}{V_{\text{ref}}^2}\right) \tag{2.6}$$

Normal shock relations

A shock wave is a disturbance that propagates in the fluid medium faster than the speed of sound. It is a thin region of highly viscous flow, and promotes an almost-discontinuous change of the fluid thermodynamic properties [13]. To analyse the shock wave phenomenon, it is considered a control volume such as shown in Figure 2.1a, where flow properties are known in the region upstream of the shock (region 1) and change to unknown values downstream of it (region 2). Although temperature rises across the shock, it occurs due to the conversion of kinetic energy into internal energy. Since no heat transfer takes place, the system can be considered adiabatic and total temperature is conserved over the shock (Equation 2.7).

$$h_{01} = h_{02}, \quad h_0 = c_p\,T_0 = \text{const.}, \quad c_p = \text{const.} \quad \rightarrow \quad T_{02} = T_{01}, \tag{2.7}$$

It is however a highly irreversible process characterised by an entropy rise. Due to the stark presence of viscous dissipative forces, flow departs from the isentropic state, and therefore isentropic relations lose validity. By applying the momentum conservation equation across the shock, it is possible to compute the Mach number downstream of it as a function of Ma before the deceleration:

$$Ma_2^2 = \frac{(k-1)\,Ma_1^2 + 2}{2\,k\,Ma_1^2 - (k-1)} \tag{2.8}$$

By re-using this result in the momentum equation and deploying the perfect gas equation of state, the ratios of the other thermodynamic quantities across the shock can be computed (Equation 2.11).

$$\frac{p_2}{p_1} = \frac{2\,k\,Ma_1^2 - (k-1)}{k+1} \tag{2.9}$$

$$\frac{\rho_2}{\rho_1} = \frac{(k+1)\,Ma_1^2}{2 + (k-1)\,Ma_1^2} \tag{2.10}$$

$$\frac{T_2}{T_1} = \left[1 + \frac{2\,k}{k+1}\left(Ma_1^2 - 1\right)\right]\frac{2 + (k+1)\,Ma_1^2}{(k+1)\,Ma_1^2} \tag{2.11}$$

Total pressure losses take place over a shock wave, a consequence of the non-isentropic nature of the phenomenon. Total pressure ratio can be computed using the static pressure ratio equation and the isentropic compression expressions to zero velocity in the individual regions (Equation 2.4). The downstream Mach number can be re-written in terms of the upstream one by deploying Equation 2.8.

$$\frac{p_{02}}{p_{01}} = \left(\frac{p_1}{p_{01}}\right)\left(\frac{p_2}{p_1}\right)\left(\frac{p_2}{p_{02}}\right)^{-1} = \left[\frac{(k+1)\,Ma^2}{(k-1)\,Ma^2+2}\right]^{\frac{k}{k-1}}\left[\frac{k+1}{2\,k\,Ma^2-(k-1)}\right]^{\frac{1}{k-1}} \tag{2.12}$$

By writing the perfect gas law in terms of stagnation properties and considering the conservation of total temperature, it can be concluded that the total density ratio across the shock equals the total pressure one (Equation 2.13).

$$p_0 = \rho_0\, R\, T_0 \quad \rightarrow \quad \frac{p_{02}}{p_{01}} = \frac{\rho_{02}}{\rho_{01}} \tag{2.13}$$

Finally, Figure 2.1b illustrates the streamwise pressure distribution in a converging-diverging nozzle for different shock strengths. Flow cases with the most downstream shocks accelerate more in the diverging part of the nozzle, thus reaching higher Mach numbers upstream of the wave, what leads to a stronger deceleration and higher losses. As a result, total pressure recovery is reduced and relative pressure level reached in the outlet is smaller. This analysis will be relevant when evaluating the results in the experimental setup, since a similar effect is expected to occur as the shock is positioned more downstream.

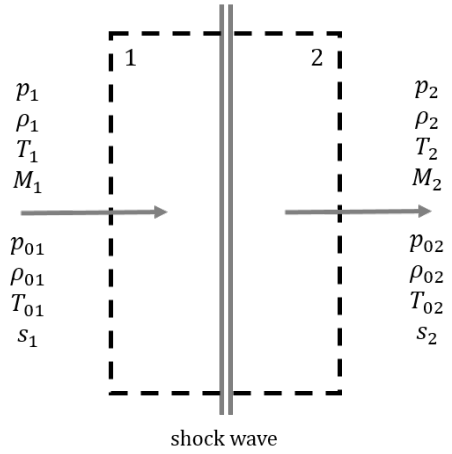

(a) Control volume over a normal shock wave.

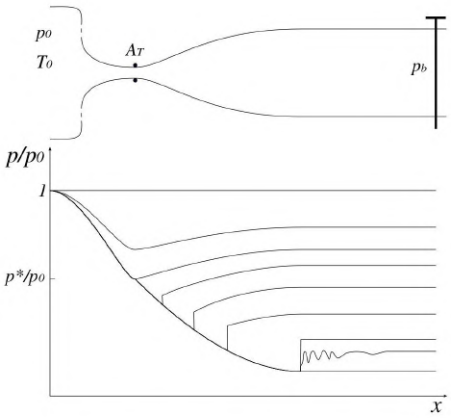

(b) Pressure recovery of a transonic flow in a converging-diverging nozzle

Figure 2.1: Shock control volume and effects of shock strength in the pressure recovery inside a converging-diverging nozzle.

2.2. Turbulent boundary layer

This section outlines the fundamental theoretical considerations on compressible turbulent boundary layer relevant for this work. It starts with the equations and interpretation of boundary layer integral parameters. Afterwards, the law of the wall is outlined alongside non-dimensionalisation procedures of compressible boundary layer profiles.

2.2.1. Integral parameters

According to White [102], the boundary layer (BL) can be characterised by means of various parameters, computed from the vertical distribution of velocity and density. Furthermore, they can be scaled to allow a comparison between flowfields produced by different geometries and conditions. The first parameter to be defined in the BL thickness. By convention, it is defined that the edge of the BL lies at a vertical distance δ from the wall where fluid velocity equals 99% of the free-stream velocity (U_∞).

$$\delta = y\,(\mathrm{u} = 99\%\,\mathrm{U}_\infty) \tag{2.14}$$

Another important BL parameter is the displacement thickness δ_1. It can be interpreted as the normal distance from the wall to which the streamlines would have to be displaced to produce an equivalent flowfield for a hypothetical inviscid case (with the same mass flow rate). For compressible flows, the equation for δ_1 is as follows:

$$\delta_1 = \int_0^\delta \left(1 - \frac{\rho(y)\,\mathrm{u}(y)}{\rho_\infty\,\mathrm{U}_\infty}\right) \mathrm{d}y \tag{2.15}$$

The reduced fluid velocity over the BL profile when compared to free-stream ultimately results in a loss of momentum. In order to quantify this, the momentum thickness parameter δ_2 is defined, which represents the loss of momentum in the boundary layer in terms of an equivalent height of uniform flow [23]. For compressible flows, the equation for δ_2 is written as:

$$\delta_2 = \int_0^\delta \frac{\rho(y)\,\mathrm{u}(y)}{\rho_\infty\,\mathrm{U}_\infty}\left(1 - \frac{\mathrm{u}(y)}{\mathrm{U}_\infty}\right) \mathrm{d}y \tag{2.16}$$

Finally, one last BL parameter is presented. The shape factor H is commonly used to differentiate between laminar and turbulent flow: turbulent boundary layers commonly have H ranging between 1.2-1.4, whereas a typical value for laminar ones is around 2.59 (based on Blasius solution). This factor is also affected by the flow pressure gradient and is thus related to skin-friction.

$$H = \frac{\delta_1}{\delta_2} \tag{2.17}$$

2.2.2. Law of the wall for turbulent flows

The space-averaged turbulent boundary layer properties can be non-dimensionalised based on quantities such as friction velocity, density and kinematic viscosity at the wall. The classical wall-unit scaling of flow properties can be seen in Equations 2.18 to 2.20.

$$\mathrm{u}_\tau = \sqrt{\frac{\tau_w}{\rho_w}} \tag{2.18}$$

$$\mathrm{u}^+ = \frac{\mathrm{u}}{\mathrm{u}_\tau} \tag{2.19}$$

$$\mathrm{y}^+ = \frac{\mathrm{y}\,\nu_w}{\mathrm{u}_\tau} \tag{2.20}$$

The turbulent boundary layer is characterised by three main regions, namely the inner layer, overlap layer and outer layer. While the former is dominated by viscous shear, which dampens velocity fluctuations, the latter is most influenced by turbulend eddy shear [102]. By scaling the quantities based on wall units, the velocity profiles of the inner layer become universal, and can be further subdivided in three characteristic regions:

- Viscous sublayer ($0 < \mathrm{y}^+ < 5$): Linear velocity profile $\mathrm{u}^+ = \mathrm{y}^+$
- Buffer layer ($5 < \mathrm{y}^+ < 30$)
- Overlap layer ($30 < \mathrm{y}^+ < 350$): Logarithmic velocity profile $\mathrm{u}^+ = \frac{1}{\kappa}\ln \mathrm{y}^+ + B$

For the logarithmic profile, κ and B are near-universal constants for turbulent flow past smooth walls, which typically assume the values of 0.41and 5.0 respectively [102]. Figure 2.2 shows how boundary layer measurements of the inner layer obtained for different Reynolds numbers collapse together when scaled using wall units. It also includes the Spalding's law of the wall, a single formula that describes the entire inner boundary layer.

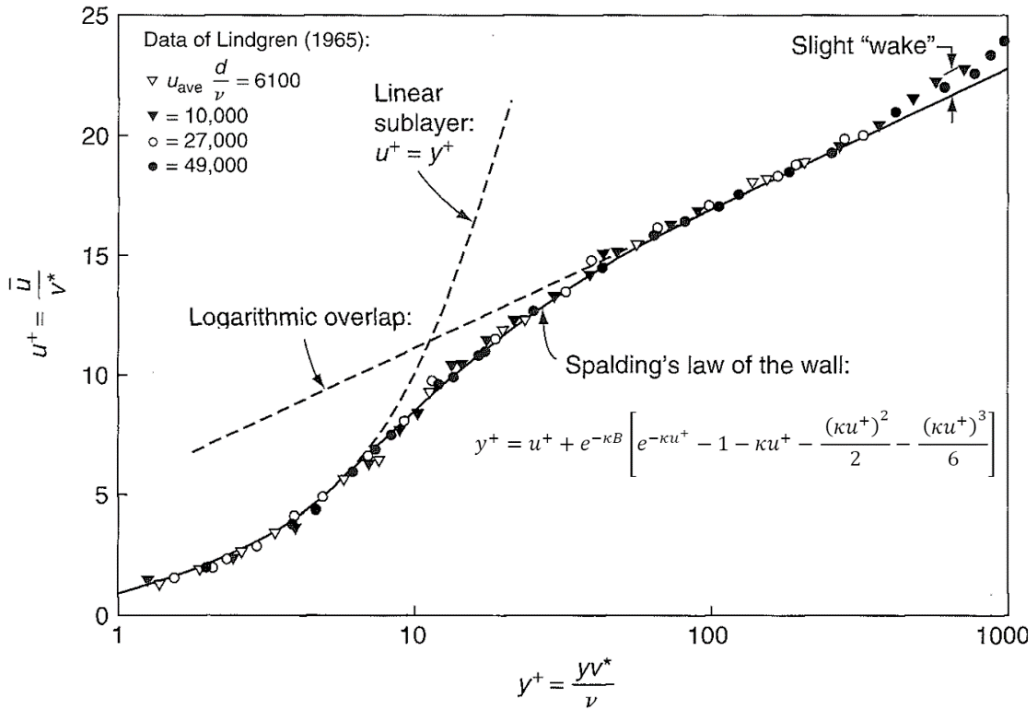

Figure 2.2: Spalding's law displays good agreement with inner boundary layer measurements. Modified from White [102].

2.3. Shock wave-boundary layer interaction

Shock waves are an equally undesirable and inevitable phenomenon when dealing with high-speed flows. They can be provoked in situations such as the increase of pressure towards the trailing edge of transonic wings, a change in flow direction on compression ramps of supersonic air intakes or the stark flow deceleration around the stagnation region on the nose of a re-entry vehicle [28]. Research on shock wave-boundary layer interaction (SWBLI) appeared in the decade of 1940 [26], motivated by deviations between theoretical inviscid and measured lift of transonic airfoils [37].

These interactions can be subdivided according to shock strength, what ultimately results in different flow topologies [36]. The information of the pressure rise caused by the shock is transmitted below the sonic line to the flow upstream of the compression in the form of boundary layer thickening [99]. On weak interactions, this forms isentropic compression waves in the supersonic part of the flow (Figure 2.3a). While the flow outside the boundary layer experiences an almost instantaneous pressure rise, inside this is smeared over a larger streamwise region, allowing the flow to remain attached.

Conversely, for stronger shocks, the pressure gradient is too steep to be withstood by the boundary layer flow, leading to the formation of a separation bubble (Figure 2.3b). This structure deflects the streamlines upwards, generating a leading oblique shock in the outer flow. A trailing shock then realigns the flow in the direction parallel to the wall. Both compression waves meet at the triple point and above a single normal shock leg is formed, characterising a lambda shock. Flow that passed through both shock legs experience a smaller pressure loss when compared to particles that cross the single normal stretch above the triple point. Stronger shocks are commonly observed for laminar flows, since they are more susceptible to separation under highly adverse pressure gradients [47].

Shock waves are a source of highly positive pressure gradients and shear layers. They are dominated by viscous forces which increase entropy, making shocks a substantial source of drag [29]. Shock waves can produce drag in two ways:

- Directly, due to entropy generation in the thickness of the shock, what creates the individual *wave drag* component.
- Indirectly, by thickening the boundary layer, thus enhancing the *viscous drag* component.

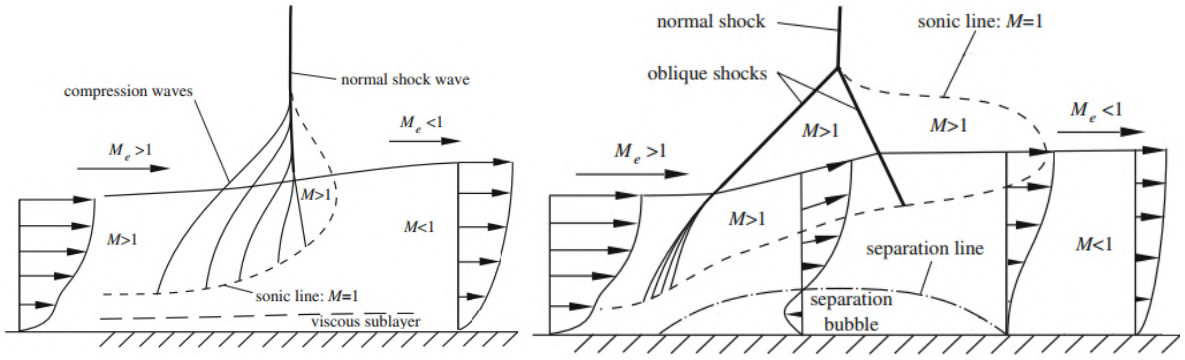

(a) Schematics of a weak SWBLI.

(b) Schematics of a strong SWBLI.

Figure 2.3: Schematics of weak and strong shock wave-boundary layer interactions [99].

Since shocks cannot be avoided in most situations, control techniques have been proposed to limit their negative effects. When aimed at reducing wave drag, these techniques will rely on the principle that total pressure recovery through a number of oblique shock legs is greater than across a single normal shock [19]. As shown in Figure 2.4, they will attempt to replace a normal shock by a large lambda-system, approximating the compression to an isentropic process, what consequently reduces total pressure loss and lowers wave drag. To achieve larger reductions of wave drag, it is desired to move the triple point upwards, thus smearing the pressure rise over a larger distance.

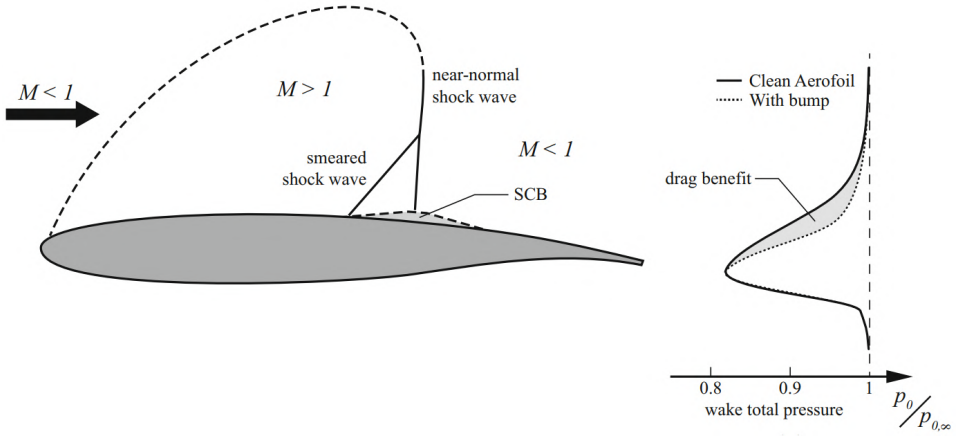

Figure 2.4: Shock control over a transonic airfoil by means of surface deformation. A larger pressure recovery in the wake translates in wave drag reduction [19].

It must, however, be mentioned that shock control can trigger antagonistic flow mechanisms. For example, a successful improvement of the profile drag might lead to detrimental effects on the boundary layer, following an increase of friction drag. As is argued by Kral [55], “the design trade-offs of a particular method of control must carefully be evaluated and compromises are often necessary to reach a particular design goal.”

2.4. Perforated plates and streamwise slots

The passive control of SWBLI using perforated plates consists of replacing a smooth solid surface by a porous plate covering a cavity. With the plate positioned underneath the shock, a recirculating flow pattern is formed through the cavity, from the downstream high-pressure part of the interaction to the upstream low-pressure region. The resulting blowing mechanism provokes a rapid thickening of the boundary layer, which is perceived by the flow supersonic portion as a ramp effect. The upward streamlines deflection induces an oblique wave followed by a trailing shock, that re-aligns the flow parallel to the wall. As a result, the strong normal shock is replaced by a lambda-structure and the pressure rise region is enlarged, decreasing total pressure losses and consequently wave drag [58].

Bur and Délery [70] conducted a thorough analysis of perforated plates mounted on the wall of a supersonic wind tunnnel. Pressure gradient smearing and bifurcation of the shock consistently indicated a reduction of the wave drag component. However, LDA measurements showed that boundary layer downstream of the controlled interaction became less stable (smaller momentum thickness) and had higher levels of turbulence, what detrimentally enhanced viscous skin-friction drag.

The efficiency of controlling the interaction is strongly dependent on the relative position between the perforated plate and the shock [84]. When compared to a shock located in the middle of the plate, an upstream position benefits from a large suction region after the pressure rise, and air is blown to a small and focused area. This strengthens the leading oblique shock, but the intensified blowing also encourages local separation. Conversely, a downstream shock location limits the supply of suctioned air, while the blowing region is enlarged. As a result, the ramping effect and thus the leading oblique wave are weakened, and the shock structure approaches its uncontrolled form (Figure 2.5a).

The streamwise slots technique consists of a longitudinally cut plate covering a cavity, and follows the same principle of perforated plates. Cuts are regularly spaced, hence the recirculating flow pattern is formed only locally, as opposed to perforated plates whose porous material covers the entire span of the interaction. Nonetheless, the technique is capable of controlling the entire shock structure, while viscous losses remain confined to narrow regions behind the slot [9]. Additionally, slots introduce streamwise vortices which could be used to delay downstream separation [45].

Surface pressure distribution around slots produced by Smith [10] indicate that they indeed have the potential of globally improving the shock while acting only locally on the flowfield (Figure 2.5b). With increasing lateral distance from the slot, the leading oblique wave moves downstream while the main leg occurs further upstream. This indicates that for increasing lateral distance the shock structure between the slots relaxes towards an uncontrolled interaction. However, the process is rather slow, and an adequate spacing ensures a global control.

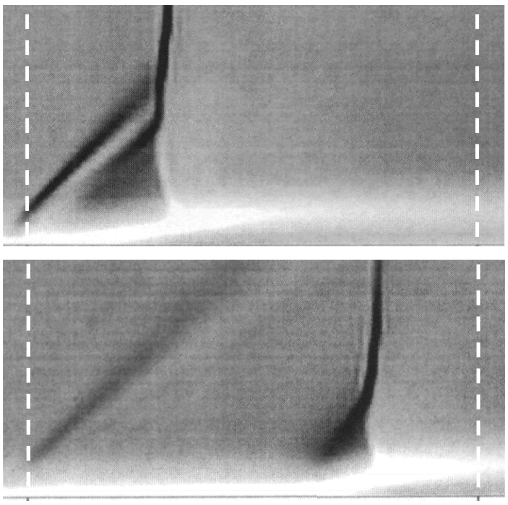

(a) Shock at upstream (top) and downstream (bottom) positions over a perforated plate [84]

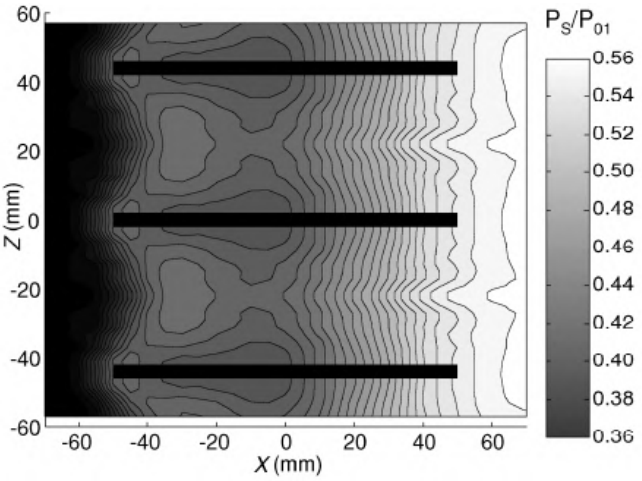

(b) Pressure contours around streamwise slots [10]

Figure 2.5: Schlieren images and pressure contours of interactions controlled respectively by perforated plate and slots.

2.5. Transonic bumps

This section outlines the literature on transonic bumps. This passive flow control device aims at improving the SWBLI by simply introducing a deformation in the surface contour. Bumps deflect the supersonic flow upwards at their leading edge, thus compressing it before the shock wave and smearing the pressure rise. Its main purpose is therefore to reduce wave drag, but secondary benefits can also be achieved, such as buffet alleviation and streamwise vortex shedding.

On-design performance

Studies around shock control bumps were inaugurated in the late 1970's. Some early designs of transonic airfoils considered the adoption of a hump to mitigate problems caused by strong shocks [85], a potential which was experimentally confirmed some years afterwards [83]. Later, in 1992, Ashill et al. [68] were the first to deploy a shock control bump as a wave drag reduction technique for laminar flow airfoils. These initial promising results stimulated more thorough research on this method, which culminated in the major EUROSHOCK II project [31], with multiple works addressing the topic. Numerical and experimental analysis of the RAE5225 supercritical airfoil with such device placed on its suction side indicated drag reductions of 8 and 14% respectively, complemented by the capacity of alleviating buffet effects [24] [49].

The beneficial impact of bumps can be seen seen in Figure 2.6a, where the pressure distribution over the upper surface of a supercritical airfoil displays a clear two-step pressure rise. It is well established that bumps can produce a positive net benefit on the efficiency of transonic wings, measured in terms of the lift-to-drag ratio [61]. However, they are mostly effective for high C_L values, when a sufficiently strong shock wave is formed (Figure 2.6b). For lower lift configurations, the contribution of the wave drag component is smaller, and smooth uncontrolled surfaces perform better [100]. It is thus argued that the full potential of shock control bumps will only be explored in next-generation wing designs, which can be developed considering the advantages of this technique [19].

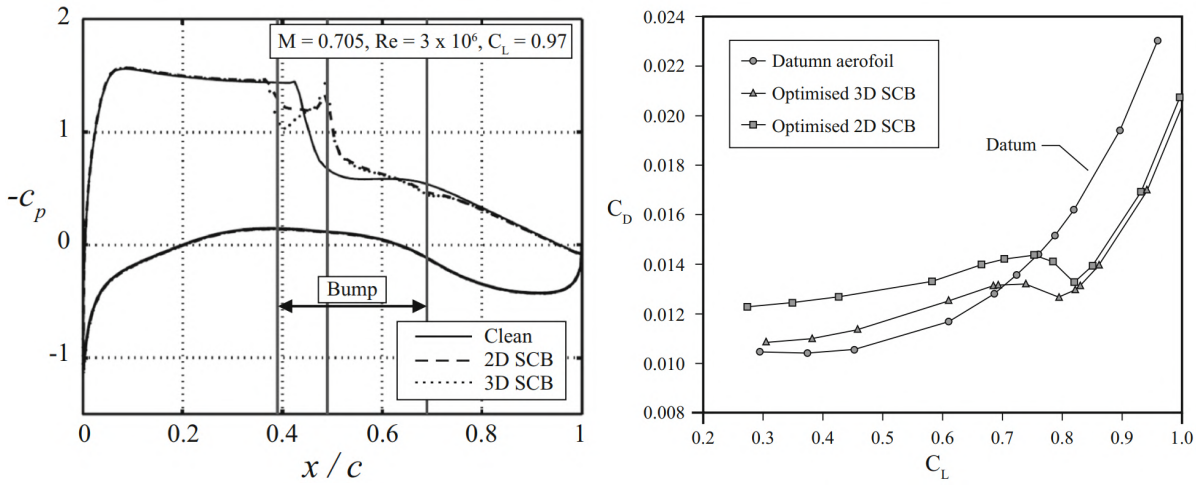

(a) C_P distribution with 2D shock control bump [32]

(b) Lift-drag polar with 2D and 3D shock control bump [61]

Figure 2.6: Pressure coefficient distribution and lift-drag polars showing the potential benefits of shock control bumps, but also the limitations of their effectiveness.

2D vs 3D shock control bumps

Two-dimensional devices are fundamentally characterised by having an infinite width, being mostly applied to two-dimensional flows. These flows are uniform in the spanwise direction, hence the geometry of the aerodynamic device remains constant over the span of the controlled region. On the other hand, three-dimensional devices do not cover the entire interaction span, having therefore a finite width. As opposed to their two-dimensional counterparts, these apparatus will act locally, thus restricting the detrimental side-effects of flow control to the vicinity of the device (similarly as seen previously for streamwise slots).

In light of these advantages, recent studies have focused more on three-dimensional bumps. When correctly designed and positioned, they are capable of globally producing the desired lambda-shock structure, being as effective as the two-dimensional variants [45] [60]. For increasing lateral distance between the devices, shock structure relaxes towards an uncontrolled interaction. Still, this relaxation is rather slow, and control effects are sustained over the spanwise direction. Qin et al. [61] compared the performance of 2D and 3D bumps over the transonic RAE5243 aerofoil. While both yielded drag reductions around 20% when shock was at the optimal location, the 3D array proved to be more robust against shock position variations. A double bump configuration with a spacing of $s_D/\delta_1 = 60$ produced a high total pressure saving of 30% while the boundary layer remained largely unaffected [66]. Another benefit of the 3D variant is reduced installation costs and complexity [19].

Off-design effects

In the EUROSHOCK II framework, it was identified that bumps can negatively affect the airfoil performance when operating at off-design. In a study conducted by Caballero [21], when the airfoil angle of attack was reduced, shock moved upstream and no longer impinged over the bump. This introduced a secondary shock system, leading to an increase in both wave and viscous drag components. Numerical simulations of bumps mounted on a full regional-jet model indicated that their effectiveness drops drastically at off-design conditions, potentially having detrimental effects for drag and buffet levels [22].

Multiple 3D control geometries (mostly asymmetric and wedge-shaped) were analysed by Ogawa et al. [66]. It was found an optimum shock position for wave drag reduction at the bump's crest (Figure 2.7c). However, the device performance was considerably affected by shock movement. For positions upstream of the optimum point, flow re-expanded over the bump, triggering additional shock systems at the crest due to re-acceleration (Figure 2.7b). But a downstream displacement proved to be the most detrimental for bump effectiveness: in this case, the formation of a significant re-expansion inside a secondary shock system was observed at the crest, followed by a thickening of the boundary layer downstream, what neutralised the total pressure recovery promoted by the lamda-structure (Figure 2.7d). Nonetheless, it is still argued that bumps can have a positive impact when operating at off-design, such as improved shock stability by pinning down the front shock leg [57].

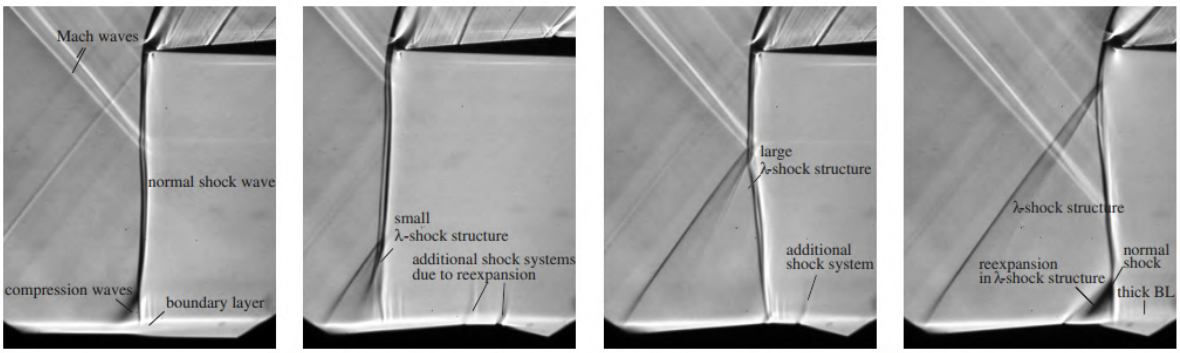

Figure 2.7: Variation of the flow structure over a wedge-shaped asymmetric bump with respect to shock position [66].

Surface parametrisation

Initial studies of transonic bumps used simple geometries often based on symmetric sinusoidal functions. Further investigations aimed at determining the ideal contour for the surface deformation, and parametrisations with the shape of asymmetrically loaded beams were adopted [59]. A bump shape optimisation study performed by Sommerer [11] concluded that the most important parameters to influence drag reduction are bump maximum height, its position and also shape asymmetry. Parametrisation methods with different number of degrees of freedom were used, but they proved to have minor influence in the resulting flow.

The main difference was noted between wedge-shaped and smooth contour bumps (Figure 2.8). While the former produces a leading oblique shock, forming the characteristic lambda-structure, the latter induces multiple compression waves which eventually coalesce in a normal shock [48]. Studies

indicate that, although smoothly contoured deformations might produce larger drag reductions when the shock is at the design point, improvements achieved by more angular wedge bumps are less susceptible to shock movement [57]. In summary, off-design performance is strongly linked with the control device geometry.

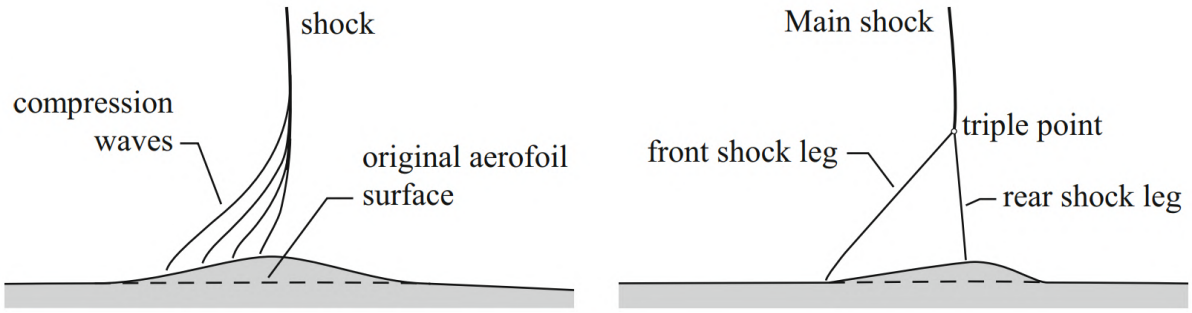

Figure 2.8: Effect of a smooth contoured (left) and wedge-shaped (right) control bump on the shock structure [19].

Another decisive parameter on bump effectiveness is the leading deflection angle, for it determines the strength of the oblique wave and consequently the pressure rise upstream of the shock. Total pressure recovery was analytically computed as a function of the leading shock deflection angle, and it was found an optimum value of θ_1=4.9° for the bump's ascending ramp [66]. However, experimental results showed that for 3D bumps the boundary layer would spill off the top of the surface deformation to its sides. This leads to a smaller effective flow deflection perceived by the outer flow, producing slightly weaker leading oblique waves.

Vorticity generation

A distinguished flow structure found over 3D bumps is the pair of vortices shed in the wake [103], and recent studies have explored the potential of this device to control the boundary layer downstream. Although its shape is not optimised for vortex production, the strength of primary vortices formed at on-design conditions is around 20% of a typical vortex generator [75], and this phenomenon has been associated with a delay of buffet onset in transonic airfoils equipped with 3D bumps [32]. The vorticity generation mechanism itself is still an open question in the literature. Wong et al. [104] attributed the event to flow separation along the bump side flanks, causing the flow to roll up in a streamwise vortex. However, since the geometry in this study had sharp edges, this proposition does not explain the vortex production for smoother bumps. Other authors propose that the action of spanwise pressure gradients cause a shear layer wrap up into a pair of vortices, but there is no consensus if their source is located at the ramp [75], on the crest [18] or towards the end of the bump tail [32].

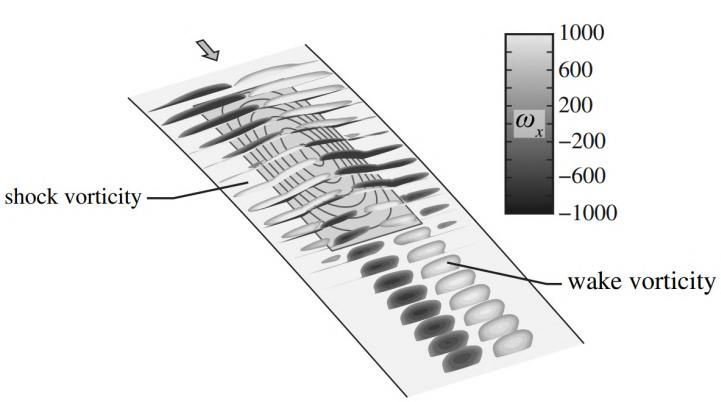

(a) Vorticity distribution over a smoothly contoured bump [74]

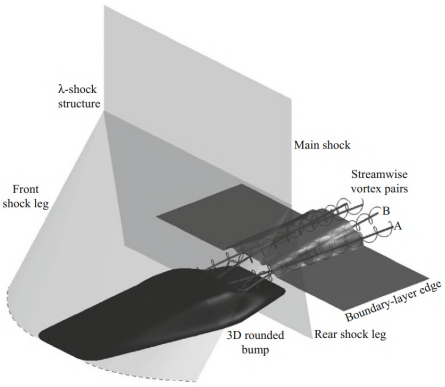

(b) Lambda-structure over bump with streamwise vortices [66]

Figure 2.9: Vorticity generation over shock control bumps.

Shortcomings and future concepts

To conclude this overview of transonic bumps, the shortcomings of this technique will be briefly evaluated. A brief description of the flow behaviour over a bump is provided to support this analysis. The simplified schematics of the flow over a 2D symmetrical surface deformation is presented in Figure 2.10. It is first assumed an incoming supersonic flow upstream of the device. At the bump's leading edge, streamlines are positively deflected by an angle of $+\theta$, what produces an oblique shock. Further downstream, around the crest, it can be seen that the deformation provokes a negative turning by an angle of $-2\,\theta$, and at the trailing edge the streamlines are again realigned to the horizontal direction.

Based on this description, it is possible to clarify the two main characteristics of effective bumps, and also to understand their limitations. The first aspect is the optimum shock location, which lies at the bump's crest so that the supersonic portion of the flow only experiences a positive deflection before the shock. However, if Ma is still larger than 1 after the deformation's apex, it suffers a stark re-expansion, as streamlines are negatively turned by twice as much as they were on the leading edge ($-2\,\theta$), an extremely undesirable effect. For this reason, shock displacements downstream of the optimum location are the most detrimental to the interaction, for they lead to re-acceleration prior to the shock, offsetting the benefits of the flow control device. To avoid this, it is required that the normal shock lies at the crest, thus ensuring that the negative turning occurs at subsonic speeds.

Another desired feature is shape asymmetry. Flow compression is convected from the bump's leading edge in the upward and downstream directions, following the Mach angle. The oblique wave eventually meets the normal shock leg at the triple point, completing the lambda-structure. All streamlines below the triple point experience a two-step pressure rise, as opposed to the single leap across the normal leg, and thus suffer lower total pressure losses. Therefore, it is desired that the triple point is located as high as possible, to ensure that a larger portion of the flow crosses the oblique shock. This is achieved by increasing the distance between the leading edge and the normal shock leg, which for optimal conditions lies at the bump's crest. Considering a fixed bump length, asymmetric shapes, with a downstream displaced apex, can produce larger lambda structures, as opposed to symmetrical ones. However, the drawback is a steeper slope after the crest, what might not only produce higher re-expansions with shock displacement but also lead to flow separation [66].

In summary, the two main shortcomings of bumps are their dependency on shock location and the fact that only their ascending portion is beneficial for the interaction. The former renders their performance sensitive to shock movement, preventing them from being used in real applications with a broad range of operating conditions. On the other hand, the latter forces the devices to assume long (and consequently tall) geometries that increase the frontal area of the airfoil, while also increasing the risk of flow separation.

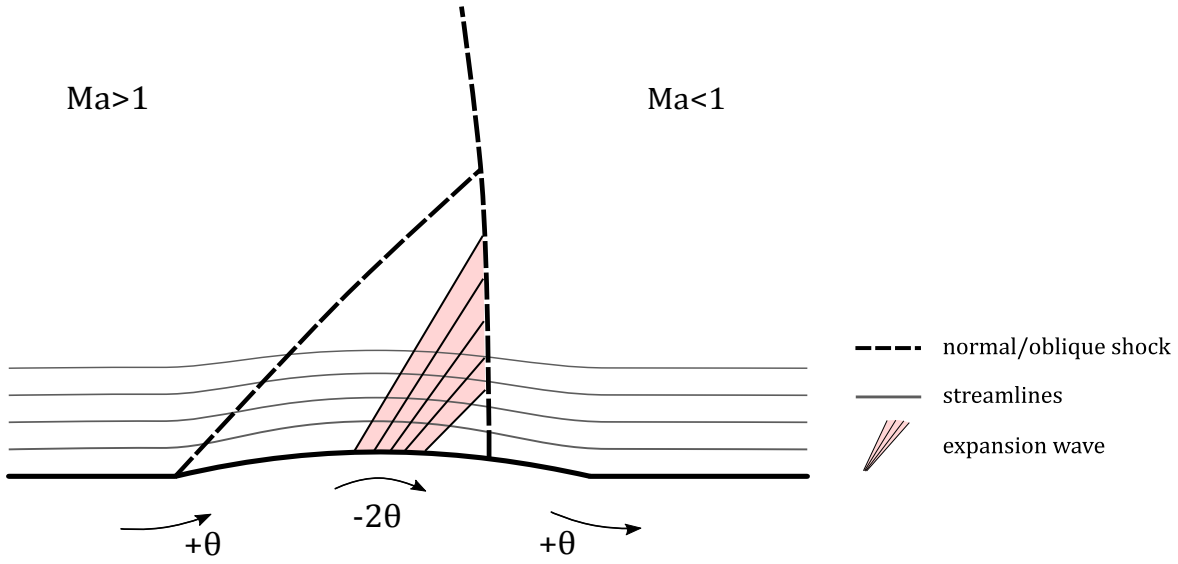

Figure 2.10: Schematics of a typical off-design shock structure over a bump.

In order to overcome the dependency of passive devices to flow conditions, research is being made on morphing (active) transonic bumps. This would allow to deploy shock control bumps in favourable conditions, and deactivate them for off-design operations [16] [81]. This approach is undermined by issues usually associated with active techniques, such as higher complexity and added weight. New approaches to the design of morphing bumps, which optimises the surface actuation while limiting material strain, might increase the potential of adopting this technology [64]. However, material compliance still constrains morphing bump to assume simpler shapes.

2.6. Dimpled surfaces

Dimples can be defined as shallow dents in the surface of a body. They're most famous for their applications in golf balls, where their role is to transition the boundary layer from laminar to a turbulent state. This delays flow separation in the back of the body during flight, thus lowering pressure drag and doubling its range when compared to a smooth ball [50]. Conversely, investigations have also explored the potential of dimples to reduce skin-friction in already turbulent flows. In 1977, Kiknadze, initially researching means of increasing heat transfer of cooling systems, by chance observed that dented surfaces reduced flow resistance [40]. Later, he patented the technology as Tornado Like Jets (TLJ) [52].

More recently at DUT, studies on dimpled surfaces have been reanimated, and the latest results are compiled in Figure 2.11. Despite the surge of research in the topic, the actual improvement in terms of viscous drag is still unclear. Works by van Nesselroij [93] and Vervoort [97] succeeded in measuring drag reduction, but display disagreeing trends. Larger Reynolds numbers were covered by van Campenhout [91], however his study mostly recorded larger drag in the analysed range. On top of that, recent DNS results from Spalart et al. [80] point in the direction of an increase of at least 1% in total drag. This lack of agreement stems from the difficulty of quantifying small drag differences, what plainly demands for more accurate measurement approaches. For a more complete overview of aerodynamic applications of dimples, the reader is referred to van Campenhout [90].

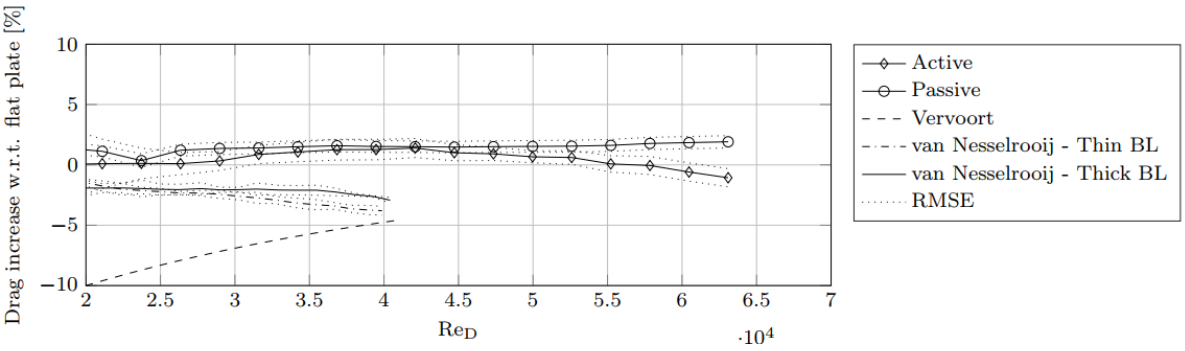

Figure 2.11: Drag variation trend against Reynolds number of best dimple design [92].

Drag reduction mechanism

There is no formed consensus on the flow mechanism that leads to dimple drag reduction. Kiknadze defends that counter-rotating flow formed in deep surface indentations cause shear stresses in the upstream direction, what opposes drag and consequently reduces it [53]. Numerical simulations from Veldhuis and Verwoort [96] identified a similar structure for deeper dents, arguing it should play a role in the total drag balance. However, experimental measurements recorded a drag increase for the deeper geometries, thus indicating that the upstream shear caused by recirculating flow does not compensate the detrimental effects of flow reattachment (Figure 2.12a). Conversely, the authors defend that drag decrease is only achieved by shallower dents, which promote a reduction of shearing forces that outweighs the pressure drag increase (Figure 2.12b). An additional theory published in Der Spiegel suggested that the tornado-like structures serve as ball-bearings that guide the main flow, reducing its resistance [105]. Nonetheless, no scientific evidence was provided to support this proposition.

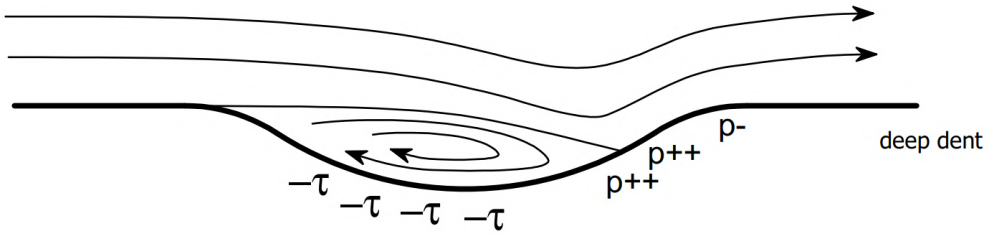

(a) Schematics of recirculating flow inside deep dimples that supports the upstream shear drag reduction theory.

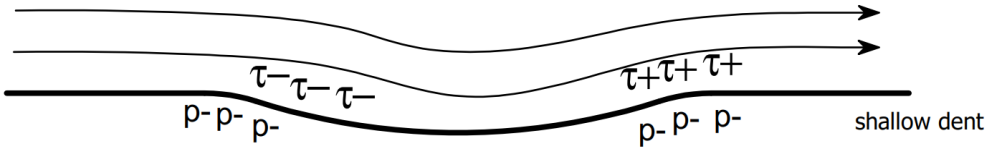

(b) Schematics of decelerating flow inside shallow dimples that supports the reduced shear shear drag reduction theory.

Figure 2.12: Representation of the flow over deep and shallow dimples which supports two drag reduction theories [96].

Currently, the most accepted explanation for the dimple drag reduction mechanism is the “Spanwise Shear” theory, independently postulated by Tay [87] and van Nesselroij [93]. It dismisses the relevance of an inner vortical structure, given that flow did not recirculate in designs that yielded reduced skin friction. Conversely, flow remained attached inside the indentations, forming a converging-diffusing topology which induces an oscillating velocity component in the spanwise direction. The theory proposes that this alternating spanwise shear would interact with the turbulent structures of the boundary layer and lead to drag reduction, in a similar fashion as the spanwise wall oscillation technique. PISFV measurements performed by van Campenhout [92] provided further evidence to support this theory. They clearly indicate that the streaklines close to the surface follow a lateral oscillating motion, thus agreeing with numerical predictions of spanwise shear distribution [93] (Figure 2.13).

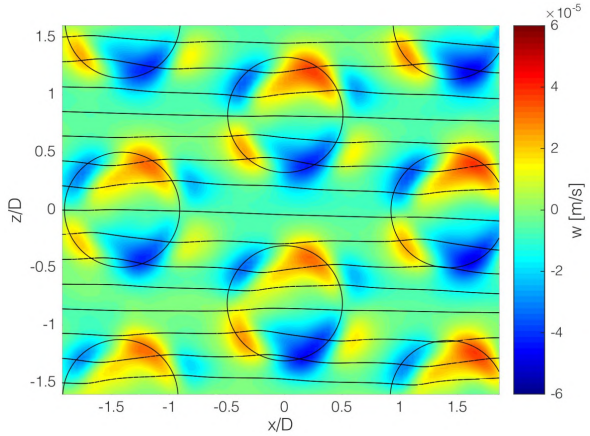

(a) Spanwise velocity contours obtained using PISFV [91].

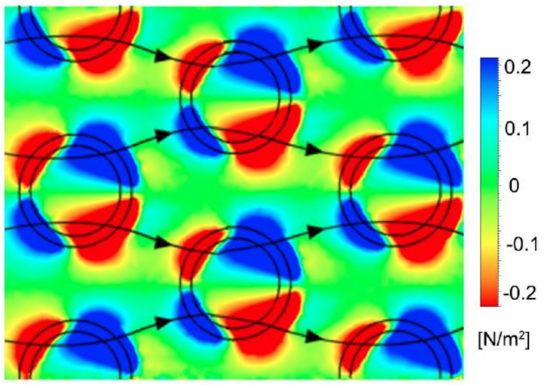

(b) Spanwise wall shear prediction from RANS simulation [93].

Figure 2.13: Experimental and numerical evidence that support ”Spanwise shear” drag reducing mechanism theory. Flow from left to right and U_∞=30m/s.

Surface parametrisation

The geometry of dented surfaces is defined by multiple degrees of freedom, all of which can potentially influence their final performance. The d/D depth-to-diameter ratio, arguably the main geometrical feature, has been kept shallow in latest publications. Vida [98] states that friction reduction is obtained for d/D=0.1, while drag reductions below 5% were measured for even shallower geometries, with d/D=0.05 [93] [86]. With respect to the dimples distribution over the surface, staggered dimples seem to be more effective in producing a periodical spanwise component, while flow-aligned patterns yielded an increase of drag [93]. The effect of the dimple edges has also been investigated. Sharp edges delay changes

in flow structures until higher Re: the flow is not smoothly directed into the dimple, thus requiring more inertial force to change its structure [20]. Conversely, it is stated that rounded edges produce smaller flow resistance, justifying its preference for drag reduction applications [88]. Additionally, works have focused on identifying the effects of area coverage [86] and dimple shape [106].

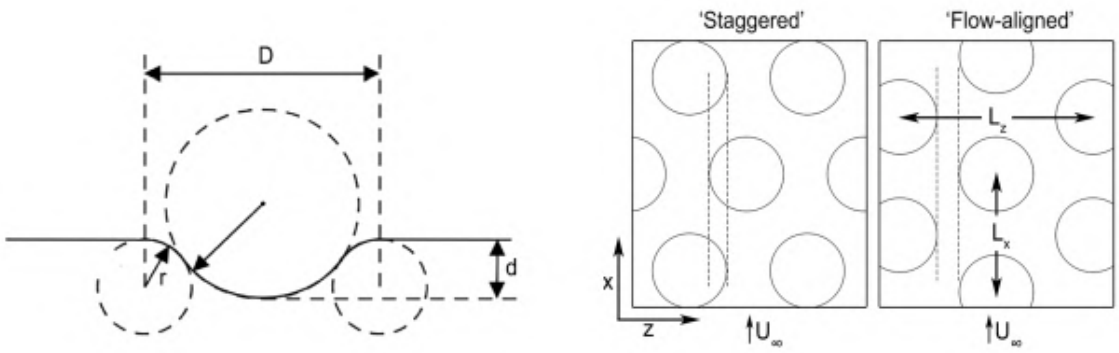

Figure 2.14: Geometrical parameters that define the geometry of a dimpled surface. Dimple depth is exaggerated for representation purposes [92].

Inflow conditions

Studies of dimpled surfaces produced at DUT give an insight of the impact of inflow conditions and pressure gradients on the performance of dimples. A marginal influence of the boundary layer thickness on drag reduction was identified, with thicker ones reducing the dimples effectiveness [93]. Moreover, the drag increase measured by van Campenhout [91] for his dimpled plates was attributed to the favourable pressure gradient introduced by the experimental setup. This condition would suppress turbulent coherent structures, rendering the spanwise-shear drag reducing mechanism inoperable. It is thus suggested that dimples should be solely applied on neutral or adverse pressure gradient flows, where these structures are maintained and promoted.

Application in high-speed flows

So far, the vast majority of aerodynamic investigations of dimples aimed at reducing viscous drag, and were restricted to incompressible low-Re flows. The only exception found in the literature is the work of Kontis et al. [51], in which dimples were placed at the leading edge of semi-cylindrical blunted shock generators with the intent of controlling the interaction with a glancing wave. No conclusive effect was determined and results were highly dependent on the orientation relative to the leading edge (Figure 2.15). It was only identified that dimples prevented the shock from moving too far downstream on the fin, what could lead to a delay of buffet onset. This application differs from other shock control devices such as transonic bumps, for the device interacts solely with the supersonic portion of the flow. It might alter the boundary layer conditions upstream of the compression and act as a leading oblique shock generator.

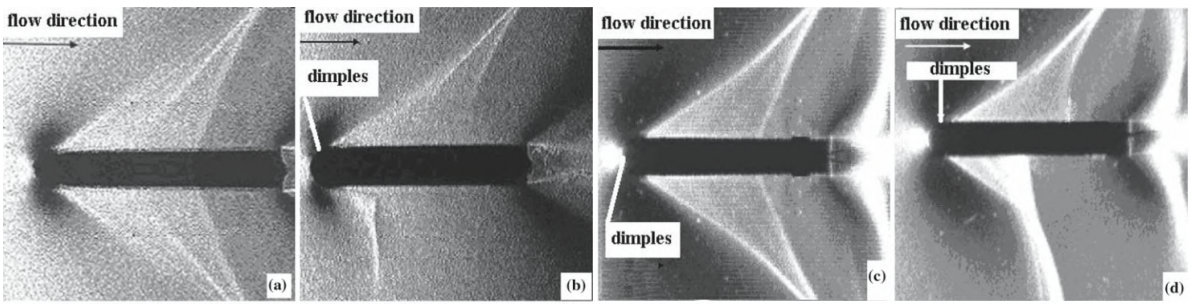

Figure 2.15: Effect of dimples on a glancing shock wave for different positions with respect to the leading edge [51].

Potential of dimples as a wave drag reduction technique

To conclude this section, it will be given a prognosis of the effects of a dimpled surface in a supersonic flow, similarly as done for bumps. A simplified schematics of the flow deflections over a round symmetrical dimple is presented in Figure 2.16. The incoming supersonic flow is negatively deflected at the dimple's leading edge by an angle of $-\theta$. Further downstream in the interior of the indentation it is turned upwards by $+2\theta$, being finally realigned to the horizontal direction at the trailing edge.

As opposed to what happens over transonic bumps, flow is expanded when entering the dimple, an undesired effect. Then it starts being compressed in the interior of the indentation, given the gradual upwards turning. If flow is still supersonic at its trailing edge, a secondary expansion fan is formed. In order to avoid this second acceleration, it is expected that the optimum shock location for the flow over dimples should lie directly over the trailing edge. This also ensures that the flow experiences the full possible compression.

A dimple in transonic flow can thus be regarded inherently as being the opposite of a shock control bump. Dimple edges clearly produce detrimental effects, with an inevitable acceleration at the leading one. Conversely, benefits for the interaction are produced at its interior, where flow is smoothly deflected upwards. In this sense, the whole length of the device favours the interaction, as opposed to bumps, where flow compression occurs only until its apex. Furthermore, a detrimental $-\theta$ at the leading edge is compensated downstream by a twice as large positive turning. With respect to its shape, a symmetrical dimple should be capable of producing compression waves in its interior, as opposed to leading oblique shocks, thus promoting a more isentropic pressure rise that would increase the total pressure recovery. On the other hand, an asymmetric shape with a larger curvature radius in the front would create a faster turning of the flow and hence produce an oblique wave, which could have the advantage of improving shock stability.

It is expected that the performance of surface indentations will be sensitive to shock displacement, but to a lesser degree given the absence of a sharp negative turning, as opposed to what occurs over the bump crest for example. Nonetheless, dimples can only succeed in reducing wave drag if a positive balance is achieved between the antagonistic flow features that arise. Besides, the unavoidable expansion fan at its leading edge is bound to limit the maximum benefit achieved when controlling the shock wave.

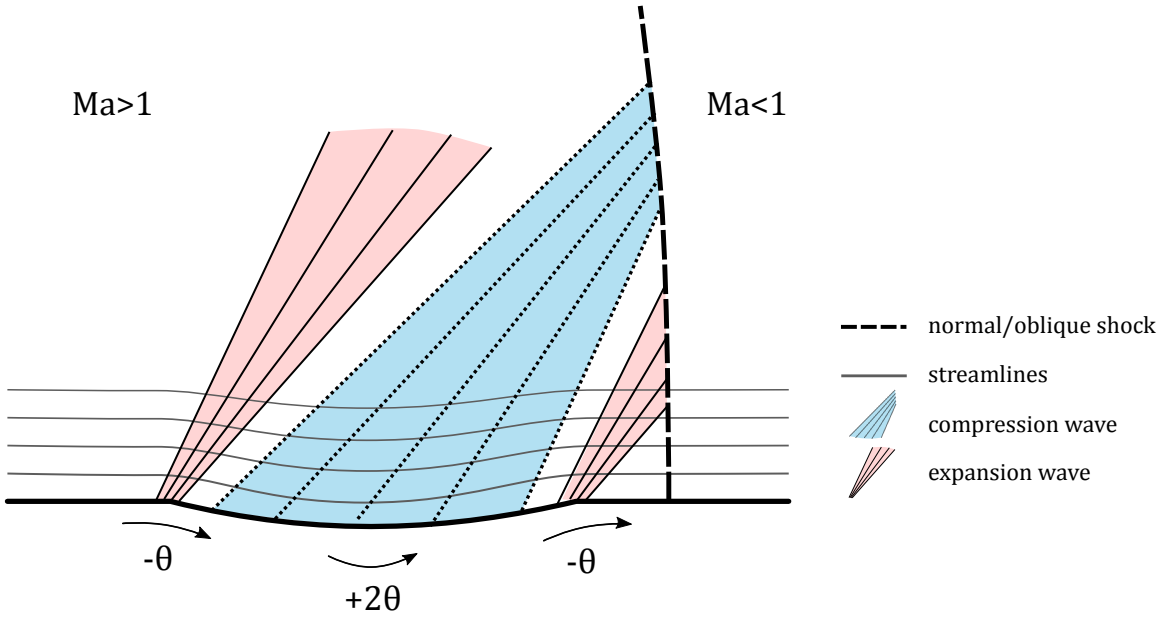

Figure 2.16: Schematics of the expected off-design shock structure over a dimple.

3

Asymmetric nozzle design

The experimental analysis of dimples in transonic flows was conducted over an asymmetric nozzle mounted in the wind tunnel. The nozzle was composed of an upper and a lower block, with test plates effectively mounted on the lower one. Their shape ultimately defined the flow conditions produced during the experiments. This chapter describes the process of re-designing the lower wall geometry, which deployed CFD simulations to tailor the resulting flowfield. First, considerations taken when designing an experiment at transonic speeds are outlined, alongside the motivations for re-designing the component. Then, simulation parameters and domain discretisation are presented, followed by the iterative process which culminated in the final lower wall geometry. The chapter is concluded by a mesh study that confirms the performance of the newly designed lower wall.

3.1. Design of experiments at transonic speeds

A main consideration to be made when experimentally analysing the aerodynamic properties of a control device in transonic regime is how to reproduce the necessary flow conditions. A straightforward approach is to have an airfoil profile subject to high subsonic speeds, and the regime of interest would naturally develop over its suction side [37]. However, due to wind tunnel size restrictions, the model would have small dimensions, resulting in a thin boundary layer and small flow structures. This prevents measurement techniques from accurately resolving local flow structures produced by the control device, thus limiting the research to global effects only.

As a result, most experimental studies are performed directly over the wall of a blowdown supersonic wind tunnel, allowing the resulting boundary layer to reach larger dimensions. The advantage of this approach is that tests are inexpensive, repeatable and focus solely on the flow close to the control device [19]. A good example is the facility at the University of Cambridge. In its initial configuration, a supersonic flow would be produced by a symmetrical confuser-diffuser nozzle attached to the test section [45] (Figure 3.1a). Although the desired conditions were achieved, the setup suffered from an increasing instability which originated from having a normal shock covering the entire channel cross-section [67]. This problem was overcome without altering the nature of the flow by installing a shock holding plate, which divides the flow in an upper unchoked part and a lower choked passage [65]. With this, a bow shock is formed ahead of the choked region. The shock position and shape are controlled by moving the holding plate forwards and backwards, and by adjusting a choking flap located downstream of the choked passage (Figure 3.1b). A similar solution was deployed Seddon [78].

An alternative way of producing transonic flows with the presence of a normal shock wave is by using an asymmetric curved test section. This method was already used in early research of shock wave-boundary layer interactions, such as in 1947 by Fage and Sargent [36]. At the DUT, the design of such testing apparatus was performed by Nebbeling [62].

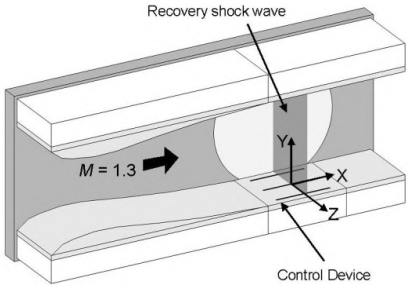

(a) Initial configuration of the supersonic wind tunnel [45].

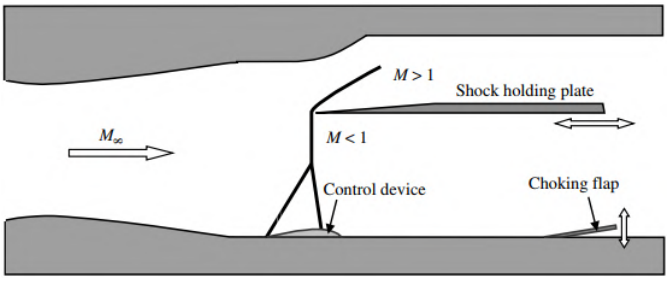

(b) Modified configuration with shock holding plate [65].

Figure 3.1: Initial and modified wind tunnel configurations at the University of Cambridge.

A curved test section is composed by non-identical upper and lower blocks which form an asymmetrical confuser-diffuser shape (Figure 3.2). While mean flow velocity is increased by varying the cross-section in the streamwise direction, flow close to the surface is accelerated or decelerated depending on the wall curvature. When properly designed, this curved test section can produce locally in the lower convex wall a supersonic pocket followed by a normal shock, flow conditions similar to those over the suction side of a transonic airfoil. The advantage of this configuration lies on the fact that a supersonic regime is never fully reached over the entire nozzle height. The shock only extends until a limited height from the lower wall, what consequently avoids the undesired unsteadiness issues reported when reproducing transonic flows using symmetrical nozzles. Additionally, the diffusing section downstream of the SWBLI allows the resulting pressure gradient to be closer to that of a transonic airfoil. Shock position can also be controlled by adjusting a choking flap downstream of the upper wall. However, as boundary layer measurements in [63] indicate, there is the risk of separation at the lower wall downstream of the compression wave, since flow has to withstand a stark adverse pressure gradient after having suffered a considerable loss of momentum.

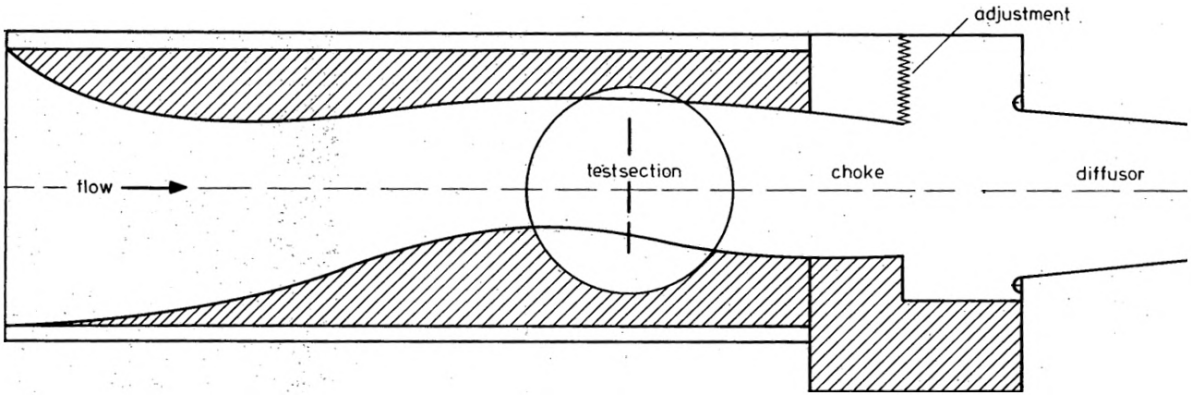

Figure 3.2: Curved test section with choke installed in the upper wall. Modified from [62].

When designing an experiment at transonic speeds, a major factor to be considered is how relevant the produced flow is when compared to that found over a transonic airfoil [19]. With respect to the boundary layer, wall-mounted experiments use the one naturally grown over the wind tunnel floor, what produces realistic values of Re_{δ_1}. Moreover, an adverse pressure gradient similar to that imposed by the convex shape of airfoils downstream of the shock must also be present, for it influences the performance of the flow control device [74]. While this feature is not present on flat-floored wind tunnels (Figure 3.3), it naturally occurs in an asymmetric test section. The main pitfall of the latter is a higher risk of flow separation, and thus its design should aim at avoiding this phenomenon. In light of this overview, an asymmetric nozzle seems to yield representative flow conditions while requiring fewer components, and is therefore the approach adopted for the experiments of the current study.

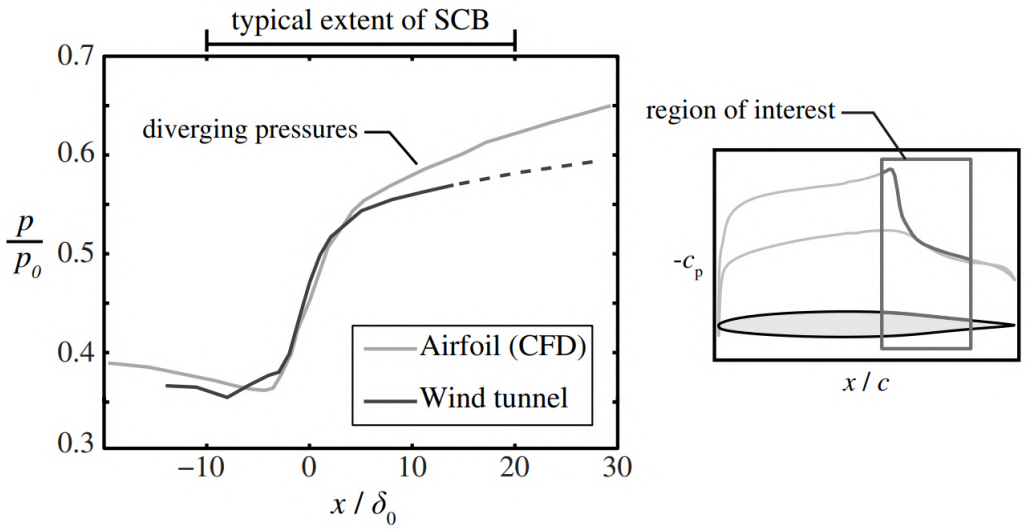

Figure 3.3: Comparison between pressure gradients over a transonic airfoil and a flat-floored wind tunnel [74].

3.2. Asymmetric nozzle re-design

In previous investigations of shock wave-boundary layer interactions at DUT, an asymmetric test section was designed to produce a transonic flow regime [62]. Its shape resulted in the formation of a supersonic pocket over the nozzle lower wall followed by a normal shock. The shock itself did not cover the entire channel cross-section, allowing for stable measurement conditions. Notably, the main component of interest is the lower wall itself, which emulates the suction side of a transonic airfoil. The upper wall mainly ensures a smooth cross-section variation over the test section.

Although all components that composed this previous setup were still available for use, the lower wall was made of a single solid block. This limited experiments to only analyse the flow field over smooth surfaces, and the influence of different shapes underneath the SWBLI could not be tested. Furthermore, boundary layer measurements performed by Nebbeling [63] over the existing nozzle indicated flow separation in the APG region downstream of the shock. This is partially a consequence of the rudimentary design methodology adopted, which failed to predict this phenomenon. These two factors motivated the re-design of lower wall shape. The main design goals for the new lower wall were:

1. Reproduce flow conditions analogous to those found over a transonic airfoil, namely a supersonic pocket terminated by a normal shock and followed by a subsonic adverse pressure gradient.
2. Ensure the normal shock does not cover the entire cross-section.
3. Avoid flow separation in the subsonic adverse pressure gradient region.
4. Design a flexible platform for future research of control techniques applied to transonic flows.

3.2.1. Simulation of initial nozzle design

The methodology adopted to design the shape of a new lower wall consisted of performing two-dimensional CFD simulations of the flow inside the channel. The initial design evaluated in this analysis was the original shape used by Nebbeling [62] (Design 0). The curves that defined the upper and lower blocks were approximated by spline curves in a CAD software. The domain to be simulated was increased by straight horizontal extensions of 0.5m upstream and downstream of the test section.

The geometry was exported to Pointwise, where a structured mesh was created inside the domain. The size of the free stream mesh elements was kept constant at 4mm. The cross-section of the channel was discretised with 120 elements. At the wall, the height of the first element was kept at $1 \cdot 10^{-5}$m to ensure a good discretisation of the inner boundary layer region, what yielded $y^+ \approx 1$. Element size would smoothly grow towards the free stream part of the flow. The mesh used to simulate the initial design can be seen in 3.4a.

The mesh was exported to the SU2 open-source solver to compute the flowfield using RANS equations. The turbulence model chosen was the Spalart-Almaras model, which can accurately predict the occurrence of flow separation, a phenomenon that the final geometry should be able to avoid. The boundary conditions were defined as in Table 3.1, and they produced an incoming Mach number at the inlet of 0.27. The computation was deemed converged when the residuals order of magnitude was reduced by a factor of 6 with respect to the initial value. Figure 3.4b shows the Mach number contour for Design 0. It also indicates the location of the origin, which was placed at the center of the lower wall leading edge and defines the global coordinate system adopted throughout the entire report.

Boundary Conditions		
Inlet	Total Pressure	195.5 kPa
	Total Temperature	290.0 K
Outlet	Static Pressure	146.0 kPa
Upper and lower channel walls	no-slip condition	

Table 3.1: Boundary conditions adopted for the simulations during the test section re-design process.

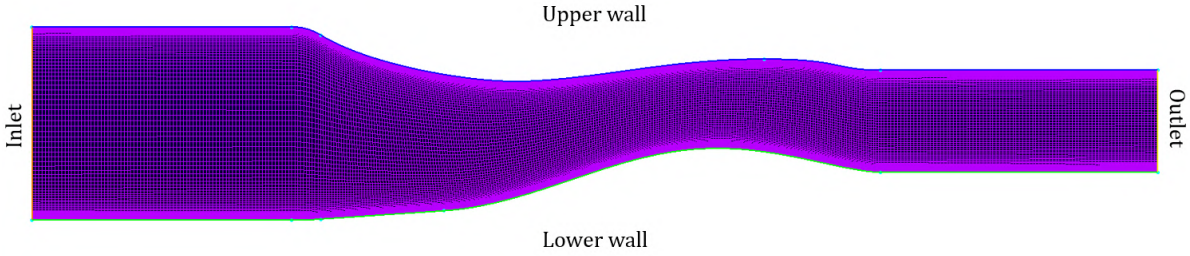

(a) Structured mesh

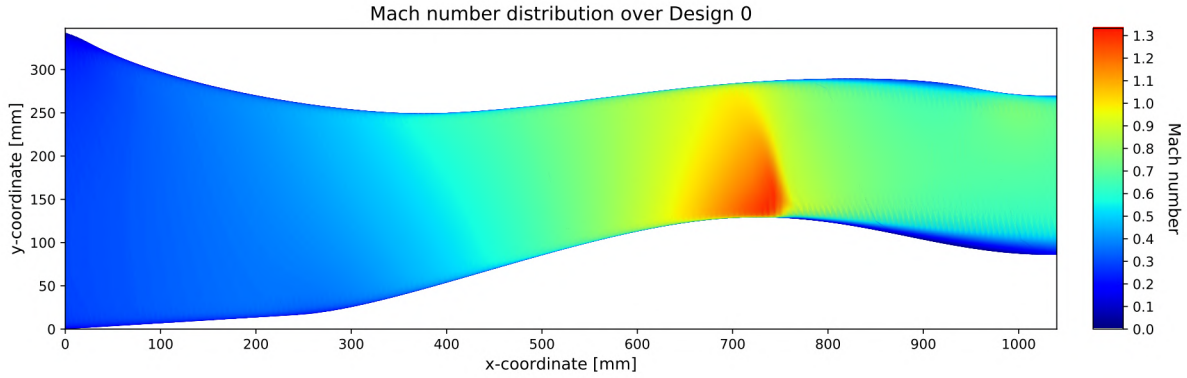

(b) Mach number distribution for lower wall Design 0.

Figure 3.4: Mesh and Mach number distribution for the initial design of the test section.

It can be seen that flow reaches a maximum Mach number of 1.35 at the crest of the lower wall, and afterwards at x=730mm a normal shock is formed. It is noteworthy to highlight that the flow near the upper wall does not reach supersonic speeds, and as a consequence the resulting shock does not cover the entire cross-section. This ensures that measurements are conducted under stable flow conditions. Finally, the simulation predicted the occurrence of a recirculating flow pattern over the lower wall in the adverse pressure region, similarly as reported by Nebbeling [63]. The relative pressure and friction coefficient distributions over the lower wall are displayed later in Figure 3.6, being compared with the results from the design iterations.

3.2.2. Nozzle design iteration

Based on the Design 0 results, the curves that define the lower wall were modified to produce a flow field that meets the re-design goals. To avoid the formation of a globally supersonic flow that would lead to a shock covering the entire nozzle, the minimum cross-section height was kept the same. However, this point was moved downstream to ensure a better optical access to the flow around the SWBLI. The geometry of the upper wall was kept the same for every simulation, since the existing block from Nebbeling [62] would be re-used in this experimental analysis. The same mesh discretisation and boundary conditions were adopted for every simulation.

The main drivers of the design iteration were the distributions of relative pressure p/p_0 and friction coefficient c_f over the lower wall. The former provided information on the Mach number upstream of the shock and on the pressure gradient downstream of it, whereas the latter was an indicator of flow separation, with negative values indicating the occurrence of this phenomenon. After some shape iterations, a lower wall geometry that best met the design requirements was achieved (Design 10). The new geometry had a steeper slope towards the crest of the lower wall, which was compensated downstream by a more gentle descent. This contributed to reduce the risk of separation downstream of the shock while maintaining at the crest a similar curvature radius, which is responsible for locally accelerating the flow.

From this result, one last geometry iteration was done (Design 11), now having in mind practical aspects of the experimental setup. The new lower wall should lodge two test sections, one to test the influence of different shapes on the SWBLI, and another downstream of it to evaluate in future works the effectiveness of control techniques under subsonic APG. With this in mind, it was decided that the first, referred from now onwards as the circular test section, at the crest of the lower wall, would be geometrically defined by an arc, which formed an angle of 8° and was centered around the point of minimum cross-section. This symmetrical shape allows for a versatile use of the manufactured test plates, since the same geometry can be attached with two different orientations. The second test section, here named the flat test section, was located downstream of the lower wall crest and was defined by a straight line with a length of 78mm. This feature would enable future investigations to perform PIV measurements parallel to the lower wall with constant wall-normal distance, in a similar way as performed by van Campenhout [92].

Figure 3.5 shows a comparison between the shapes of Designs 0, 10 and 11 near the crest, while also indicating the location of the wind tunnel optical access and streamwise position of the circular and flat test sections. In Figure 3.6 the relative pressure and friction coefficient distributions are plotted over the lower wall.

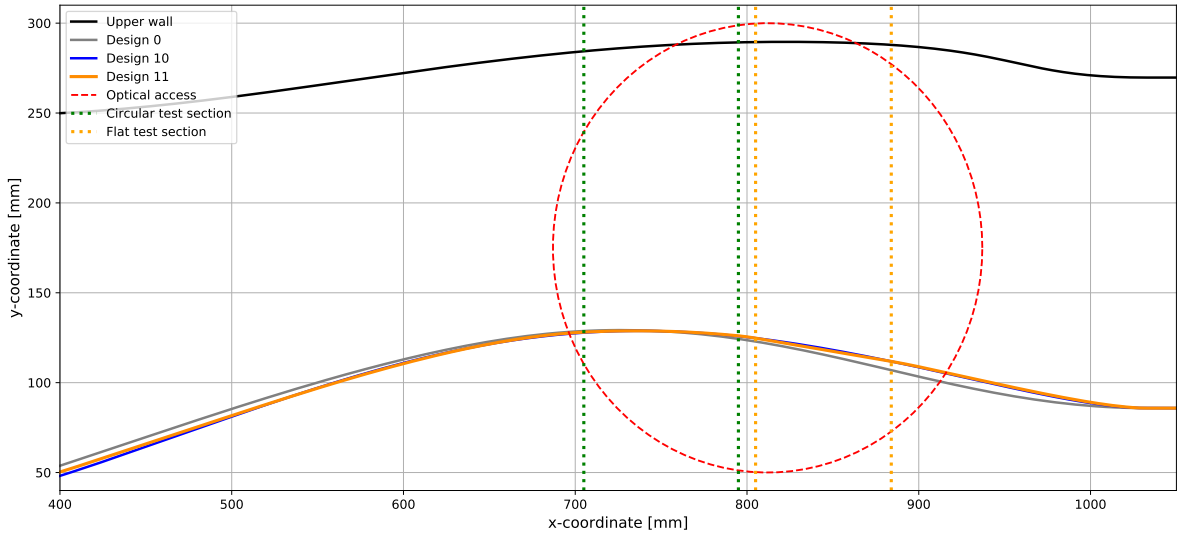

Figure 3.5: Main geometric iterations of the lower wall design.

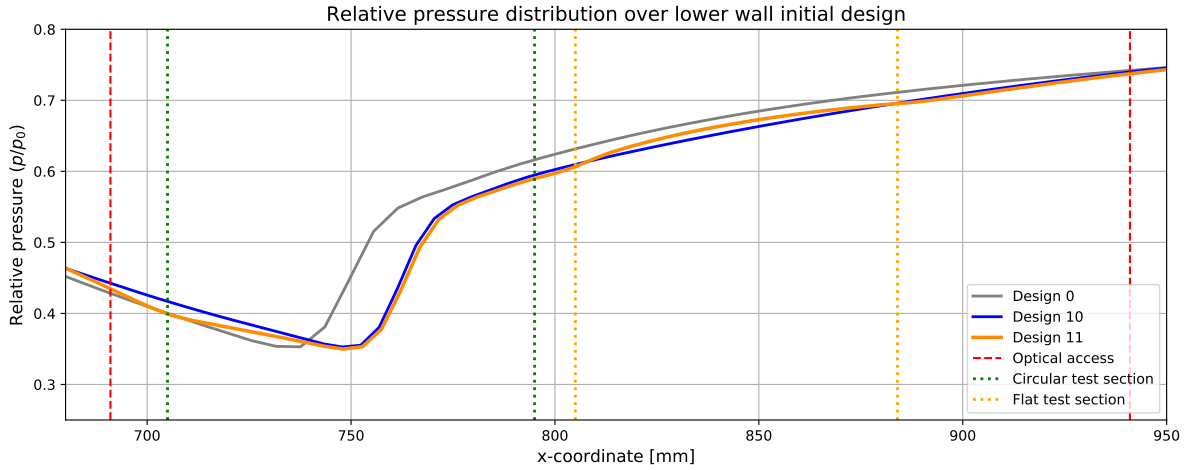

(a) Relative pressure p/p_0

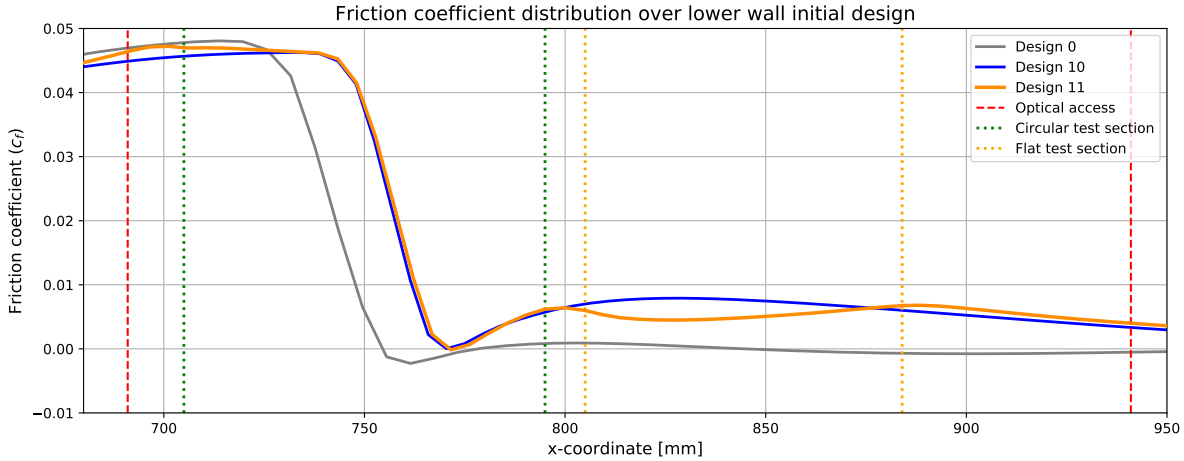

(b) Friction coefficient c_f

Figure 3.6: Relative pressure and friction coefficient distribution over lower wall Designs 0, 10 and 11.

When comparing the relative pressure and friction coefficient distributions between the first and the two last design iterations, it can be concluded that a clear improvement was achieved. The shock moved further downstream to x=760mm, what allows the flow region ahead of the SWBLI to be better captured by optical measurement techniques. Moreover, the simulation of Design 0 clearly indicates the risk of flow separation in the APG region of the original design, with values of c_f very close and even below zero. On the new designs, this quantity remains consistently positive over the entire test section.

Between the shapes of the lower wall geometry iterations, very few differences between Designs 10 and 11 can be noted. The crest region was well approximated by the arc, and only a minor divergence occurs downstream of it in the flat section. Nonetheless, this last design iteration still produced notable effects on the relative pressure and friction coefficient distributions. The plots of Design 11 are in general less smooth than the previous iterations, mainly around the flat test section, where a spline was substituted by a straight line. Still, it is not excessive, being thus a justifiable trade-off considering the experimental requirements for this section of the setup. Therefore, Design 11 was used as the new lower wall design.

Another important consideration is the equivalence of the produced flow with respect to that found over transonic airfoils, especially for the adverse pressure gradient downstream of the shock. For this, the pressure distributions over lower wall Designs 10 and 11 were compared with that found over the suction side of transonic airfoils. The reference airfoil data was taken from the work of Coliss and Babinsky [74], who simulated the section of the Pathfinder wing geometry with $Ma_\infty = 0.76$, α = 1.8° and Re=20 $\times 10^7$. In order to compare both distributions, the streamwise coordinate x was scaled based on the boundary layer height just upstream of the shock, a length scale meaningful for both the airfoil and wind tunnel flows. For the airfoil, the value provided by the authors was $(\delta)_{\text{airfoil}}$=6.0mm. For the test section simulation, it was computed at x=710mm, 50mm upstream of the shock location, yielding $(\delta)_{\text{Design 11}}$=3.5mm. The result of this analysis can be seen in Figure 3.7.

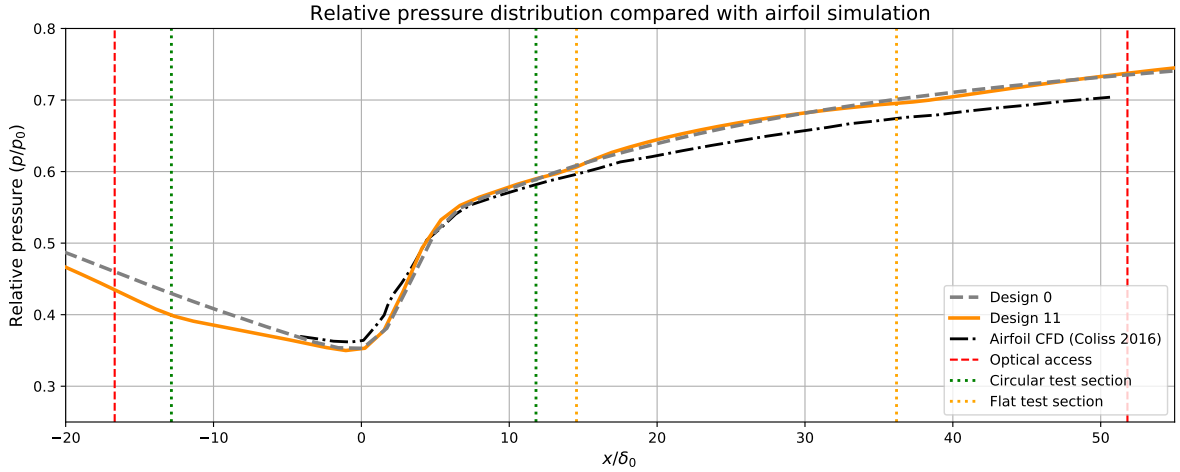

Figure 3.7: Relative pressure over lower wall designs compared with distribution over the suction side of a transonic airfoil. Airfoil data obtained from CFD simulations performed by Coliss and Babinsky [74]. Streamwise coordinate scaled based on boundary layer height upstream of shock wave.

There is a very good agreement between airfoil and wind tunnel distributions. Although, the pressure gradient over the wind tunnel lower wall is somewhat steeper than that found over the airfoil, it can still be argued that the new nozzle design naturally produces a flow representative of that found over the suction side of transonic airfoils. The distribution over Design 0, shifted downstream so that the shock location coincided with that of Design 11, displays a very similar trend in the APG region when compared to the new lower wall geometry.

A key analysis for passive SWBLI control techniques, also considered in the current work, is to evaluate their effectiveness for different shock positions. In the experimental work of Nebbeling, shock location was controlled by a choking mechanism mounted at the end of the upper wall [63]. When the choke geometry was deflected, it would alter the test section back-pressure, leading to a displacement of the shock wave. For negative choke deflections, the shock moved downstream and increased its strength, whereas positive deflections produced the contrary effect. The same mechanism will be used in the experimental setup of the current work. It was attempted to modify the shock location in the simulations by slightly changing the outlet static pressure. However, the same effect was not achieved and the shock remained pinned at the original x-coordinate. Lower outlet pressures did indeed increase the flow speed, but this was mostly convected in the wall-normal direction. As a result, the shock would cover the entire cross-section, leading to numerical instabilities and poor convergence of the computations.

This limitation of the simulations is attributed to the fact that the experimental flow conditions downstream of the nozzle are more complex than those actually simulated, since the upper and lower walls are not smoothly continuous until the wind tunnel outlet. This obstacle also prevented a direct comparison of Design 0 simulation results with the lower wall pressure distribution measured by Nebbeling [62], since the shock location in his experiments was positioned further downstream in the test section.

3.3. Mesh study

After the lower wall design was consolidated, a mesh study was performed. Its purpose was two-fold. The first was to verify the results obtained during the design iteration, which was conducted with a coarser mesh to allow the testing of various shapes. The second was to define a domain discretisation that ensured accurate results while still being computationally affordable, which would then be used in a second campaign of simulations. This second computational workstream, described with more details in Chapter 4 and Appendix C, focused on analysing two-dimensional dimples interacting with the shock, and will support the design of the experimentally tested dimpled plates.

The mesh study was performed on the final lower wall design (Design 11), referred from now on as the smooth reference case. As a starting point for refining the domain discretisation, the grid from the design iteration process was used (Mesh 0). The mesh was then further refined near the SWBLI region and results were compared to assess their sensitivity to the grid. Grid sizes evaluated can be seen in Table 3.2. In all cases, the height of the first wall element was kept at $1 \cdot 10^{-5} m$, and convergence criteria and boundary conditions (Table 3.1) were the same as for the lower wall design iteration.

	Streamwise	Wall-normal	Grid size	CPU convergence time (min)
Mesh 0	396	149	59004	112
Mesh 1	478	224	107072	234
Mesh 2	522	274	143028	353

Table 3.2: Number of elements in the streamwise and wall-normal directions, as well as the resulting total grid size, used in the mesh study.

Results of the mesh convergence study can be seen in Figure 3.9, with Table 3.3 displaying boundary layer parameters extracted upstream of the shock for the three grid sizes investigated. The disagreement between the three simulations lie on the shock location, which moves slightly downstream for increasing mesh refinement. After the pressure jump, the three curves would again merge together and follow the same pattern. The resistance against flow separation in the APG region, verified by an always positive friction coefficient distribution over the lower wall, was confirmed in the finer meshes. With respect to the incoming boundary layer parameters, there is also a good agreement between the computed values.

Grid ID	δ (mm)	δ_1 (mm)	δ_2	H
Mesh 0	3.620	0.470	0.219	2.137
Mesh 1	3.652	0.479	0.214	2.167
Mesh 2	3.534	0.471	0.219	2.179

Table 3.3: Boundary layer parameters upstream of the SWBLI for different grid sizes.

Based on the required time for the simulations (considering that the actual time is higher than CPU time) and improved computation of the shock strength and position, it was decided that Mesh 1 was the optimal domain discretisation. The distributions obtained with this grid for the lower wall design will be later compared with actual measurements from the experimental campaign, and the same discretisation was adopted in the 2D dimples simulations work stream. The final Mach number contour for Mesh 1 is presented in Figure 3.8.

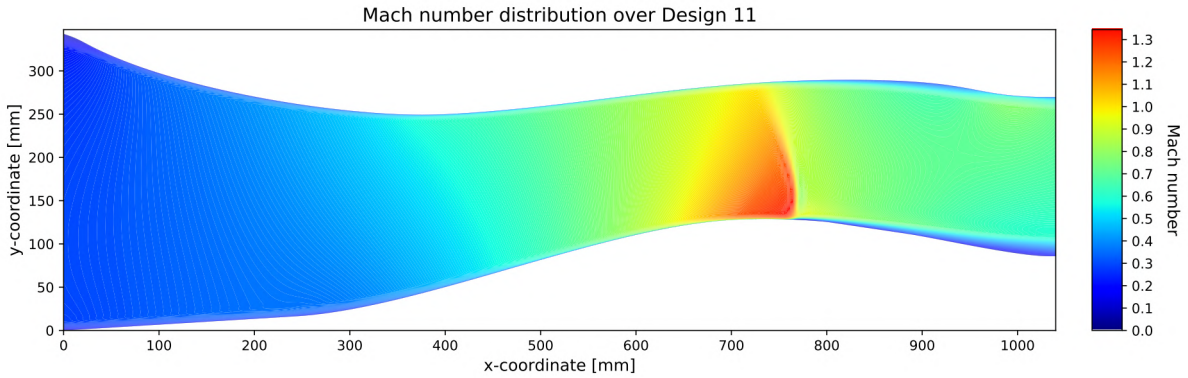

Figure 3.8: Mach number distribution for lower wall Design 11.

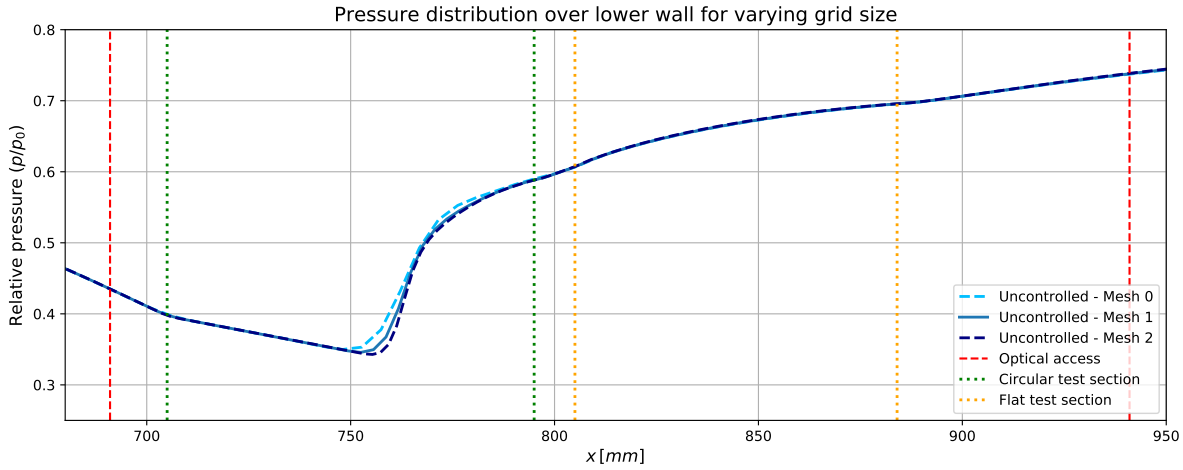

(a) Relative pressure p/p_0

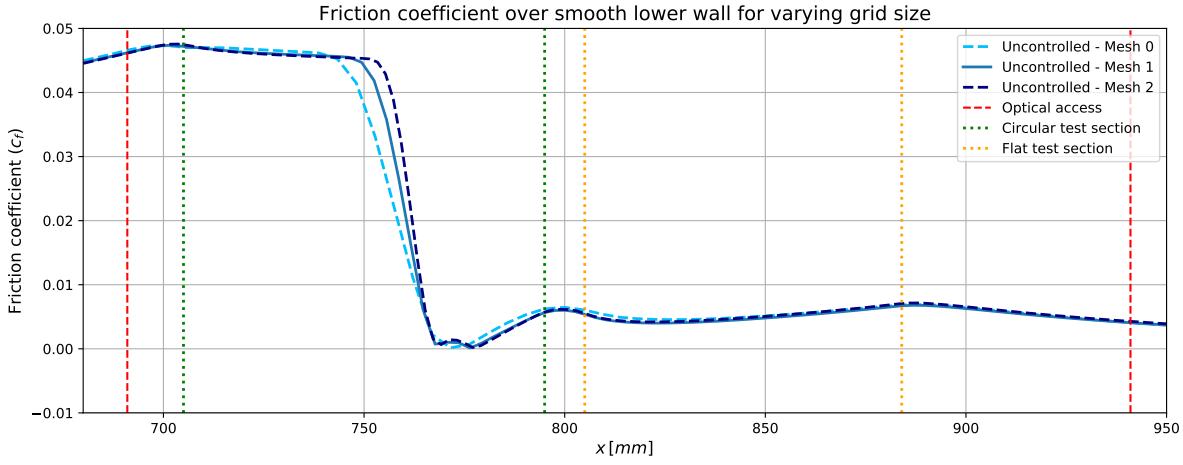

(b) Friction coefficient c_f

Figure 3.9: Friction coefficient and relative pressure distributions over smooth lower wall for different grid sizes.

4

Experiment design

This chapter outlines the methodology and motivations which drove every aspect of the experimental analysis conducted. First, it will describe the experimental facility to be used, namely the ST-15 blowdown wind tunnel, followed by the design and manufacturing process to obtain the test section. Then, the drag reduction concepts considered in this study are defined, and the dimple geometries tested in the experiments are presented. The chapter is concluded by describing the choke system, used to displace the shock in the test section.

4.1. Wind tunnel facility

The experiments were conducted in the ST-15 supersonic wind tunnel of the Delft University of Technology. A schematics of the facility can be seen in Figure 4.1. The ST-15 is a blowdown wind tunnel, a configuration in which air is stored in a large reservoir at a pressure of 40 bars and is accelerated from rest by opening a remotely-controlled valve. The flow regime produced in its test section is defined by the nozzle blocks attached to it. The test section has a width of 150mm and a length of 1044mm and an inlet height of 350mm. Uniform Mach numbers are produced by attaching symmetric blocks specific for the desired speeds. However, to generate the transonic flow conditions intended for this research, asymmetric blocks have to be deployed.

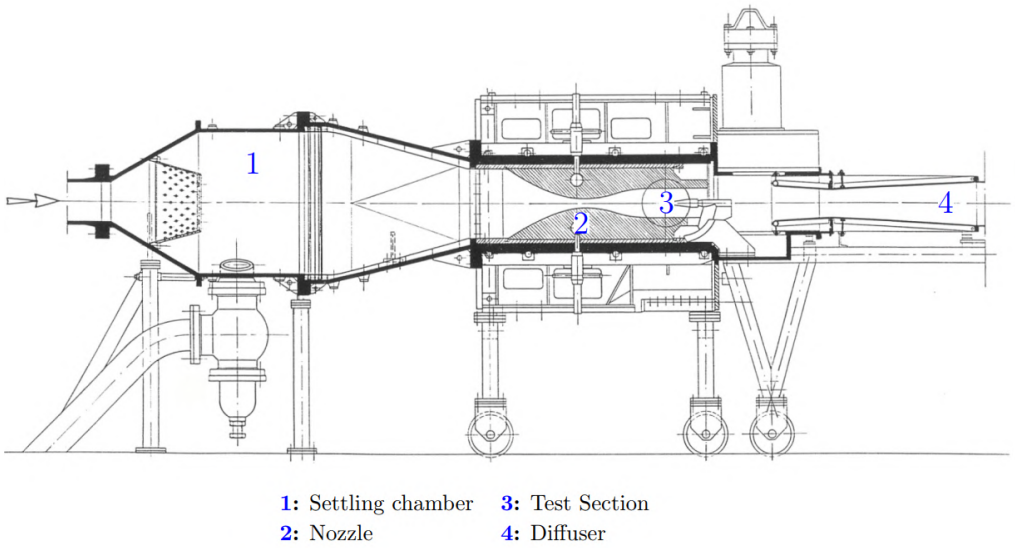

Figure 4.1: Schematics of the ST-15 blowdown wind tunnel from Flinkerbusch [38].

4.2. Assembly and manufacturing considerations for the setup

The re-design process of the nozzle lower wall was already described in Chapter 3. After its two-dimensional shape was determined, the actual components of the experimental setup had to be modelled, taking in consideration experimental and manufacturing aspects. Assembly parts should meet the following requirements imposed by the flow conditions and measurement techniques deployed:

1. Flexibility of mounting differently shaped plates in the circular and flat sections.
2. Components mechanically resistant, securely fastened to each other and fixed to the wind tunnel.
3. Tight and precise assembly between components to avoid leaks and internal recirculating patterns while ensuring a continuous surface shape.

In order to meet these requirements, the setup was composed mainly by a large lower wall block on which smaller sub-assemblies were be mounted. A more detailed description of the setup components and assembly is provided in Appendix A. The main setup components were:

1. Test section lower wall: defines the lower shape of the nozzle and the resulting flow conditions.
2. Circular test section: sub-assembly where the dimpled plates are mounted (Figure 4.3a).
3. Flat test section: location where viscous drag reducing techniques can be attached (Figure 4.3b).
4. Fastening plate: attaches the experimental setup to the wind tunnel.

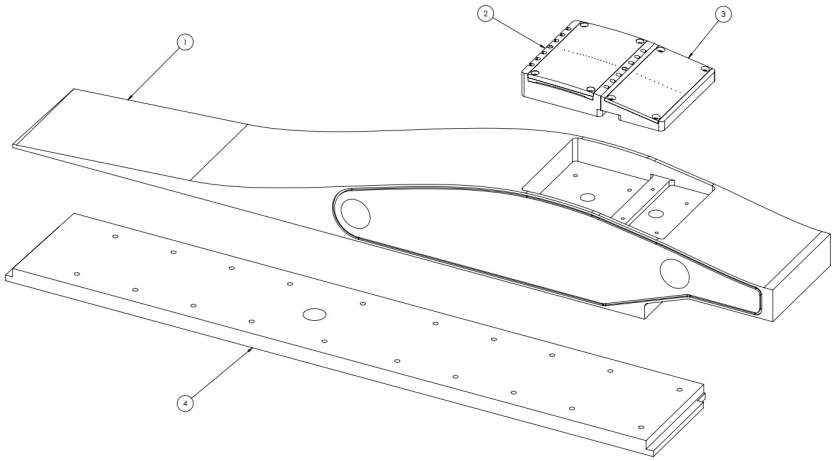

Figure 4.2: Exploded view of the main components from the lower wall experimental setup.

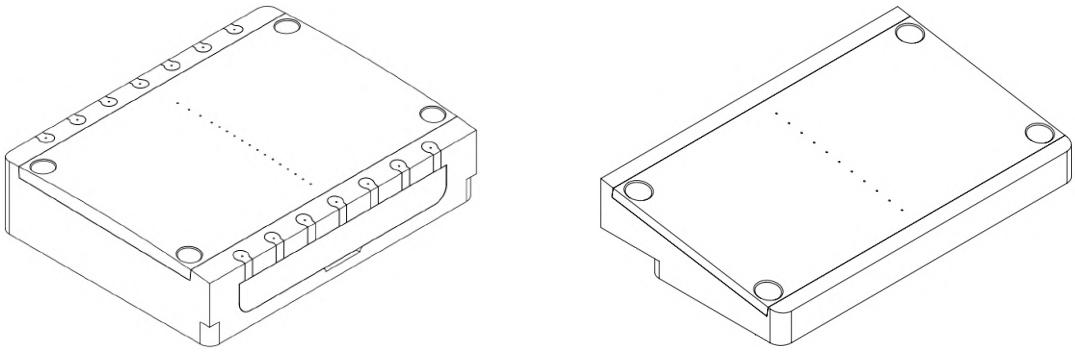

(a) Isometric view of the circular test section.

(b) Isometric view of the flat test section.

Figure 4.3: Schematics of the sub-assemblies assembled in the lower wall of the experimental setup.

4.3. Dimpled plates design methodology

The inputs that drove the design process of the dimpled plates were three-fold, and will be describonsied in this section. The first csted of identifying the degrees of freedom of the analysis that would most influence the performance of dimples on the shock wave-boundary layer interaction. The second involved proposing two different approaches with which wave drag reduction could be achieved with dimples, based on observations made from transonic bump literature. The last input considered was the results of the preliminary flow visualisation campaign and two-dimensional CFD simulations, for they provided insight on the sensitivity of the SWBLI to the degrees of freedom. Then, finally, the geometry of the dimpled plates used in the experiments can be fully defined.

4.3.1. Degrees of freedom of the analysis

For this work, a new parametrisation of the dimple geometry is proposed. It is very similar to the one suggested by van Nesselrooij [93], differing from it in only one aspect. In the works conducted at DUT until now, dimples were spherical, being thus symmetric. However, as seen in the literature review, shape asymmetry is a major degree of freedom that influences the performance of transonic bumps, and it is within the scope of this study to evaluate its effect for shock control dimples. In light of this, the indentation streamwise cross-section is defined by a front and rear sections (from leading edge to bottom and from bottom to trailing edge), both described by circumferential arcs which can assume different radii (Figure 4.4). This requires the inclusion of an extra variable. Therefore, the dimple cross-section can be fully defined in the xy-plane by the parameters: diameter (D), depth (d), edge fillet radius (r) and distance from leading edge to bottom (R). By defining these parameters, the deflection angles (θ_1 and θ_2) and curvature radii (R_1 and R_2) are implicitly specified.

From this streamwise cross-section, a two-dimensional dimple can be obtained by performing an extruded cut of a smooth reference surface in the z-direction. For a three-dimensional geometry, a circular symmetrical cross-section is drawn normal to flow direction (shaded in grey in Figure 4.4), where the desired dimple depth and width (L_w) are set. It is then used to perform two revolution cuts in a reference surface using both implicitly defined curvature radii.

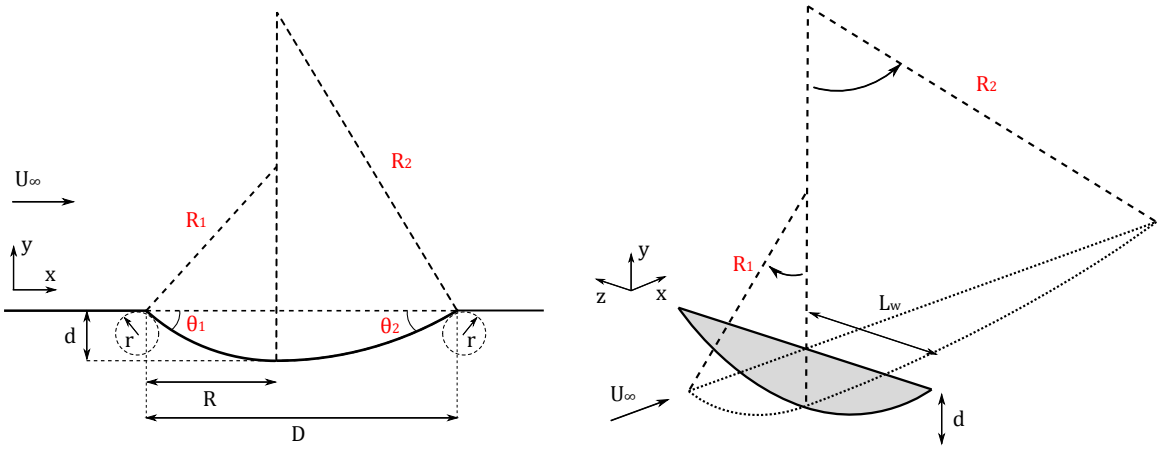

Figure 4.4: Parametrisation of the dimple geometry. Implicitly defined parameters are coloured in red.

Now the three main degrees of freedom that will drive the analysis of dimples as a shock control device are presented, being mainly supported by the transonic bump performance examination presented in Chapter 2.

Dimple size. Perturbations on the surface are convected into the freestream of a supersonic flow following the Mach angle, a function of the local Mach number. For a lambda-shock induced by deformations in the surface, a more upstream formation of the leading oblique shock leads to a larger structure in the streamwise and consequently wall-normal direction. As a result, a larger portion of the flow experiences the two-step pressure rise, what leads to a fuller total pressure profile downstream of the interaction and thus a lower wave drag.

Flow deflection angle. It directly relates to the strength of the perturbation caused in the flow, as large deflection angles lead to stronger expansion/compression waves. The flow deflection angle ultimately drives the magnitude of the pressure rise upstream of the shock, a desired flow feature that potentially increases the total pressure recovery. Taking transonic bumps as an example, Ogawa et al. [66] computed analytically the total pressure recovery as a function of the leading deflection angle, and obtained an optimum value of θ_1 = 4.9°. For surface dents, the initial deflection is negative, resulting in a flow expansion at its leading edge. This undesired effect has to be compensated by a larger positive deflection that occurs inside the dimple, which can be computed as $\theta_1 + \theta_2$.

Relative distance between the dimple and the shock wave. Although not explicitly connected to the indentation geometry, the shock displacement to be investigated has to be scaled with the dimple so to produce notable effects. Similarly as for bumps, a shock displacement further away from the optimal position is likely to reduce the effectiveness of the flow control method and possibly introduce undesired expansion fans and secondary lamda-systems.

4.3.2. Wave drag reduction approaches

Two approaches for wave drag reduction have been proposed, and they try to individually tackle the shortcomings of transonic bumps.

Smooth inverse bump

The first method proposes a dimple geometry equivalent to a symmetrical bump, but with the upside down since dimples are indentations in the surface. It is motivated by the first shortcoming of bumps identified in Chapter 2, that only the positive deflection at their leading edge is beneficial for the interaction. From one side this is advantageous, for it ensures that the first streamlines perturbation is beneficial (a positive deflection), and given that it occurs at the beginning of the geometry, pressure rise is smeared over a larger distance. However, it renders the device more susceptible to shock displacements. If the shock wave moves downstream of the crest, flow suffers a stark negative deflection of $-(\theta_1 + \theta_2)$ and consequently a stronger re-expansion. The shock optimally placed at the bump's crest prevents this phenomenon, but within the flight envelope of an aircraft, shock is likely to move to undesired positions. As reported by Ogawa et al. [66], the secondary lambda-systems that are formed rapidly offset the benefits of the leading oblique shock.

Therefore, this first approach proposes a dimple geometry defined by a long surface indentation. A detrimental expansion fan is expected at its leading edge due to the negative deflection of θ_1. However, inside the dent, flow is compressed by being gradually turned upwards. As opposed to wedge-shaped transonic bumps, where the beneficial upwards deflection is concentrated in the front of the device, in this approach it is distributed over the device's length. The smooth flow turning has also the particular advantage of allowing the formation of isentropic compression waves instead of an oblique wave, what could improve total pressure recovery.

Based on the prognosis of a transonic flow over dimples, presented in the literature review, it is expected that the optimal shock location should lie over the dimple trailing edge. It would ensure that flow fully experiences the $\theta_1 + \theta_2$ positive deflection inside the dent while avoiding re-expansion at its trailing edge. Still, a displacement of the shock is likely to deteriorate its performance. A more upstream position reduces the compression experienced by the flow, and will be followed by a small subsonic acceleration before exiting the dent. On the other hand, a downstream movement results in a secondary expansion fan, which could offset the benefits achieved by flow compression. In summary, the flow structures produced by this geometry could potentially lead to wave drag reduction, but a positive result would be dependent on a fine balance between the antagonistic expansion and compression regions, as well as on shock location.

Oblique shock generator

The second technique aims at always achieving positive wave drag reduction independent of shock position. It can be argued that the dependency on an optimal condition is the main reason that hinders the application of transonic bumps in commercial airplanes, which experience a wider range of operating conditions. Therefore, it is proposed that a small dimple is placed always upstream of the

SWBLI. Its smaller shape and starker deflection angle would generate an oblique wave to compress the flow prior to the normal shock leg. The size of the resulting lambda-system would solely depend on the normal shock location, but no additional systems are expected to appear with its displacement.

Despite the reduced dependency on shock position, the improvement of total pressure recovery, if achieved, is likely to be quite limited. In this scenario, both expansion fans at the dimple leading and trailing edges would be fully formed and convected in the main flow, thus locally increasing shock strength. As a result, the benefits of the oblique wave would have to outweigh the detrimental effects of both expansion fans in order to achieve a net improvement of wave drag.

4.3.3. Preliminary experimental and computational results

The preliminary flow visualisation campaign, described in Appendix B, had the main goal of verifying the formation of a normal shock over the re-designed test section using Schlieren measurements. But it also provided an opportunity of testing 3D printed dimple plates under the shock, and assessing how sensitive its structure was to different dimple depths. The geometries tested consisted of 2 rows of dimples with a diameter of 20mm and depth varying from 1 to 3mm.

Two important conclusions were drawn from these measurements. The first was that the shallowest geometries already produced noticeable effects on the flow field, and deeper ones displayed no signs of improvement. The second was that the flow structures arising over two rows of dimples interacted with each other, and formed an excessively complex system that prevented clear conclusions to be drawn considering the current maturity level of research on transonic dimples. Hence, a reference depth of 1mm was adopted for the final dimples, and it was decided to investigate the influence on the SWBLI of only one single row of dents.

Additionally, preliminary simulations of 2D dimples in transonic flow were performed. Dimples had not yet been tested in these conditions, and experimentally analysing the influence of all geometric parameters would lead to an excessive experimental workload. Hence, CFD computations would provide extra data to support the definition of the test plate geometries. The analysis focused on the smooth inverse bump approach, which seems to have the greatest potential of achieving wave drag reduction. A reference dimple was proposed and then modified to assess the influence of the three main degrees of freedom identified in this chapter. Simulations were kept two-dimensional to avoid large computational costs and facilitate convergence, while still yielding valuable insights on the controlled interaction. From the CFD output, it was possible to compute the mass-averaged total pressure ratio across the controlled shock, a quantity used to evaluate the performance of bumps [66].

The results of this preliminary computational study are presented in Appendix C. No dimple geometry evaluated in the simulations was able to increase the total pressure recovery over the shock, thus providing a first indication that dimples might not be able to reduce wave drag. It confirmed the presence of antagonist mechanisms in the interaction, which ultimately resulted in a total pressure deficit downstream of the shock. Nonetheless, these simulations only considered simple 2D geometries, and three-dimensional effects are still to be assessed in the experiments. A main output of this investigation was the reference dimple geometry, for which D=40mm and d=1.0mm. It produced the intended smooth pressure rise inside its geometry, influencing roughly 50% of the shock structure. Therefore, it was reused in the dimpled plate design that followed the smooth inverse bump approach.

4.3.4. Test plates design

After all inputs considered to drive the design decisions were outlined, the geometries of the test plates used in the experimental analysis of this work can be finally presented.

Smooth reference plate

The first test body to be described is the smooth reference plate (Figure 4.5). It was used to characterise the flowfield in the newly designed nozzle and served as a benchmark to be later compared with the dimpled cases. Its upper surface follows a circular arc with a radius of 647mm and an 8° angle, whereas its bottom is flat to fit the printed circular section block. The plate had a width of 140mm.

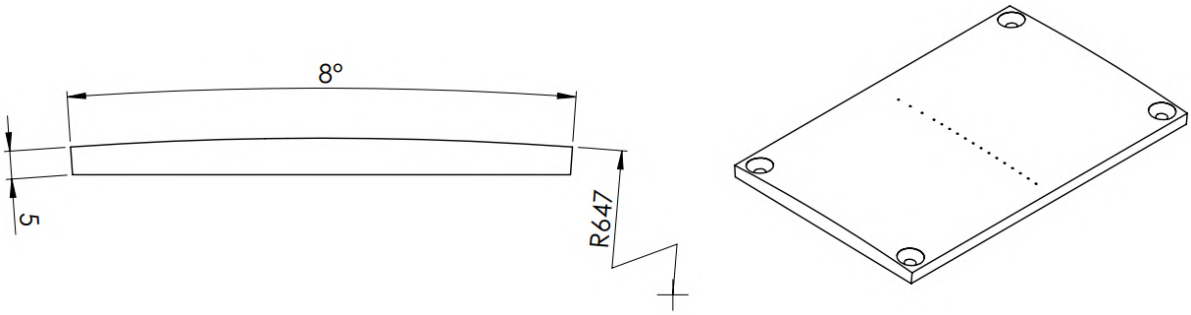

Figure 4.5: Right and isometric views of the smooth reference plate.

Dimpled plates

A total of five dimpled plate models were manufactured. They were designed to provide insight on key performance criteria, which were identified as relevant from the literature on transonic bumps. The increased understanding of the flow behaviour over transonic dimples, considered the main output of this thesis, can then be used in future works for more in-depth investigations. The dimpled test plates allowed to analyse the following aspects of passive wave drag reduction methods:

- Drag reduction approach: smooth inverse bump vs. oblique shock generator
- Device dimensionality: two-dimensional vs. three-dimensional indentations
- Shape parametrisation: symmetric vs. asymmetric shapes

The first two plates focused on assessing the two proposed drag reduction methods, namely the application of dimples as a leading oblique shock generator (D20d10-2D) and as a smooth inverse bump (D40d10-2D). Similarly to the initial studies of transonic bumps, their shape was kept largely two-dimensional in order to simplify the phenomenon by eliminating the spanwise velocity component in the middle of the plate. This facilitates the evaluation of the main flow structures, that arise when streamlines are deflected upwards and downwards, and additionally allows a direct comparison with 2D CFD data. As the identification code indicates, these surface indentations had a length of 20 and 40mm respectively (indicated by D) and both had a depth of 1.0mm (indicated by d).

As investigations on transonic bumps matured, it was noted that an array of deformations with finite width could also globally control the shock, being as effective as their 2D variants while restricting detrimental effects to their vicinity [45]. Therefore, the next two dimpled plates (D20d10-3D and D40d10-3D) were 3D versions of the previous ones. This provides an assessment of three-dimensional effects and how local modifications in the interaction are propagated to the rest of the flow.

Attempts to optimise the shape of transonic bumps indicated that asymmetric deformations were less susceptible to off-design shock locations [11]. Hence, the fifth test plate (R10D40d10-3D) consisted of an asymmetric 3D version of the inverse bump approach, a configuration expected to be vulnerable to shock movement. Although its length was kept the same as the D40d10-3D (40mm), the distance between its leading edge and bottom (denoted by R) was reduced to 10mm, as opposed to the 20mm obtained in the symmetric dent, thus rendering it an asymmetric shape. This last geometry is also a combination of the two former 3D plates. It has the same leading curvature radius and deflection angle as the oblique shock generator, and the length of the inverse bump. An overview of the geometrical parameters of the five test plates is provided in Table 4.1.

All dimples had their leading edge starting in the same x-coordinate of 719.5mm, 15mm downstream from the beginning of the circular plate. For the three-dimensional geometries, the chosen width was $L_W = 20$mm, based on the diameter of the indentations previously analysed in DUT [92]. The spacing between 3D dimples was determined by the BL displacement thickness upstream of the shock, similarly as done by Ogawa et al. [66], who tested spacings of 40, 60 and 100 δ_1. The value chosen for this analysis was 70 δ_1, to allow a good resolution of the SWBLI spanwise relaxation. The displacement thickness was computed from the Design 11 simulation results (Mesh 2), which produced $\delta_1 = 0.47$ mm at the beginning of the circular section, thus yielding a lateral spacing of $s_D = 33$ mm.

Plate ID	D (mm)	d (mm)	r (mm)	R (mm)	L_W (mm)	θ_1	θ_2
D40d10-2D	40	1.0	10	20	120	5.7°	5.7°
D40d10-3D					20		
D20d10-2D	20	1.0	10	10	120	11.4°	11.4°
D20d10-3D					20		
R10D40d10-3D	40	1.0	10	10	20	11.4°	3.8°

Table 4.1: Overview of geometrical parameters of tested dimpled plates.

A total of 4 dimples were fitted over the span of each 3D dimple plate, in a pattern mirrored around the wind tunnel symmetry. With respect to the two-dimensional dimple geometries, they did not cover the entire span of the nozzle lower wall, given that plates still interfaced with the sides of the block. The circular plates had a width of 140mm and the 2D shape of the dimple covered 100mm. At the edges, the geometry of half a 3D dimple is adopted for a smooth surface transition, hence producing a total indentation width of 120mm. It can thus be expected that the flowfield will be two-dimensional around the symmetry of the test section, where all measurements will be made. All dimples had rounded edges with a radius r=10mm. Test plates were manufactured by CNC milling aluminium blocks.

4.4. Shock displacement

Shock displacement is expected to considerably influence the effect of dimples in the SWBLI, the same way as occurs with other passive shock control methods, such as bumps and perforated plates. First, the shock locations o interest have to be defined. Then, the choke system is described, a mechanism mounted on the upper wall responsible for moving the shock wave during measurements.

4.4.1. Shock locations

In order to assess the effects of shock displacement, three shock locations were evaluated. The centered shock position was determined as being the optimum for the inverse bump configuration. From the prognosis provided for a transonic flow over an indentation, it is expected that the prime location lies over the dimple trailing edge. This way, the full compression potential of the indentation is harnessed while avoiding the formation of a second expansion fan. Then, two off-design shock positions are to be analysed, one upstream and another downstream of the optimum location. The former was placed over the bottom of the symmetrical indentation (D40d10-2D & 3D), for it would be analogous to the optimum shock position for shock control bumps, namely at their crest. Conversely, for a symmetrical analysis, the latter was placed downstream with the same spacing with respect to the centered shock as the upstream location.

Shock displacement relative to the centered case was $\Delta x_S = \pm 20$mm, close to the range of ± 25mm evaluated by Ogawa et a. [66]. With respect to the oblique shock-generating dimples (D20d10-2D & 3D), they were envisioned to be placed always upstream of the normal shock leg, and the chosen shock locations guarantee this, with the upstream one positioned just over their trailing edge. Figure 4.6 shows the cross-section of the indentations analysed alongside the three shock locations of interest. Figure 4.7 shows a top view of the five dimpled plates used in the experiments, in which the three shock locations of interest are identified with respect to the control devices.

4.4.2. Choke system

The objective of the choke system is to perform a remote fine tuning of the shock location, thus allowing multiple flow cases to be analysed in a single wind tunnel run. It consists of a metallic plate that covers the full span of the upper wall, and its leading edge at x=815mm coincides with the centre of the optical access window. It is mounted to the main upper block structure in such a way that it can be set at different heights, ultimately changing the shape of the upper nozzle wall. Additionally, it is equipped with a mechanism controlled by an electronic circuit that deflects a small flap located at its trailing edge.

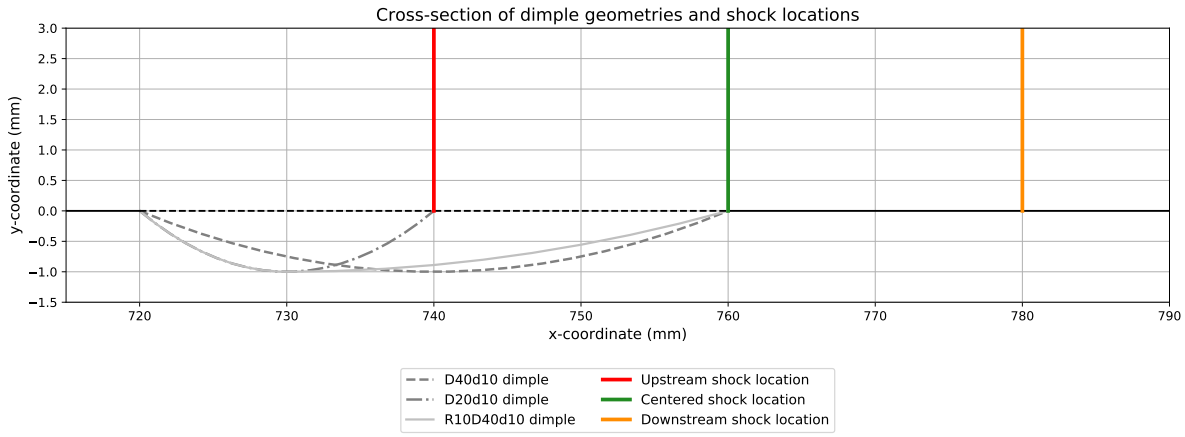

Figure 4.6: Cross-section of dimple geometries with shock locations.

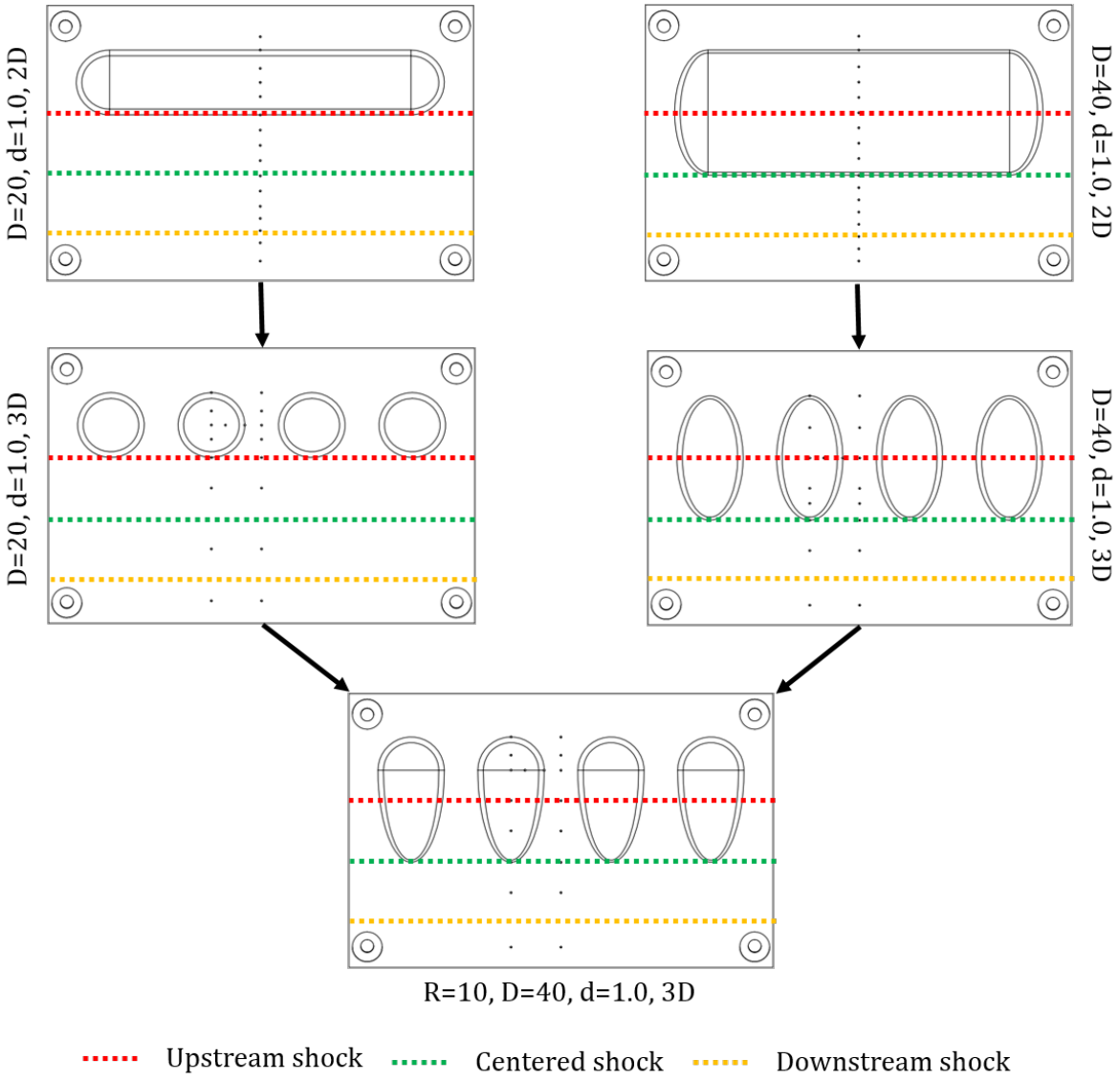

Figure 4.7: Top view of the five dimpled plates, alongside shock locations and pressure tap distribution. Flow direction is from top to bottom.

The main component of the electronic circuit is a step motor, whose rotation is converted to the deflection of a flap, hinged at the end of the choke plate. The motor displacement is done by a feedback loop. A reference voltage is externally provided by a DC power supply, located in the wind tunnel control room. Attached to the flap is a rod that slides in and out of a potentiometer when the system moves. The feedback loop compares the potentiometer readings with the power supply input, and defines if the motor should move as to deflect the flap upwards or downwards. The input voltage ranged from 0 to 2V, with the maximum input yielding the largest deflection. Each value corresponded to a unique flap deflection, what should ensure good repeatability of flow conditions. Furthermore, the input signal from the power supply was reduced by a factor of 10 before being sent to the feedback loop, what increased the input sensitivity and consequently reflected in a finer tuning of the shock position.

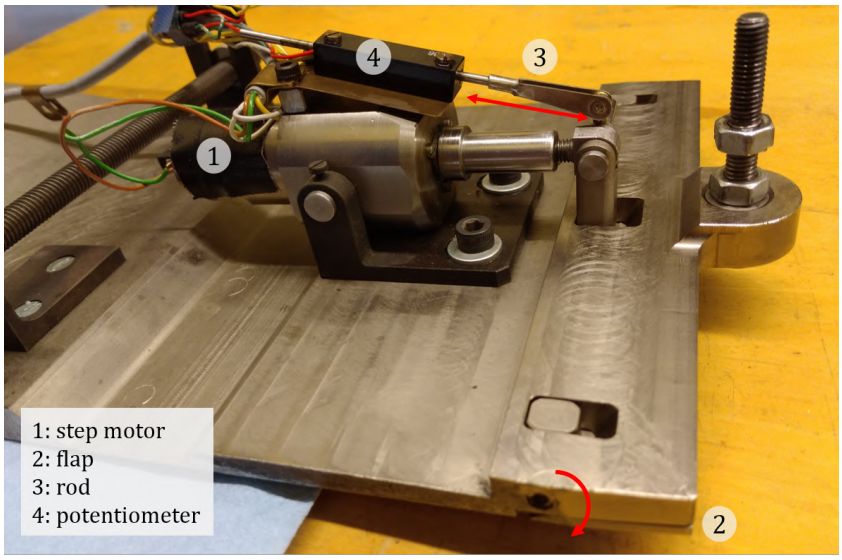

(a) Choke system mounted in the end of the upper wall of the test section. Red arrows indicate the mechanism movement during choke deflection.

(b) Upper and lower test section blocks assembled in the ST-15 wind tunnel.

Figure 4.8: Setup components mounted in the wind tunnel test section, with a focus on the choke system components and its working mechanism.

5

Measurement methodology

This chapter describes the methodology adopted for the different measurement techniques deployed during the experimental analysis. It covers the motivation for choosing each technique, the acquisition parameters as well as their setup and hardware. The techniques used were Schlieren visualisation, surface pressure measurement and Particle Image Velocimetry (PIV). Finally, the experimental considerations and organisation of both measurement campaigns are outlined.

5.1. Schlieren visualisation

Schlieren is arguably the main visualisation technique for compressible flows. It is based on the principle that light does not propagate uniformly in inhomogeneous mediums [12]. Light direction is altered when there is a change in the environment's refraction index, which in turn is dependent on the medium density. When two parallel light beams pass through an inhomogeneous medium with different refractive indices, they are deflected at different angles, allowing for the visualisation of flow structures with substantial density gradients. This is particularly useful in high-speed aerodynamics to identify compression and expansion waves in the flowfield.

The refractive index n is in essence the ratio between the local and vacuum light speed, and relates to the medium density as shown in the Gladstone-Dale equation:

$$n = \frac{c}{c_0} = 1 + K\,\rho \tag{5.1}$$

where:

- K: the Gladstone-Dale constant
- ρ: fluid medium static density
- c and c_0: light speed in the specific medium and in vacuum respectively

In the context of this work, Schlieren will provide a qualitative characterisation of the flow structures that arise from the interaction between shock and dimple, supporting the interpretation of pressure distributions recorded in the test plates surface. The measurement technique setup is now described. Light emitted from a source passed through a pair of lenses and a pin hole in order to become a single collimated source. It was then reflected by a mirror to illuminate the test section. Afterwards, it was again reflected to pass by a knife edge before being captured by the camera's sensor. In the test section, differences in the medium's refractive index distribution caused deflections in the light path, which in turn resulted in a larger or smaller light blockage at the knife edge. Hence, changes in the density distribution ultimately modified the gray-scale in the final image captured by the camera.

A schematics of the setup used for the measurement campaign can be seen in Figure 5.1a, and the equipment is further detailed in Table 5.1. It must be noted that the system is sensitive only in the direction normal to the knife-edge (Figure 5.1b). For the purposes of capturing the normal shock wave over the test section lower wall, the knife edge was vertically oriented.

ID	Item	Description
1	Light source	LED THORLABS MCWHLP1: 405 [nm] light, 1200 [mW] power, THORLABS-LEDD1B controller
2	Collimating lens	F2.5 f = 178 [mm]
3	Convex lens	Focal length f = 100 [mm]
5, 6	Mirrors	Large parabolic mirrors (parallel to test section)
8	Convex lens	Focal length f = 150[mm]
9	Camera	Photrom Fastcam SA1.1

Table 5.1: Detailed overview of the equipment used in the Schlieren setup.

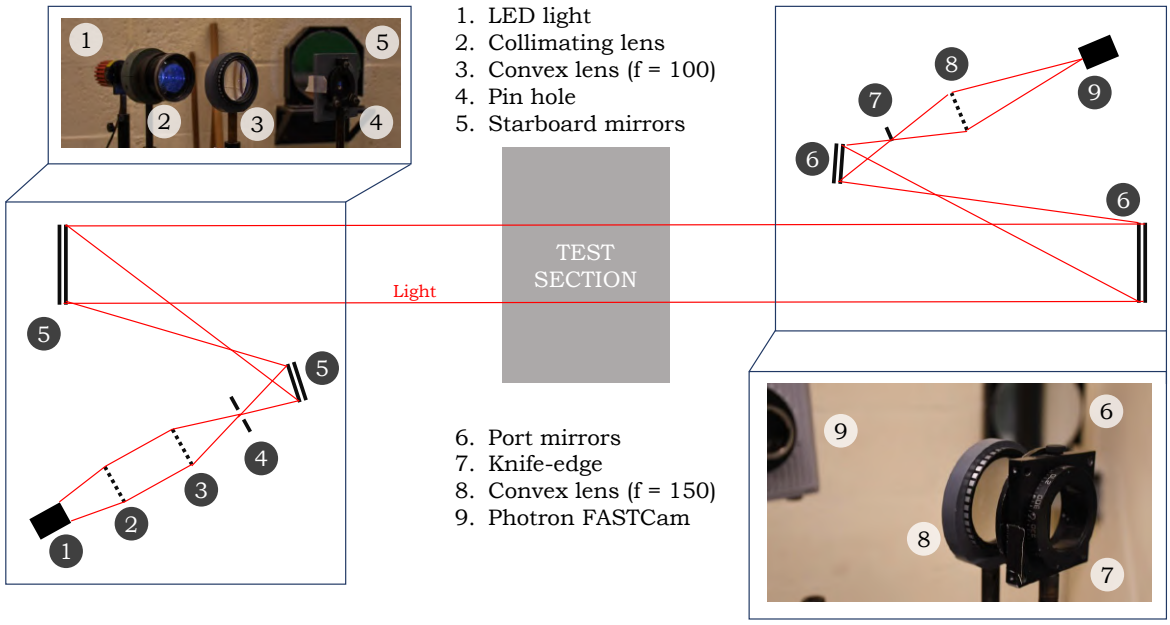

(a) Overview of the setup used for the Schlieren technique

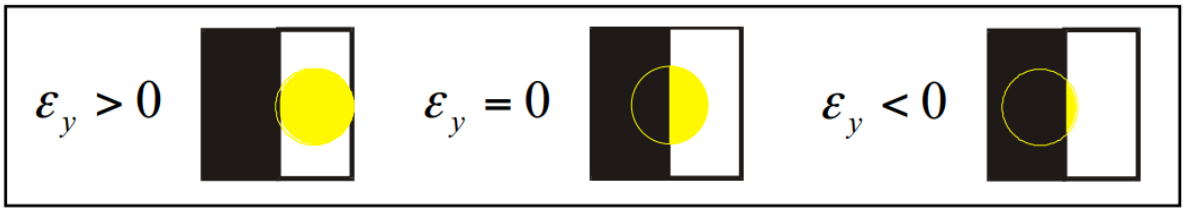

(b) Schematics of light blockage at the knife for larger and smaller light path deflections

Figure 5.1: Setup adopted for the Schlieren visualisation, including the schematics of the knife edge blockage.

The resolution of the Schlieren image was obtained by placing a calibration plate with millimetre paper over the test section and computing how many pixels were present over a known distance. The resolution obtained was of 4.61 pixels per millimetre, and allowed the images to be scaled to metric length dimensions during post-processing. Images were recorded for all measurements at a low frequency of 50 frames per second.

During the Schlieren recording of a wind tunnel run, it was of prime importance to have a real-time identification of the current shock location for a given choke deflection. This was obtained by placing vertical strings over the optical access window at the three shock locations of interest with the aid of a calibration plate. Figure 5.2 shows the scaled Schlieren image of the test section without flow motion. Coordinates follow the test section global coordinate system defined in Chapter 3.

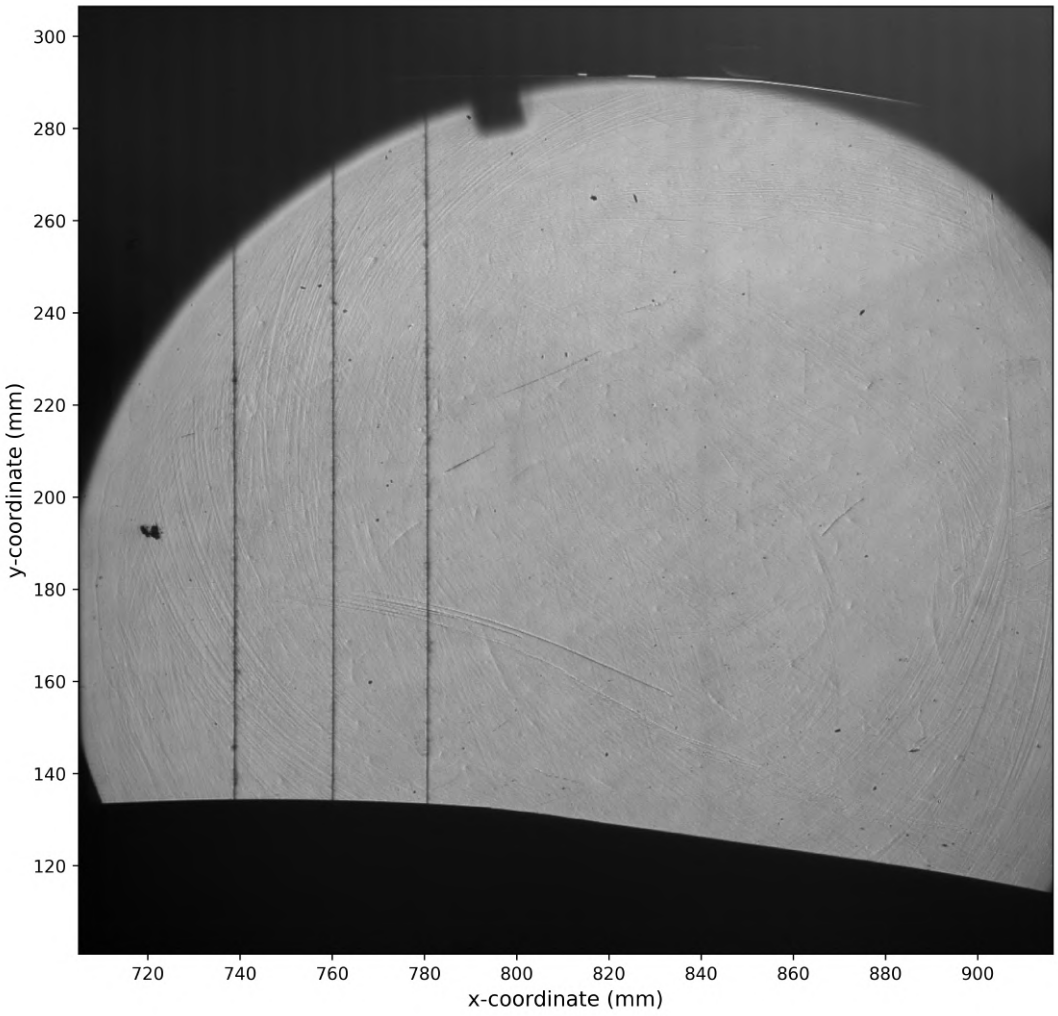

Figure 5.2: Test section image captured by the Schlieren system, scaled to actual model dimensions and positioned relative to the assembly coordinate system.

5.2. Surface pressure measurements

Surface pressure measurement is a simple technique that allows for a good understanding of the flow phenomena that occurs close to the wall, such as expansion and compression regions. Results will be used to characterise the flow over the smooth reference case of the newly designed lower nozzle wall and to measure the influence of dimples in the SWBLI. Additionally, data acquired can be easily compared with results from the CFD simulations. The technique consists of drilling small orifices, also referred as taps, in the model surface, where pressure information is retrieved by capillary tubes and read by a scanner. In this section, the surface pressure taps distribution is presented, followed by a description of the equipment used to acquire this information.

Additionally, surface pressure measurements also provided data that characterised and validated the experimental setup in the following aspects:

- **Time required for the flow to reach steady conditions.** The time evolution of pressure measurements indicate the interval necessary for the pressure and hence the flow to stabilise after the wind tunnel is started.
- **Two-dimensionality of incoming flowfield.** Measurements can be performed upstream of the circular test section over both wind tunnel side walls, allowing an evaluation of the spanwise uniformity of the incoming flow.
- **Hysteresis effects.** A key assessment of dimple performance will be its sensitivity to shock displacement, which can produce different flow conditions depending on the movement direction. By performing runs with an upstream- and then downstream moving shock, in which the same choke deflection is applied, it is possible through the pressure measurements to evaluate the influence of hysteresis effects.
- **Repeatability of flow conditions.** Measurements of the smooth reference case were conducted in different days, after the setup and pressure tubing was removed and re-assembled in the wind tunnel. An agreement between independent measurement runs indicates repeatability of the flow conditions.

5.2.1. Pressure tap distribution

When defining the taps distribution, it was necessary to strike a balance between having a good discretisation of the pressure evolution and avoiding an excessive impact of the orifices in the flow physics. Other factors considered were the limited amount of pressure tubes that could be conducted within the lower test section wall and outside the wind tunnel through the plug, as well as the total number of reading ports available in the two scanners used. This constrained the analysis to a total of 30 simultaneous pressure readings over the lower wall.

Streamwise pressure taps

To validate the lower wall new design, streamwise pressure measurements were performed at the wind tunnel symmetry plane, over the circular and flat test sections. The spacing between taps is most critical for the circular section. It has to be small enough to capture the shock location by accurately resolving its steep pressure gradient. Therefore, a higher density of taps was placed over the range covered by the shock positions. This is less problematic over the flat section, where pressure displays a smoother behaviour. Also, the flat test section is shorter than the circular one, thus demanding less measurement points.

In light of this, 17 pressure taps were placed over the smooth circular plate and 11 over the flat one. Within the region where the shock would be placed, taps were positioned every 4mm, whereas to measure the adverse pressure gradient at the flat region a constant spacing of 6mm was used. The taps located over the circular section are indexed with the letter C, whereas those over the flat one with the letter F, and their numbering grows in the streamwise direction. The pressure tap distribution for the smooth circular and flat plates can be seen in Figure 5.3.

Spanwise pressure taps

The positioning of spanwise taps served to measure the flow profile over the width of the wind tunnel. The acquired information was used to assess how two-dimensional the flow was in the test section.

This acquisition was performed at two streamwise locations, upstream and downstream of the circular test section. Therefore, printed pressure taps were mounted at the front and rear edges of the circular block, at seven equally spaced locations. The distance between the taps was determined as being $s_D/2$ (half of the 3D dimples spacing), what yields 16.5mm. This way, the spanwise pressure taps are either located halfway between dimples or at their centerline. The front spanwise taps are indexed with the letters FP and the rear ones with RP, and the numbering increases from the left wind tunnel door to the right (with an observer oriented against the streamwise direction). The spanwise pressure tap distribution can be seen in Figure 5.3.

Upstream lateral pressure taps

Twelve streamwise pressure taps had been drilled at the centreline (y=175mm) of both wind tunnel lateral doors. They start in the beginning of the test section at x=70mm and extend up until x=620mm, just before the optical access window, with a spacing varying between 40 and 60mm. These taps mainly provide information of the flow development upstream of the circular test section, where the shock will be located. Given the supersonic nature of the flow, it is expected that these readings remain unchanged when shock is displaced. Moreover, they will serve as a validation of the simulation results and can also be regarded as a measure of the two-dimensionality of the incoming freestream flow. The lateral taps at the left wind tunnel door are indexed with SL, and the ones on the right with SR, their numbering increasing in the streamwise direction.

Taps distribution over dimpled plates

Besides providing a good representation of the flow for different shock locations, the positioning of taps over dimpled plates had to capture the influence of the control device geometry and allow for a comparison between the different test plates. For the 2D geometries, all taps were positioned in the middle of the plates, in the streamwise direction, since the resulting flow is expected to be two-dimensional close to the symmetry of the channel. The first tap, upstream of the dimple, was placed at the same location as for the smooth plate. Inside the indentation, one tap was positioned at its bottom and additional ones were distributed symmetrically around it. It was made sure that there were pressure readings at the leading and trailing edges to capture the expansion fans intensity.

For 3D plates, the two-dimensional flow assumption is no longer valid. Considerable three-dimensional effects would be present and had to be assessed, in spite of the constrained amount of simultaneous pressure readings. Hence, one column of streamwise taps was placed over the centreline of the dimple (dimple plane) and another at the channel symmetry (symmetry plane), each with eight parallel taps. Their purpose was to capture the spanwise relaxation of the controlled interaction. Although less taps results in a poorer discretisation of the physical phenomenon, the analysis of 3D plates results can be supported by the more refined measurements over the 2D ones.

For the shock locations downstream of the indentation, at least one tap was positioned after the pressure rise. For the 3D dimples taps were also located at their leading and trailing edges. Finally, for a more insightful description of the spanwise effects, two additional taps were positioned between both tap columns at the x-coordinate of the dimple bottom. As a result, each 3D dimpled plate had a total of 18 pressure taps. In Figure 4.7, presented in the previous chapter, the pressure tap distribution can be seen for each of the five dimpled plates.

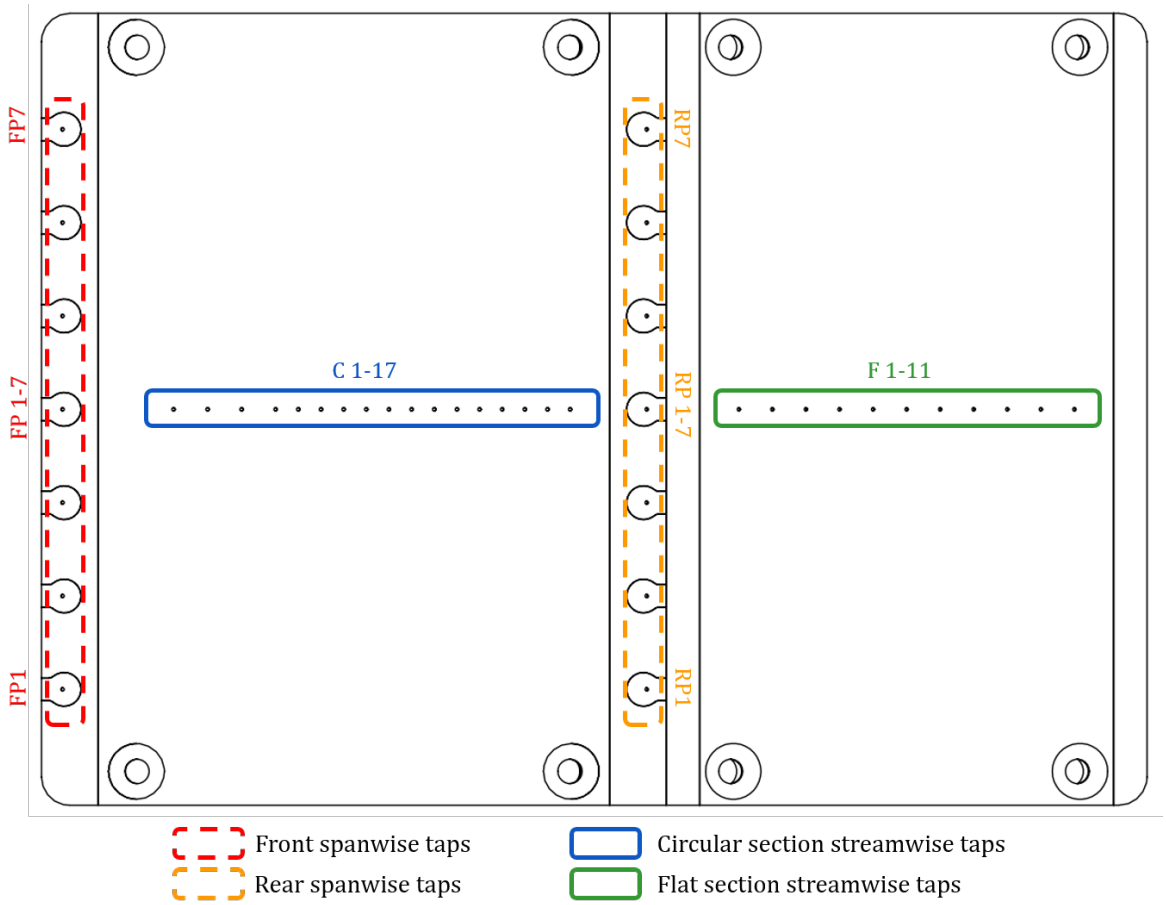

(a) Top view of the circular and flat test section models, with the streamwise and spanwise taps indicated for the smooth reference case. Flow goes from left to right.

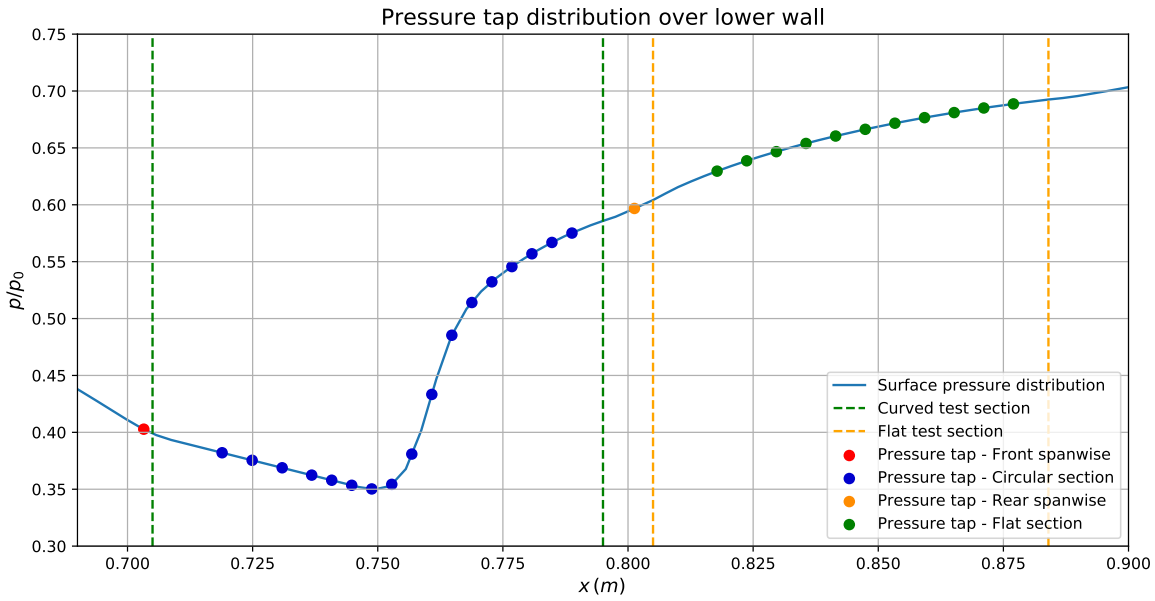

(b) Interpolation of CFD results with tap locations to indicate the resolution of the surface pressure measurement given the tap distribution.

Figure 5.3: Tap locations over models and resolution of pressure distribution over the smooth reference case.

5.2.2. Pressure scanner

Flexible tubes were attached to the taps in order to retrieve the pressure information. The capillaries had an outer and inner diameters of 1.8 and 1.2mm respectively, and were conducted inside the lower wall block and connected to a plug located at the side door of the wind tunnel (for more detailed description, see Appendix A). The plug contained 30 metallic tubes that would connect the interior of the wind tunnel to its exterior. An equivalent amount of pressure tubes would transmit the pressure information from the plug to two pressure scanners. Apart from the 30 surface pressure readings, the stagnation pressure was also being measured by means of a capillary connected to the ST-15 settling chamber.

The scanners deployed (Scanivalve DSA 3217/16Px) were able to simultaneously read 16 independent input ports. They had a differential pressure limit (manometric) of 15 and 30 psid respectively (equivalent to approximately 1.03 and 2.06 bars), what fits the current experiment conditions, since flow total pressure was limited to 2 bars (absolute value).

All pressure measurements were conducted at an acquisition rate of 10Hz, and the final pressure value of each input port for a given flow case was computed by time-averaging the readings over 3 seconds (thus consisting of 30 measurements). The standard deviation of these 30 data points was calculated and used as a measure of uncertainty. The average total pressure, acquired in the wind tunnel settling chamber, was computed from the moment flow stabilised in the beginning of a run (at around 10s) until it was terminated. Surface pressure values were normalised using the total pressure recorded from the same run they were measured.

5.3. Particle image velocimetry (PIV)

Particle image velocimetry is currently a well-established technique, capable of measuring non-intrusively the velocity distribution of large parts of the flow field [73]. It consists of seeding the flow with tracer particles, which are illuminated by a laser sheet at a specific rate. A camera is synchronised with the laser pulses, allowing it to capture the particle distribution for consecutive images. By computing particle displacement from one image to the other for a known time interval, it is possible to reconstruct the velocity field. This is achieved by dividing the image pair in interrogation windows and performing a cross-correlation step, which yields the spatial shift of a set of tracers over the time interval. The actual displacement is calculated by converting pixels to length units using the image resolution, measured by placing a calibration plate over the plane where the laser sheet will be formed (PIV plane).

For the current work, it is relevant to investigate the normal shock structure formed over the test section lower wall and understand how it is influenced by different dimple geometries. By acquiring velocimetry data over the shock interaction, the resulting expansion and compression regions can be quantified. To perform this analysis, 2C-2D PIV measurements with a FOV covering the SWBLI were made. This measurement technique will provide information for the following analysis:

- **Velocity distribution over the controlled shock wave-boundary layer interactions**: quantitative information on expansion and compression regions produced by the surface indentations
- **Evaluation of three-dimensional effects**: comparison between the shock structure produced over the centreline of 3D dimples and their two-dimensional counterparts.
- **Spanwise relaxation of the controlled interaction for three-dimensional devices**: comparison between velocity field over the dimple centreline and test plate symmetry.

5.3.1. PIV plane locations

PIV measurements were performed over planes parallel to the longitudinal cross-section of the wind tunnel. As can be seen in Figure 5.4, two planes were used in the current work: one coinciding with the symmetry plane of the test section (Plane 1), and another over the centreline of the 3D dimples (Plane 2). Considering the arrangement adopted for the 3D dimples over the test plates, it can be concluded that Plane 2 is an offset of Plane 1 by 16.5mm.

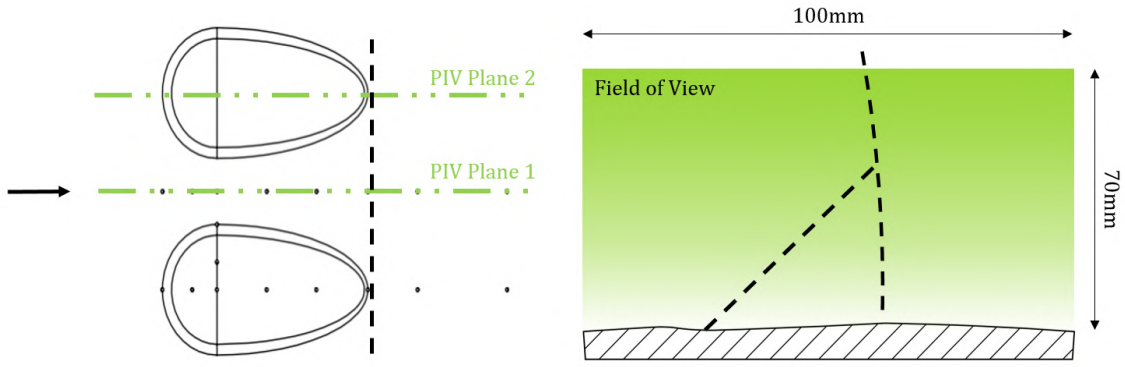

Figure 5.4: Top and right view of the asymmetric 3D dimple with indication of the Field of view, PIV planes and pressure taps. Plane 1 coincides with wind tunnel symmetry, whereas Plane 2 is placed over clean indentation (without taps).

It must be mentioned that the quantitative techniques, surface pressure and PIV measurements, were performed separately over two individual 3D dimples located in the middle of the channel. This was made possible by how the control devices were arranged over the test plates, with an even number of dents positioned over the channel centreline. As a result, it is reasonable to assume that the resulting flowfield is symmetric over the center of the wind tunnel, thus allowing the streamwise pressure taps to be placed over one dimple while performing PIV measurements over the other. Therefore, the velocity distribution recorded over Plane 2 was not perturbed by the small orifices from the taps, while also avoiding undesired laser sheet reflections from inside the holes.

5.3.2. PIV setup

In the PIV measurements for the current work, a light source produced a laser beam that was shaped in the form of a thin sheet by a set of spherical and cylindrical lenses. The laser sheet was shined into the back of the ST-15 test section through a lateral optical access. Inside, a mirror deflected the laser sheet by an angle of 45° to align it with the streamwise plane. The mirror was attached to a vertical support, mounted on the bottom of the wind tunnel by a fastening plate that allowed it to be laterally traversed and produce parallel planes over the span of the test section. The light sheet was oriented so to illuminate the flow just above the test section lower wall. A schematics of the PIV setup adopted in the current work can be seen in Figure 5.5.

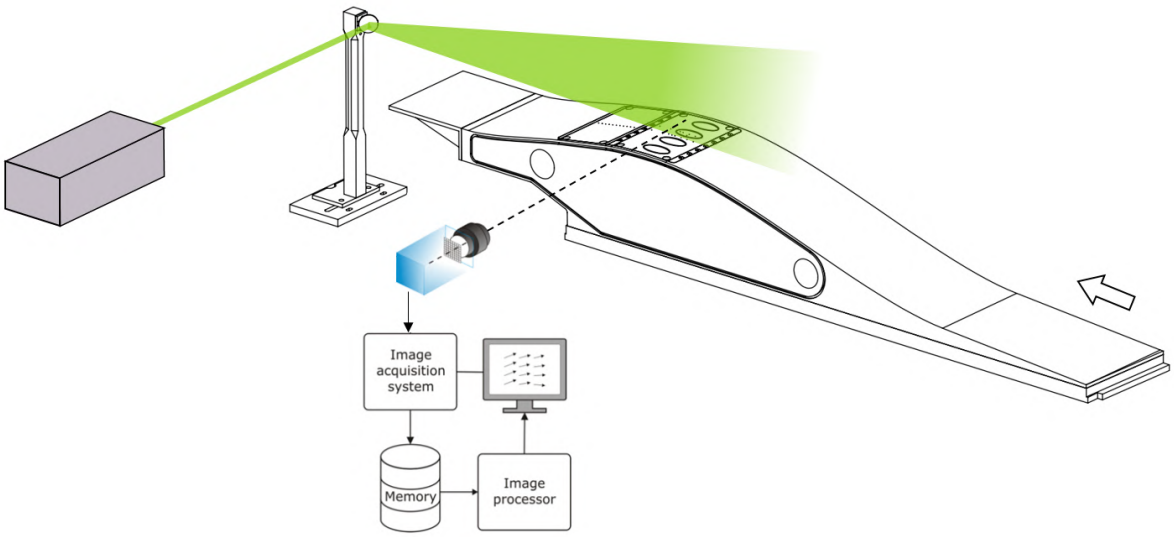

Figure 5.5: Schematics of the PIV setup used. Adapted from [77].

The resulting laser sheet had a thickness Δz of 1.5mm and reached a height of 70mm over the measurement region. When setting up the laser sheet, a small misalignment was observed, of 1mm over 70mm in the vertical direction (1.4%) and 2.5 over 100mm in the horizontal direction (2.5%). These were deemed acceptable given the laser sheet sensitivity to mirror probe positioning.

The digital image recording hardware used during PIV measurements consisted of a single sCMOS CLHS camera from LaVision. The device had a resolution of 2560 x 2160 pixels, maximum frame rate of 50Hz and a pixel size of 6.5 μm. It was fitted with an AF Nikkor lens, focal length f of 50mm, 1:1.8. The light source deployed was a double-pulsed ND:Yag Evergreen 200 laser by Quantel (wavelength λ = 532 nm, 200mJ per pulse), with a maximum repetition rate of 15Hz. The light source and imaging device were synchronised using LaVision's programmable timing unit. Tracer particles were seeded in the wind tunnel settling chamber using the PIVTec DEHS seeder, which produced particles with a diameter d_p 0.9μm.

The equipment deployed helped overcome the difficulties of performing PIV in high-speed flows. The presence of shock waves introduces a large spatial variation of the particle seeding density and a discontinuous refractive index distribution over the field of view [76]. Poor light scattering was avoided by using a high-power light source. Furthermore, it is more challenging to produce a uniform flow seeding in blowdown wind tunnels than in closed-return ones, for particles cross the test section only once. With this in mind, the seeder was chosen based on its capability of introducing large volumes of tracers at a high pressure, thus ensuring an appropriate concentration of particles in the interrogation window. Particles were also very small to avoid velocity lag, especially in the shock region [54].

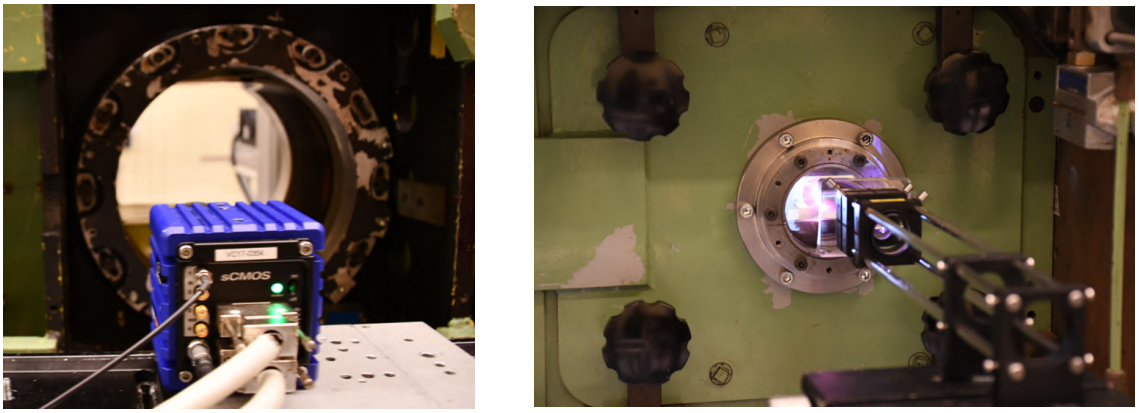

(a) Camera in front of the main optical access

(b) Set of lenses responsible for shaping the laser sheet.

Figure 5.6: Key components of the PIV setup, namely the imaging sensor and the set of lenses that formed the laser sheet prior to entering the wind tunnel.

5.3.3. Measurement parameters

The Field of View (FOV) was oriented normal to the test section lower wall and parallel to the free stream flow direction. It covered the region from the leading edge of the circular test plates to the interface between the circular and flat section blocks. It had therefore a length of 100mm, leading to an image resolution of 25.6 pixels/mm. Although the recorded field of view reached a height of 84mm, the actual measurement area was restricted vertically by the laser sheet height, which only illuminated particles up until 70mm above the lower wall surface.

Knowing the field of view dimensions, camera resolution and pixel size, the magnification factor M can be computed. Using Equation 5.2, a value of 0.1644 was obtained. Then, using the lens focal length f and the thin lens equation, the image and object distances d_i and d_o are determined (Equation 5.3). The resulting values were 58.3 and 350.5mm respectively, and the latter was used as a reference to position the camera with respect to the test section. Camera was oriented so to ensure that the image recording plane was parallel to the object plane, what minimised optical distortion and allowed images to be scaled only later, during post-processing.

$$M = \frac{\text{Sensor size}}{\text{Object size}} = \frac{\text{Pixel size} \times \text{Resolution}}{\text{Object size}} \tag{5.2}$$

$$\frac{1}{f} = \frac{1}{d_i} + \frac{1}{d_o}, \quad M = \frac{d_i}{d_o} \tag{5.3}$$

Subsequently, the minimum and optimal values for the aperture opening of the lens ($f\#$) are calculated. Minimum $f\#$ ensures that the focal depth is larger than the laser sheet thickness, in other words, that all illuminated particles are in focus. Optimal $f\#$ yields a particle image diameter d_τ large enough to accurately identify tracers in consecutive images and to cross-correlate them. The chosen value of d_τ was 3 pixels, to avoid peak locking. Equations 5.4 and 5.5 produced minimum and optimal values for $f\#$ of 3.4 and 12.9, respectively. Although the $f\#$ setting closest to the optimal was 11, a value of 8 was chosen for the measurements, to increase the amount of light captured by the camera. This was motivated by the fact that the reduced refractive index found in compressible flows together with small particle size reduce the intensity of scattered light [76].

$$f\# > \frac{M}{M+1}\sqrt{\frac{\Delta z}{4.88\,\lambda}} \tag{5.4}$$

$$f\# = \sqrt{\frac{d_\tau^2 - \left(M\,d_p\right)^2}{(2.44\,\lambda)^2\,(1+M)^2}} \tag{5.5}$$

Finally, the light pulse separation Δt was chosen. This parameter directly influences particles displacement between consecutive frames, which should be smaller than the interrogation window used to cross-correlate the images. Considering a maximum flow speed in the test section of 350 m/s (taken from the preliminary CFD simulations), the Δt of 1.5μs used in the measurements would yield a physical tracer displacement of 0.53mm or 13.4px between images, what would allow cross-correlations with a window size of 32x32 pixels. Assuming a cross-correlation uncertainty of 0.2 pixels, similarly as proposed by van Oudheusden et al. [95], a maximum instantaneous velocity uncertainty of 5.2m/s (1.49%) can be computed. Nonetheless, larger particle displacements (and consequently flow speeds) are expected to be measured at expansion regions over the dimpled plates.

5.3.4. Data acquisition and processing

Measurements were performed at a rate of 15Hz, which was the highest repetition rate achieved by the light source. Given the camera's storage limitation, only 300 image pairs could be kept simultaneously in the device before being transferred to the computer memory. As a result, each image recording campaign lasted 20s. Three velocimetry acquisitions were performed for each flow case, producing a statistically meaningful data set with 900 image pairs each. The software LaVision DAVIS 8.4 was used to process the image pairs captured during the PIV measurements. The sequence adopted for processing them is described below:

Image pre-processing. The acquired image pairs were first pre-processed so to enhance the contrast of the illuminated particles, allowing a more accurate evaluation of their displacement. First, a filter was used to subtract the minimum pixel intensity over 19 consecutive images, thus decreasing background effects on the data set. Then, particle intensity was locally normalised using a scale of 6 pixels, in order to reduce the influence of regions in the background with substantial light reflection. Figure 5.7 shows how the pre-processing step is capable of removing background reflections and enhancing particles contrast.

Cross-correlation. First, a mask was applied in all pre-processed images, to exclude the top portion which was not illuminated by the laser and to define the circular contour of the lower wall (mask indicated in Figure 5.8a by the green region outside the vector field). They were then were cross-correlated using a multi-pass scheme with decreasing window size. A single pass was first performed with a rectangular window with a size of 64x64px, thus following the one-quarter rule which requires that particle displacement should be 25% of the correlation window size. The final step used circular windows with a size of 32x32px. In both steps an overlap of 75% was adopted.

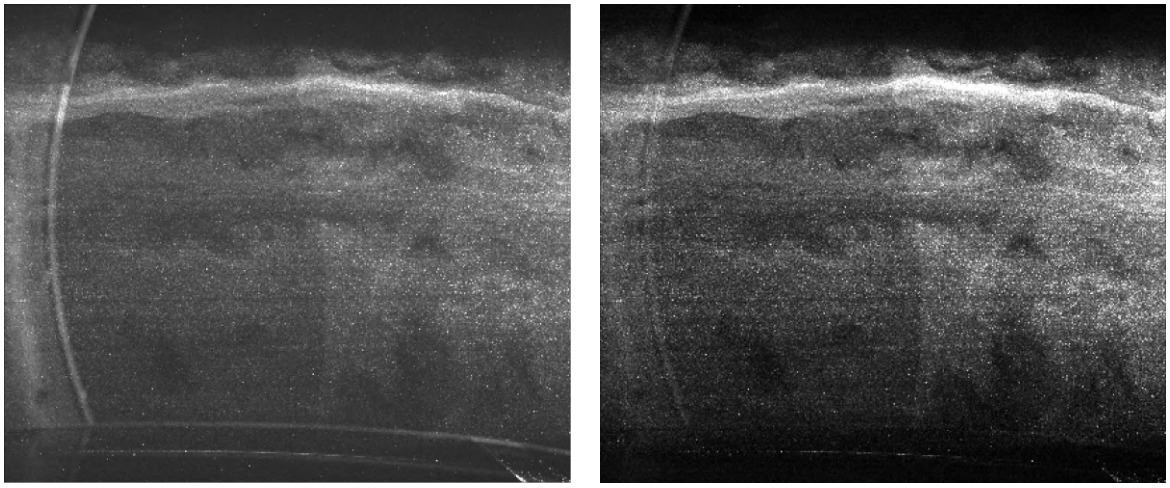

(a) Raw image (b) Pre-processed image

Figure 5.7: Raw and pre-processed images of the seeded flow over the smooth reference plate. The sudden increase of particle brightness indicates the location of the shock wave.

Vector post-processing. Particle displacement vectors were post-processed using the 'universal outlier detection' method. A filter region of 7x7 vectors was established and the minimum number of vectors was set to 4. Vectors were removed if the residual was higher than 2 and re-inserted for residuals smaller than 3. Empty spaces were filled up by interpolating neighbouring data. The final vector spacing obtained was of 0.313mm.

Image scaling. Images were scaled by a 3D printed calibration plate. Its lower face matched the smooth plate contour over the measurement region, allowing it to be accurately positioned in the test section (Figure 5.8b). For each flow case, images were recorded with the calibration plate placed at the spanwise location corresponding to the laser sheet. A millimetre paper glued to it allowed the computed image resolution to be verified. By knowing the exact image resolution and the light pulse separation, it is possible to compute the velocity field from the particle displacement between two images.

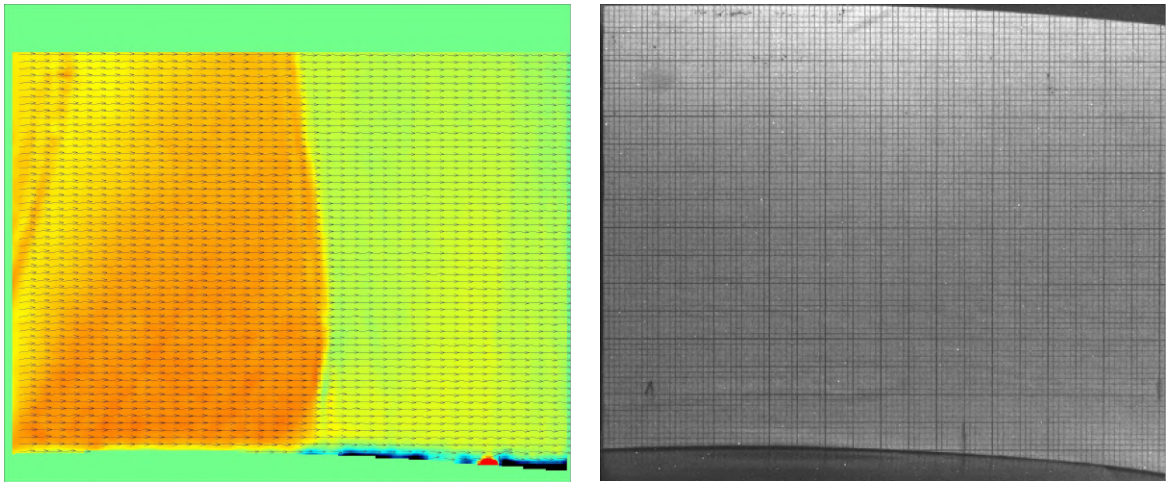

(a) Particle displacement in pixels of a single image pair. (b) Calibration plate placed over the smooth reference plate.

Figure 5.8: Displacement vectors in pixels from a (good) cross-correlated image pair taken over the smooth plate. Color map ranges from 2 (blue) to 16 pixels (red). Next to it, the calibration plate used to scale the displacement vectors to metric units.

During PIV measurements, it was noted that shock position oscillated considerably more during the acquisition runs, despite choke deflection remaining fixed. This phenomenon was attributed to unsteady flow structures formed between the wind tunnel side wall and the mirror probe, which would ultimately vary the back pressure during the run, thus displacing the shock. It occurred more substantially during the Plane 2 measurements: the closer proximity between the probe and the side of the channel likely enhanced the unsteady structures. As a consequence of this, the individual velocity fields had to be filtered before the mean distribution was computed. The procedure adopted to compute the mean velocity vectors for every measured flow case is described in Appendix E.

5.4. Measurement campaigns

The measurement techniques were deployed in two separate campaigns. The first covered Schlieren and surface pressure measurements, considered more classical experimental techniques. Then, a second campaign was performed exclusively for velocimetry data acquisition using PIV.

5.4.1. Schlieren and pressure measurement campaign

In the first measurement campaign, Schlieren imaging of the flowfield was performed in parallel with surface pressure acquisition. Therefore, it provided qualitative information of the flow structures as well as a quantitative pressure distribution over the wall. All six test plates (smooth plate and the five dimpled plates) were deployed in this campaign. Depending on the objective of each run, different pressure taps were connected to the two scanners, given the restricted number of reading ports. In every run, total pressure was measured in the settling chamber and later used in post-processing to normalise the other readings.

During each run, shock was placed at the three locations of interest outlined in Chapter 4. This was done by changing the input voltage on the power supply. For every test plate configuration, two runs were performed, one with the shock being displaced from the most upstream position towards downstream (referred to as Run 1), and another in the opposite direction (Run 2). This allowed to investigate the effect of hysteresis on the setup, since on both runs the same input voltage was provided to the choke system. Schlieren images were always recorded for both runs, in order to analyse disagreements between them. Table 5.2 shows the measurement plan for the first campaign.

ID	Test plate	Shock displacement	Pressure taps
1	Smooth	Downstream	FP4, C1-17, RP4, C1-11
2		Upstream	
3	Smooth	Downstream	SR1-12, SL1-12
4	Smooth	Downstream	FP3-4, C1-18, RP3-4, C1-7
5		Upstream	
6	D40d10 2D	Downstream	FP3-4, C1-18, RP3-4, C1-7
7		Upstream	
8	D20d10 2D	Downstream	FP3-4, C1-18, RP3-4, C1-7
9		Upstream	
10	D40d10 3D	Downstream	FP3-4, C1-18, RP3-4, C1-7
11		Upstream	
12	D20d10 3D	Downstream	FP3-4, C1-18, RP3-4, C1-7
13		Upstream	
14	R10D40d10 2D	Downstream	FP3-4, C1-18, RP3-4, C1-7
15		Upstream	

Table 5.2: Test matrix adopted during the Schlieren and pressure measurement campaign.

5.4.2. PIV measurement campaign

The second measurement campaign focused solely on acquiring velocimetry data of the shock interaction over test plates. Two parallel measurement planes were adopted: Plane 1 crossed the symmetry of the test section, and Plane 2 coincided with the centreline of the 3D dimples. The smooth reference plate and all five dimpled plates were measured using Plane 1. Conversely, only the three 3D dimples were evaluated also with Plane 2, given that, for the others, flow was assumed to be constant around the centre of the channel. Therefore, a total of 9 flow cases were evaluated during the PIV measurements, and for each of them three acquisition campaigns were performed to obtain a large enough set of data. In all of them, only the centered shock location was assessed. It should be mentioned that first all measurements were done using Plane 1, and afterwards the mirror probe and camera were moved to obtain the velocity distribution over Plane 2.

During the Schlieren campaign, it was identified that the resulting shock location was quite sensitive to the plate assembly and choke system input voltage. Besides, for different plates, the voltage provided to place the shock in the same location differed. As a result, it was decided to first carry out a Schlieren visualisation every time a new test plate was mounted in the wind tunnel, in order to accurately determine the input voltage which would place the shock at the desired position. The run would start with choke at its maximum deflection (which placed the shock in the beginning of the plate), and voltage would then be lowered until the main shock leg was positioned in the centered location.

Thereafter, three consecutive PIV acquisition runs were done. They would all start with the choke at its maximum deflection, and the voltage would be lowered always to the same value previously determined in the Schlieren run, thus ensuring complete measurement consistency. After the input voltage reached the designated level, five seconds would elapse to allow the flow to reach steady conditions, and then the seeding was activated. Image acquisition was initiated two seconds afterwards, when seeding could be considered uniform. After the 300 images were taken, the seeder was turned off and the run was terminated 2s later, to ensure all particles were flushed away from the test section.

The test matrix of the second measurement campaign is presented in Table 5.3.

ID	Test plate	Shock position	PIV plane
16, 17, 18	Smooth	Centered	Plane 1
19, 20, 21	D20d10 2D		
22, 23, 24	D40d10 2D		
25, 26, 27	D20d10 3D		
28, 29, 30	D40d10 3D		
31, 32, 33	R10D40d10 3D		
34, 35, 36	R10D40d10 3D	Centered	Plane 2
37, 38, 39	D20d10 3D		
40, 41, 42	D40d10 3D		

Table 5.3: Test matrix adopted during the PIV measurement campaign.

6

Schlieren and pressure results

In this chapter, the Schlieren and surface pressure measurement results are presented. Since both techniques were deployed simultaneously in the first measurement campaign and can be considered more classical measurement approaches, their results are grouped together. All results are plotted using the global coordinate system defined in Chapter 3.

6.1. Schlieren results

The Schlieren images of the flowfield over the six test plates are displayed in this section. First, the uncontrolled reference shock structures are presented (acquired over the smooth plate), followed by the modified interactions for the five dimple designs. The tag on their top-right corner indicates the plate geometry used, as well as the shock position on the test plate (white dashed line).

Smooth reference case

Before initiating the analysis of the Schlieren images captured for the different flow cases, a reference shock structure must first be defined (Figure 6.1).

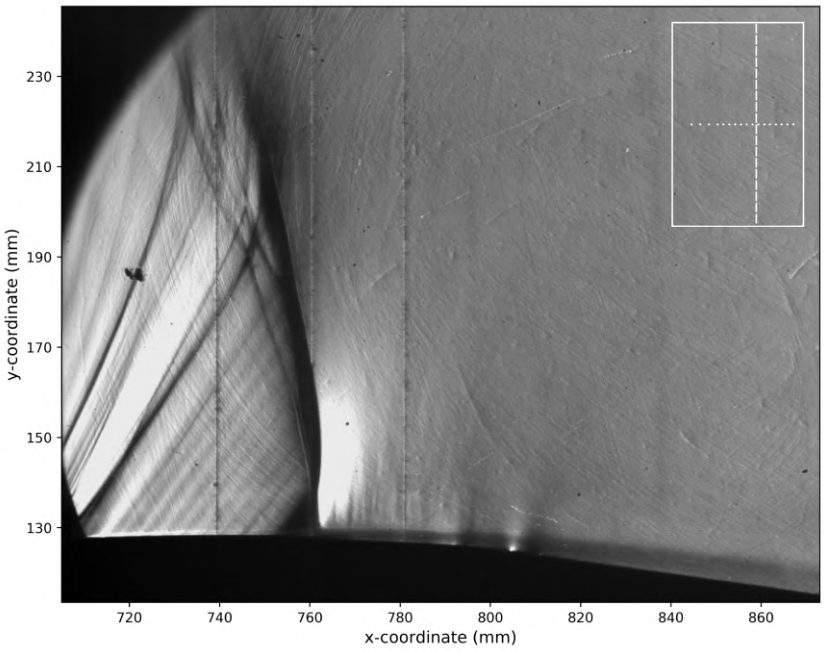

Figure 6.1: Reference shock structure.

The reference shock is formed over the smooth plate and is located at the centered position. It can be identified in the image by the black vertical contour at x=760mm, which starts at the surface of the lower wall (y=128mm) and reaches a y-coordinate of approximately 215mm, therefore not covering the entire channel cross-section. At the wall, it is normal to the wall surface, but further away from the plate it assumes a curved shape. Upstream of the shock, flow has a positive vertical component, and since normal shocks are always perpendicular to flow direction, its structure naturally becomes arched.

Besides the reference centered position, the shock was also placed further upstream and downstream, thus covering all locations of interest. The images for these three cases are consolidated in Figure 6.2, for which the following observations can be made:

- **Shock grows as it moves downstream.** The shock wave becomes taller as it is displaced downstream, indicating that larger portions of the flow upstream of it become supersonic. The opposite occurs when the channel becomes more choked by positively deflecting the choke flap, what displaces the shock upstream and decreases its size.
- **Small perturbations in the flow are captured by the Schlieren images.** An oblique wave is present in all images, departing from upstream of the optical access. It seems to emanate from the point where the circular section and lower wall blocks interface, and is likely caused by a small gap in the assembly. Also, oblique fringes are observed upstream of the shock, caused by the small taps drilled in the surface of the test plates. Despite being captured by the highly-sensitive Schlieren measurement, they are not expected to influence the flow substantially.

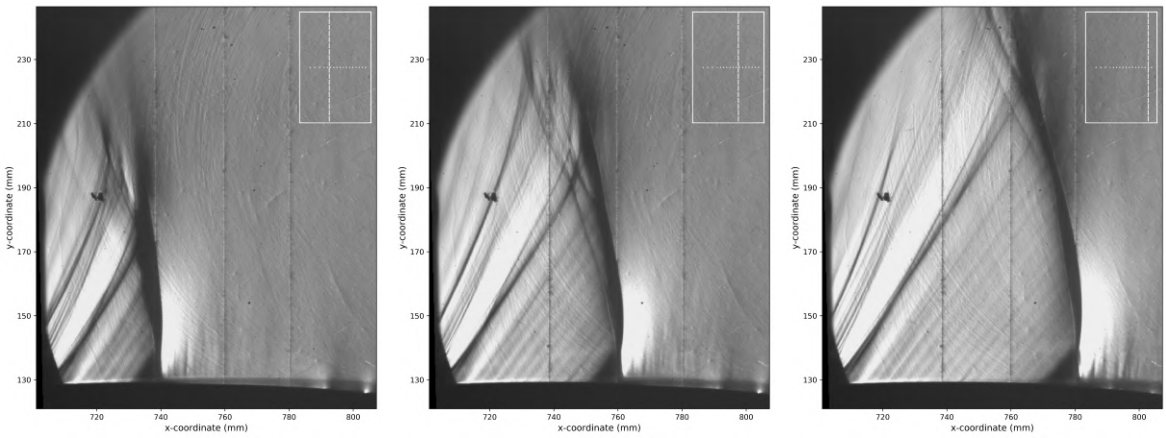

(a) Upstream shock (b) Centered shock (c) Downstream shock

Figure 6.2: Schlieren images of the flowfield over the smooth reference plate for the three shock locations of interest.

2D dimpled plates

After the uncontrolled shock was defined for the three locations, the dimpled plates were mounted in the circular section. The first dimples tested were the 2D ones, which produced an almost two-dimensional flowfield. This resulted in a clear Schlieren visualisation, given that the technique averages the flow structures that arise over the span of the wind tunnel in a single image. The dimple geometry is indicated in every image by a white dashed line, and its depth was exaggerated for graphical purposes. For the 2D dimpled plates, the following observations can be made:

D40d10 - 2D plate (Figure 6.3). Compression waves are formed inside the dimple, a result of the smooth upwards deflection promoted by the geometry. When the shock is located at x=760mm, in the centered position which coincides with the dimple trailing edge, a small flow re-expansion takes place. This phenomenon deforms the shape of the shock, creating a downstream curved leg in the region close to the wall. As the shock is displaced downstream, a bright region forms after the compression waves, indicating flow re-expansion. The shape of the shock changes again, with a clear formation of a triple point. Underneath it, where the portion of the flow influenced by the dent passes, the main shock leg assumes a strong curvature in the downstream direction.

D20d10 - 2D plate (Figure 6.4). In the centered shock location, an oblique wave emanates from the interior of the dimple, caused by the rapid upwards deflection experienced by the flow. It re-expands right afterwards as it leaves the indentation, indicated by the bright region in the image. The resulting shock structure has a clear triple point, with the normal leg below it being curved downstream. As the shock moves downstream, the resulting structure is only enlarged, and no new features arise.

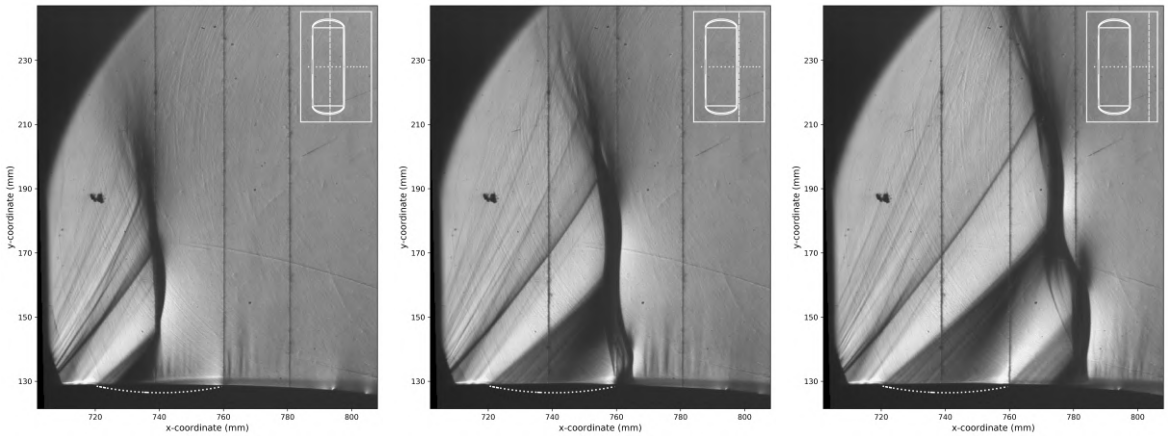

(a) Upstream shock (b) Centered shock (c) Downstream shock

Figure 6.3: Schlieren images of the flowfield over the D40d10 2D dimple plate for the three shock locations of interest.

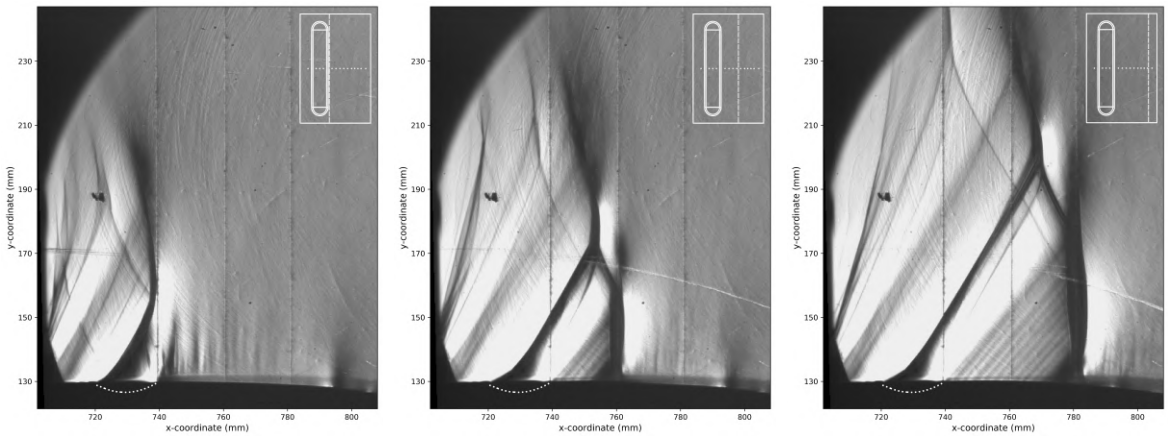

(a) Upstream shock (b) Centered shock (c) Downstream shock

Figure 6.4: Schlieren images of the flowfield over the D20d10 2D dimple plate for the three shock locations of interest.

3D dimpled plates

The interpretation of Schlieren images taken for the 3D dimpled plates is less straight-forward. Effects caused in the flow by the dimples are propagated in the spanwise direction, giving rise to three-dimensional features which are simultaneously portrayed in a single image. Still, the resulting structure can be easily compared with that of their two-dimensional counterparts.

D40d10 - 3D plate (Figure 6.5). Compression waves depart from the dimple interior, forming a dark region in the image. However, they produce a larger angle with the surface when compared to the 2D version of this test plate. Perturbations in a supersonic flow are propagated following the Mach angle, which increases with decreasing local Mach number. It can thus be expected that a weaker expansion takes place when the flow enters the 3D dimple. As the shock moves downstream, it becomes clear that the portion of the main shock leg that is hit by the compression waves is curved upstream. A small bright spot at x=760mm indicates the flow re-expansion when it leaves the dimple.

D20d10 - 3D plate (Figure 6.6). The resulting shock structure over the spherical dimples for all three shock locations is quite similar to that observed for the 2D version of this test plate. There is only a slight difference in the shape of the main shock leg, which suffers a smaller deformation. This is an indication that flow re-expansion is weaker in the three-dimensional case.

R10D40d10 - 3D plate (Figure 6.7). Flow features that arise over the asymmetric dimple can be regarded as a fusion of those found for the two other 3D plates. For the upstream shock, the image is very similar to the one for the D20d10-3D plate but without the small flow re-expansion, given that here the shock is still inside the indentation. As the shock moves downstream, an oblique shock is clearly emanating from the foremost portion of the dent, similarly as for the spherical dent, but the main leg shape is equivalent to that for the D40d10-3D.

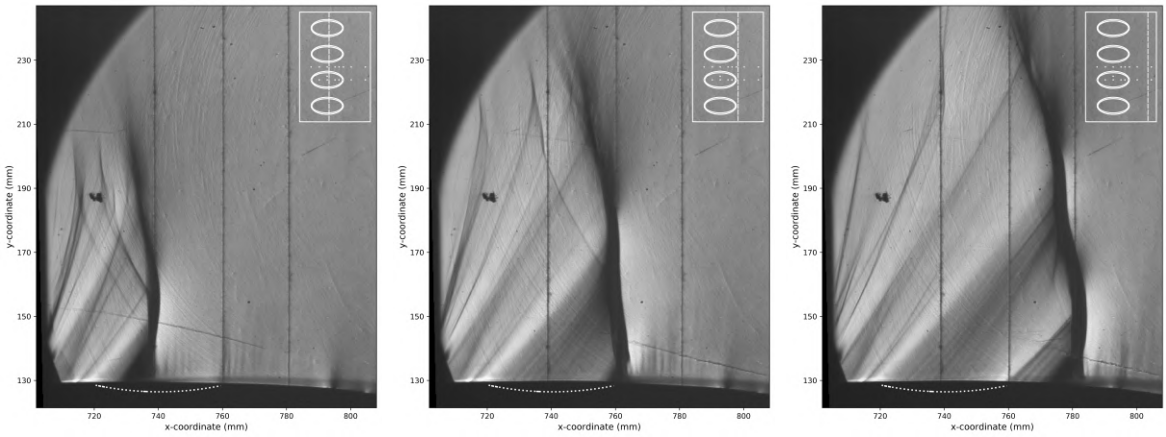

(a) Upstream shock (b) Centered shock (c) Downstream shock

Figure 6.5: Schlieren images of the flowfield over the D40d10 3D dimple plate for the three shock locations of interest.

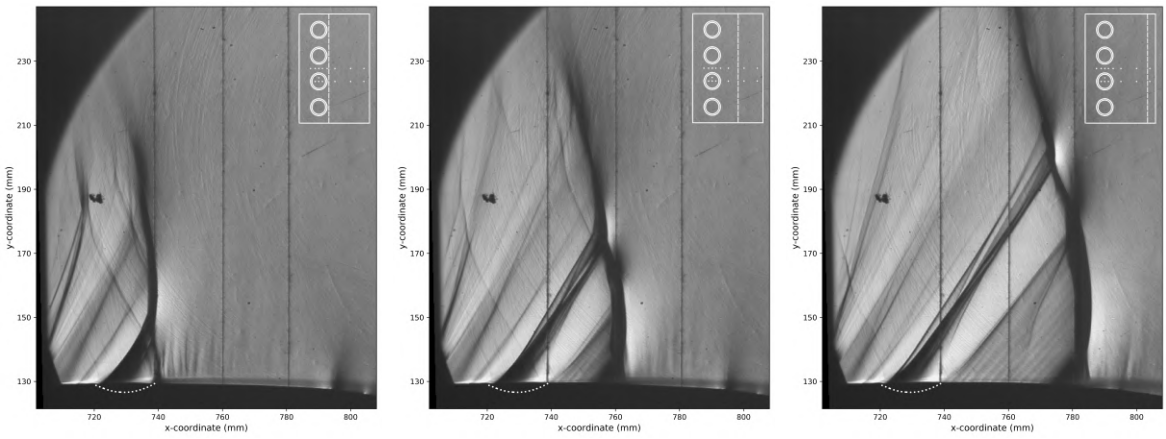

(a) Upstream shock (b) Centered shock (c) Downstream shock

Figure 6.6: Schlieren images of the flowfield over the D20d10 3D dimple plate for the three shock locations of interest.

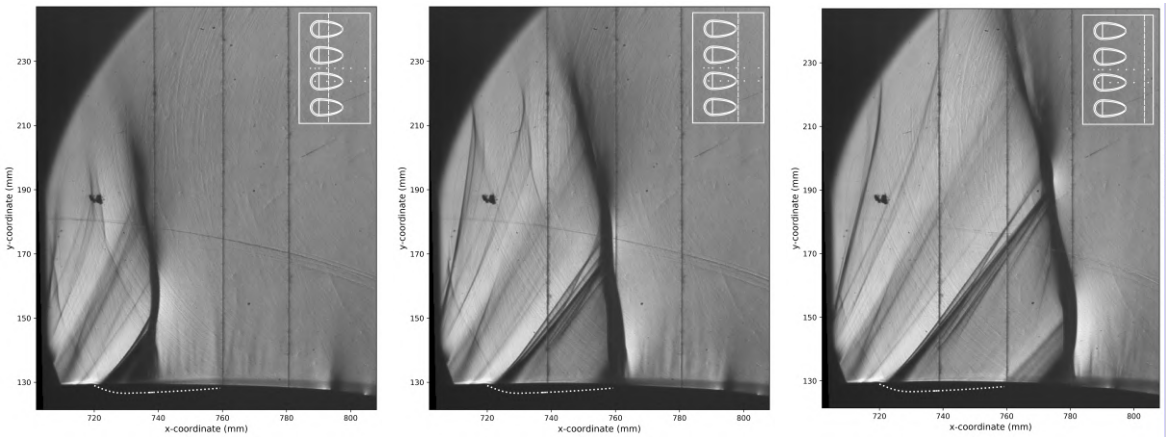

(a) Upstream shock (b) Centered shock (c) Downstream shock

Figure 6.7: Schlieren images of the flowfield over the R10D40d10 3D dimple plate for the three shock locations of interest.

6.2. Surface pressure results

Here, the surface pressure results are presented. First, the measurements performed to validate the re-designed test section are shown, being compared to CFD simulation plots. Then, readings for the different test plates are displayed, first the 2D ones and then their 3D counterparts. At every measurement run performed to generate pressure data, shock was placed at the three locations of interest. For the two-dimensional plates, distributions obtained for the two consecutive runs are shown, to evaluate the effects of hysteresis. Run 1 always refers to measurements performed with the shock moving from the upstream location to the downstream one, and Run 2 represents the opposite movement. For the three-dimensional dents, to facilitate the comparison between their results with those of 2D plates, only the results from Run 1 were plotted. Run 2 results for the 3D dimpled plates are presented in Appendix F. Black dashed vertical lines in the plots indicate the location of dimples leading and trailing edges. Every point in the following graphs is an average of 30 measurements, and error bars were plotted based on their standard deviation.

6.2.1. Test section validation

The test section validation plots are presented in Figures 6.8, 6.9 and 6.10.

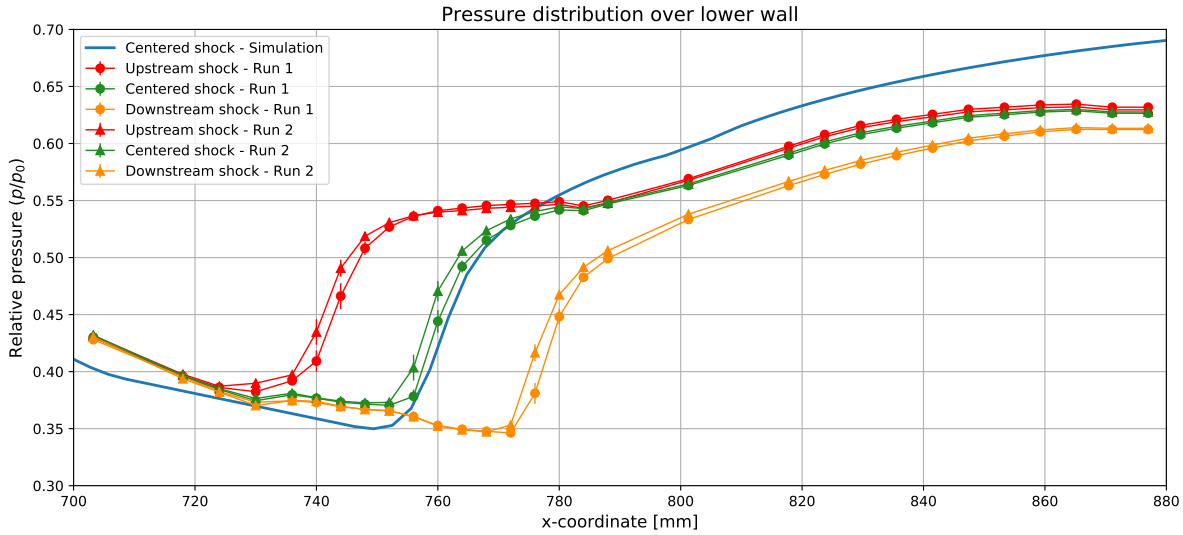

Figure 6.8: Relative pressure distribution over the circular and flat test sections of the lower wall.

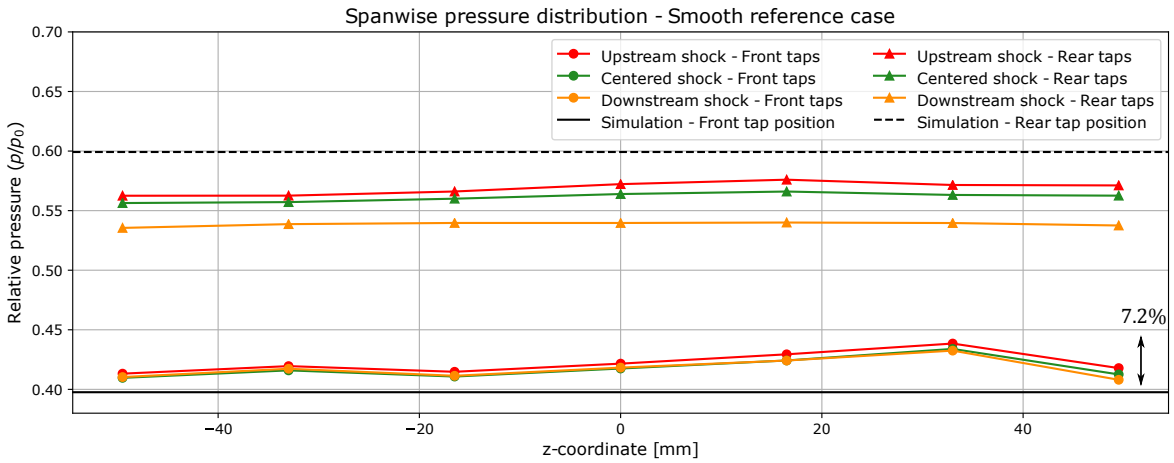

Figure 6.9: Pressure distribution over the spanwise taps located upstream and downstream of the circular section.

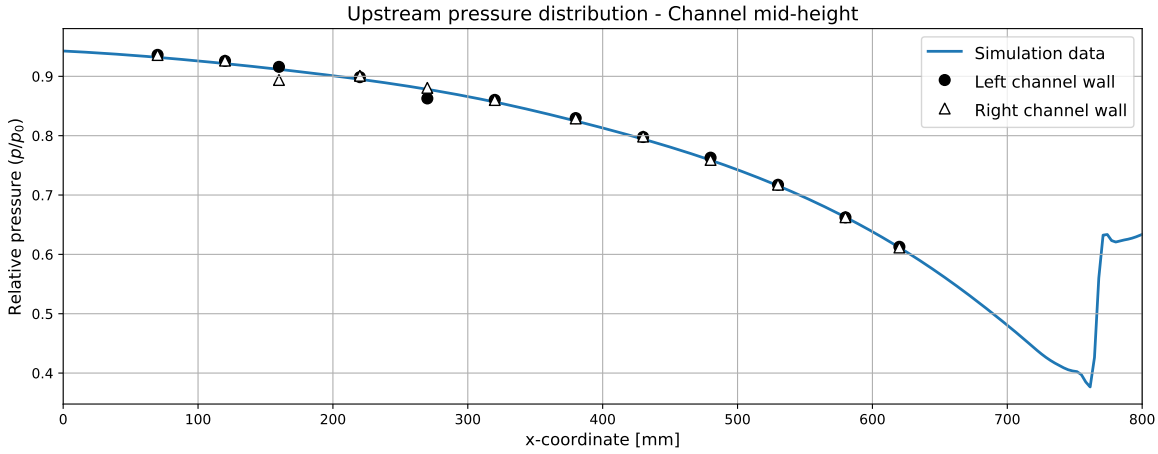

(a) Distribution upstream of optical access.

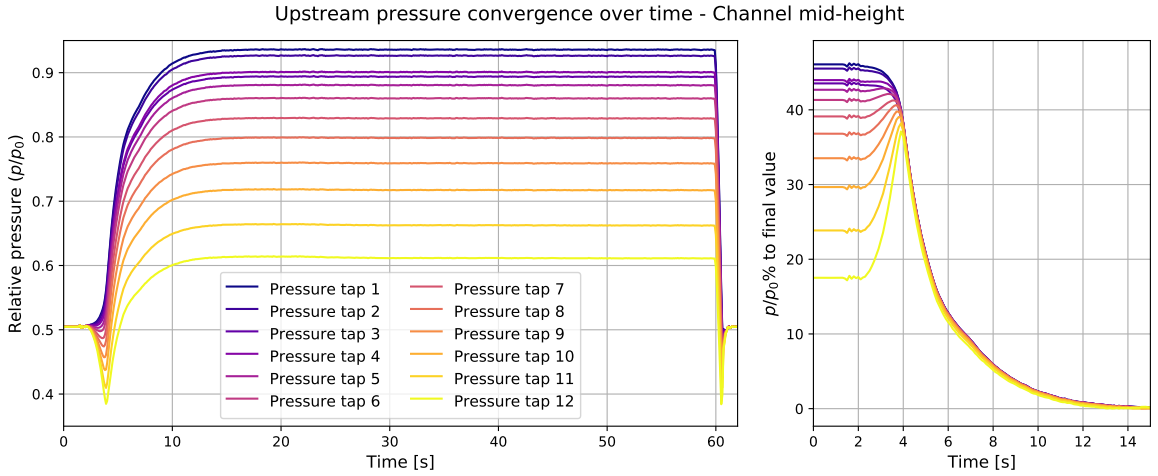

(b) Pressure readings over run time conducted over the right door.

Figure 6.10: Relative pressure upstream of the optical access, measured at channel mid-height (y=175mm) on both side doors of the wind tunnel. Shock was placed over the three locations of interest during the run.

From the surface pressure measurements conducted to validate the test section, the following observations can be drawn:

- **The further downstream the shock is, the stronger it becomes.** This is expected, for the flow is allowed to reach higher speeds (represented by smaller values of p/p_0 upstream of the shock). Consequently, the pressure level downstream of the interaction (represented by the 11 last data points of Figure 6.8) also decreases with the downstream displacement of the shock.
- **Pressure recovery levels decrease with shock intensity.** As mentioned in Chapter 2, it was expected for the flow inside a converging-diverging nozzle that a stronger the shock would lead to a reduced downstream pressure recovery, due to increased losses.
- **Hysteresis effects play a small role in the resulting shock location.** Small disagreements were observed over the shock in the three distributions from Figure 6.8. Although the same voltage was provided for the choke on both runs, the shock during Run 1 was consistently located slightly more downstream (around 1.5mm) than for Run 2.
- **Slight disagreements between the pressure measurements and the simulation results.** Pressure distribution measured for the centered shock follows a similar behaviour as the computed one, and shock was found at the same x-coordinate. However, there is indication that speeds reached in the experiment are lower than those simulated, for a higher p/p_0 value was recorded just before the shock. Divergences are stronger downstream of the interaction, with CFD results predicting a steeper pressure recovery.

- **Measurements and CFD results display a notable agreement at channel mid-height upstream of the optical access** (Figure 6.10). Also, readings over time indicate that flow takes around 12 seconds to stabilise when wind tunnel is started. As would be expected, pressure levels remain unaltered upstream of the shock when this is displaced.
- **Incoming flow is two-dimensional.** This is supported for the free-stream flow by the agreement between readings over the left and right wind tunnel doors (Figure 6.10a). On the other hand, front spanwise tap plots display a total variation of 7.2%, what might indicate that close to the wall incoming flow is not as uniform (Figure 6.9). However, oil flow visualisation shows perfectly parallel streaklines upstream of the shock (Appendix D), and these disagreements in the pressure readings are attributed to small surface imperfections near the taps.

6.2.2. Two-dimensional plates

The pressure distribution over the two-dimensional plates are presented in Figures 6.11, 6.12 and 6.13.

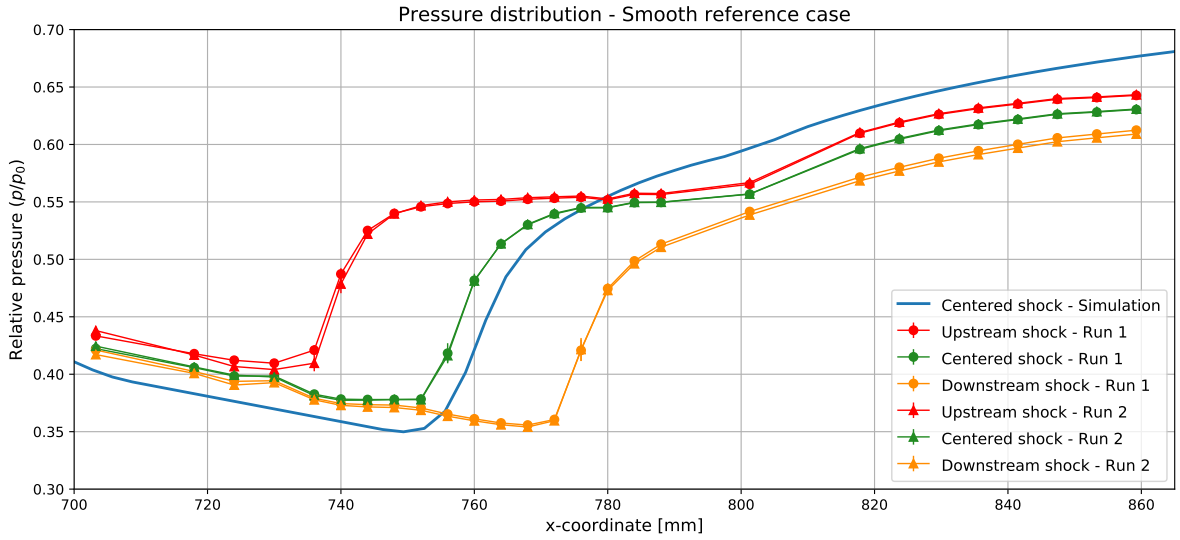

Figure 6.11: Relative pressure distribution for the smooth reference plate.

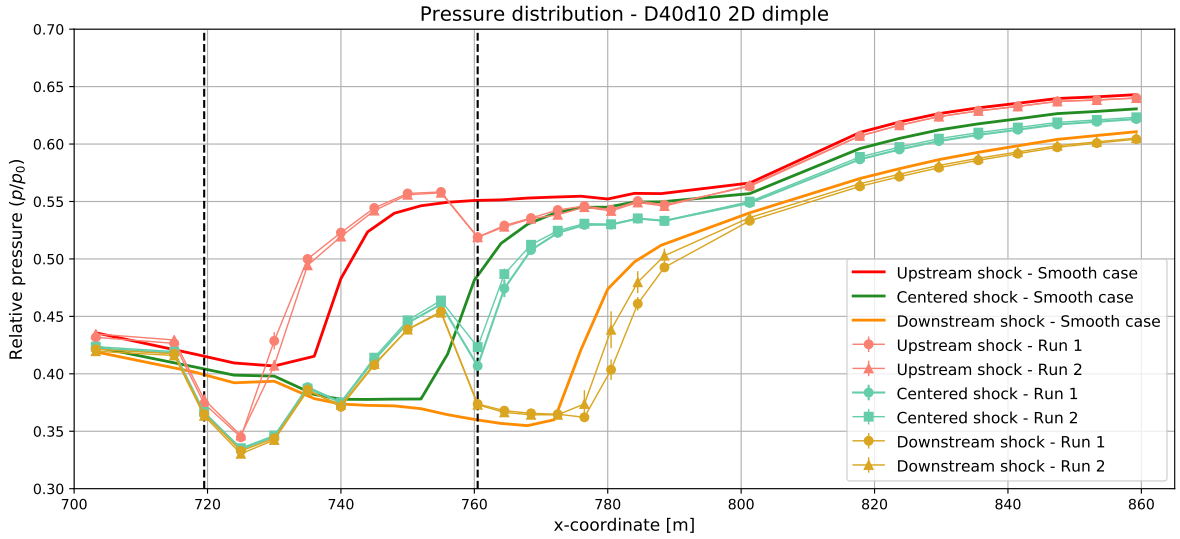

Figure 6.12: Relative pressure distribution for the D40d10 - 2D dimple plate.

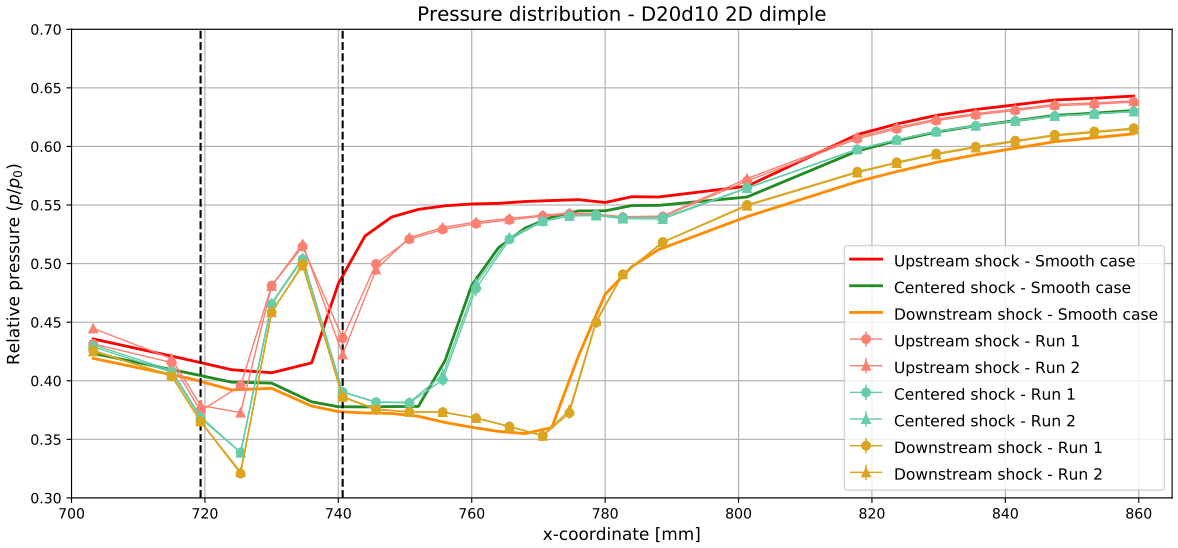

Figure 6.13: Relative pressure distribution for the D20d10 - 2D dimple plate.

From the two-dimensional test plates results, the following observations can be drawn:

Smooth reference plate (Figure 6.11):

- **Measurements are sufficiently repeatable.** For consistency, the smooth reference plate was measured another time, after the pressure tubing was modified for the dimpled plates measurements (only the first 8 taps over the flat test section were activated). Results coincide with those displayed previously, with a further reduced influence of hysteresis effects. These results are used in the subsequent plots to compare the controlled flow with the reference case.

D40d10 - 2D plate (Figure 6.12):

- **Substantial flow expansion over the dimple leading edge.** Given the downwards deflection when entering the surface indentation, the still-supersonic flow is accelerated. Speed increase is similar for all three shock locations.
- **Larger deceleration region for upstream shock location.** After expanding, flow is compressed in the interior of the dimple. For the upstream shock position (x=740mm), pressure rise due to upwards deflection merges with the shock, producing an extended pressure rise region.
- **Gentle flow compression inside the dimple for centered and downstream shock locations.** Smooth pressure rise takes place inside the indentation. Briefly at the dimple bottom, a slight acceleration occurs and pressure follows the behaviour of the smooth reference case. Afterwards, flow is further compressed on the second portion of the dent.
- **Flow re-expansion at dimple trailing edge at every shock location.** At the end of the dimple (x=760mm), flow is again negatively deflected to realign it with the test plate surface. For the downstream shock, flow strongly re-expands in this region, almost returning to smooth case levels. To a lesser degree, the same is observed for the centered shock, despite the fact that, in this flow case, shock location coincides with the dimple trailing edge. Also, a small subsonic re-acceleration occurs for the upstream shock in this region.

D20d10 - 2D plate (Figure 6.13):

- **Pressure distribution is less sensitive to shock location.** For all shock locations, distributions are quite similar, with pressure returning to smooth case levels downstream of the dimple. Only for the upstream shock location there is a reduced flow re-expansion, given that shock coincides with the dimple trailing edge. This re-acceleration is responsible for slightly pushing the shock to the right when compared to the reference smooth case.
- **Stark flow compression inside dimple indicates the formation of an oblique shock.** A steep gradient occurs inside the D20d10-2D, as opposed to a smoother increase for the D40d10-2D.

6.2.3. Three-dimensional plates

The pressure distribution over the three-dimensional plates are presented in Figures 6.14, 6.15, 6.16 and 6.17. For the first two plates (D40d10-3D and D20d10-3D), measurements performed over the plate symmetry and dimple centreline are displayed simultaneously. For the last one (R10D40d10-3D), both streamwise readings are plotted in separate graphs for an easier comparison with other cases.

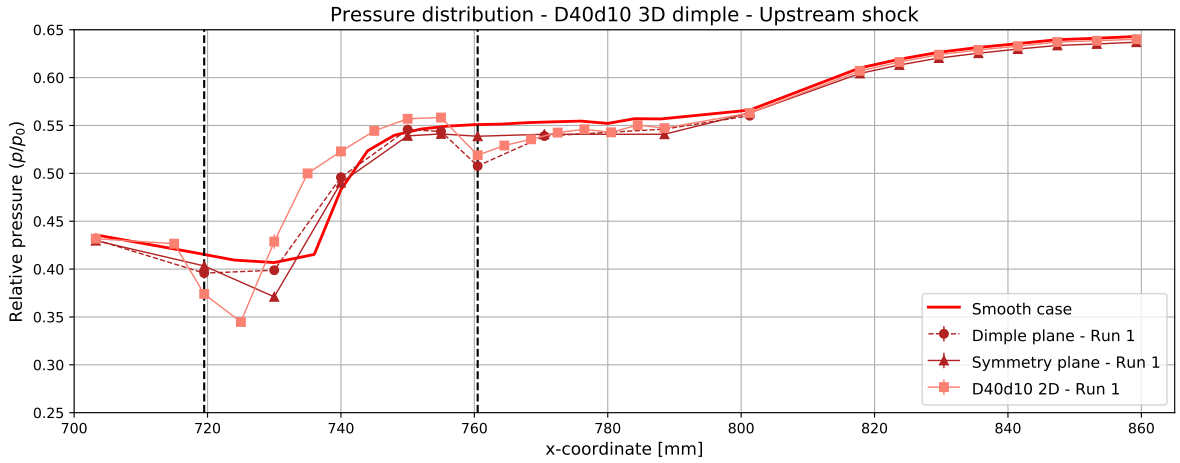

(a) Upstream shock location.

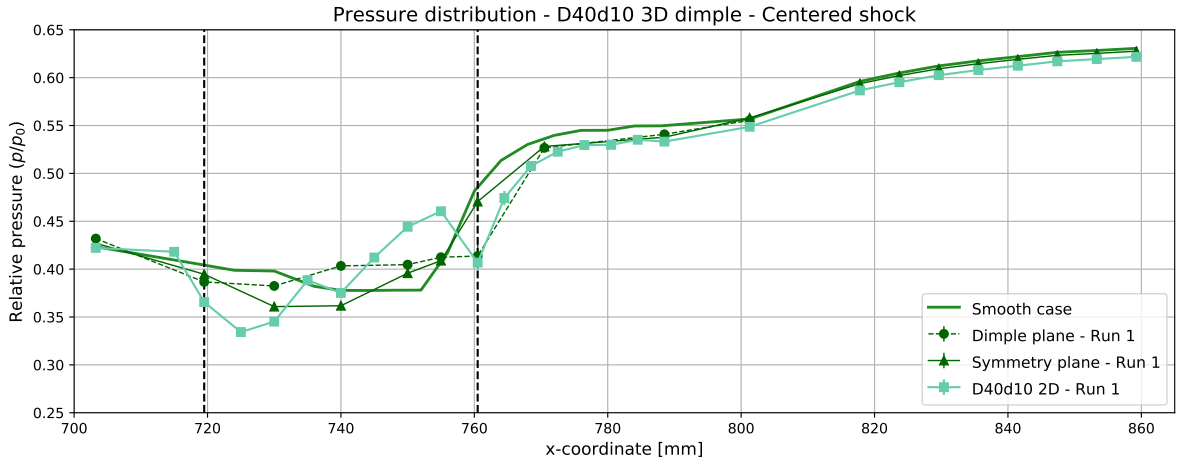

(b) Centered shock location.

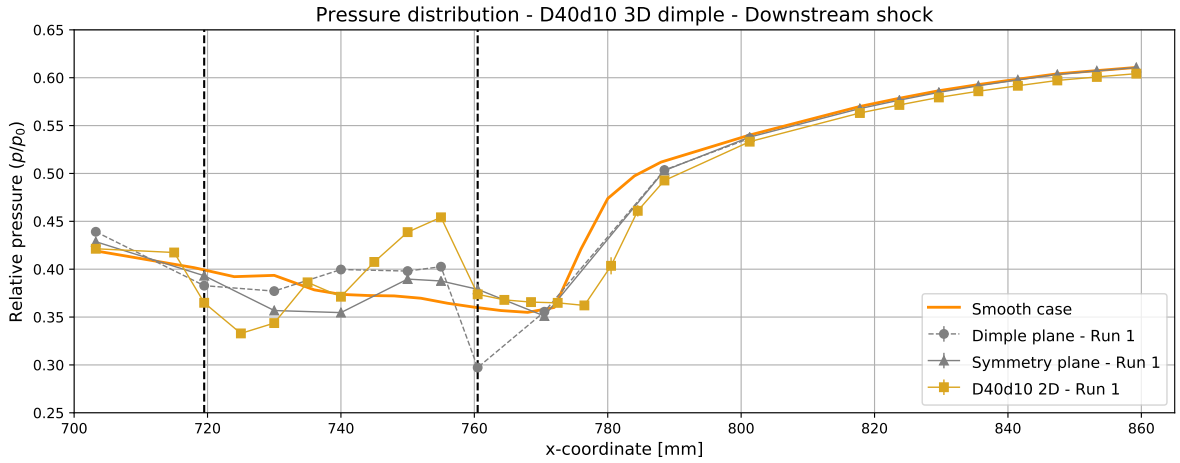

(c) Downstream shock location.

Figure 6.14: Relative pressure distribution over the plate symmetry and dimple centreline for the D40d10 - 3D dimpled plate.

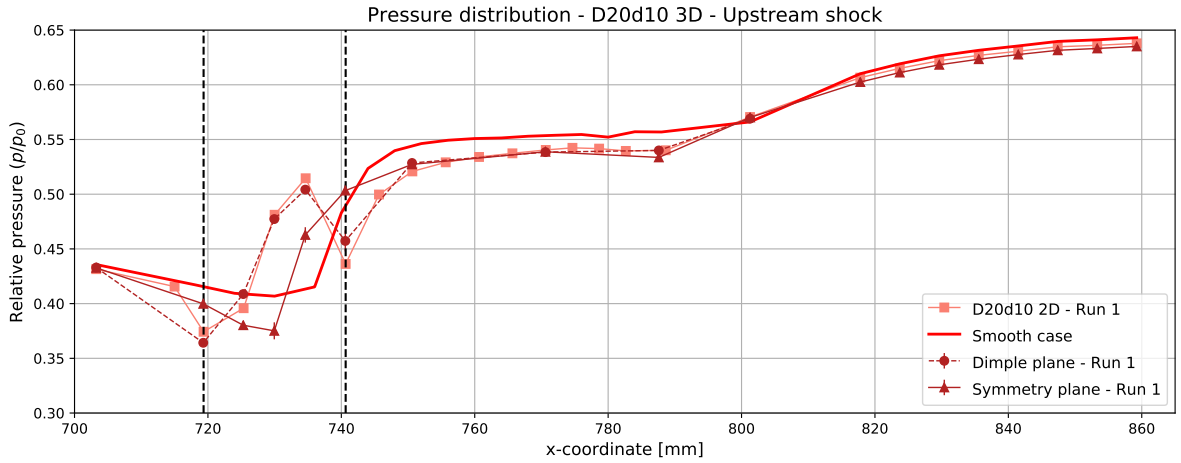

(a) Upstream shock location.

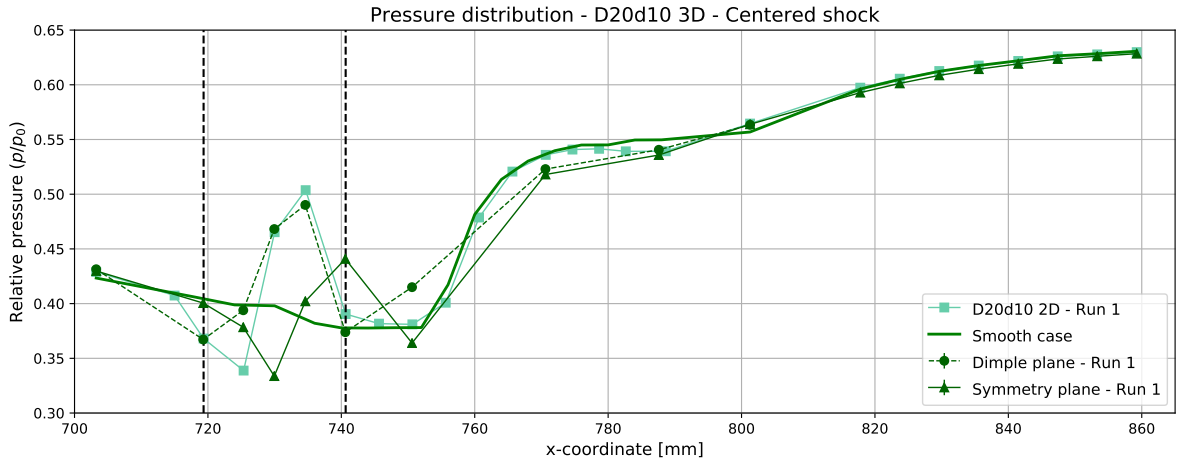

(b) Centered shock location.

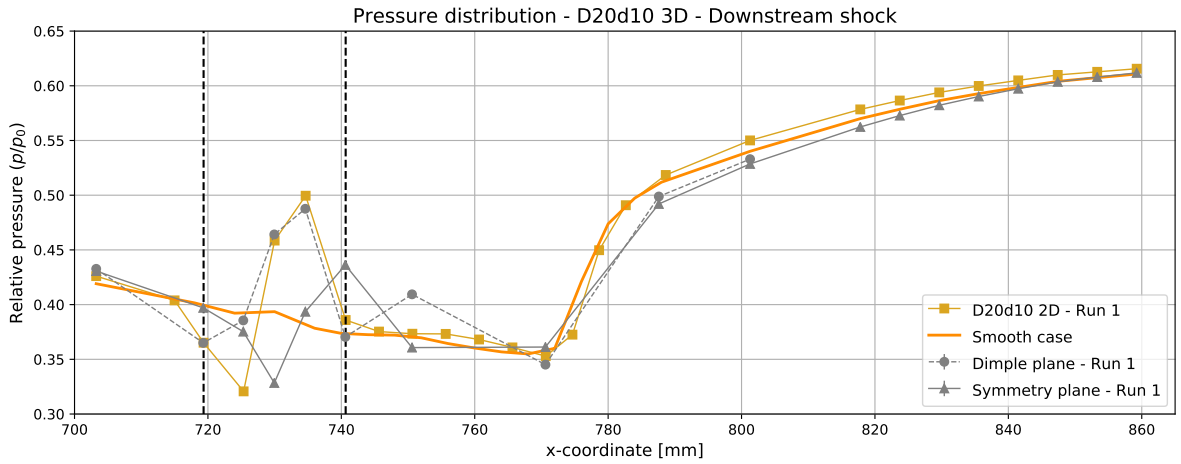

(c) Downstream shock location.

Figure 6.15: Relative pressure distribution over the plate symmetry and dimple centreline for the D20d10 - 3D dimpled plate.

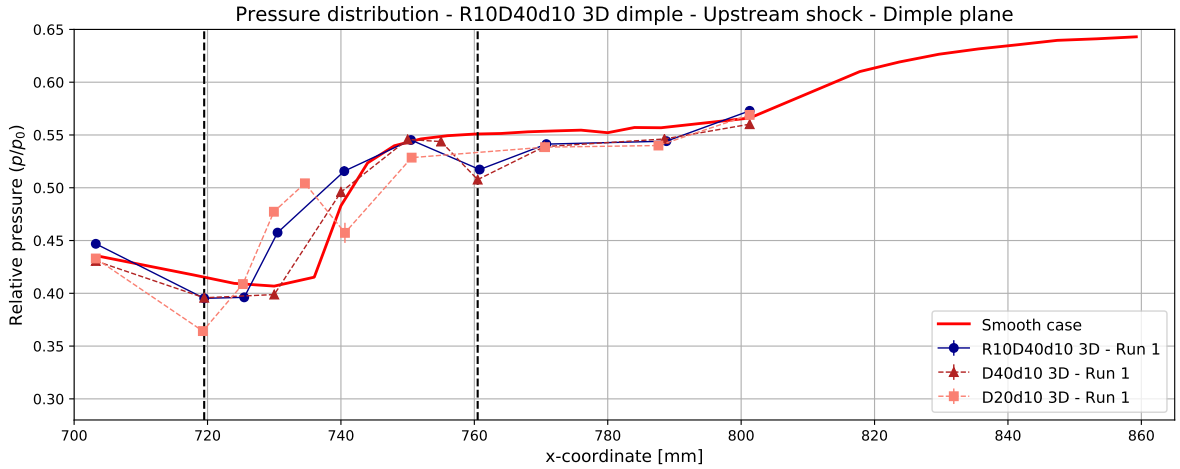

(a) Upstream shock location.

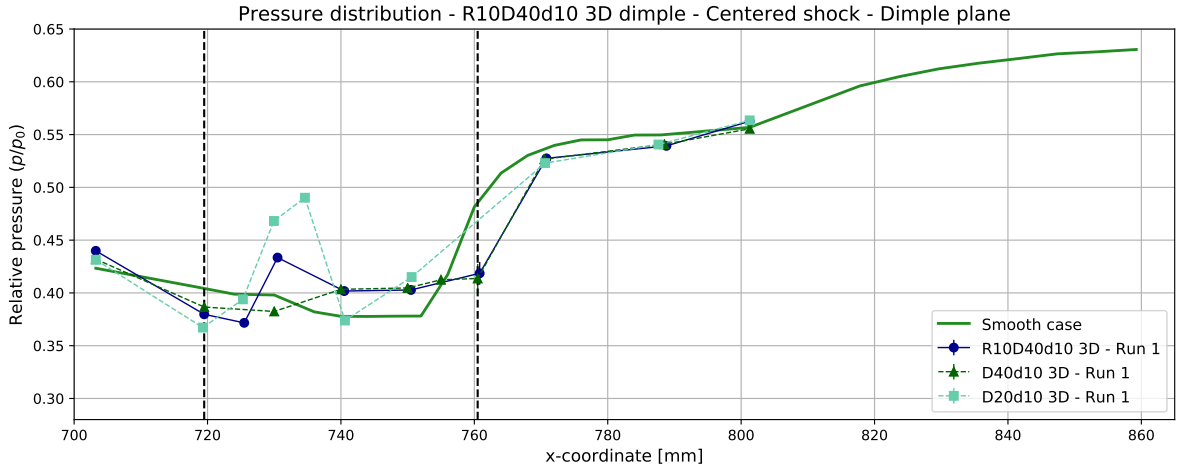

(b) Centered shock location.

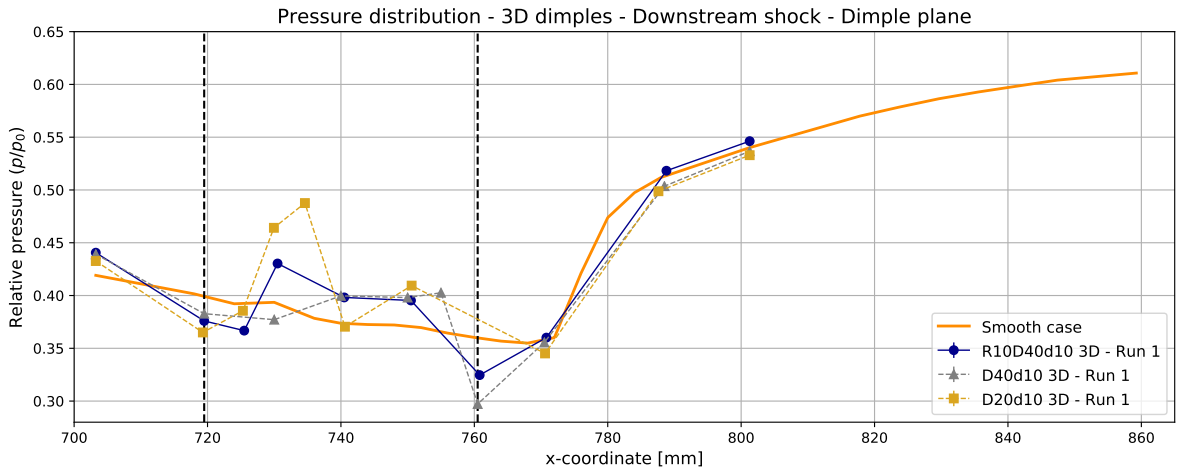

(c) Downstream shock location.

Figure 6.16: Relative pressure distribution over the dimple centreline for the R10D40d10 - 3D dimpled plate.

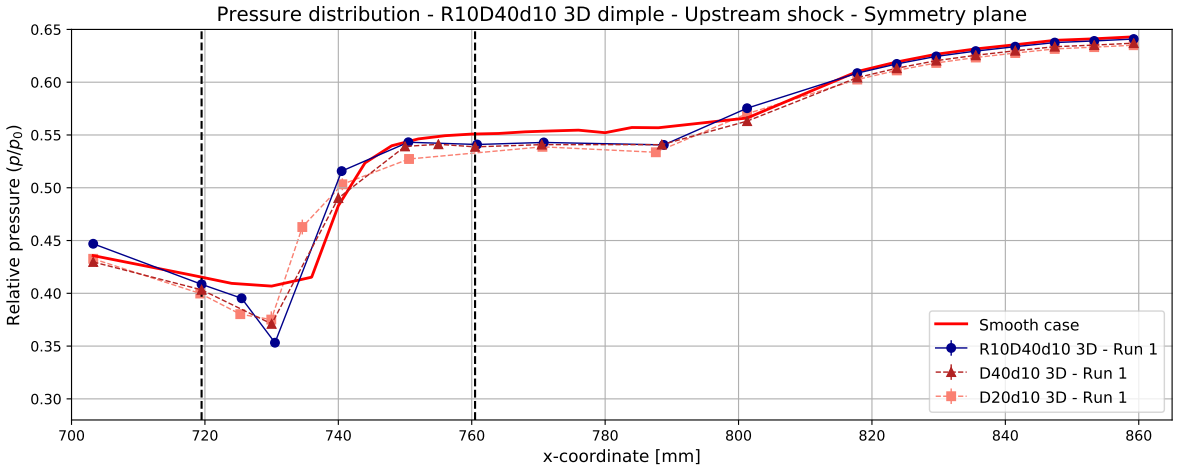

(a) Upstream shock location.

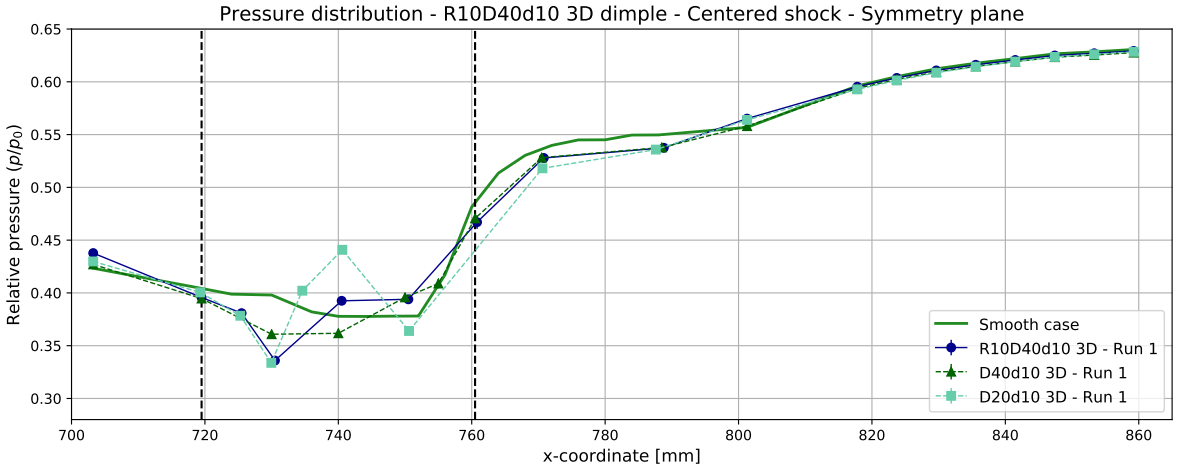

(b) Centered shock location.

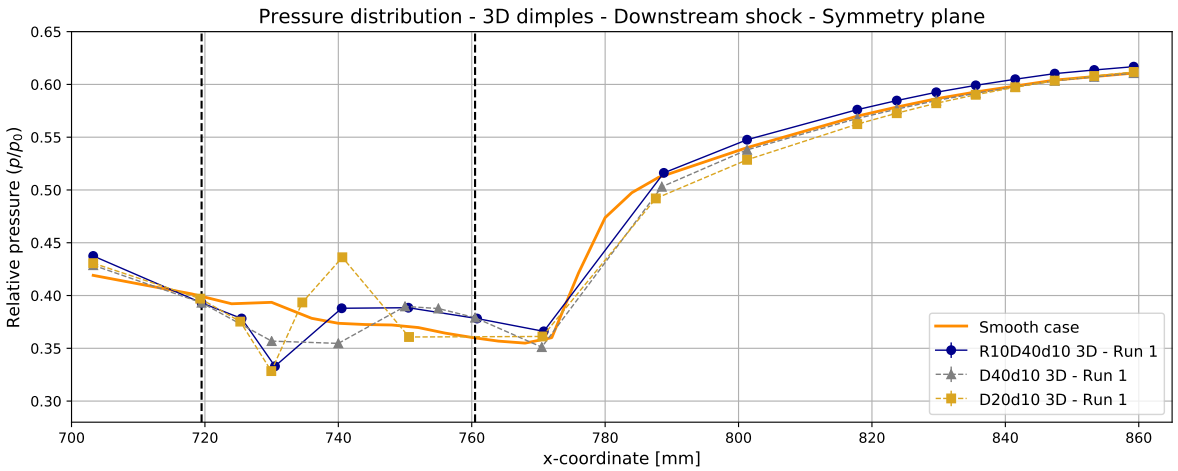

(c) Downstream shock location.

Figure 6.17: Relative pressure distribution over the plate symmetry for the R10D40d10 - 3D dimpled plate.

From the surface pressure measurements conducted over the three-dimensional test plates, the following observations can be made:

D40d10 - 3D plate (Figure 6.14):

- **Flow expansion at dimple edge is reduced and shifted downstream.** Over the dimple centreline, the minimum value of p/p_0 reached is larger than that of the two-dimensional geometry, what indicates smaller velocities. Over the plate symmetry, between two dimples, a slight flow expansion is also observed, with pressure at x=760mm lying below the smooth reference level.
- **Less pronounced flow compression inside the dimple.** Pressure rise achieved inside the indentation for the centered and downstream shock locations was considerably weaker than that seen for the 2D geometry. For the upstream location, flow compression produced by the geometry merges with that resulting from the shock itself, similarly as for the 2D variant.
- **Reduced pressure rise at the shock for the centered case.** Pressure values before the shock over the dimple and symmetry planes are clearly above the smooth reference level, for the centered position (Figure 6.14b). This could indicate a weaker shock close to the wall.
- **Stark flow re-expansion at dimple trailing edge for downstream shock location.** Flow seems to strongly accelerate when exiting the three-dimensional dimple, much more than observed for its 2D counterpart. Afterwards, pressure returns to levels comparable to the smooth reference case just before flow reaches the shock.

D20d10 - 3D plate (Figure 6.15):

- **Weakened expansion at dimple leading edge, but intensity maintained over plate symmetry.** Flow suffered a more modest pressure drop when entering the dimple. However, this expansion was propagated in the spanwise direction and reached the symmetry plane further downstream with an intensity equivalent to that for the 2D geometry.
- **A clear spanwise propagation of the structures formed by the dimple is observed.** Both the oblique wave generated in the dent's interior and the flow re-expansion that occurred at its trailing edge are consistently observed 5-10mm further downstream at the plate symmetry.
- **Secondary compression downstream of dimple trailing edge.** In Figures 6.15b and 6.15c, a secondary compression is observed over the dimple centreline, after the trailing edge re-expansion and before the shock. This phenomenon does not reach the symmetry plane, where pressure seems to follow the smooth reference case behaviour, and was not recorded for the 2D variant.

R10D40d10 - 3D plate (Figure 6.16 and 6.17):

- **Intermediary flow expansion at dimple leading edge.** Pressure minimum reached when flow enters the indentation lies between the values from D20d10-3D and D40d10-3D, with a tendency towards the former given that both geometries are identical in the foremost portion of the dent. Minimum position is halfway from that of the other two distributions.
- **Weaker oblique shock inside the dimple and re-expansion at trailing edge.** Steep compression gradient in the front portion of the asymmetric dimple indicates the formation of an oblique shock, which is less pronounced than that of the D20d10-3D (Figure 6.16). Afterwards, pressure follows the behaviour of the longer D40d10-3D dimple. For the downstream shock, a local stark re-expansion takes place when flow exits the dimple, similar to what was seen in Figure 6.14c but with a lower intensity.
- **Reduced pressure drop over the shock for the centered location.** In Figures 6.16b and 6.17b, as seen for the D40d10-3D, pressure levels are below the smooth reference case over the rearmost portion of the dimple, what could indicate a weaker shock.
- **Asymmetric dimple displays hybrid behaviour of the other two 3D plates.** Over both measurement planes, pressure plots for the R10D40d10-3D are largely bounded by the distributions of the other two 3D plates.

A main characteristic of the flow over the 3D dimpled plates is the spanwise propagation of the structures formed locally over the devices. For a closer inspection of this phenomenon, four spanwise pressure readings were performed at the bottom of the indentations, from the dimple centreline until the plate symmetry. The results of these measurements are displayed in Figure 6.18 for the three plates with the shock at the three locations of interest. The only exception is the upstream shock distribution for D40d10-3D, given that in this case the shock was placed directly over the four pressure taps, causing unstable measurements.

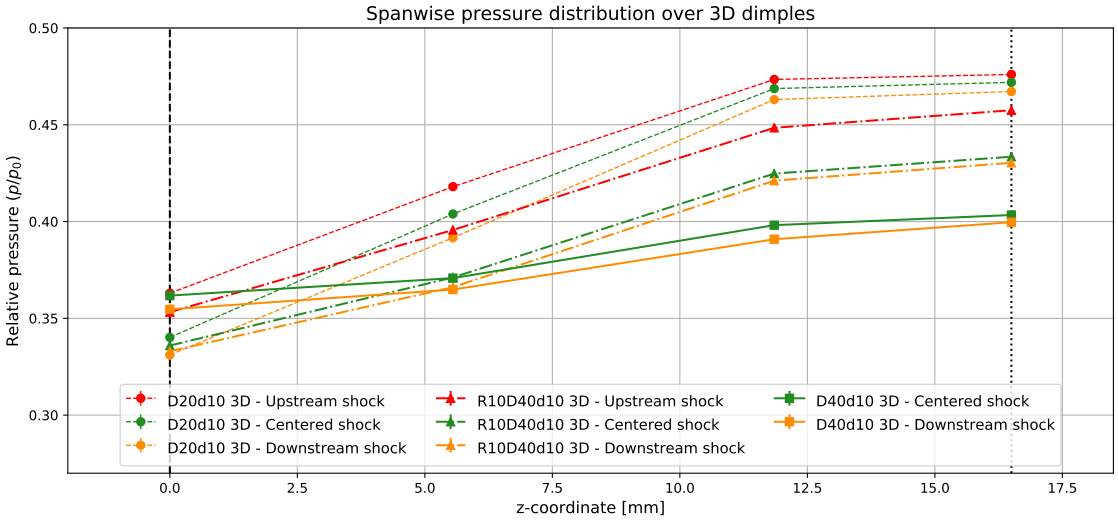

Figure 6.18: Spanwise pressure distribution from the 3D dimples centreline to the test plate symmetry plane. Dashed line represents the plate symmetry and the dotted one the dimple centreline.

For the centered shock over the D20d10-3D and R10D40d10-3D plates, pressure levels are quite similar over the symmetry, where flow is still experiencing the expansion propagated from the dimple leading edge. However, as the dimple centreline approaches, it can be seen that the pressure rise is substantially stronger for the spherical dimple, supporting the observations of a weaker oblique shock produced by the asymmetric indentation. Another observation to be made is that the spanwise pressure gradient is considerably less pronounced for the D40d10-3D dimple when compared to the other 3D plates. Finally, it is interesting to note that there is little pressure variation between the tap at the dimple centreline (z=16.5mm) and that just next to it, located halfway between its centre and the edge, at z=11.85mm. The spanwise gradient only becomes more relevant further away from the centreline, as can be seen from the tap reading over the edge (z=5.5mm).

7

PIV results

This chapter contains the most relevant results from the PIV measurements. Different manipulations were applied to the velocimetry data, and results include not only mean velocity contours, but also velocity gradient and standard deviation distributions. The chapter is concluded with a computation of the momentum flow retention across the shock, which allows an objective final comparison between the test plates. All results are plotted using the global coordinate system defined in Chapter 3.

7.1. Overview

The last measurement technique deployed is also the one that yields the largest amount of insights. Velocimetry data over the shock interaction can be used not only to support observations made from the results presented until now, but also to gather new information from the flow phenomenon. To properly organise the interpretation of these results, first, the average velocity distributions over the field of view will be presented. Then, further manipulations of field data are performed, resulting in distributions of U-component standard deviation and streamwise gradient. Finally, vertical velocity profiles are plotted at different x-coordinates. All PIV measurements were performed with the shock at the centered location.

For all six flow cases, velocimetry data was extracted at the symmetry plane (Plane 1). Additionally, for the three-dimensional ones, measurements were also performed over the dimple centreline (Plane 2). With data from a total of nine flow cases, to which different manipulations were applied, the amount of graphs to be presented grows quickly. In order to keep the presentation of results objective and concise, only the most relevant plots are included in this chapter. Nonetheless, the remaining contours also provide valuable information, and can be found in Appendix F.

In every plot raised for the dimpled plates, the dimple geometry is indicated by a white line contrasting with the dark blue mask applied over the lower wall. For measurements made directly over the dimple geometry, that is, over Plane 1 for the 2D plates and Plane 2 for the 3D plates, the dimple is represented by a full line. Conversely, measurements made over Plane 1 for the 3D dimples recorded the flowfield between two devices, in a region where the plate surface was effectively smooth. Hence, in these cases, the dimple geometry appears as a dotted line. Flow is always from left to right.

7.2. Velocity distributions

The U- and V- velocity component distributions for the smooth plate and the five dimpled test plates are displayed from Figure 7.1 to 7.7.

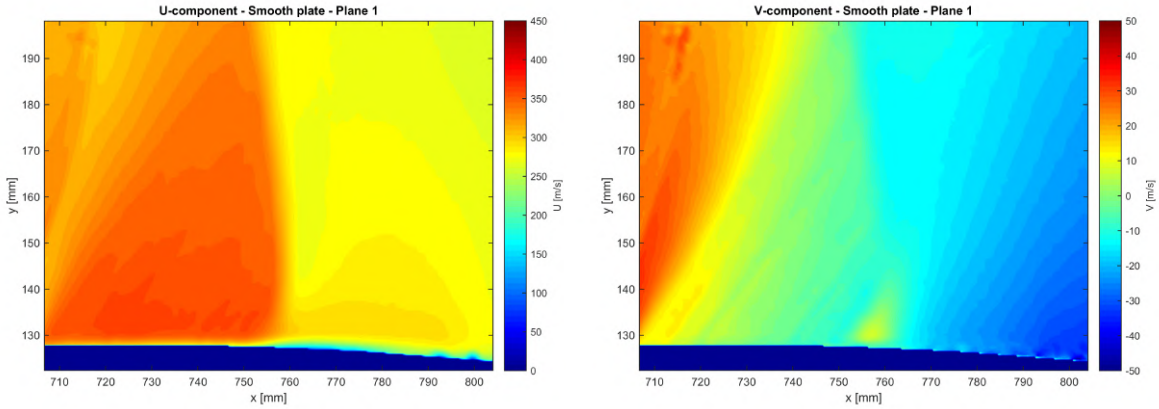

(a) U-component (b) V-component

Figure 7.1: Distributions of the mean U and V velocity components for the smooth reference plate over Plane 1.

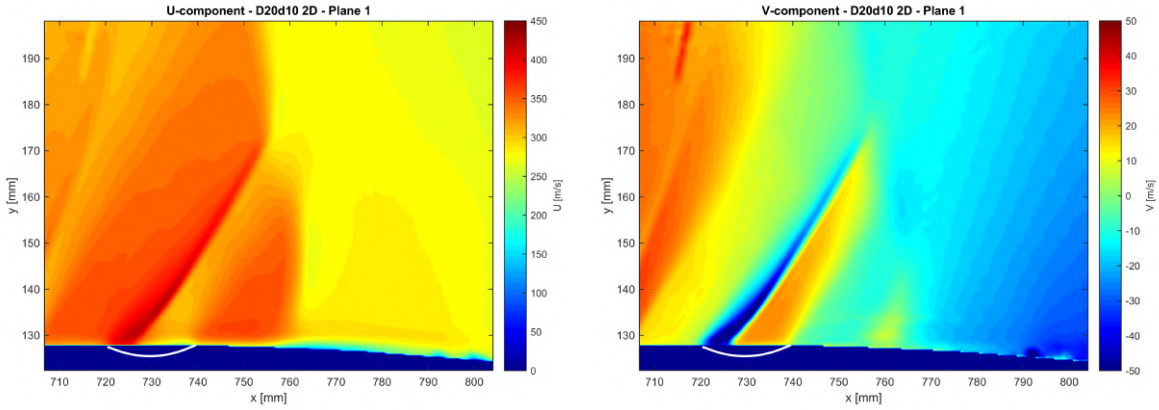

(a) U-component (b) V-component

Figure 7.2: Distributions of the mean U and V velocity components for the D20d10-2D dimpled plate over Plane 1.

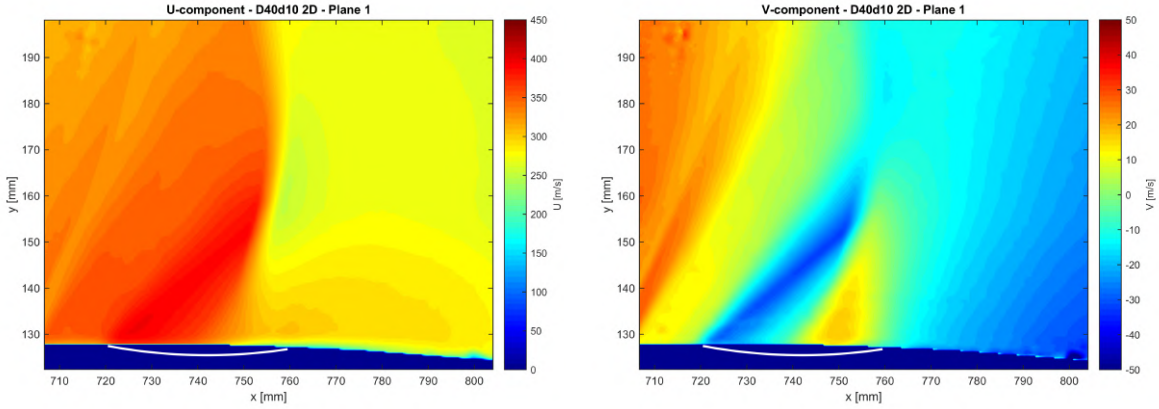

(a) U-component (b) V-component

Figure 7.3: Distributions of the mean U and V velocity components for the D40d10-2D dimpled plate over Plane 1.

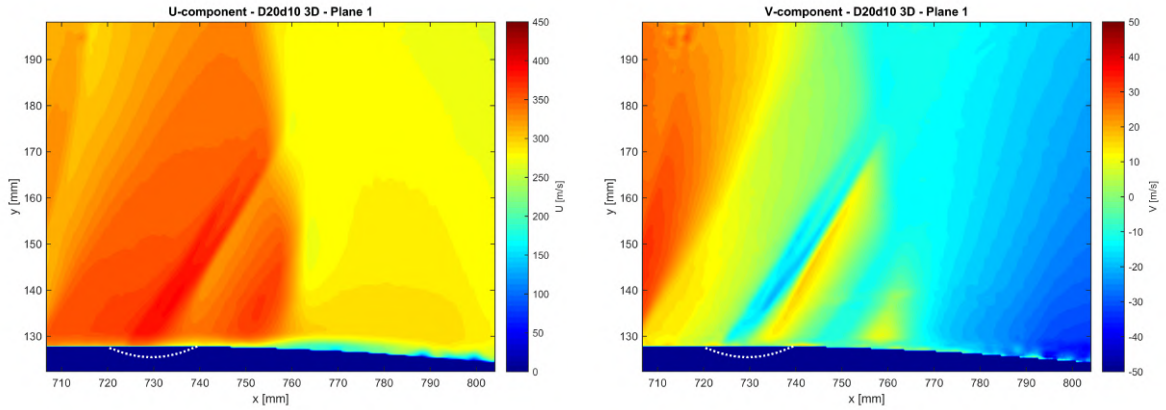

(a) U-component (b) V-component

Figure 7.4: Distributions of the mean U and V velocity components for the D20d10-3D dimpled plate over Plane 1.

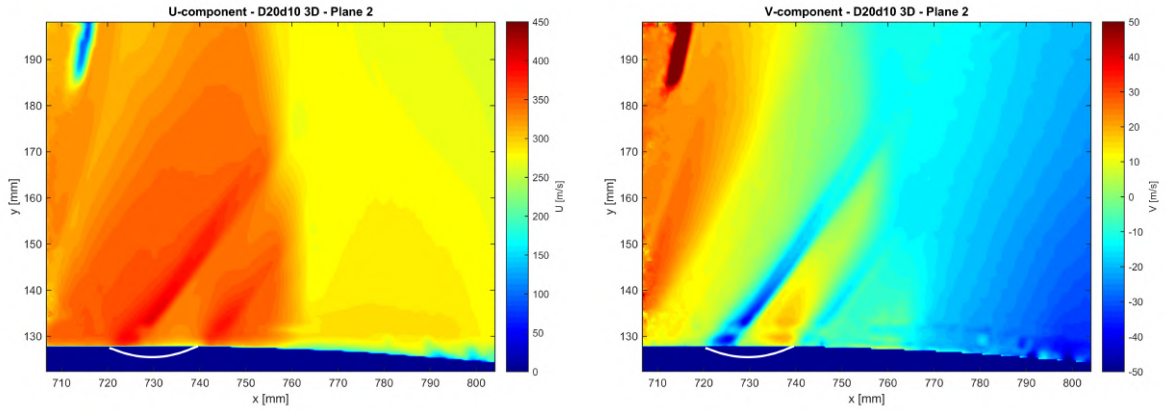

(a) U-component (b) V-component

Figure 7.5: Distributions of the mean U and V velocity components for the D20d10-3D dimpled plate over Plane 2.

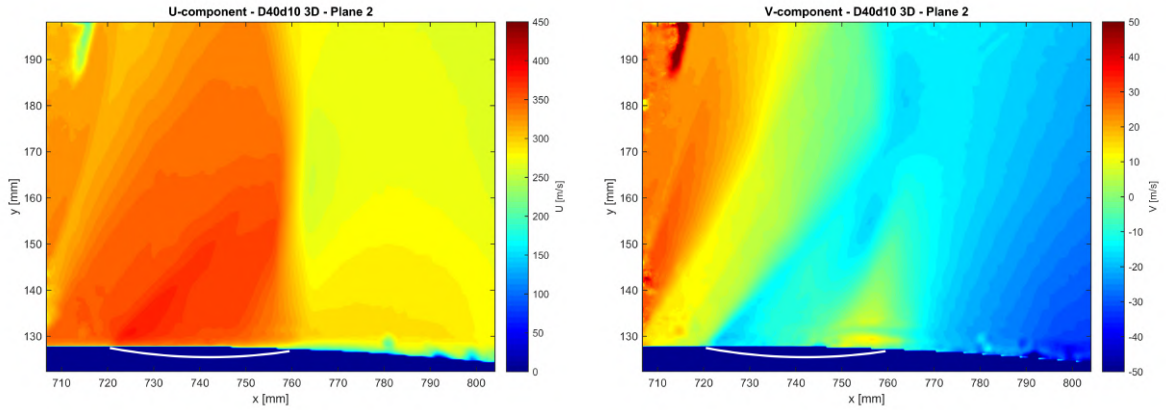

(a) U-component (b) V-component

Figure 7.6: Distributions of the mean U and V velocity components for the D40d10-3D dimpled plate over Plane 2.

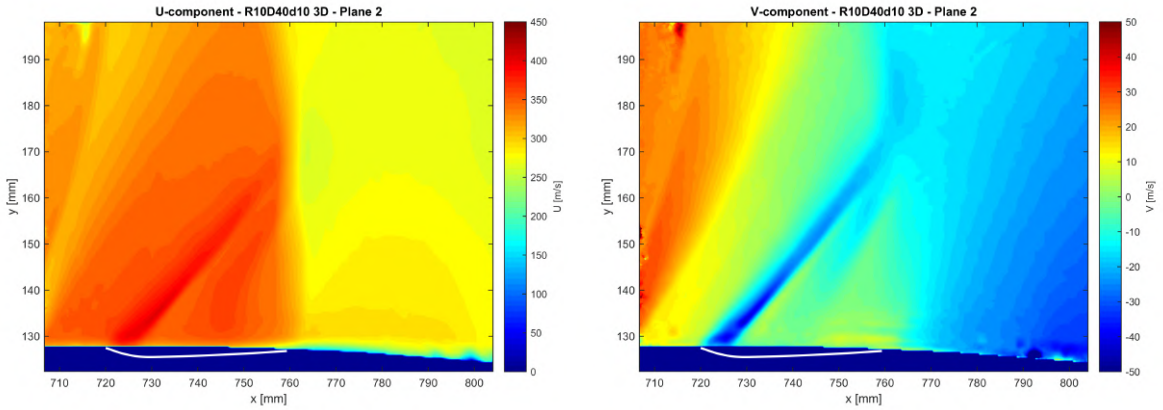

(a) U-component

(b) V-component

Figure 7.7: Distributions of the mean U and V velocity components for the R10D40d10-3D dimpled plate over Plane 2.

The following remarks can be made from the velocity distributions over the test plates:

- **Complete shock structure could not be measured with PIV.** Given the restrictions imposed by the laser sheet limited height, the interaction could only be measured until a height of y=200mm. As can be seen in the Schlieren images, the shock at the centered location extended until y=215mm. Nonetheless, the main phenomena of interest is completely within the field of view.
- **Upwards flow deflection at shock location caused by boundary layer thickening.** The V-component distribution for the smooth case indicates the natural flow movement in the asymmetric test section nozzle (Figure 7.1b). At x=760mm, although the majority of V-components in free stream are already pointing downwards, following the descending curvature, a small pocket of positive vertical velocity is formed close to the wall. This upwards streamlines deflection is a result of the boundary layer thickening that occurs at the shock foot.
- **3D geometries provoked less-pronounced perturbations, as opposed to their 2D variants.** The streamwise velocity contour for the D20d10-2D displays a strong acceleration when flow enters the dimple. Additionally, the V-component distribution shows consecutive regions of negative and positive values between x=720 and 740mm, characterising a stark flow turning caused by the dent. Its 3D variant, however, induces smoother perturbations in the flow even at the dimple centreline. These are propagated in the spanwise direction, being perceived at the symmetry plane with reduced intensity and a downstream offset of around 5mm (Figures 7.4 and 7.5).
- **Secondary compression observed downstream of the spherical dimple.** After the expected re-expansion when exiting the indentation at x=740mm, flow is suddenly decelerated before the normal shock wave. This is only observed at Plane 2 measurements (Figure 7.5). The same phenomenon was captured by the surface pressure measurements from Figure 6.15.
- **Structures produced by asymmetric dimple are a combination of those found over the other two 3D plates.** Given their geometric similarities, both spherical (D20d10-3D) and asymmetric (R10D40d10-3D) dimples resulted in an equivalent downwards flow turning at x=720mm followed by the formation of an oblique shock wave (Figure 7.7). Subsequently, however, its V-component distribution indicates a slower flow turning, as a result of a smaller curvature radius in the ascending region. This effect is comparable to that seen for the elongated D40d10-3D, but with the asymmetric variant producing an even gentler deflection at the trailing edge (x=760mm).

It must be mentioned that, especially for the Plane 2 measurements, an elongated region with reduced speed can be identified at the top left corner of the images. This is not related to any flow phenomena, but is a consequence of laser sheet reflections with the optical access rim. They created a constantly bright region in the images, which influenced the subsequent displacement vectors calculation. This poorly-correlated region does not however influence the results interpretation, being located away from the main regions of interest.

7.3. U-component standard deviation

The distribution of U-component standard deviation for different test plates is presented in Figure 7.8. It is here used to measure the effect of the dimple on the stability of the shock structure. In this analysis, only measurements over Plane 1 are considered. When the mirror probe was set to produce the laser sheet over the 3D dimple centreline (Plane 2), the aerodynamic interference between its structure and the wind tunnel wall caused the shock to oscillate substantially during measurements. Although the velocity fields were post-processed to improve the quality of average distributions (process described in Appendix E), it is not possible to segregate the effects of dimple on shock stability from those caused by probe interference. This renders a comparison with the smooth reference case invalid.

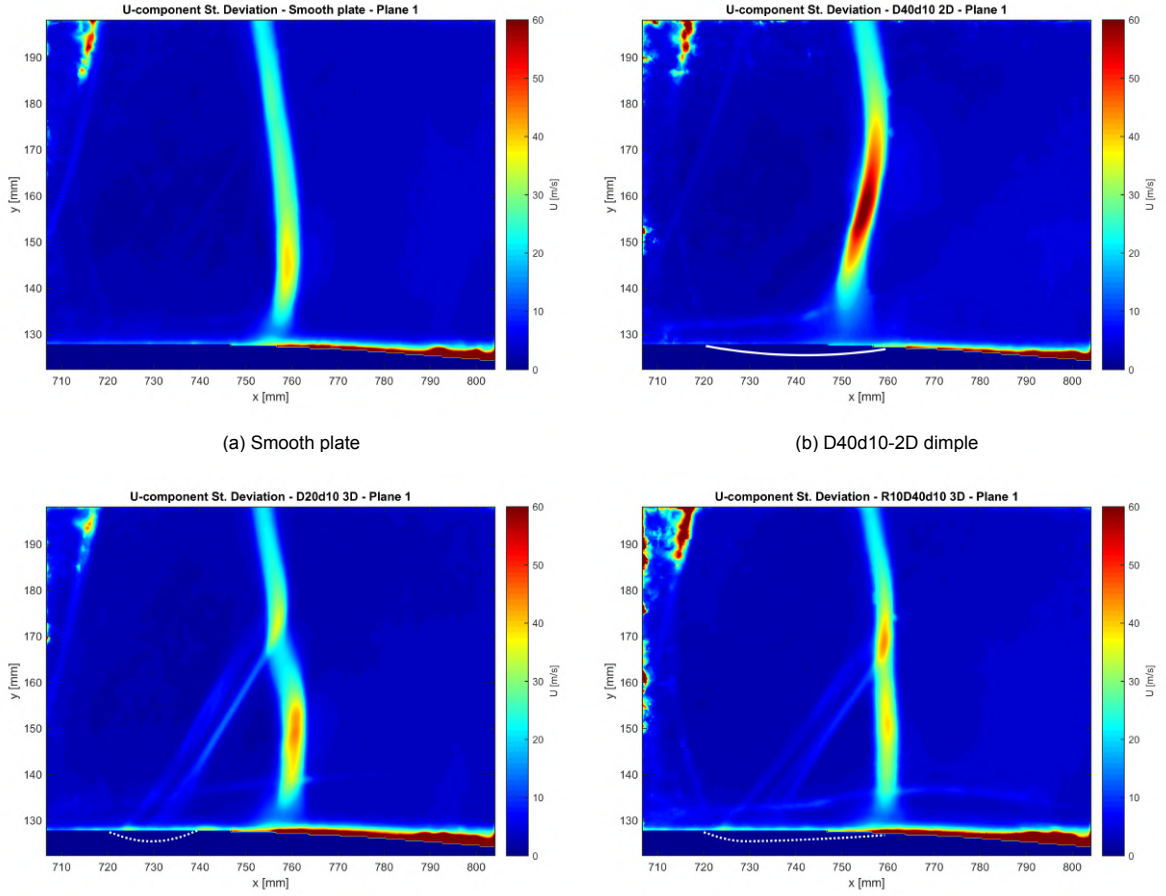

(a) Smooth plate

(b) D40d10-2D dimple

(c) D20d10-3D dimple (plane 1)

(d) R10D40d10-3D dimple (plane 1)

Figure 7.8: Distributions of the U-component standard deviation for different test plates.

In general, the dimpled plates have a negative effect on the shock stability. Higher values of the velocity standard deviation at the shock leg are interpreted as a higher oscillation of the wave during the measurement interval. The worst result was recorded for the D40d10 2D dimpled plate, which displayed the highest shock location uncertainty. It is also interesting to note that the main shock structure seems to have become slightly less stable also in the halfway between two three-dimensional surface indentations. Nonetheless, the oblique shocks propagated from the D20d10 and R10D40d10 3D dimples display low uncertainty, and seem to remain pinned at the front portion of the dent. Although comparable results are not available over the dimple centreline, a similar result would be expected in this region.

7.4. U-component streamwise gradient

Now, the gradient of the U-component in the streamwise direction is presented for different test plates in Figure 7.9. In this context, this quantity is used to assess the strength of the resulting shock, thus indicating if the control devices are capable of reducing its intensity.

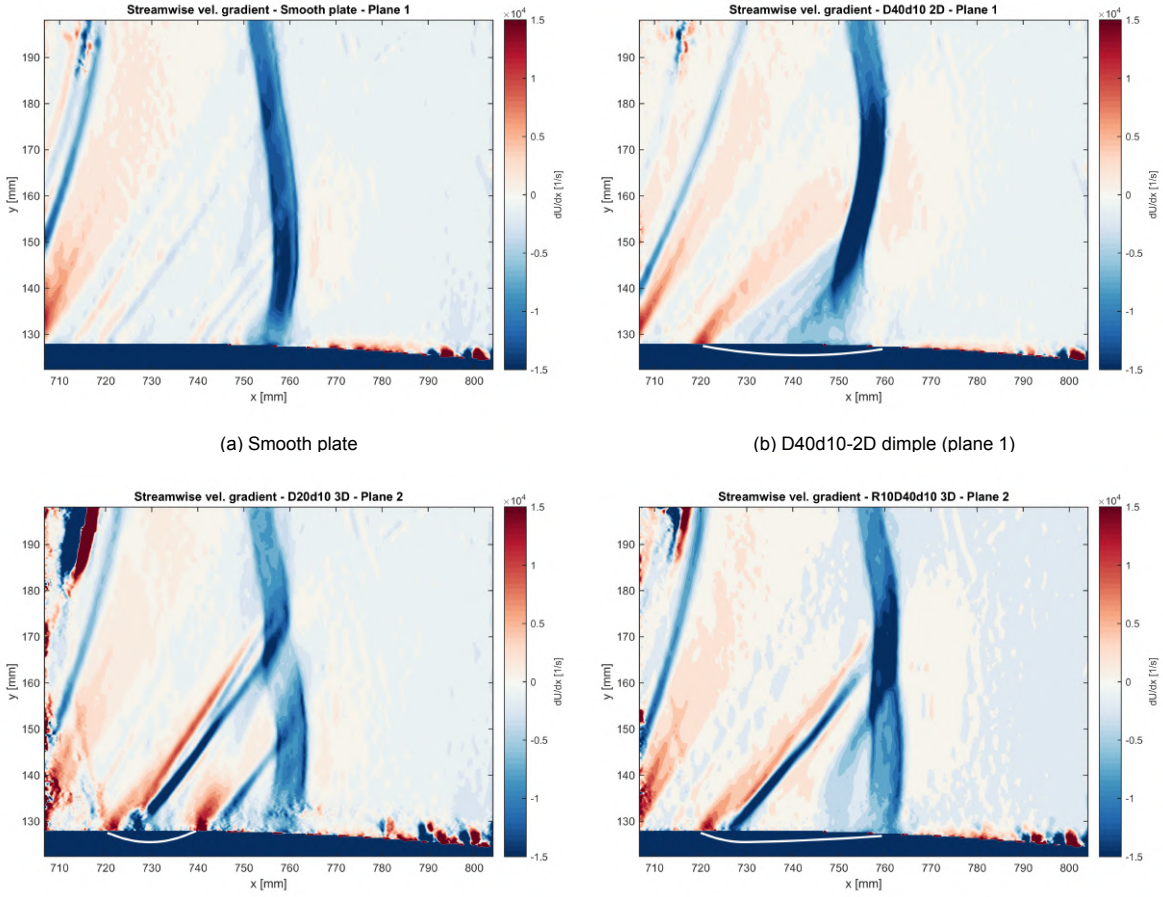

(a) Smooth plate

(b) D40d10-2D dimple (plane 1)

(c) D20d10-2D dimple (plane 2)

(d) R10D40d10-3D dimple (plane 2)

Figure 7.9: Distributions of the U-component gradient in the streamwise direction for different test plates.

From the smooth plate result, it can be seen that the negative velocity gradient is rather uniform along the shock structure. The distribution for the D40d10-2D plate in Figure 7.9b represents well the antagonistic flow mechanisms over the dimple. Streamlines close to the wall experience an almost isentropic compression, represented by a relaxed negative gradient. However, further away from the wall, the expansion fan that emanates from the dimple leading edge at y=720mm impinges on the normal shock, resulting in a starker velocity deceleration.

Also for the 3D dimples, it can be seen that on the spot where the expansion fan hits the main shock leg, a starker gradient is observed. However, while the fan expands continuously from the leading edge of the D40d10-2D plate, the same is not observed for the D20d10-3D and the R10D40d10-3D, whose flowfield is characterised by an oblique wave running adjacent to the leading expansion waves. As would be expected, just below the point where the oblique waves impinge on the shock, a less pronounced deceleration is observed, especially for the D20d10-3D. Still on the spherical dimple, the already mentioned flow deceleration after the flow re-expansion can be observed, in the form of a secondary oblique wave propagating from the wall at x=745mm. As a whole, it seems like the gradient intensity over the shock structure influenced by the D20d10-3D is smaller than that over the smooth reference case.

In all images, an oblique wave followed by an expansion fan can be seen emanating from upstream of the field of view. It most likely originates from the interface between the lower wall and the printed circular section block, and is a result of an imperfect assembly of the components.

7.5. Vertical velocity profiles

In this section, the velocity magnitude profiles are raised at different streamwise locations, what allows for more direct comparisons between the flow cases. As a result, the flow speed distribution just before of the shock can be analysed, as well as the velocity deficit downstream of it. In order to account for small deviations of flow conditions at individual measurements, velocities were normalised using a reference value. It was computed upstream of the interaction, as the mean velocity magnitude value around x=708.6mm between y=160 and 190mm (thus avoiding the oblique wave upstream of the FOV). The computed values for each flow case ranged from 323.3 to 326.1m/s, what indicates a good repeatability of incoming flow conditions. The profiles are displayed in Figures 7.10 to 7.12.

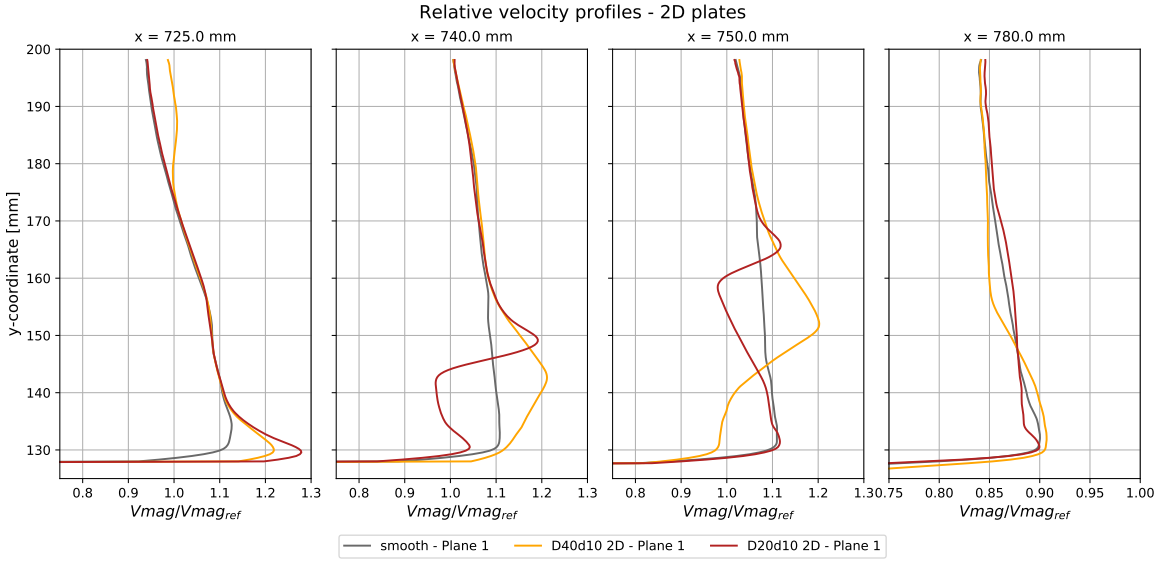

Figure 7.10: Velocity magnitude profiles for the smooth, D40d10-2D and D20d10-2D plates.

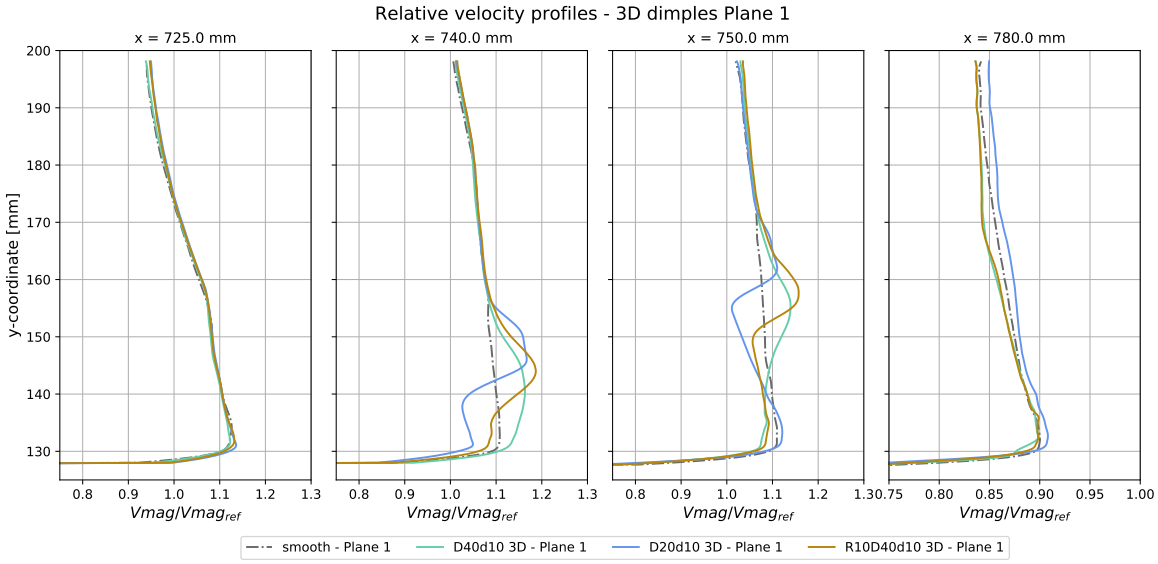

Figure 7.11: Velocity magnitude profiles for the three-dimensional dimpled plates over Plane 1.

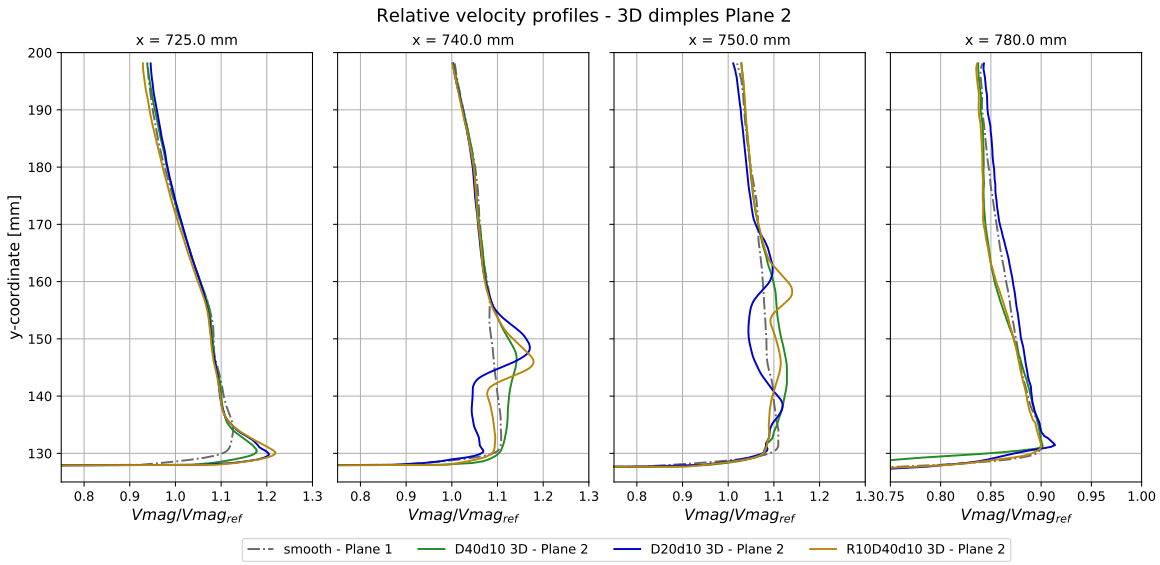

Figure 7.12: Velocity magnitude profiles for the three-dimensional dimpled plates over Plane 2.

The locations chosen to raise the vertical profiles coincide with key regions of the flowfield. The first is just 5mm after the leading edge of the dimples, and allow to assess the behaviour of the flow when entering the indentation. The second, at x=740mm, coincides with the middle of the long dimples and with the trailing edge of the spherical one. The third profile shows the velocity distribution just upstream of the shock, what provides an indication of its strength over the vertical axis. Finally, the last one is positioned downstream of the normal shock, at x=780mm, where full subsonic flow is established.

From the PIV velocity distributions presented earlier, it can be noted that effects caused by the surface indentations in the supersonic portion of the flow only reach a maximum height of y=175mm. Above that point, flow should not be influenced by their presence and is expected to be identical for all flow cases. This is confirmed by the velocity profiles, which display a large agreement beyond y=175mm in the first three streamwise positions, where flow is still supersonic.

By analysing the 2D plates profiles, it can be clearly observed how differently the two dimple designs operate. While rapid accelerations and decelerations occur over the D20d10-2D, the D40d10-2D induces gentler modifications in the flow. It is interesting to observe that in spite of the D20d0-2D producing larger speeds when flow just entered the indentation, this maximum is rapidly dampened when convected upwards in the flowfield, and, upstream of the shock, the velocity deficit produced by the oblique wave dominates the profile. The opposite occurs for the other plate, for which we see the velocity surplus expanding while it is propagated upwards. In the two last velocity profiles, the curves from the smooth and D40d10-2D plates cross each other at almost the same y-coordinate. For the 2D dimple, decelerated streamlines close to the wall in the x=750mm profile experience a weaker shock, and thereafter move with a higher downstream speed than the smooth case. The opposite occurs in the accelerated region just above it.

The 3D dimpled plates seem to produce effects comparable to those from their two-dimensional counterparts, but with lower intensity. Flow expansion at the dent's leading edge is less pronounced, as well as the compression inside of it. An extreme example of this is observed for the D40d10-3D plate, which fails to decelerate (and thus compress) the flow in its interior over the dimple centreline, in contrast with what occurs for its 2D version. Both elongated and asymmetric dimples produced a downstream velocity profile less full than the smooth reference case. However, the opposite occurred for the spherical dimple (D20d10-3D): velocity profiles downstream of the shock display over both PIV planes a consistent velocity surplus with respect to the reference case, indicating a higher recovery across the interaction.

7.6. Momentum flow ratio

In order to quantify the global effect of the surface indentations on the shock, the momentum flow ratio was computed for every flow case. It is here reasoned that a larger momentum retention across the interaction is an indicator of a weaker shock, which ultimately produces smaller wave drag. Hence, the mass-averaged momentum flow was computed over the vertical axis at two positions, one upstream, at the same location where the reference velocity magnitude V was extracted, and another downstream, at x=780mm, where the last velocity profiles were raised. Values were calculated until y_c=196mm, close to the end of the interaction.

The mass-averaged momentum flow was numerically computed following Equation 7.1, adapted from the mass-averaged total pressure expression from the work of Ogawa et al. [66]. Density and velocity were non-dimensionalised (ρ_r, u_r), yielding a normalised output.

$$\overline{M} = \frac{\int_0^{y_c} (\rho_r\, u_r)(\rho_r\, u_r^2)\, \mathrm{d}y}{\int_0^{y_c} \rho_r\, u_r\, \mathrm{d}y}, \quad \text{where } \rho_r = \rho/\rho_0, \quad u_r = u/V \tag{7.1}$$

The velocity streamwise component was directly extracted from the velocimetry data and normalised with V. On the other hand, the relative density ($\rho_r = \rho/\rho_0$) was not measured, and, moreover, the total density drop over the shock also had to be taken into account in the downstream location (given that $\rho_{02} < \rho_{01}$). Therefore, the following procedure was adopted to compute the relative density profile in both locations.

To overcome this, first, Mach number and relative density distributions were computed from the velocity distribution using the isentropic flow relations presented in Section 2.1. Then, the Mach number profile upstream of the shock was raised for every flow case, by searching for the location with the minimum pressure gradient (which identifies the shock position) and recording the value of Ma just before the deceleration. Note that these values were captured at slightly different x-coordinates, for the shock structure was not perfectly vertical. With the upstream Ma profile, it was possible to compute at every y-coordinate the losses across the wave by using normal shock relations, what yielded a total density loss profile that was used to correct for the relative density downstream of the interaction. Upstream Mach number and total density ratio profiles computed can be seen in Figure 7.13. The same plot for the R10D40d10-3D dimple is found in Appendix F.

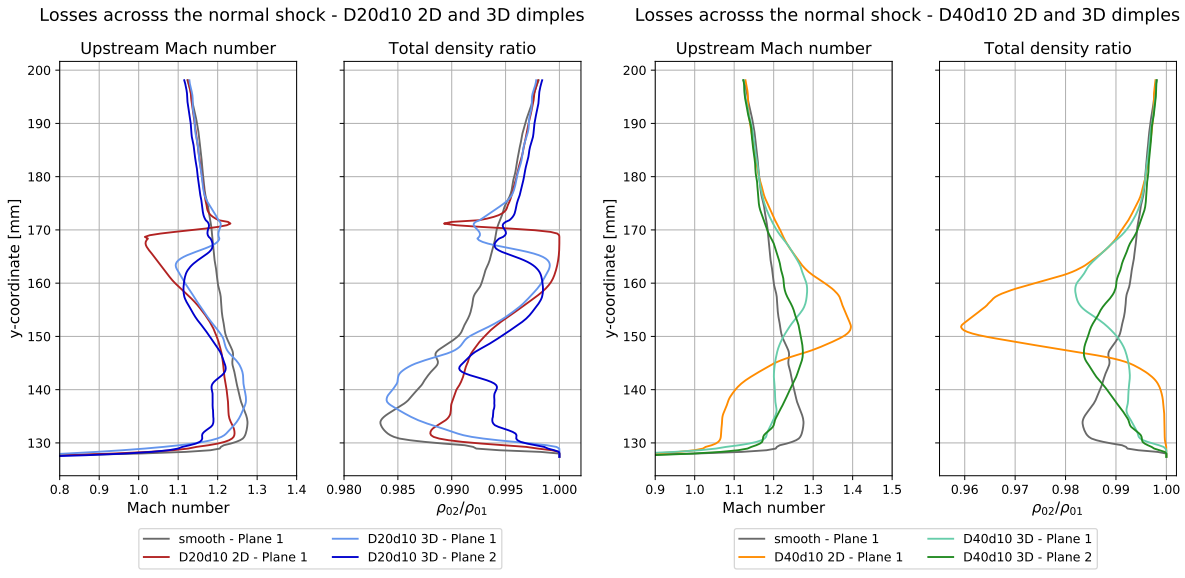

(a) D20d10 2D and 3D plates

(b) D40d10 2D and 3D plates

Figure 7.13: Upstream mach number and total density ratio profiles using normal shock relations.

It can be noted that, given the small Mach number reached in the flow field, the total density ratio usually remains above 0.98. An exception is seen for the D40d10-2D profile, for which the stark acceleration produced at the dimple leading edge is propagated upwards and provokes large losses around y=150mm. Conversely, profile regions which were still experiencing compression before the shock suffered almost no loss across the shock, such as for the D20d10-2D between y=160 and 170mm.

Finally, the mass-averaged momentum flow could be computed in both upstream and downstream locations. The ratio between both values indicates how much momentum was retained across the shock for each flow case, providing an indication of potential wave drag reduction. Momentum error is expressed by Equation 7.14. Velocity uncertainty is easily obtained at both locations from the standard deviation of the PIV distributions. However, that of the density is more complicated, since it was indirectly computed by means of isentropic and normal shock relations. For the sake of simplicity, it was only considered the effect of the former quantity, which was propagated to compute the momentum ratio error. The value of the mass-averaged momentum flow ratio for every flow case is presented in Figure 7.14.

$$M = \rho\, u^2 \quad \rightarrow \quad \sigma_M = M\left[\left(\frac{\sigma_\rho}{\rho}\right)^2 + \left(\frac{\sigma_{u^2}}{u^2}\right)^2\right]^{1/2} = M\left[\left(\frac{\sigma_\rho}{\rho}\right)^2 + \left(\frac{2\,\sigma_u}{u}\right)^2\right]^{1/2} \tag{7.2}$$

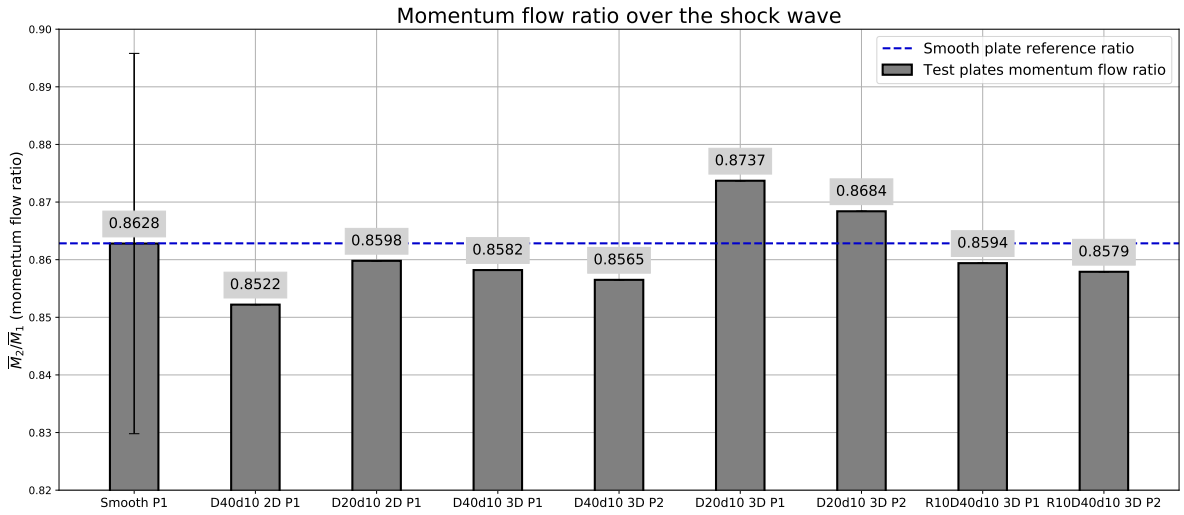

Figure 7.14: Mass-averaged momentum flow ration for all test plates.

The first thing to be mentioned is that the error bar, computed for the smooth reference case, covers the entire range of the computed values. Although discarding the density contribution yields a poor error estimation, it was not needed to increase the complexity of its computation given that the influence of the velocity uncertainty was already large enough. Therefore, it won't be possible to draw a completely definite conclusion of the test plates overall performance.

That being said, there is still a significant indication that indeed the D20d10-3D plate is capable of retaining more momentum across the shock structure. This occurs over both planes, and more so over the symmetry one, where the momentum ratio was 1.2% larger than that for the smooth plate. All other dimpled plates displayed a worse performance than the smooth case, and the one that got the closest to the reference level was the two-dimensional variant of the D20d10. On the other hand, both D40d10 2D and 3D displayed a considerable deterioration of downstream recovery, with the former resulting in a 1.2% reduction. All in all, the variations with respect to the reference level are rather small. This occurs because the ratio is computed across the complete shock structure captured by the PIV field of view, while the effects produced by the surface indentations on the interaction only reached a limited height away from the wall.

8

Discussion and conclusions

In this chapter, the results from the measurement techniques deployed in the campaigns will be discussed. Based on the observations made, conclusions are drawn for the research questions posed in the beginning of this work. Finally, this chapter proposes recommendations for future research.

8.1. Discussion

The results discussion is split in two parts. The first concerns the experimental reproduction of the desired flow conditions, a key aspect of this work. Then the second addresses the assessment of dimples as a shock control control device, with parallels being drawn to transonic bumps.

8.1.1. Reproduction of flow conditions

The first goal of the current study was to generate the conditions of interest for the experimental analysis, namely a transonic flow. It was opted to use an asymmetric nozzle, which would produce over its lower wall a supersonic pocket, terminated by a normal shock wave and then followed by an adverse pressure gradient, similarly as found over transonic airfoils. Taking the previous design from Nebbeling [62] as a reference, CFD simulations were performed to re-design the nozzle lower wall and tailor the resulting flowfield. The experimental setup was manufactured using the final geometry of this iterative process as a base, and measurements were performed to validate it.

In general, the re-designed setup successfully produced a flow field which allowed the study of control devices applied to normal shock waves. The shock could be remotely displaced over a wide range of positions using the choke mechanism, and would increase in size when moved downstream, as a larger portion of the flow before it reached supersonic speeds. It was placed well within the wind tunnel window, allowing the use of optical techniques, and did not cover the entire cross-section height, what ensured stable measurement conditions. Pressure distributions along the wind tunnel walls (Figures 8.1a) confirmed that incoming flow was two-dimensional and remained stable throughout the entire run. Oilflow visualisation also indicated that streamlines were parallel to each other close to the wall (Appendix D), and minor divergences in the spanwise tap readings (Figure 8.1b) are attributed to surface imperfections near the orifices. Additionally, the setup did not seem to suffer much from hysteresis effects, and pressure readings recorded with a downstream moving shock largely agreed with those for which the wave was moving in the opposite direction.

During the design iteration process, described in Chapter 3, the simulated pressure distribution was compared with that computed for a transonic airfoil by Coliss and Babinsky [74]. Parallels could be drawn between both cases by normalising the x-coordinate with the incoming boundary layer height. Now, the same can be done with the surface pressure measured along the setup. The incoming boundary layer height was approximated from PIV data of the smooth reference case at x=710mm, upstream of the interaction, and then used to scale the streamwise coordinate. The value obtained was $(\delta)_{\text{PIV}}$=3.13mm, slightly below the simulated $(\delta)_{\text{CFD}}$=3.5mm. It must be mentioned that PIV measurements focused on capturing the freestream behaviour, hence vector spacing was sub-optimal to accurately evaluate BL height. The results are presented in Figure 8.2.

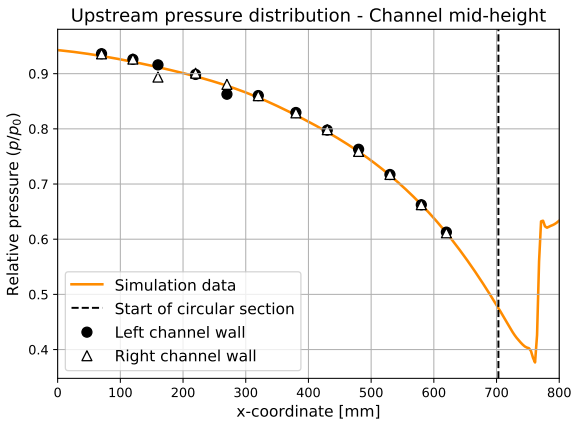

(a) Freestream pressure upstream of circular section.

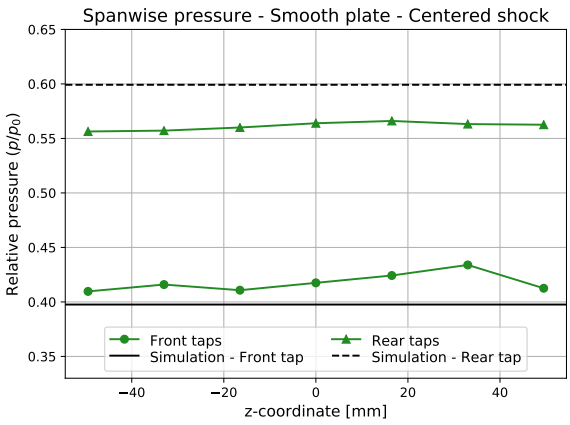

(b) Spanwise pressure for the centered shock.

Figure 8.1: Pressure distributions used to validate the flow conditions over the asymmetric nozzle.

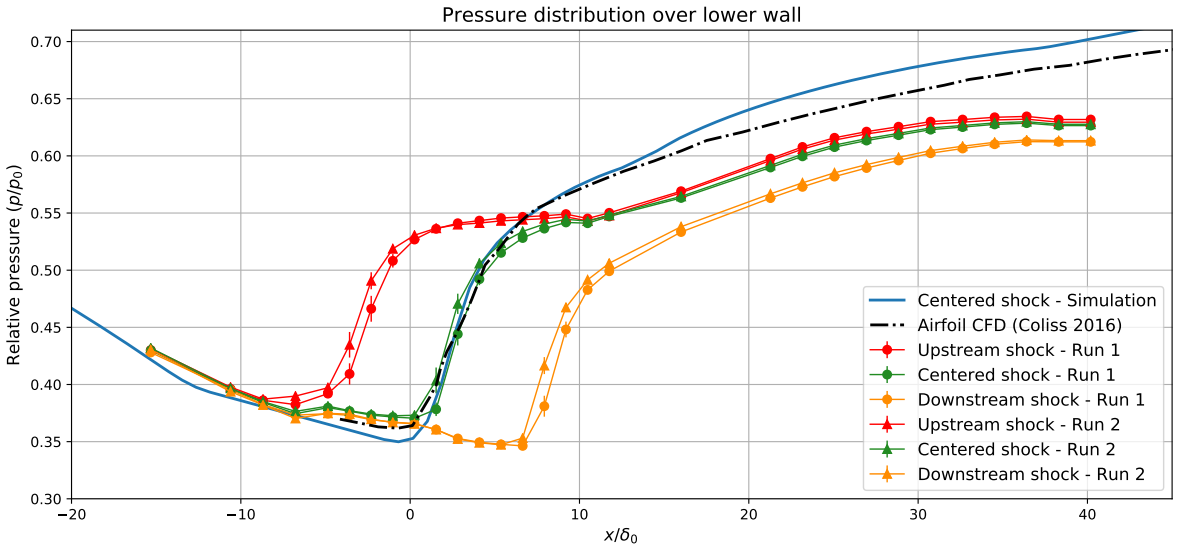

Figure 8.2: Pressure distribution with x-coordinate normalised with incoming boundary layer height.

Pressure measured over the test section diverges considerably from the airfoil simulation in the adverse gradient region. It seems to recover more slowly from the rise across the shock. Still, it appears to follow the same slope angle as the airfoil between x/δ=10 and 28, but towards the end the distribution over the lower wall flattens down. This is likely a consequence of the more gentle descent adopted in the lower wall shape downstream of the shock, aimed at avoiding separation.

When comparing with the lower wall simulation, an even greater divergence occurred in the APG region, which can be attributed to the computational model overestimating the pressure recovery downstream of the shock. Another plausible explanation is that, during the experiments, the choke plate mounting, which had a vertical degree of freedom, resulted in a different upper wall geometry than that simulated, thus modifying the flow behaviour in the APG.

Furthermore, flow reproduced experimentally also departed moderately from the simulated one upstream of the shock, with pressure measured for the centered shock location not reaching the same minimum level as the computations. Measurements indicate a minimum p/p_0 value of 0.377, which corresponds to a Mach number of 1.267 upstream of the shock, whereas in the simulation it reached p/p_0=0.35, that correlates to Ma=1.322. These divergences with the simulation can be clearly observed in Figure 8.1b, which compares the pressure acquired over the front and rear spanwise taps with that computed numerically at the same locations. The values for the front taps are clearly above the simulation pressure level, suggesting lower incoming speeds at the start of the circular test section. On the other hand, rear taps readings are considerably below the CFD computations, confirming a slower pressure recovery downstream of the shock for the wind tunnel flow.

Albeit the divergences close to the wall over the circular section, pressure measurements at channel mid-height display a very close agreement with the simulated curve (Figure 8.1a). They were recorded along the side walls of the wind tunnel, and the last acquisition point was located just upstream of the circular section. Therefore, it can only be concluded that some unforeseen event takes place between the last side wall pressure tap (x=620mm) and the first one over the circular section (x=703mm) to justify the disagreement between the pressure distributions.

This divergence can be explained by the oblique wave which emanated from upstream of the PIV field of view. Schlieren images already accused the presence of such structure, but its influence in the incoming flow could only be clearly understood by plotting the streamwise velocity gradient contours. Incoming flow is slightly slowed down when entering the field of view as it crosses this oblique shock, and then re-accelerates. Its cause is likely a mounting misalignment or the change of surface roughness between the lower wall and the circular test section block, which leads to a minor upwards deflection in the flow. Given that in this region flow is already supersonic, an oblique wave is formed, what results in the measured deficit of incoming velocity. In Figure 8.3, the Schlieren image for two flow cases is shown superimposed with the respective contour of the U-component streamwise gradient. The upstream oblique shock (UOS) is indicated in the image.

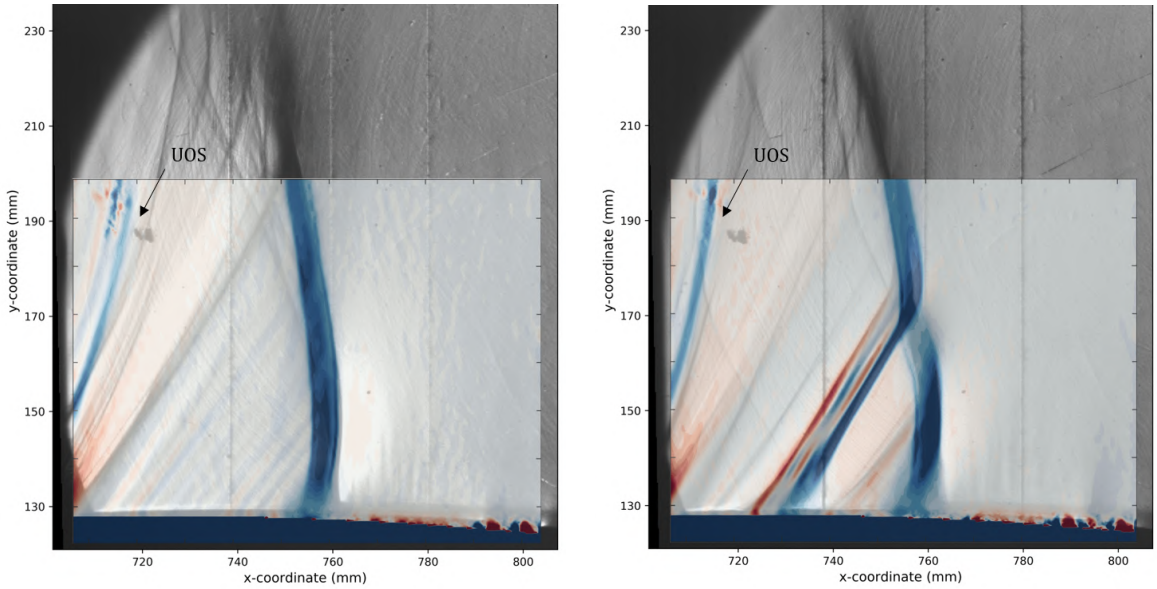

(a) Smooth plate (PIV at Plane 1)

(b) D20d10 3D dimple (PIV at Plane 1)

Figure 8.3: Schlieren image of two flow cases superimposed with the contour of the U-component streamwise gradient.

The superimposed images also attest for the good repeatability of conditions achieved for each flow case. It shows that the shock was placed at the same position during independent measurements, which were conducted in distinct acquisition campaigns. However, this was only achieved by performing Schlieren visualisation either during or just before deploying each measurement technique. Shock location was very sensitive to deflections in the choke mechanism, whose assembly also had some slack. Every time a new plate was mounted on the test section, a slightly different input voltage would place the shock in the desired position. Therefore, to ensure consistentcy in the measurements, a preliminary run had to be executed with Schlieren to determine the correct voltage input.

Albeit the disagreements of the pressure distribution and the challenges of reproducing the same shock locations, the newly designed test section can still be considered a good platform to reproduce transonic flows equivalent to those found over high-subsonic airfoils and to test different flow control methods in this regime.

8.1.2. Shock control by means of dimpled surfaces

The ultimate goal of this study was to investigate the physics of a transonic flow over surface dents. By analysing the resulting flow structures, it is possible to form a preliminary judgement of their potential as shock control devices. It is natural to draw parallels with more matured methods, and in this case, due to geometric similarities, dimples will be evaluated following the main features and performance criteria adopted in the transonic bumps literature, outlined in Chapter 2. Finally, a brief comparison between the results for dimples from the numerical and experimental approaches is provided.

2D vs 3D dimples

Initial transonic bump designs consisted of a two-dimensional surface deformation that covered the entire span of the controlled region [24]. However, it was identified that an array of bumps with finite width would also be capable of globally producing a lambda-shock structure, being as effective as their 2D counterparts while restricting detrimental effects to their vicinity [45] [60]. As a result, the focus of recent investigations shifted towards three-dimensional devices.

Nonetheless, when considering the early stage of studies on dimples in transonic flow, there is considerable value in analysing the effects of two-dimensional devices. The flow field is simplified when the spanwise velocity component is virtually eliminated, what allows for a clearer analysis of the main structures that appear on the interaction. In light of this, two 2D dimples were designed (D20d10-2D and D40d10-2D), whose indentation covered almost the entire span of the test plate.

The measurements performed over the two-dimensional devices provided an initial characterisation of the features that were expected to appear. Three main structures were identified:

- **Expansion fan at dimple leading edge.** Supersonic flow enters the dimple and is deflected downwards, what produces an acceleration fan.
- **Compression inside the dimple.** In the dent interior, streamlines experience an upwards (positive) deflection, what compresses the flow. The pressure rise occurred smoothly in the form of compression waves over the D40d10-2D dimple, due to its gentle slope. Conversely, the D20d10-2D promoted a more abrupt change of direction, causing the formation of an oblique wave and a steeper pressure rise.
- **Re-expansion at dimple trailing edge.** As flow exits the dimple, it is again deflected negatively to become parallel to the wall surface, and therefore undergoes another acceleration.

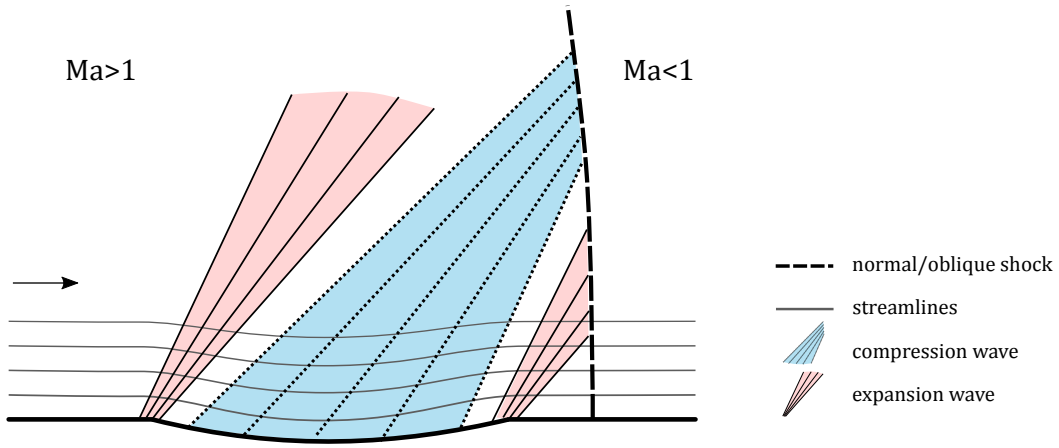

Figure 8.4: Main flow structures identified over the elongated 2D dimple in transonic flows.

These structures largely agree with the prognosis of a transonic flow over a surface dent, presented at the end of Chapter 2. It was noted that the location of the shock could influence these structures to different extents, depending on their proximity with each other. For example, the re-expansion over the D40d10-2D trailing edge is weaker when the shock is at the centered location, and is fully eliminated when it is displaced further upstream.

Observations made from 2D plates results supported the analysis of the more complex flow field over the three-dimensional variants. The D20d10 and D40d10 3D dimples were designed using the streamwise cross-section of their 2D versions, in order to assess the effect of device dimensionality in the shock interaction. Figure 8.5 shows the vertical velocity distribution recorded for both the 2D and 3D dimple variants, evidencing the similarities and divergences between them.

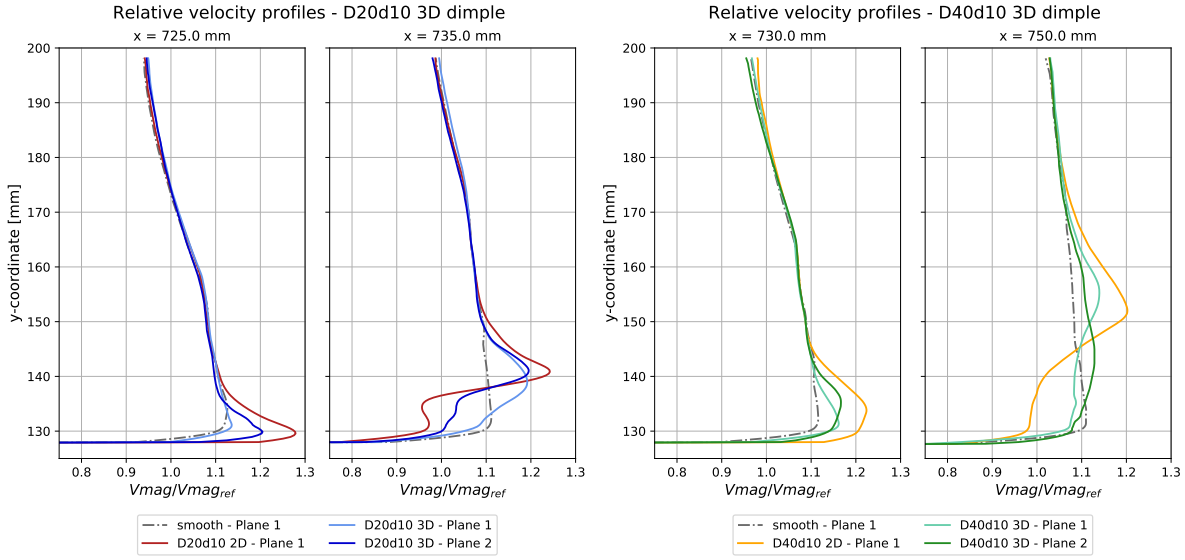

(a) D20d10 2D and 3D plates

(b) D40d10 2D and 3D plates

Figure 8.5: Comparison by means of velocity profiles of the effects caused by flow dimensionality over the dimpled plates.

It could be noted throughout the measurements that the main flow structures identified for the two-dimensional devices were still present over the 3D dimples centreline, but with noticeable modifications. For example, the leading edge expansion fan was significantly stronger over the D20d10-2D plate, as opposed to its 3D version (Figure 8.5a). Since the speed upstream of the oblique wave was reduced, a smaller deceleration should be expected, what is confirmed in the profile at x=735mm, around y=135mm, by a less pronounced velocity deficit. Divergences are even larger for the D40d10-3D. The profile raised between dents (Plane 1) displays only a faint similarity with the D40d10-2D curve, while that acquired at x=750mm over Plane 2 seems to have almost no correlation with the 2D version, despite both measurements having been performed directly above the same indentation cross-section. In general, effects of expansion and compression regions were considerably less pronounced over the three-dimensional dimpled plates.

Furthermore, a novel structure was identified downstream of the D20d10-3D plate. Surface pressure distributions indicated that, after re-expansion took place at the spherical dimple trailing edge, flow was re-compressed before the normal shock leg. The same phenomenon did not occur over its 2D counterpart, for which pressure after the dent followed the same trend as the smooth case. This secondary compression occurred in the form of an oblique wave, as could be noted from the pressure gradient contours, and only took place around the dimple centreline, not being perceived in measurements over the symmetry plane. It was present not only for the centered shock position, for which PIV measurements were done, but also for the downstream one, and can be observed in Figure 8.7 in the pressure tap located at x=750mm.

These deviations can only be linked with the spanwise velocity component that is introduced when flow becomes fully three-dimensional. They seem to affect the entire flow field, and modify regions where the flow cross-section is still locally considered 2D, such as over the plate symmetry and the dimple centreline, where pressure and PIV measurements were effectively performed. These divergences caused by three-dimensional effects can be summarised by a key flow feature already identified over shallow dimples: the converging-diffusing topology.

At supersonic speeds, particles suffer compressions and expansions as they are turned positively or negatively, and the intensity of these processes relates to the absolute deflection suffered. When flow passes over a three-dimensional dimple, it experiences not only vertical but also lateral deflections. As it enters, streamlines converge towards the dimple centreline, diverge when exiting and finally realign themselves with the main flow direction downstream of the dent. These lateral movements take place simultaneously with the vertical deflections used so far to explain the physics of this flow. They were also visualised with oil flow over dimpled plates tested in the preliminary campaign (Appendix B). Similar measurements were regrettably not performed for the final test plates. A representation of the flow mechanics over dimples in the vertical and horizontal planes can be seen in Figure 8.6.

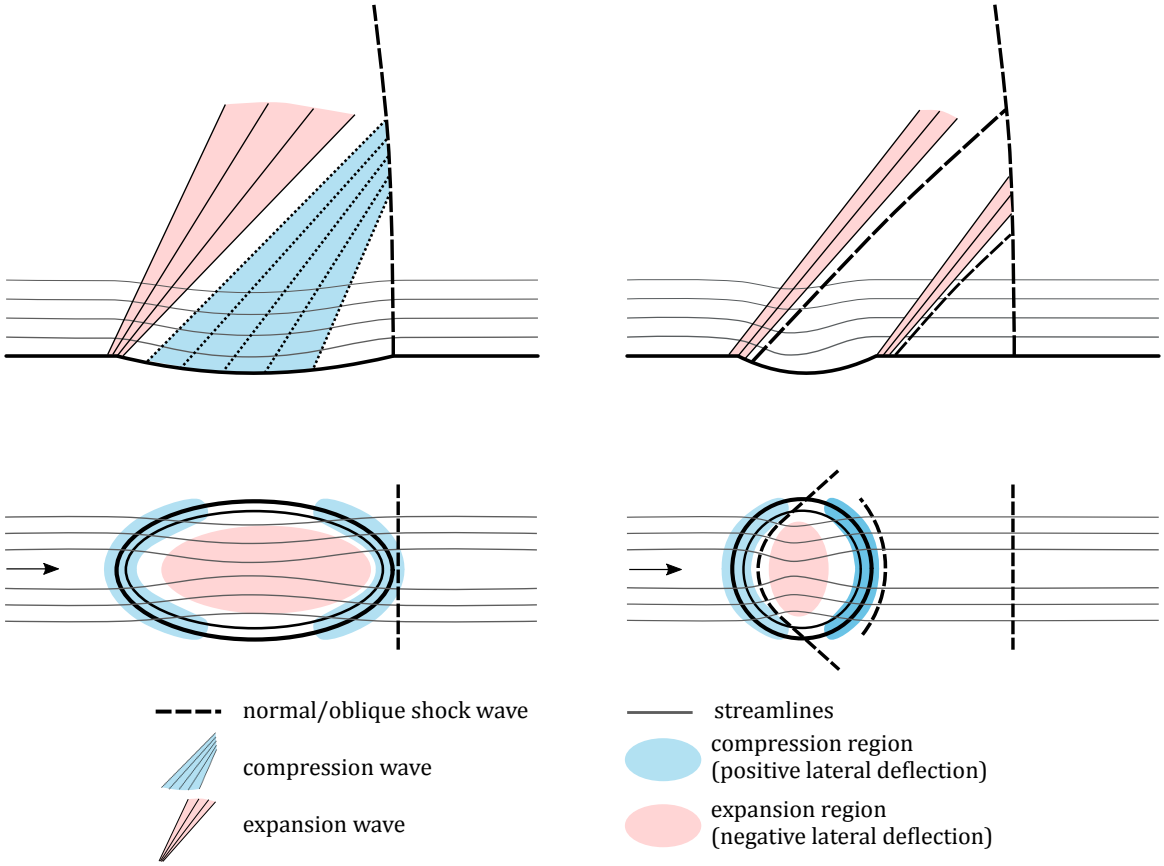

Figure 8.6: Schematics of the flow mechanics for the D40d10 (left) and D20d10 (right) 3D dimples over the vertical and horizontal planes. For the D40d10 3D, shock is placed at the optimum location.

With this insight it is now possible to understand the divergences observed between the 2D and 3D plates. When considering both streamline deflections that occur over the 3D dimple leading edge, there is a negative vertical turning similarly as that for the 2D case, but also a positive one towards the device centreline over the horizontal plane. This secondary deflection counters the effects of the main one, thus explaining the weakened expansion region identified in all 3D plates.

The opposite movement occurs close to the trailing edge. In this region, streamlines are being negatively deflected both over the vertical plane, as they are re-aligned with the wall surface, and horizontally as they diverge from the centreline. This explains the stark flow re-expansion noticed for the D40d10-3D at the downstream shock location (Figure 8.7). This combined effect results in a pressure rise $\Delta p/p_0$ of 0.1, as opposed to 0.08 experienced over its two-dimensional version.

The diverging pattern also justifies the less pronounced compression obtained inside the D40d10-3D. This design aimed at slowly increasing the pressure in its interior by promoting a gradual vertical deflection of the streamlines. In the 2D variant, after the leading edge expansion, pressure went considerably above the smooth plate level towards the second portion of the indentation. For the 3D plate, it is likely that in this region streamlines are also diverging horizontally, what prevents a more effective compression. As a result, while flow inside the 2D dimple was compressed up to p/p_0=0.45, for the 3D variant only a value of 0.4 was reached before trailing edge re-expansion (Figure 8.7).

Finally, the converging-diffusing pattern can explain the appearance of the secondary oblique shock downstream of the spherical dimple. After flow laterally diverges when exiting the dimple, it has to re-align itself with the main flow direction. Since flow is still supersonic, this re-alignment occurs by means of an oblique wave. Streamlines divergence is presumably more pronounced for this dimple design as a result of its small curvature radius, what consequently leads to a stronger lateral re-alignment.

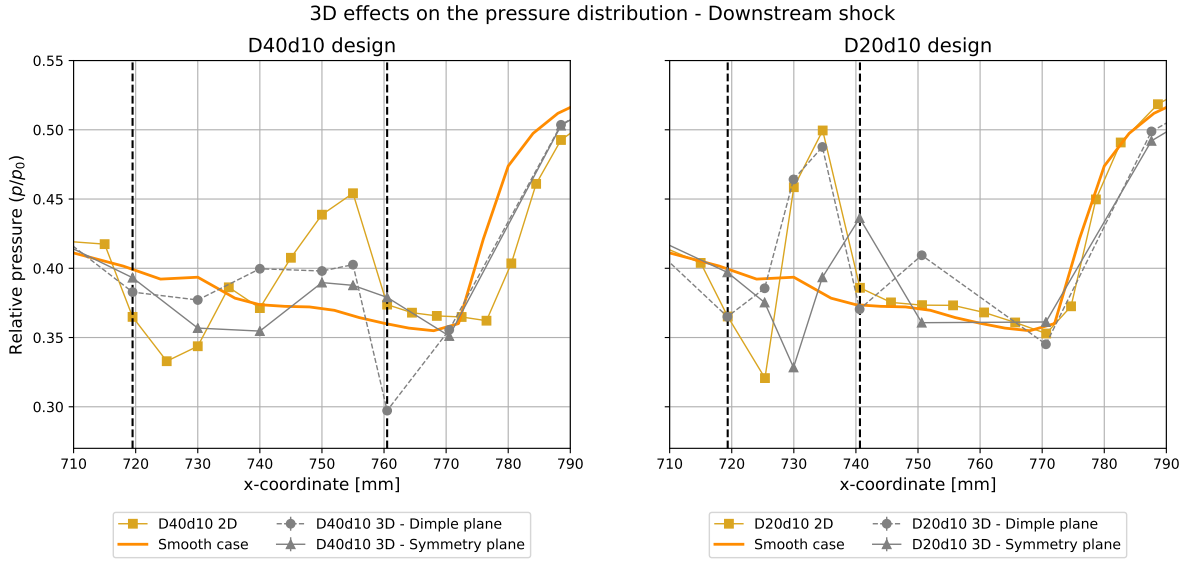

Figure 8.7: Divergences in the pressure distribution over 2D and 3D dimples for the downstream shock, evidencing the effects of the spanwise velocity component.

Spanwise relaxation of the interaction

As mentioned, the key aspect of three-dimensional shock control techniques is that they are capable of globally influencing the interaction by promoting local perturbations. Features such as expansion fans and oblique shocks formed over the devices are propagated in the spanwise direction, thus influencing a larger portion of the flow. With increasing lateral distance from the surface deformation, the shock structure relaxes towards an uncontrolled interaction. This, however, occurs rather slowly, and by setting an array of closely-positioned devices, the modified shock structures overlap, being possible to achieve a global control of the phenomenon [19].

In the present work, dimples were placed with a spacing of 33mm between them. The spacing was scaled based on the displacement thickness upstream of the shock, computed in the simulations as $\delta_1 = 0.47$ mm, what yielded a separation of $s_D = 70\,\delta_1$. Given that pressure and PIV measurements were performed both over the dimple centreline and at the symmetry plane, located halfway between two dents, it was possible to capture well the spanwise propagation of the shock.

It was noted that most structures formed over the indentation centreline were convected laterally, being found 10mm downstream over the symmetry plane. There was no clear indication that downstream propagation reduced the intensity of expansion fans and oblique shocks towards the symmetry. In fact, the disturbances appear to be equally strong away from the dimple, as is the case of the leading edge expansion depicted for the spherical dimple in Figure 8.5a. For the D40d10-3D, the velocity distribution recorded over Plane 1 at x=750mm displayed a closer agreement with the 2D variant than that over Plane 2, which lies directly over the dent itself (Figure 8.5b).

These observations can be explained by two factors. The first is that it seems like the dimples are too close to each other, hence the flow structures reach the point halfway between the two dents still with considerable intensity. The second is that the converging-diffusing topology is no longer present in this region, what eliminates the counteracting effect it produces in some structures. For example, it was argued that the leading edge expansion strength is reduced over the dimple because streamlines are also being positively deflected as they converge towards the centre of the device. Over the plate symmetry, this horizontal deflection no longer occurs, but the vertical turning is still propagated. Even if the latter loses strength further away from the dent, it is not being subdued by secondary effects. Instead, it can also be argued that the flow topology has an opposite effect close to the symmetry. When streamlines converge around the leading edge, they consequently diverge between the devices, what adds to the acceleration effect in this region propagated from the vertical negative turning at the dimple. Figure 8.8 shows the interpolated pressure distribution over the D20d10-3D plate, exemplifying how the structures formed over the 3D dimple centreline (at z=16.5mm) are laterally propagated in the flowfield. This plot is equivalent to that raised for streamwise slots by Smith [10] (Figure 2.5b).

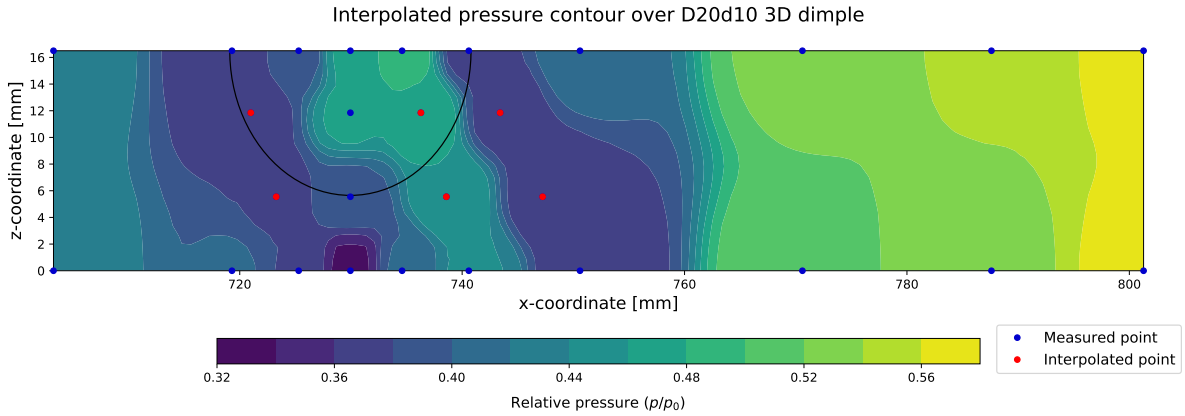

Figure 8.8: Interpolated contour of pressure distribution over the surface of the D20d10-3D dimple. Flow from left to right.

By comparing the distribution of the angle formed between the velocity vectors and the x-axis, it is confirmed that streamline vertical deflection reaches the symmetry plane with less intensity (Figure 8.9). Turning also seems to be more uniformly distributed and smeared out, whereas above the dent flow direction is sharply reversed over small regions. When taking the momentum flow ratio results into account, it was noted that flow at the symmetry consistently retained more momentum than over the dents. This trend was observed for every 3D plate, but especially for the D20d10-3D, whose performance was superior than the smooth reference case. A plausible explanation is that the smeared flow turning minimises losses across the oblique shock, thus yielding a higher efficiency over this location.

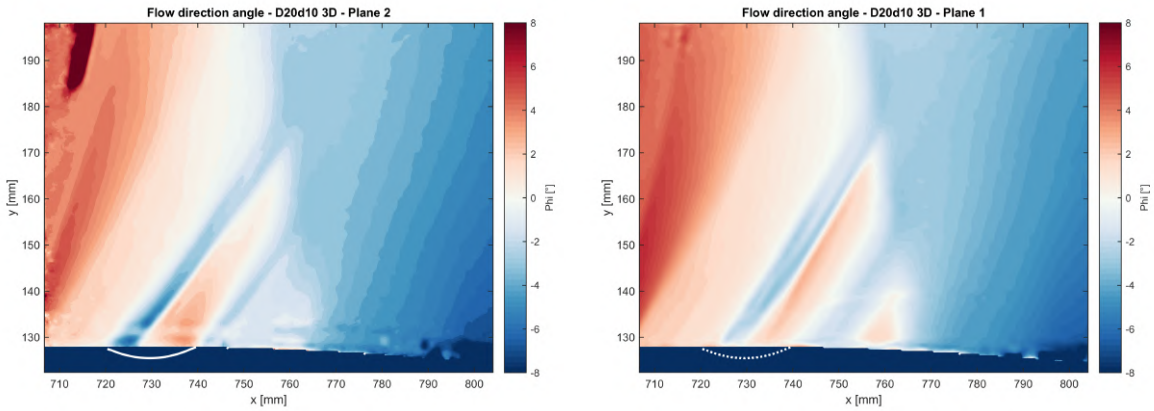

(a) Measurement over dimple centreline.

(b) Measurement halfway between two dimples.

Figure 8.9: Spanwise propagation of flow deflection for the D20d10 3D dimple.

Shock displacement

An important assessment to be made when analysing passive shock control devices is to evaluate the effects of shock displacement in their performance. The first studies of transonic bumps already indicated that shock movement could lead to the formation of undesired secondary shock systems that would offset the improvement in total pressure recovery [66]. This performance criteria was evaluated in the current study by placing the shock at three pre-designated locations for every test plate. The flow field that resulted from each shock position was measured using Schlieren and surface pressure readings.

In general, the upstream shock location prevented the surface indentations from producing any positive effects in the shock structure. It interrupted the upwards flow deflection and consequently the development of oblique shocks or compression waves, thus reducing the intensity of the first compression step. As a consequence, Schlieren images for different test plates look rather similar, with the premature structures formed in the interior of the dimples merging with the normal shock leg. On the other hand, the detrimental expansion fan that occurs when flow enters the dimple remained unaffected. Hence, flow is still accelerated when it reaches the shock, what most likely leads to higher losses.

When considering the other two locations, the test plate most influenced by shock movement was the D40d10-2D. For the shock positioned over the dimple trailing edge, the resulting structure proved to be highly sensitive to minor displacements. While the main part of the leg was at the centered location, the portion close to the wall would curve downstream and suffer a small re-expansion, as streamlines there would already exit the dent (Figure 8.10a). This undesired curvature could only be removed when the entire shock was displaced further upstream (Figure 8.10b). As the pressure measurements confirm, this slight movement leads to large changes in the flow conditions near the wall, for it preserves the flow compression upstream of the shock (Figure 8.11). In the aft shock position, a large expansion region appeared after the dimple trailing edge.

A similar instability could not be observed over the 3D variant of this plate (Figure 8.10c). Given that it does not directly control the entire span of the interaction, the shock structure is less sensitive to the dimple presence and overrides the potential local re-expansion at the trailing edge. This is confirmed by the absence of a leg curvature near the wall and pressure distribution drop at the end of the dent.

Conversely, D20d10 2D and 3D dimpled plates proved to be the least affected by the shock being displaced downstream of the centered position. As the shock moved to the aft location, its structure grew and the leading oblique wave impinged on the main leg at a higher point. This ultimately increased the flow region that was influenced by the dimple: in the centered location, the oblique wave hits the main leg at 48% of its total height, while further downstream this ratio increases to 58%. The resulting structure would only enlarged when displaced, and no new features appeared in the process.

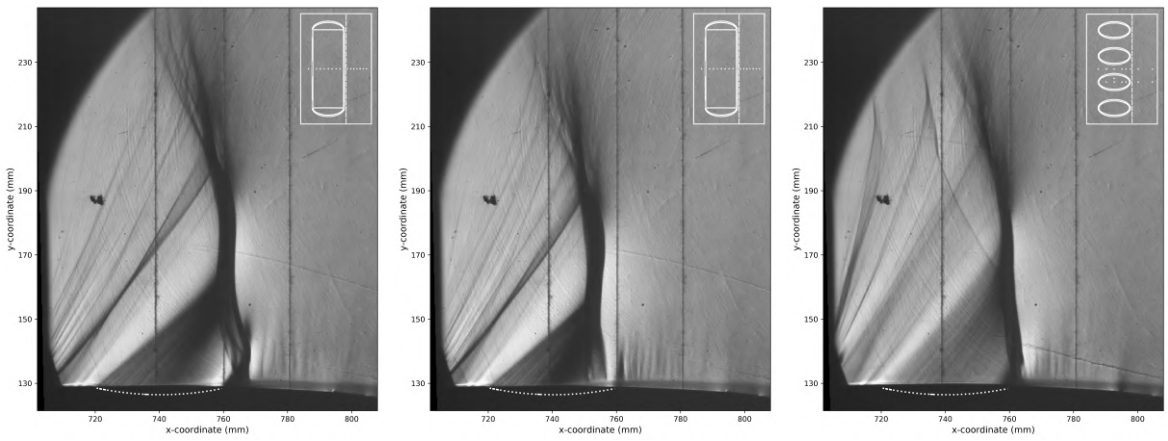

(a) Downstream displacement (b) Upstream displacement (c) Test plate 3D variant

Figure 8.10: Effects in the shock struchture of small displacements around the trailing edge of the D40d10 2D plate.

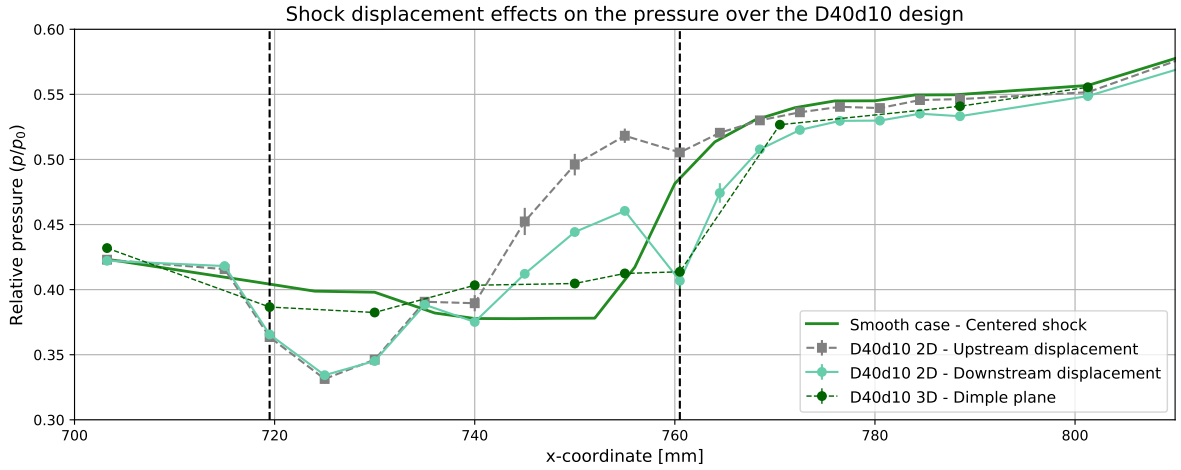

Figure 8.11: Resulting pressure distribution for small shock displacements

Shape asymmetry

Shape optimisation studies of shock control bumps indicated that different geometry parametrisation approaches have little effect on the performance of the flow control technique [11]. They do, however, suggest that shape asymmetry plays a major role. Wedge-shaped bumps would produce a leading oblique shock, as opposed to the compression waves found over smoothly contoured surface deformations. Both designs perform equally well at on-design conditions, but the former is less compromised by the shock moving to off-design positions.

With this in mind, an asymmetric shock control dimple was tested in the current study. Its design was defined by displacing the bottom of the elongated D40d10-3D dimple forward. The resulting geometry had a smaller curvature radius in the front portion, equal to that from the D20d10-3D, while in the rear the radius was larger than that for the D40d10 design. The idea behind this was to combine the production of an oblique shock with a reduced flow turning at the trailing edge.

From the momentum flow ratio computed with the shock at the on-design location (centered), the elongated and asymmetric dimples had almost the same performance, both lying below the reference case level. In order to assess the effects of off-design conditions, the results recorded for the downstream shock location shall be analysed. Figure 8.12 provides a direct comparison between the 3D dimples in this scenario using Schlieren and pressure measurements.

The flow over the asymmetric dimple is indeed a combination of those produced by the other two designs. The oblique shock is somewhat weaker than that from the spherical dimple (as seen in the pressure distribution), what is expected given that flow experiences a smaller upwards deflection at the bottom of the indentation. However, the compression achieved is not entirely preserved in the dimple interior, with the measurement at x=740mm indicating a pressure decrease after the oblique wave, likely caused by the laterally diverging flow pattern.

When flow exits the dent, a strong re-expansion was recorded. This results from the combination of negative vertical and horizontal deflections, as streamlines simultaneously re-align with the plate surface and diverge from the dimple centreline, similarly as for the D40d10-3D. However, a weaker re-expansion occurs for the asymmetric design, as a consequence of the smaller vertical turning at its trailing edge, produced by the larger rear curvature radius. This is confirmed by a less bright region in the Schlieren image and a more modest drop in the pressure distribution at x=760mm. Hence, it can also be concluded for dimples that, albeit performing similarly at on-design condition, an asymmetric shape would be capable of minimising the negative effects that appear at off-design conditions.

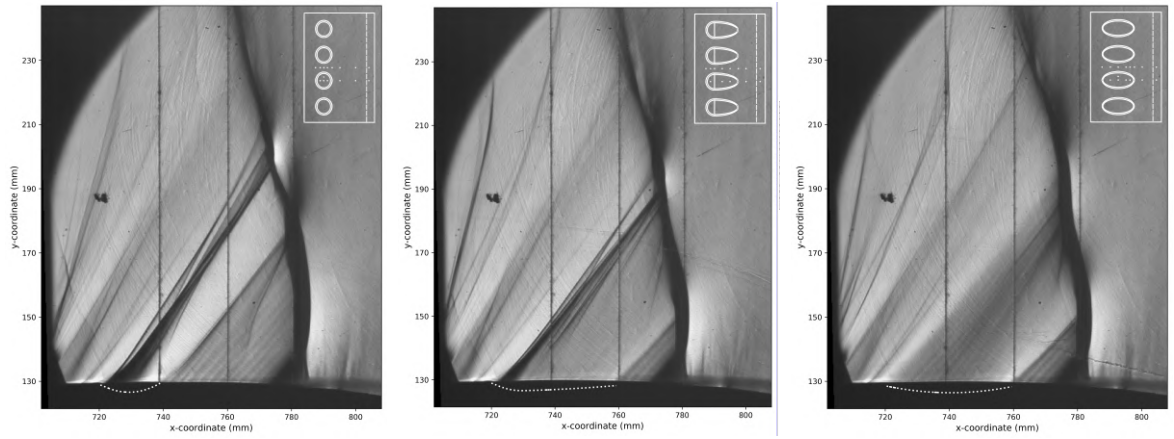

(a) D20d10-3D (b) R10D40d10-3D (c) D40d10-3D

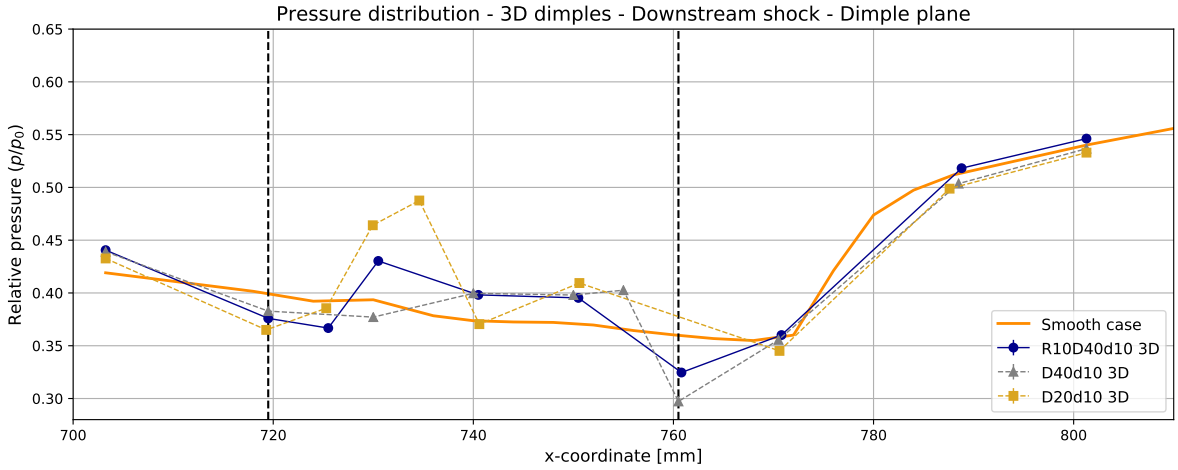

(d) Pressure distribution

Figure 8.12: Effects of shape asymmetry in the shock structure and pressure distribution.

Wave drag reduction strategies

During the test plate design phase, two approaches were proposed for shock control dimples to successfully reduce wave drag. Each individually tackled the two main shortcomings of transonic bumps. The first issue identified was that only the ascending part of the bump was beneficial for the interaction. This results in either very long geometries or shorter and highly asymmetric ones which suffer from flow separation after the crest [66]. The second problem was the sensitivity of the device's performance to shock location. A shock displacement downstream of the bump's crest would trigger secondary lambda shock systems which would rapidly offset any benefits achieved by the leading oblique wave.

The D40d10 configuration was designed to address the first issue. The elongated dimple, dubbed as the inverse bump, aimed at slowly turning the flow upwards over its entire length, thus increasing the pressure upstream of the shock by means of compression waves. Measurements conducted over this design's 2D version indicated that flow was indeed gradually compressed, and streamlines close to the wall did not experience the steep velocity gradient characteristic of normal shocks. However, the expansion fan generated at its leading edge stretched vertically as it propagated downstream, resulting in a large portion of the profile with surplus velocity, which in turn experienced larger losses across the shock. This feature overruled the benefits achieved near the wall, what led to this design retaining the least amount of momentum across the interaction.

Its three-dimensional variant was capable of reducing the expansion fan intensity, on account of the counteracting effect induced by the converging streamlines at its leading edge. But the spanwise velocity component also brought a drawback: streamlines would diverge (hence expand) in the dimple interior, instead of experiencing a more pronounced upwards turning. This can be clearly seen in Figure 8.13, which compares the flow angle distribution over the centreline of the 3D device and its two-dimensional counterpart. While in the 2D case there is a clear downwards deflection followed by a considerable reverse upwards, the 3D dimple only promotes slight deviations in the streamlines path. As a consequence, the D40d10-3D failed at compressing the flow in its interior, a feature evidenced in the pressure distribution plots. On top of the limitations found at on-design conditions, a downstream shock displacement would trigger flow re-expansion at the trailing edge, what caused further performance deterioration. In light of this, it can be stated that the inverse bump approach is not suitable for wave drag reduction purposes.

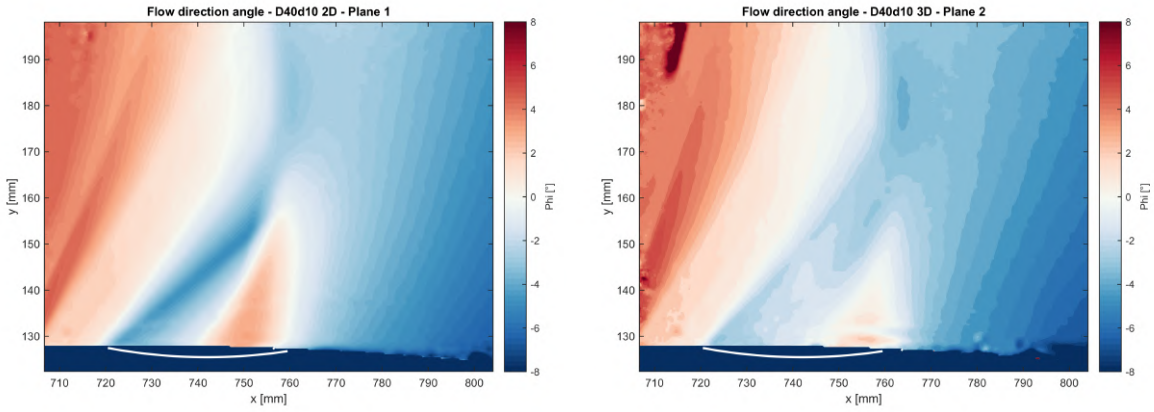

(a) D40d10 2D Plane 1

(b) D40d10 3D Plane 2

Figure 8.13: Comparison between the flow direction distribution for the 2D and 3D variants of the D40d10 design. Angle computed relative to the horizontal line.

Going forward, the D20d10 configuration tackled the second bump deficiency. Its geometry was very similar to that tested previously for viscous drag reduction applications in low-Re flows [92]. It was intended to be positioned fully upstream of the shock and act as an oblique shock generator, thus promoting an initial flow compression. It had therefore no specific on-design shock location, as it was expected that flow re-expansion would occur at its trailing edge in every situation. Results for this design's 2D variant show that its small curvature radius caused sharp internal deflections that produced a velocity peak close to the wall, followed by a stark deceleration characteristic of an oblique shock. Despite producing close to the leading edge speeds higher than the D40d10, this velocity peak would slowly diffuse as it propagated downstream. Additionally, the expansion fan was prevented from spreading over a larger chunk of the vertical profile, thus remaining narrow. These two effects are attributed to the close proximity of the oblique shock, and result in a less detrimental leading edge expansion for this dimple design. Figures 8.14a and 8.14b shows the streamwise velocity gradient distribution for the D40d10 and D20d10 2D designs, allowing for a direct comparison of how the leading edge expansion fan propagates in both cases, with the former exhibiting a more pronounced growth as it travels away from the wall.

The three-dimensional version of this configuration also benefited from the suppressing effect the converging streamlines have on the leading edge expansion. Nevertheless, its compression seemed to be less compromised by the diverging movement. This discussion is supported by Figure 8.14c, which shows the oil flow visualisation perfomed over the test plates used in the preliminary campaign (described in Appendix B), focusing on the first row centre dimple. It is assumed that the second row did not largely affect the first one, considering flow was still supersonic. The oblique shock emanates from the front portion of the dent (indicated by the red dashed line), and streamlines immediately diverge. Then, they follow a linear trajectory until being again turned at the trailing edge. The sudden streamlines diverging motion occurs at the oblique wave's foot, what might explain how flow compression was preserved. Conversely, since pressure rise occurs gradually over the D40d10-3D dimple, streamlines continuously ramify, what offsets the benefits by expanding the flow.

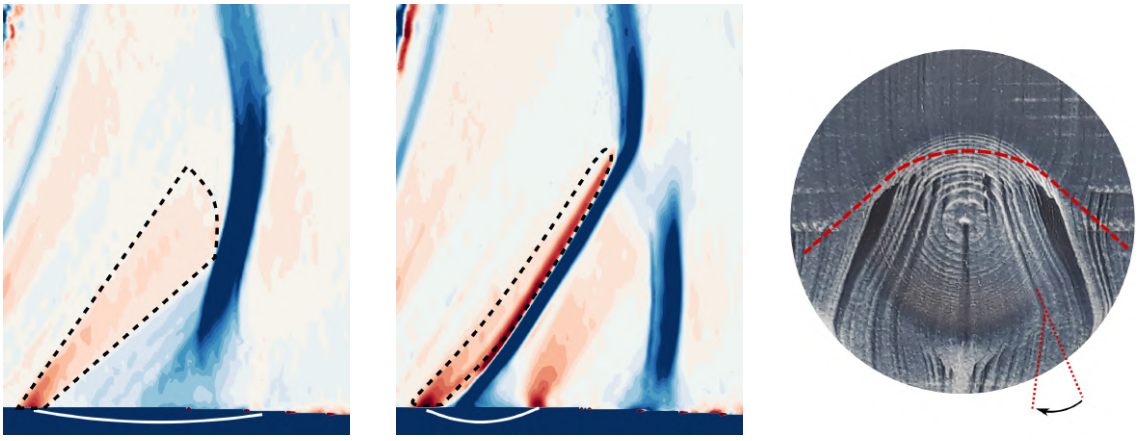

(a) D40d10 2D expansion fan (b) D20d10 2D expansion fan (c) Streaklines over D20d10 3D

Figure 8.14: Comparison between the leading edge expansion fan propagation for the D40d10 and D20d10 designs, alongside the oilflow visualisation of streaklines over the spherical dent.

Downstream of the dent, the spanwise component is again instrumental, for it induces a secondary oblique wave as streamlines are re-aligned with the main flow direction after diverging from its centre-line. This motion is shown in Figure 8.14c by the inwards turning arrow. In summary, the converging-diffusing topology acts twice in subduing the negative influence of the expansion regions intrinsic to this design, and plays a major role in its overall performance, which displayed in both measurement planes a momentum retention across the interaction larger than the smooth case.

It is reasonable to imagine that the dimple effectiveness should not deteriorate much if the shock moves away from the centered position. In fact, as Schlieren images indicate, a downstream shock displacement would increase the portion of the shock structure influenced by the device, what could enhance the improvements achieved. In conclusion, there is substantial indication that the leading oblique shock configuration has a potential of reducing wave drag. Its efficacy should thus be further investigated using measurement techniques with smaller error margins, such as total pressure probes, what would allow for a definite evaluation of its effectiveness. With respect to the other components of drag, it is expected that viscous drag should remain unaltered, similarly as observed for transonic bumps [49]. Conversely, a pressure drag rise presumably occurs, since low pressure is acting in the front of the indentation interior, while higher values are found towards its rear portion.

Finally, the asymmetric dimple aimed at producing achieving a steeper pressure rise by means of an oblique shock, while controlling the re-expansion intensity at the trailing edge. Although its oblique shock was weaker than for the spherical dimple due to a smaller deflection in its interior, it produced a more pronounced compression when compared to the inverse bump configuration (Figure 8.12d). However, the diverging streamlines pattern subsequently caused the pressure at x=740mm to drop to the same level as the D40d10-3D design. As a result of this adverse effect, the R10D40d10-3D design retained less momentum across the shock than the smooth reference case.

Comparison between experiments and simulation

In order to support the definition of the test plate designs, CFD simulations were performed for different dimple geometries. Computations were kept two-dimensional to reduce the numerical effort and degrees of freedom analysed. They focused on the inverse bump approach, allowing a preliminary analysis of the flow structures over the indentations and their overall performance. The main outcome of this workstream was the D40d10 design, used in two test plates (D40d10 2D and 3D). Given that this geometry was also assessed in the wind tunnel, one can compare the results from both methodologies.

Pressure measured for the D40d10 2D and 3D plates is compared with the simulation of the same geometry in Figure 8.15. Similarly as for the smooth case, speeds reached in the experiment are lower than those simulated, what is confirmed by the higher levels of the measured pressure before x=720mm. For the 2D plate, it can be noted that pressure rise inside the dent does not display the same gradual behaviour as seen in the simulation, and instead follows briefly the trend of the smooth case curve in the center of the dimple (x=740mm).

Moreover, the CFD analysis pointed out that none of the simulated geometries were capable of producing a total pressure recovery higher than the uncontrolled interaction. This was confirmed by the D40d10-2D momentum flow ratio lying below the smooth plate value. Notwithstanding, this design performance was improved in its three-dimensional variant, whose momentum ratio was closer to the smooth plate value, despite still remaining underneath it. It can be concluded that results from a 2D dimple numerical analysis cannot be directly generalised to a 3D geometry, for the additional spanwise velocity component has notably a stark influence in the resulting flowfield. A further evidence is the large disagreement between the pressure distribution measured over the three-dimensional dent and that obtained in the simulation for the 2D device. This signifies the need of an independent simulation for 3D devices if their global performance is to be evaluated numerically.

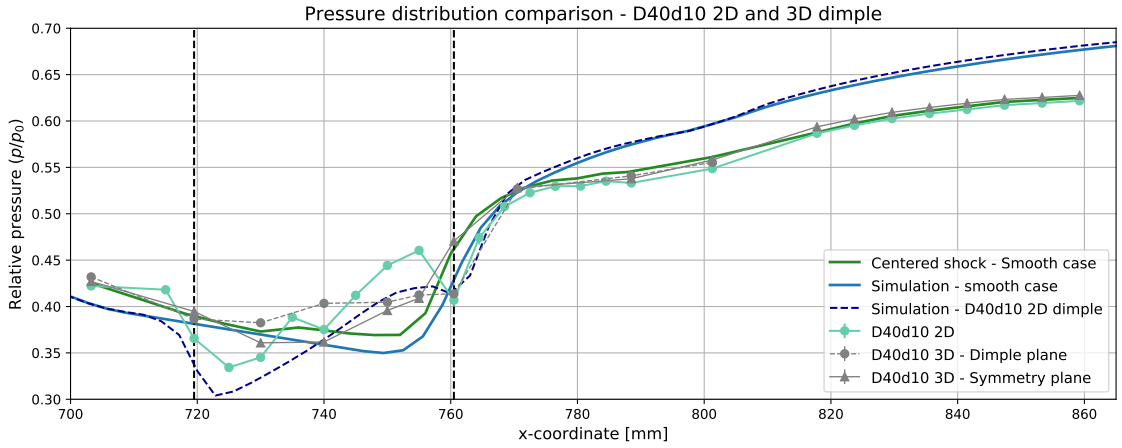

Figure 8.15: Measured and computed pressure distribution for the smooth reference case and the D40d10-2D dimpled plate.

Another interesting assessment to make is a comparison between the shock structures that resulted from both approaches. Experimentally this information was captured by the Schlieren visualisation, whereas from the simulations the streamwise density gradient can be calculated, providing an equivalent output. These are presented in Figure 8.16. It is evident how well the D40d10-2D Schlieren image agrees with the numerical density gradient contour. On the other hand, the shock structure for the 3D plate is considerably different, thus strengthening the argument that, in this flow case, 2D simulation results cannot be extrapolated for a higher dimension. A final conclusion of this comparison is that CFD computations are capable of providing good prediction of the flowfield features, and should be deployed in future analysis of dimples at transonic speeds, provided that the physics simulated represent well the relevant flow phenomena.

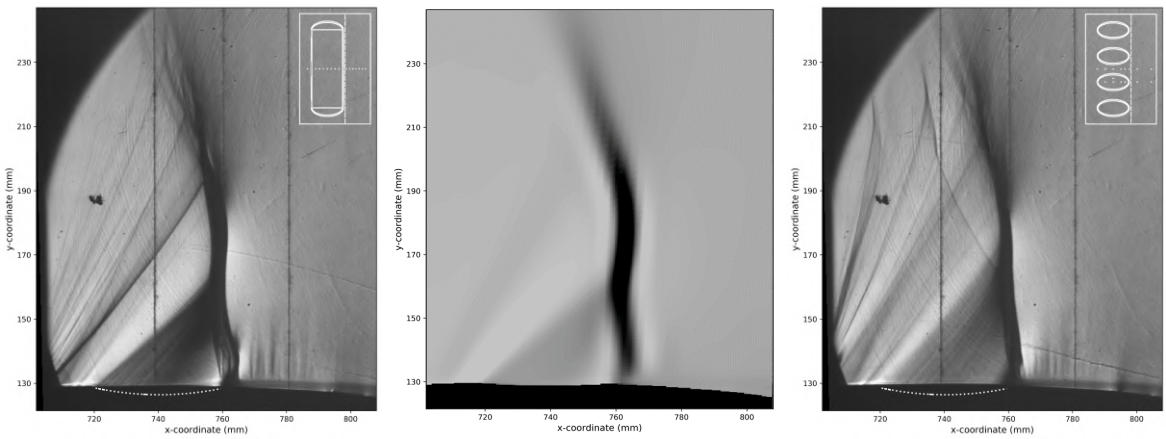

(a) D40d10-2D experiment (b) D40d10 simulation Mesh 2 (c) D40d10-3D experiment

Figure 8.16: Comparison between Schlieren images and density gradient distribution acquired experimentally and numerically for the D40d10 design.

8.2. Conclusions

Three research questions were posed based on the objectives of this work. Now they can finally be answered, based on the results obtained in the numerical and experimental analysis and the discussions included in this chapter.

1. **Can the transonic flow conditions found over wings be experimentally reproduced over an asymmetric nozzle while avoiding flow separation?** The newly designed asymmetric nozzle lower wall was able to produce over its surface a supersonic pocket terminated by a normal shock, while avoiding flow reversal in the subsonic APG region. However, the maximum Mach number reached was limited by imperfections in the components assembly, which gave rise to oblique shocks upstream of the test section. Also, the adverse gradient diverged from that of a transonic airfoil towards the end of the flat section, a consequence of the reduced curvature adopted to avoid separation. Nevertheless, the setup delivered stable and repeatable conditions and can be regarded as a flexible platform to conduct future experiments at transonic speeds.

2. **How is a transonic flowfield modified by a dimpled surface?** The characteristic structures that appear in a transonic flow over dimples can be divided in two categories. The main structures are found over the vertical plane and result from the streamlines' ascending and descending movement. These are an expansion fan over the dimple leading edge, followed by a compression in its interior (in the form of either isentropic waves or oblique shock), and a re-expansion as flow re-aligns with the wall surface after exiting the dent. The secondary structures are associated to the spanwise velocity component that appears for 3D geometries. Over the horizontal plane, streamlines assume a converging-diverging pattern, which ultimately affects the intensity of the main structures. Converging streamlines at the dimple leading edge reduce flow acceleration, whereas diverging ones limit the compression achieved inside the dimple and enhance trailing edge re-expansion. This topology was also responsible for inducing a secondary oblique shock downstream of the D20d10-3D dimple, as streamlines re-aligned with the main flow direction.

3. **Which shape and dimensions should a surface indentation assume in order to effectively control the shock wave?** The effectiveness of a shock control dimple hinges on a fine balance between antagonistic mechanisms that arise in the flowfield. Two-dimensional geometries do not seem to yield a positive net, and the control over the entire interaction span results in a more unstable and sensitive shock structure. The D20d10 design, however, indicates that compression through an oblique shock is more advantageous than by isentropic waves, given that it limits the negative effects of the leading expansion fan. A positive outcome was only reached when the three-dimensional devices introduced a spanwise component to the velocity field. The converging-diverging topology produced a suppressing effect on the leading edge expansion, but also proved to be detrimental to the performance of elongated geometries. In the end, spherical dimples emerged from this experimental analysis as the control device with the highest potential of reducing wave drag. They were capable of compressing flow upstream of the main shock leg by means of an oblique wave, and prevented the achieved benefits from being neutralised by detrimental structures (ie. expansion fans and diverging streamlines).

The main outcome of this thesis was the preliminary indication that spherical dimples can work as a wave drag reduction method. It represents a break of paradigm in the way shock control devices have so far been designed. Both transonic bumps and perforated plates rely on the normal shock being positioned over them, so that streamlines can be deflected upwards, either directly by means of a surface deformation or indirectly by inducing a recirculating flow pattern. This requirement leaves them susceptible to shock displacement, which can easily offset their performance. The leading oblique shock generator configuration proposes a different approach. Spherical dimples are positioned upstream of the shock, not underneath it, what ensures that a large portion of the flow crosses the oblique wave and experiences a two-step pressure rise. The detrimental expansion fans are not avoided, but spanwise excitation seem to be able to counter their negative effects. The presence of both fans is likely to restrict the maximum reduction achieved, but on the other hand renders the device less sensitive to shock movement, allowing it to effectively operate in a broader flight envelope. And it still retains the advantageous practical aspects of dented surfaces, such as low maintainability requirements, no energy expenditure, small design restrictions and easy fitting on aircraft wings [92].

8.3. Future research recommendations

Motivated by the outcome of this work, further investigation of dimples in transonic flow is deemed academically significant. It should aim at increasing our understanding of the flow physics, as well as evaluating with more accuracy the potential of these devices to control a normal shock wave. Future research recommendations involving both experimental and numerical analysis are listed below:

- **Perform measurements with a total pressure probe.** The overall performance of the devices covered in this analysis could only be assessed by means of computing a mass-averaged momentum flow ratio across the shock. This required the use of corrections using isentropic flow and normal shock relations, and yielded a result which does not directly quantify wave drag. Furthermore, alone the uncertainty from the velocity propagated in the final momentum expression already produced a too large error margin which prevented any definite conclusion to be drawn. Therefore, future experimental campaigns should include the use of a total pressure probe, in order to measure directly the recovery over the shock with a higher accuracy.
- **Reconstruct the pressure field from velocimetry data.** Pressure field reconstruction could be performed using the results from PIV measurements. However, the outcome would still suffer from considerable computation uncertainties. For more details, the reader is referred to a review on the approach authored by van Oudheusden [94].
- **Conduct particle image surface flow visualisation (PISFV) to quantify the spanwise velocity component.** This technique was previously used by van Campenhout et al. [91] to analyse the converging-diffusing flow topology over dimples. As this pattern seems to also influence the performance of shock controlling dimples, it is deemed fundamental to deploy this technique once again. By quantifying the lateral deflection magnitude, it would be possible to better understand its influence on the main structures that occur over the vertical plane. An overview of PISFV can be found in literature reviews by Dittrich and van Campenhout [25] [90].
- **Perform three-dimensional CFD simulations.** The experimental evaluation of 3D flow structures can easily increase the complexity of measurement techniques and data analysis. This is especially true for high-speed flows, which are produced in wind tunnels with reduced physical and optical access. On the other hand, CFD simulations provide a full solution of all fluid properties in the entire domain, enabling a more complete assessment of the flow physics. The experimental data acquired in the current study would then be instrumental, supporting the validation of simulations. Accurate computations could be used to test the influence of small modifications in the geometric parameters and optimise the surface indentations for future experimental campaigns.
- **Apply dimples to transonic airfoils.** From the perspective of analysing the physics of the phenomenon, there are clear advantages of performing measurements over the wall of the wind tunnel. Incoming boundary layer and resulting structures are larger, what allows measurement techniques to accurately resolve the flow field. However, even if conditions are equivalent to those found over transonic wings, it is still not possible to directly assess its influence on the efficiency of an actual lift-generating body. Only by mounting these devices on a wing model it is possible to assess their influence on the lift-to-drag ratio, which is what ultimately matters for a successful application.
- **Evaluate the efficacy of compliant dimples.** Another way of reducing the device's sensitivity to shock location is by placing a free-deforming surface over the controlled region. The sudden drop of skin-friction at the shock would deform a compliant material to a dimple-like shape, which could promote a preliminary flow compression upstream of it.

Appendix

A

Experimental setup components

This Appendix provides a more detailed description of the various parts that compose the experimental setup. Furthermore, it contains instructions on how to assemble all components and finally attach them to the ST-15 wind tunnel.

A.1. Test section lower wall

As described in Chapter 3, the test section lower wall was re-designed, with the purpose of avoiding undesired flow separation and to allow an easy mounting of different test plates. Its main dimensions follow those of previously manufactured Mach blocks used in the ST-15 wind tunnel, what ensures a proper fitting. It is attached to the test section by means of a fastening plate, to which the lower wall is bolted in several positions. A cavity was milled on the crest of the geometry, where the circular and flat section blocks are fixed by means of threaded inserts attached to its bottom. Inside, two vertical holes conduct the pressure measurement flexible tubes to the bottom of the block, which are then directed to the wind tunnel exterior. Two large lateral holes serve to position the struts of a winch, used to place the heavy setup inside the wind tunnel. On the sides of the block, a shallow groove was cut to house rubber chords which seal eventual gaps between the setup and the wind tunnel side doors. A drawing of the lower wall block is shown in Figure A.1, where the above-mentioned features are indicated. The block was manufactured using CNC machining, given that a highly precise geometry is paramount for a smooth interface with the multiple parts assembled to it.

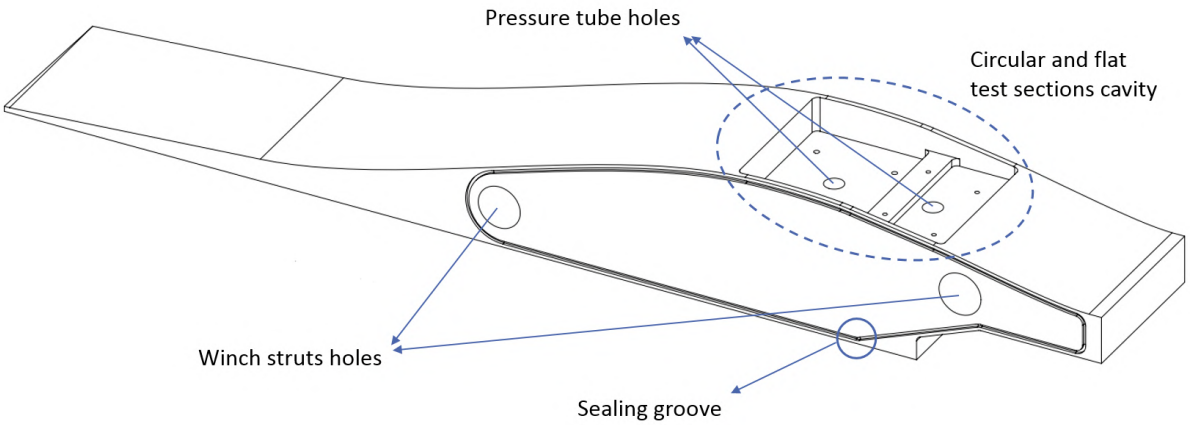

Figure A.1: Isometric view of the lower wall with its main features indicated.

A.2. Circular test section

The circular test section sub-assembly (Figure A.2) was designed to analyse the effects of different dimpled plates on the shock wave-boundary layer interaction. The components that integrate it are listed in Table A.1 alongside their respective manufacturing methods. In order to extract the necessary information from the complex flow over this section while meeting the design requirements, this sub-assembly was composed by multiple parts, and the main ones are described in more detail below:

- **Circular section block.** Structural component of the circular test section, responsible for attaching the sub-assembly to the lower wall block. It also conducts the tubes from surface pressure measurements to exit the wind tunnel.
- **Circular validation plate.** Smooth metal plate used to produce an uncontrolled reference flow. Small holes are drilled in the streamwise direction to allow surface pressure measurements. The smooth validation plate can be substituted by shock-interacting dimpled plates.
- **Front and back pressure taps.** Spanwise surface pressure measurements, used to infer spanwise effects of three-dimensional dimple geometries.
- **Cover front and back.** Covers the grooves on the front and back of the circular section block, where pressure tubes from the spanwise surface pressure measurements are organised. Aims at reducing internal flow circulation and reinforces the block structure.

ID	Part name	Manufacturing method
1	Circular section block	3D printing
2	Circular validation plate	CNC machining
3	Pressure taps front (x7)	3D printing
4	Pressure taps back (x7)	3D printing
5	Cover front	3D printing
6	Cover back	3D printing
7	M4 countersunk bolts (x4)	N/A (procured)
8	M4 socket head cap bolts (x4)	N/A (procured)

Table A.1: Table with components list of the circular test section sub-assembly.

Pressure taps

The printed pressure taps were placed in seven spanwise locations, in the front and back of the circular sub-assembly. In their upper surface they have 0.6mm holes, where the pressure information is retrieved. The hole is internally enlarged to 1.7mm, allowing the attachment of small metallic tubes, which in turn will hold the flexible pressure tubes (capillaries), conducted to the exterior of the wind tunnel. The capillaries are organised in dedicated grooves printed in the front and back of the circular section block, which have their individual covers. A drawing off the front pressure tap can be seen in Figure A.3.

Circular validation plate

The circular validation plate was machined out of aluminium and had 17 streamwise holes drilled to allow the recording of surface pressure. The holes have a diameter of 0.6mm in its upper surface and 1.7mm in the lower surface. Similarly as was done for the pressure taps, metallic tubes are partially fixed to the holes at the bottom by means of a glue collar. Capillaries were attached to the remaining length of the rigid tube.

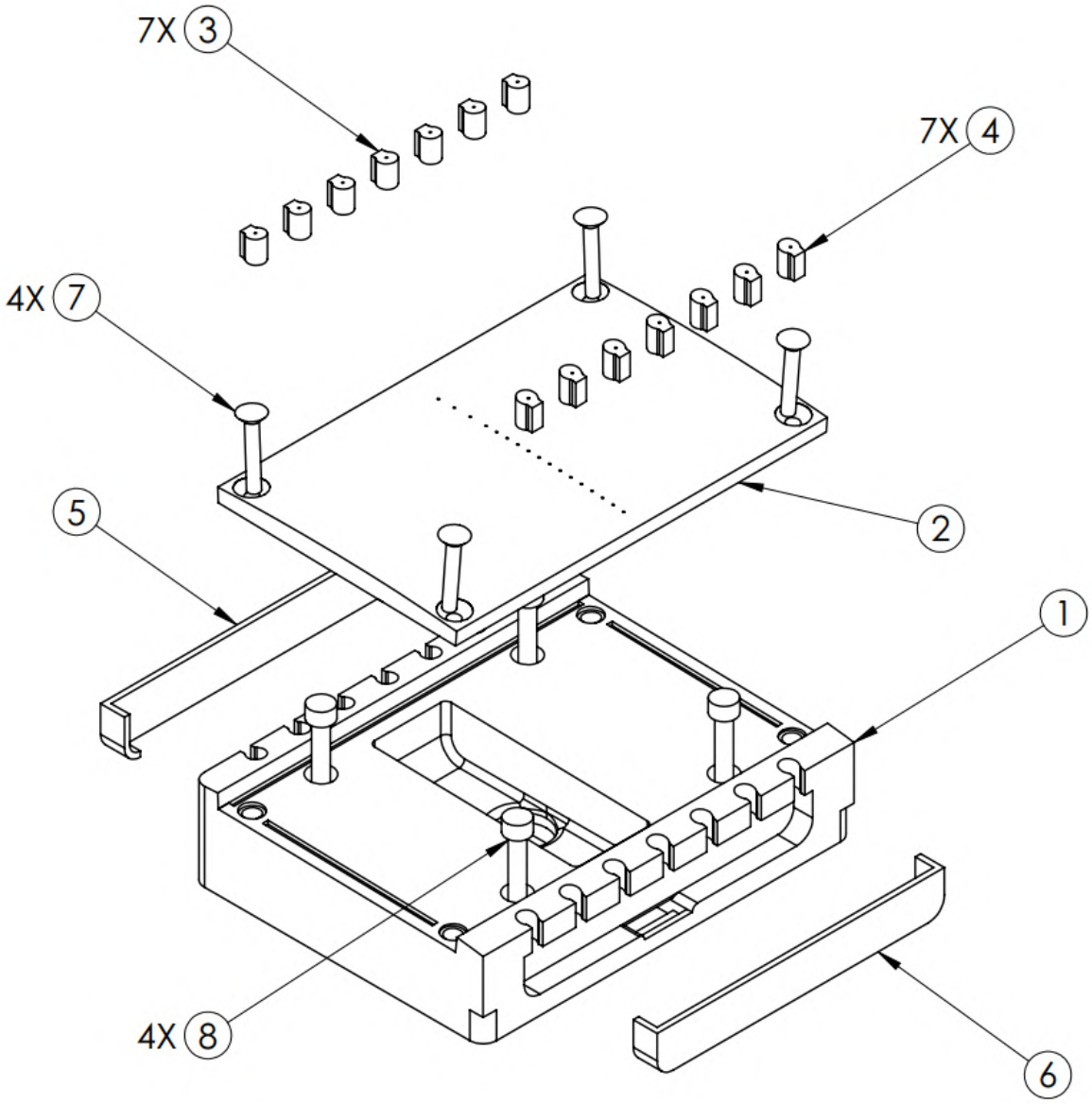

Figure A.2: Exploded view of the main components of the circular test section. Part number ID found in Table A.1

A.3. Flat test section

The flat test section sub-assembly (Figure A.4) provides a platform for future evaluation of different viscous drag reducing methods acting on a subsonic flow with adverse pressure gradient. The components that integrate it are listed in Table A.2 with their respective manufacturing methods.

ID	Part name	Manufacturing method
1	Flat section block	3D printing
2	Flat validation plate	CNC machining
3	M4 countersunk bolts (x4)	N/A (procured)
4	M4 socket head cap bolts (x4)	N/A (procured)

Table A.2: Table with components list of the flat test section sub-assembly.

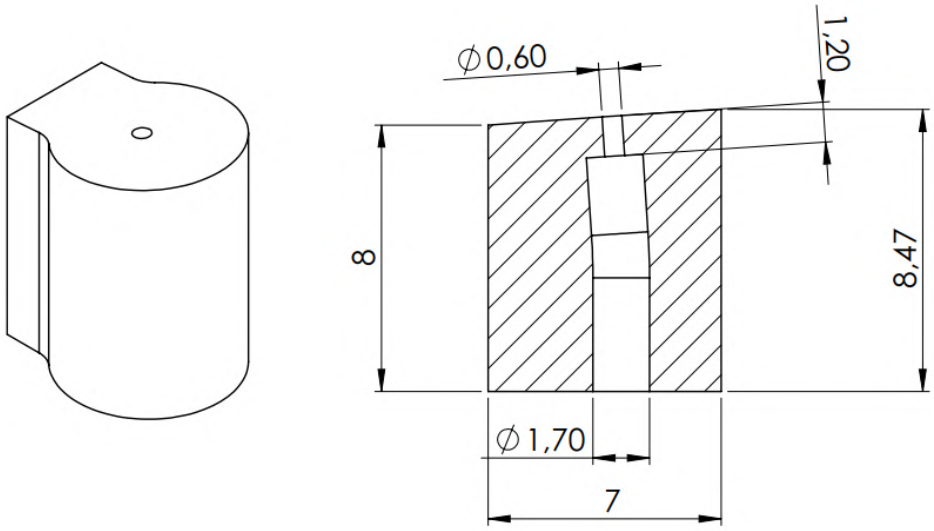

Figure A.3: Isometric and cross-section views of the pressure tap attached over the span in the front of the circular section block. Metallic tube and capillary are fixed on its bottom, where the hole assumes a larger diameter.

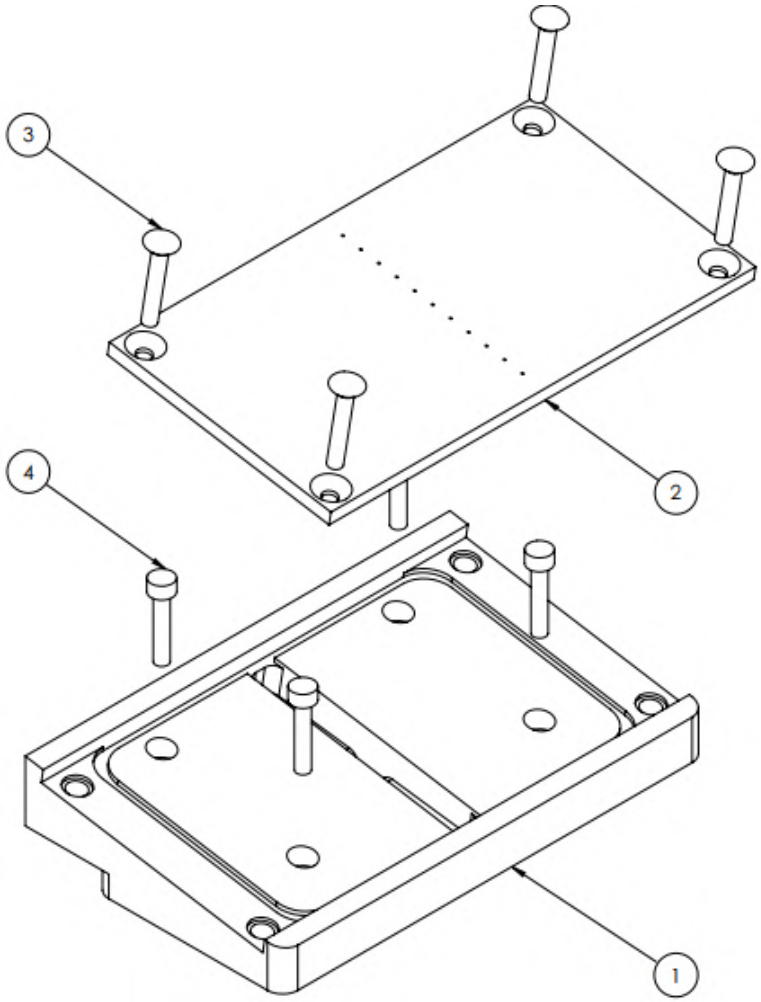

Figure A.4: Exploded view of the main components of the experimental setup. Part number ID found in Table A.2.

Pressure tubes organisation

After the sub-assemblies are properly fastened to the lower test section wall, all pressure tubes should be passing through its two vertical holes. Tubes are then guided through the groove on its bottom to exit at the back (Figure A.5). Finally, they shall be connected to the wind tunnel exterior, where pressure information is read and recorded by pressure scanners. This is done by means of a plug mounted at a side wall of the test section, designed to accommodate up to 30 pressure tubes (Figure A.6). For the validation of the experimental setup, all streamwise capillaries from the circular and flat validation plates are attached to the plug. Additionally, one capillary from the front and another from the back spanwise taps are used. The remaining 11 spanwise pressure taps were activated only during validation measurements over the width of the test section, and otherwise remained closed to avoid internal flow circulation.

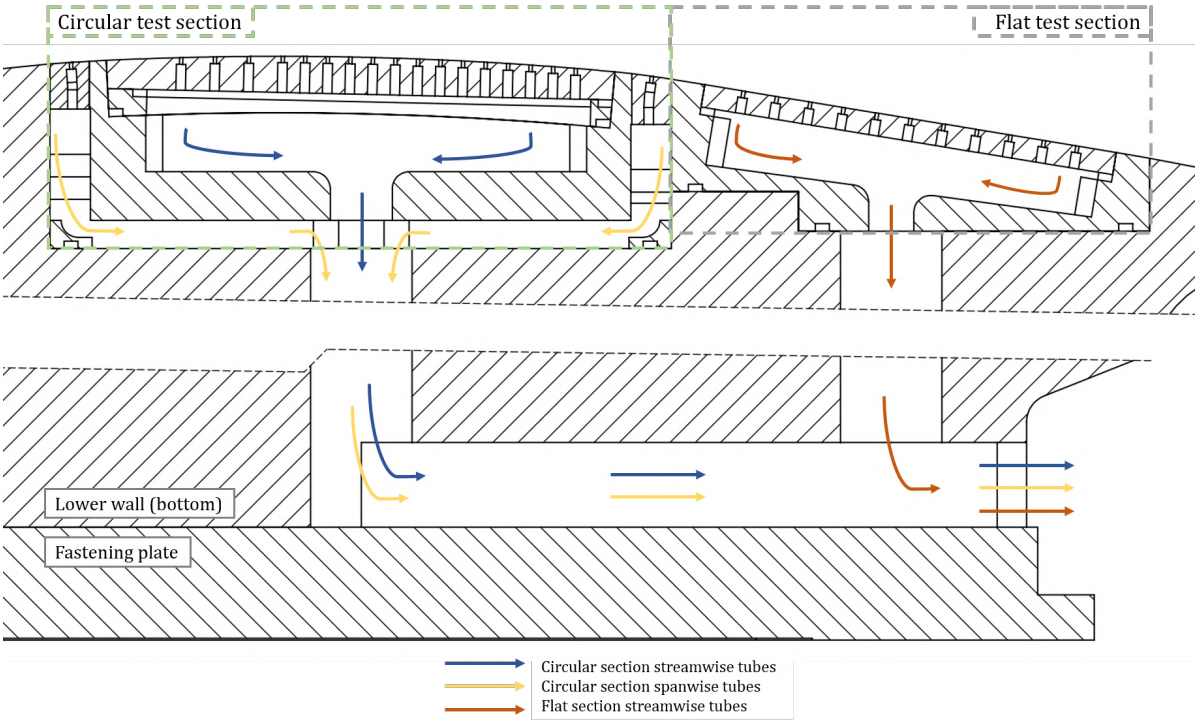

Figure A.5: Longitudinal cross-section of the experimental setup assembly showing the paths of the flexible tubes from the streamwise and spanwise surface pressure measurements. Break line is used to simplify the drawing.

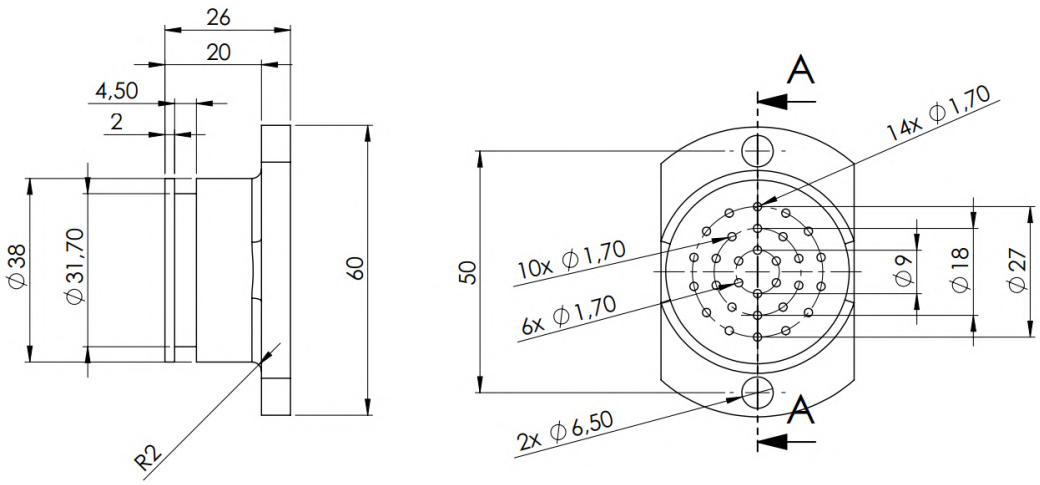

Figure A.6: Drawing of the plug where capillaries are attached (right and front views).

A.4. PIV mirror probe

In order to produce the desired measurement planes during the PIV campaign, a new mirror probe was designed. The laser sheet was emitted laterally to the interior of the wind tunnel through a small optical access. A mirror placed on the top of a vertical probe, mounted downstream of the test section, reflected the light in an angle of 45° towards the region where the shock occurred. The advantages of this design are its ability to be moved sideways, thus producing parallel planes at different spanwise locations, and reduced cross-section for smaller channel blockage. It was manufactured by conventional machining out of metal, to withstand the large forces acting on it. The mirror probe can be seen in Figure A.7, and its components are listed below:

1. Mirror support: Small metallic support to which the mirror is attached at an angle of 45°, ensuring the correct deflection of the laser sheet.
2. Vertical support: Holds the mirror at the height of the laser optical access, and provides three vertical positions. Structure is chamfered on its edges to avoid flow separation at the sides and reduce channel blockage, what decreases the resulting choking effect.
3. Support base: Welded to the vertical support, the base allows the probe to be firmly fixed to the wind tunnel.
4. Fixing plate: Attached to the bottom of the wind tunnel, the fixing plate allows the probe to slide sideways and be fixed at different positions.

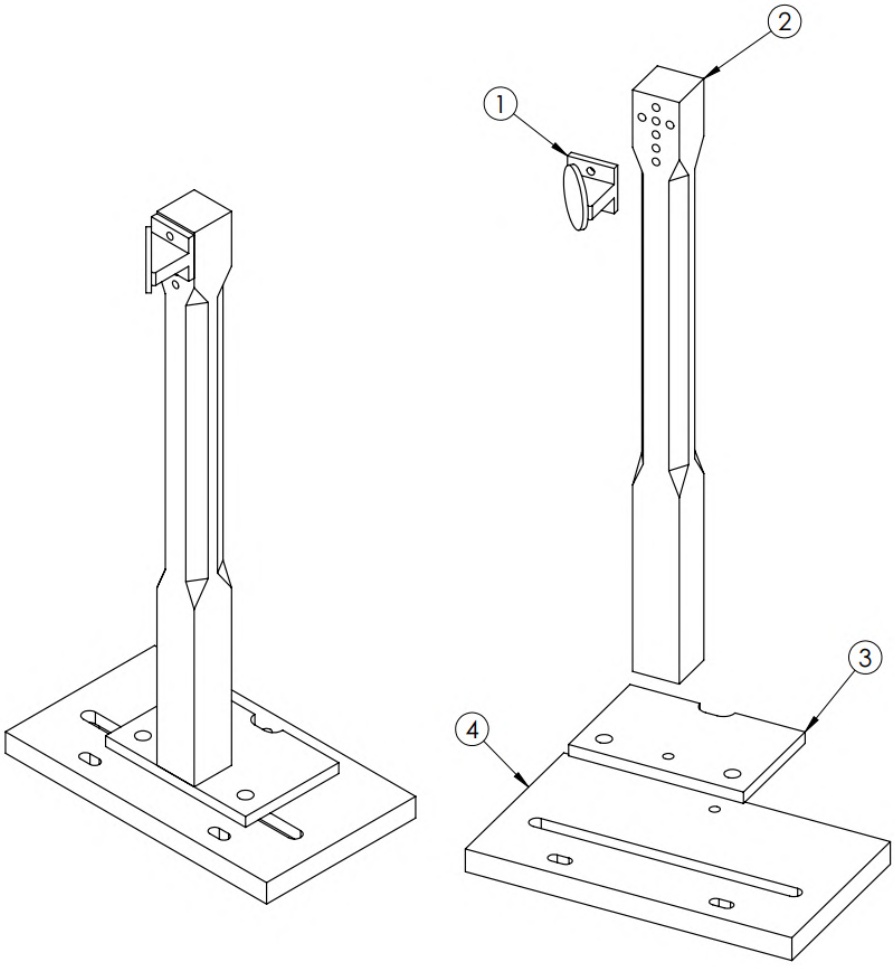

Figure A.7: Isometric and exploded view of PIV mirror probe designed for the velocimetry measurements.

B

Results of initial flow visualisation

This Appendix shall present the results from the initial measurement campaign, which aimed at gaining experience with the experimental setup and insights on how the shock interacts with a dimpled surface.

B.1. Objectives

The initial measurements involved solely visualisation techniques: Schlieren and oil flow visualisation. The goals of these initial measurements were three-fold:

1. Verify if the pair of test section blocks, with the newly designed lower wall, would produce the desired flow conditions with a stable normal shock.
2. Assess the effectiveness of moving the shock by means of the choke deflection mechanism, and evaluate the repeatability of the conditions produced.
3. Test initial designs of shock-interacting dimples to analyse flow sensitivity to the indentation geometry.

Three shock locations of interest were tested (shown in Figure B.1): on the upstream edge of the first dimple row (1), centered between the two rows (2) and on the downstream edge of the second row (3). The tested plates had two rows of shock-interacting dimples, the first with three and the second with two indentations. The indentations had a diameter of 20mm, the same as in [91], and three different depths were tested: 1mm, 2mm and 3mm. I n order to reduce costs, the three dimpled plates were 3D printed, what led to a rough surface finishing and an imperfect fit with the circular section block. The dimpled plates were deemed sufficient for this preliminary campaign, but improvements were necessary for the final measurements.

All objectives set for this preliminary campaign were met. It allowed a better insight on the working principles of the wind tunnel, the assembly of all components of the experimental setup and the ability of indentations with various depths to deflect the flow. Shock location was controlled while the wind tunnel was running by changing choke deflection, achieved when varying the input voltage on its servo motor. Although the gaps around the printed plates and their roughness resulted in undesired small perturbations in the flow (captured by the Schlieren images), it did not affect the interpretation of the effect of the surface indentations in the SWBLI.

B.2. Results

The results of the measurement campaign are now discussed. Figures B.3a, B.4a and B.5a present the reference cases, with the normal shock wave impinging over a smooth plate at the three positions of interest. The equally spaced expansion lines upstream of the shock are due to perturbations in the flow caused by the pressure taps drilled on the plate. Next to them, Figures B.3b, B.4b and B.5b show the results for the dimpled plate with the smallest depth analysed (1mm). For each pair of images, the choke deflection and flow conditions were the same.

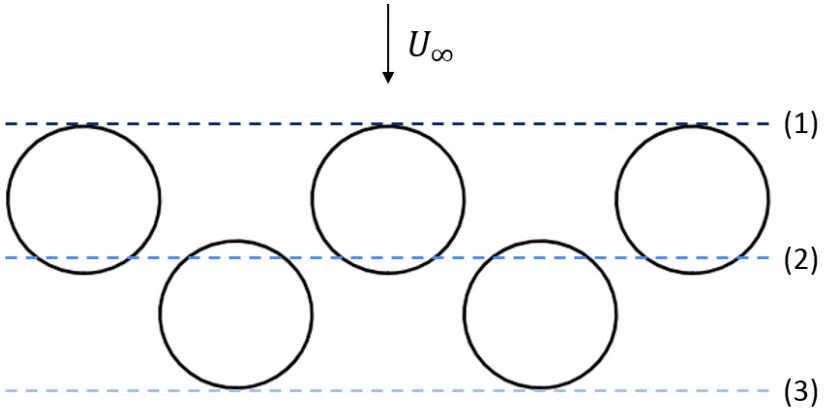

Figure B.1: Top view schematics of the three shock locations analysed in the initial measurement campaign: upstream (1), centered (2) and downstream (3).

Compression waves are formed close to the wall at the leading edge of the first dimple row, and meet the main shock leg downstream. Independent of shock location, the first wave remained pinned to the dent's leading edge. When shock was displaced to the downstream position, a clear re-expansion region formed afterwards between the two rows of dimples (identified by a bright region in the image). Next, the effect of deeper dimples on the interaction can be seen in Figures B.6a and B.6b. Deeper geometries produce larger flow deflections, what resulted in stronger re-expansion regions.

The main observation made from the Schlieren visualisation was that the shallowest geometry was capable of interacting substantially with the shock. The images for deeper dimples produced only evidence of stronger flow re-expansion. Thus, it was concluded that a 1mm depth is sufficient for shock control applications in the experimental facility used in this work.

As a conclusion of the first measurement campaign, oil flow visualisation was performed for the 1mm deep indentations with the shock in the centered location (Figure B.7). It is observed that the flow topology over the first dimple row follows a converging-diffusing pattern, whereas the second displays symmetric bubbles of recirculating flow. These strongly relate respectively to the stages 1 and 2 of the flow topology over dimples observed by Tay [20] (Figure B.2).

The symmetric shape of the oil pattern suggests that the spanwise velocity component should be small over the centreline of the dimples, and that at this plane flow can be regarded as two-dimensional. However, outside this region, the interaction is rather complex and highly three-dimensional. This increases the difficulty of reaching any definite conclusion using Schlieren, because the produced images overlay the flow structures over the span, being thus more appropriate for 2D cases. Also, when two rows are acting on the flow, a complex interaction evidently takes place between them, which overly increases the complexity of the analysed phenomenon, considering that the study of transonic dimples currently still finds itself in a preliminary stage. It was thus deemed more appropriate to focus the efforts of the main measurement campaigns on characterising the interaction over a single row of indentations.

(a) Stage 1. (b) Stage 2.

Figure B.2: Flow topology stages 1 and 2 identified over dimples in the work of Tay [20].

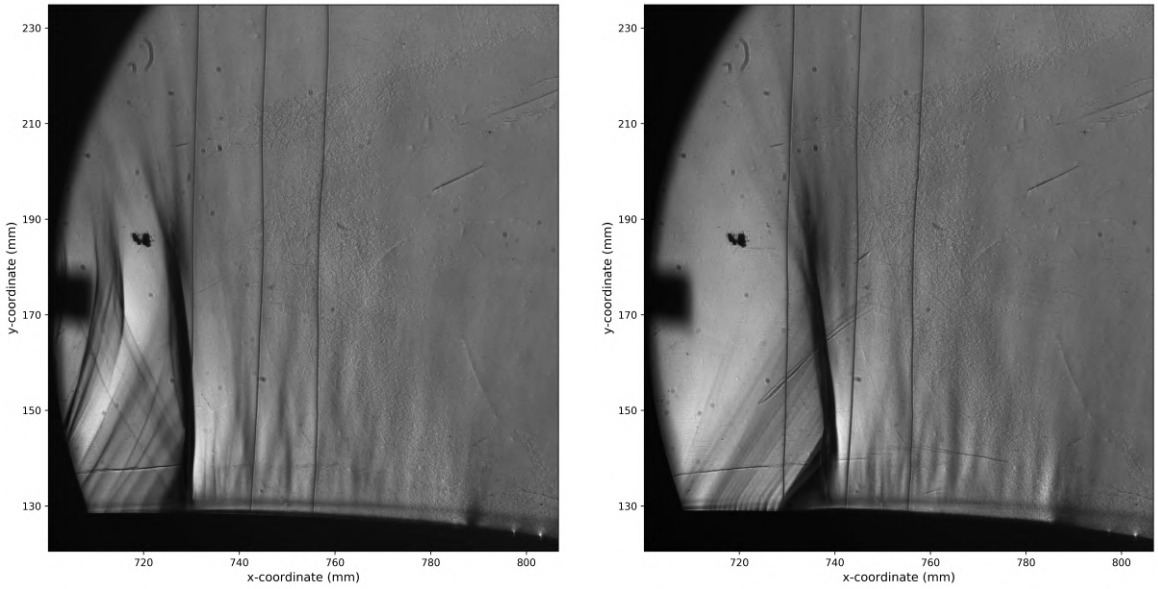

(a) Smooth plate.

(b) Dimpled plate 1mm.

Figure B.3: Schlieren images of a SWBLI over a smooth plate and a dimpled plate with the shock in the upstream location.

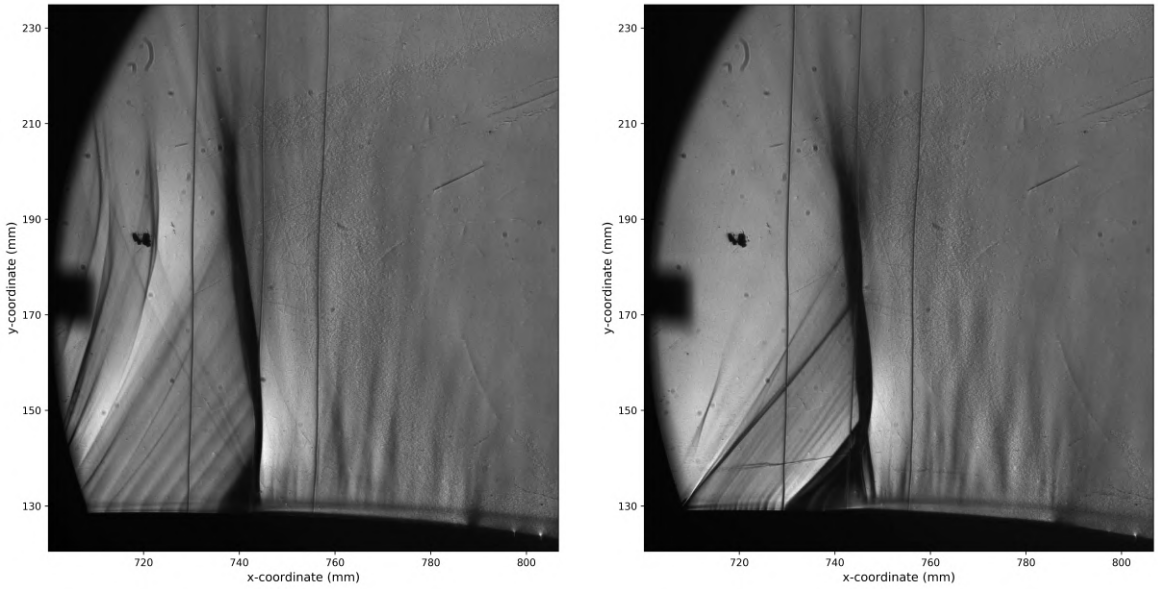

(a) Smooth plate.

(b) Dimpled plate 1mm.

Figure B.4: Schlieren images of a SWBLI over a smooth plate and a dimpled plate with the shock in the centered location.

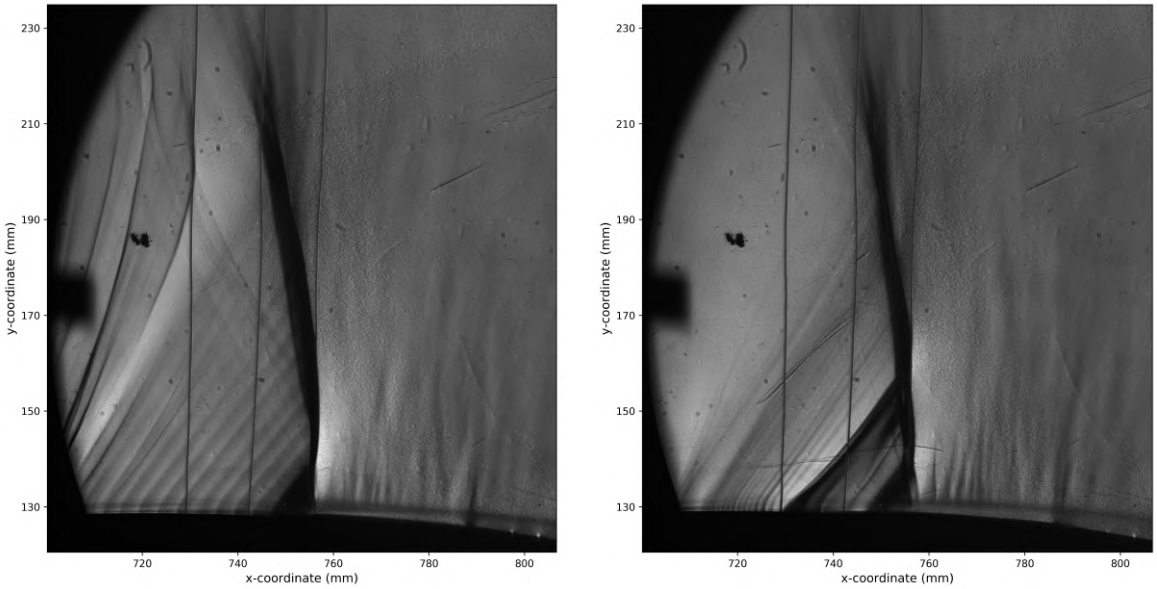

(a) Smooth plate.

(b) Dimpled plate 1mm.

Figure B.5: Schlieren images of a SWBLI over a smooth plate and a dimpled plate with the shock in the downstream location.

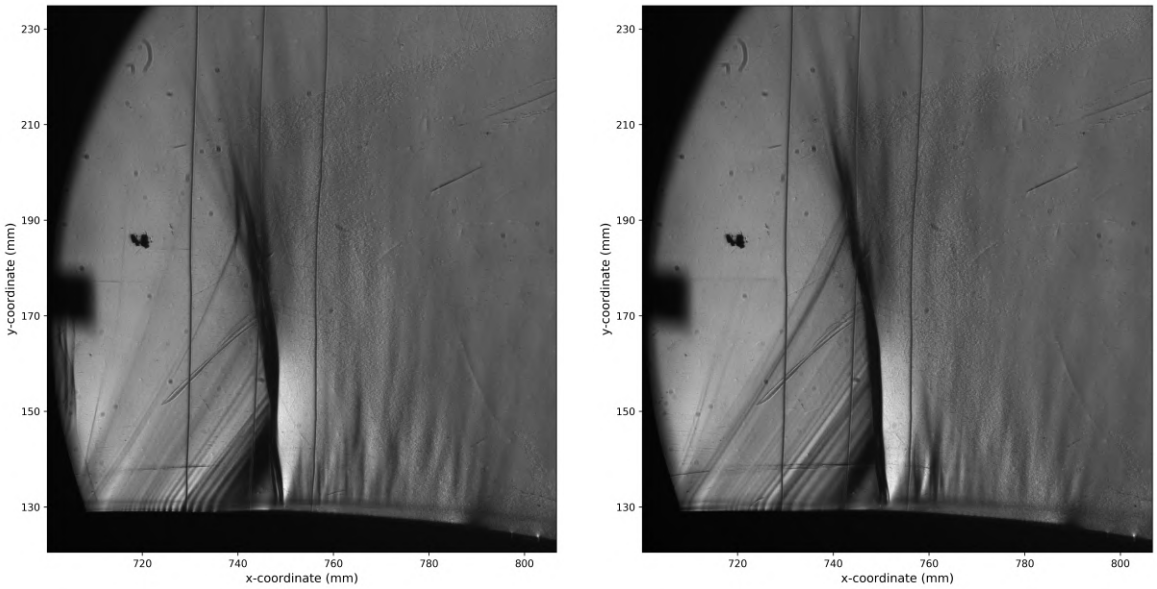

(a) Dimpled plate 2mm.

(b) Dimpled plate 3mm.

Figure B.6: Schlieren images of a SWBLI over dimpled plates with 2mm and 3mm depths and the shock in the centered location.

Figure B.7: Oil flow visualisation over the test plate covered with 1mm deep dimples (flow from top to bottom of the image).

C

CFD simulation of transonic dimples

This appendix presents the methodology and results of the two-dimensional dimple CFD simulations performed. First the motivation for these computations will be outlined. Then a reference dimple geometry is defined and the results from its simulations are compared with the smooth case. The next step is to assess the effects of varying the geometry degrees of freedom in the shock structure. The different geometries tested are defined and its respective results are presented. The quantities plotted in the results were mainly pressure distributions over the lower wall, total pressure profiles upstream and downstream of the SWBLI and qualitative density gradient in the x-direction.

C.1. Total pressure profile computation

Before tackling the work stream of simulating dimples in a transonic flow, it is briefly described how the total pressure profiles presented in the results were computed. Given that the simulation provides a complete solution of the flow field, it is possible to quantify the pressure recovery across the shock, what ultimately indicates the dimple effectiveness in reducing wave drag. This is done by computing the ratio of the mass-averaged total pressure $\overline{p_0}$ from before and after the interaction, as done by Ogawa et al. [66]. For this, the wall-normal p_0 profile was raised upstream and downstream of the SWBLI, where the mass-averaged value could be evaluated . The upstream profile was located at the beginning of the circular section, and the downstream one at the beginning of the flat section (Figure C.1).

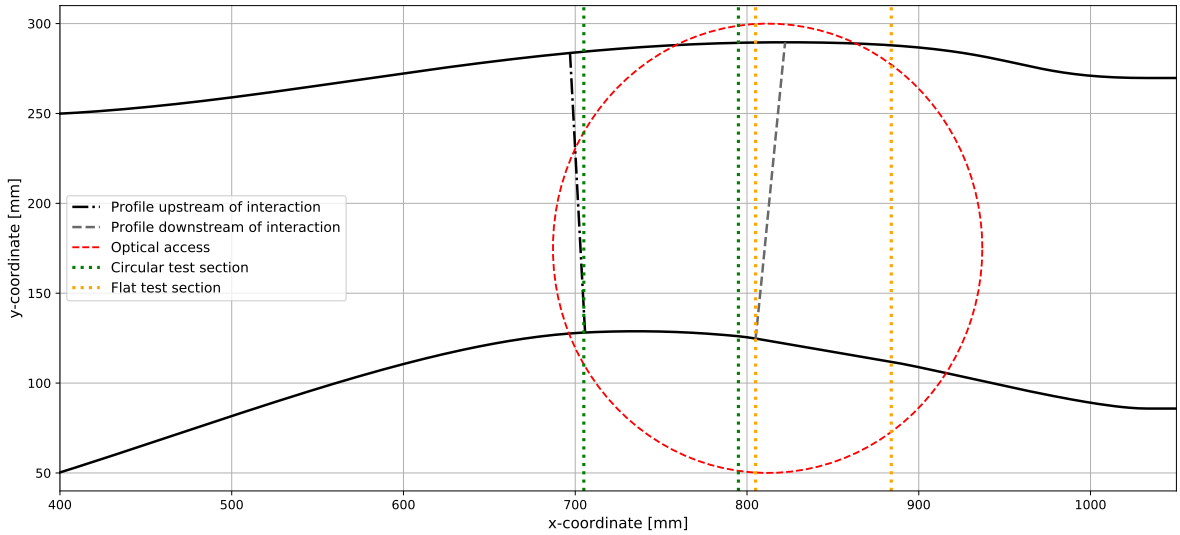

Figure C.1: Cross-sections of the transonic nozzle upstream and downstream of the SWBLI where the total pressure and boundary layer profiles were computed.

C.2. Two-dimensional dimple simulations

The study of dimples as means of controlling the SWBLI is the first of its kind and, as a result, there is no direct reference data to guide the geometry scaling. Parallels can be drawn with transonic bumps but only to a limited extent, given the inherent geometrical differences. It is clear that the amount of degrees of freedom that could be tested is too large to be covered in a single study. Therefore, a balance had to be struck between experimental effort and generation of insightful data to assess the potential of this device. The solution found was to perform simple CFD simulations of dimples interacting with the shock that would support the design of dimpled plates used in the experimental campaigns. The goals of this work stream were two-fold:

1. Gain insight on the sensitivity of the SWBLI to variations of the degrees of freedom.
2. Obtain reference results to compare with experimental data and support assessment of wave drag reducing potential.

The simulations were kept two-dimensional, similarly as during the geometry iterations (described in Chapter 3). This avoided large computational costs and simplified the convergence of the solution. But still provided valuable information on the streamwise pressure development over the lower wall and the total pressure profile downstream of the interaction. The pressure distribution measured during the experiments can be later compared with the numerical results.

C.2.1. Reference dimple geometry

The next step was to determine a reference dimple geometry. Considering the size of the circular section and results from the initial flow visualisation campaign (Appendix B), the chosen reference geometry had 40mm of length, depth of 1.0mm, and was placed so that the shock would be located at its trailing edge (x = 760mm), which is the expected optimal shock location. This dimple was simulated using the boundary conditions from Table 3.1. The relative pressure distribution over the lower wall and total pressure profiles (upstream and downstream of the interaction) are presented in Figure C.2.

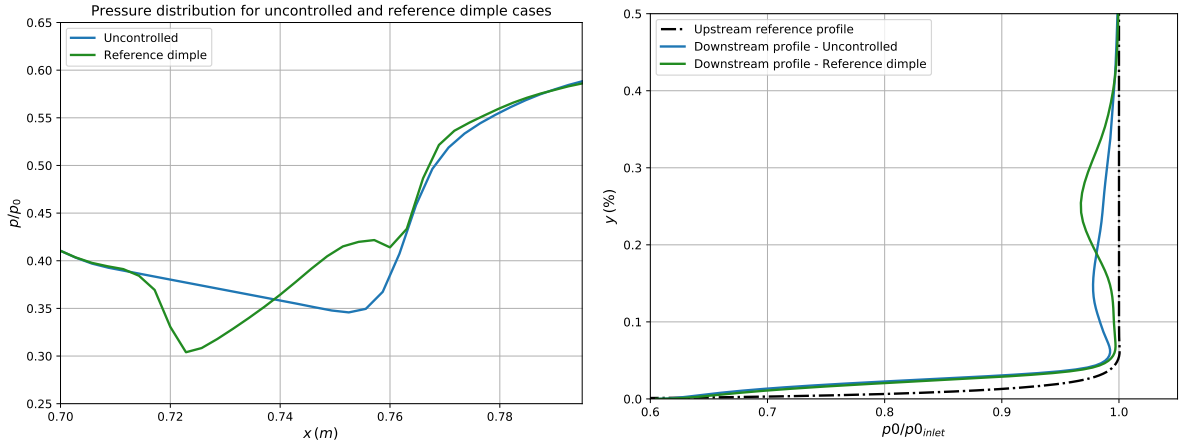

(a) Relative pressure p/p_0

(b) Total pressure profile $p_0/(p_0)_{\text{inlet}}$

Figure C.2: Relative pressure distribution and total pressure profile for the reference dimple.

The results largely agree with the prognosis made for a transonic flow over a dimple. Flow expands at the dent leading edge, causing a decrease of relative pressure. Then a smooth pressure rise takes place inside the dimple, characteristic of compression waves. As a result of this compression, flow close to the wall suffers a reduced pressure rise over the shock. This is reflected on the total pressure profile downstream of the SWBLI, which displays, for the controlled case, a larger pressure recovery between y=5% and 18%. Given that the shock is located at the dimple's trailing edge, a re-expansion region is not formed. However, the negative effect of the leading expansion fan is perceived further away from the wall. On the spot where it impinges on the normal shock, around y=25%, the local Mach number is higher than in the uncontrolled case, what results in larger pressure losses in this region.

This reference dimple simulation was performed using Mesh 1, found in the mesh study (Chapter 3) to yield the best relation between accuracy and computational effort. In order to confirm this choice before conducting further simulations, the reference geometry was again simulated using Mesh 2. The comparison of the relative pressure distribution and total pressure profiles yielded by both grids is presented in Figure C.3. In C.4 the density gradient in the x-direction is shown for the uncontrolled and reference dimple cases, a result which can be subsequently compared with Schlieren visualisations.

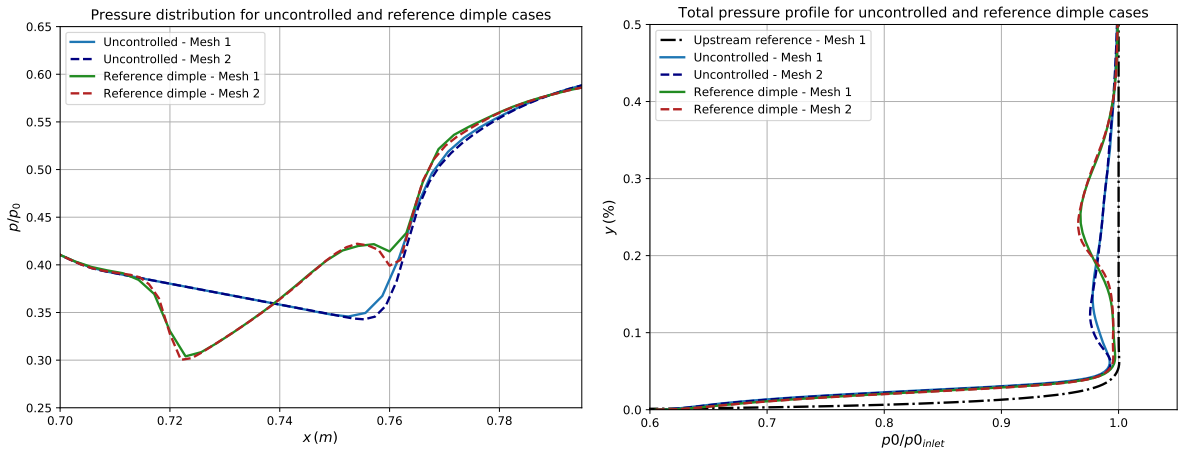

(a) Relative pressure p/p_0

(b) Total pressure profile $p_t/(p_0)_{\text{inlet}}$

Figure C.3: Relative pressure distribution and total pressure profile for the reference dimples with different grid size.

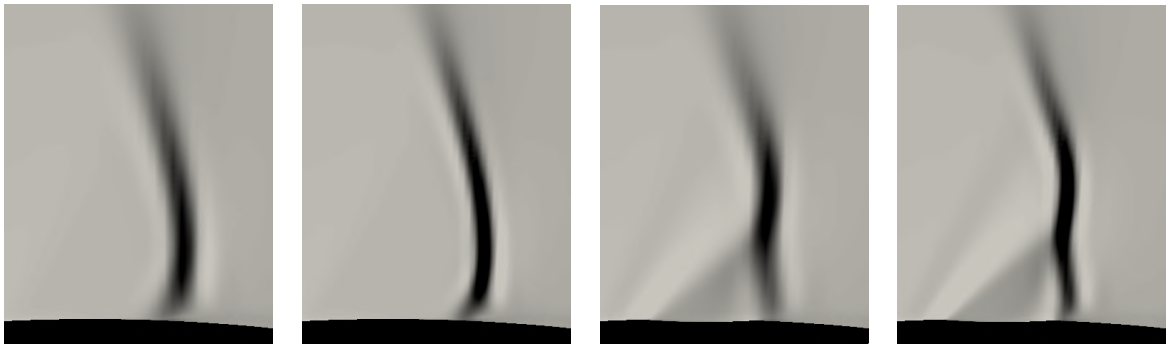

(a) Mesh 1 uncontrolled

(b) Mesh 2 uncontrolled

(c) Mesh 1 dimple

(d) Mesh 2 dimple

Figure C.4: Qualitative density gradient distribution for the reference dimples with different grid size.

From the results obtained by both meshes, the following observations can be made:

- The shock moves slightly downstream for the finer mesh, similarly as observed during the mesh study. For the flow over the dimple, this leads a small re-expansion at the dent trailing edge before the normal shock leg.
- A more refined grid produces sharper density gradient plots, but the shock structures for both meshes are equivalent.
- A slightly larger total pressure loss is observed for Mesh 2 around y=12%: a downstream displacement of the shock increases its strength, leading to higher losses.

C.2.2. Degrees of freedom variation

Based on the reference dimple shape, other shapes were simulated to evaluate the influence of the geometric parameters. The three most influential degrees of freedom to be tested in the simulations were:

- Variation of deflection angle: performed by varying dimple depth d
- Variation of size: performed by maintaining the d/D ratio for differently sized indentations
- Variation of relative location with the shock: performed by varying the distance between the dimple trailing edge and shock location x_S

As mentioned during the lower wall design process, the shock could not be displaced by changing the outlet conditions. Therefore, the dimple geometry itself had to be moved in the CFD analysis to evaluate the influence of shock location. This has the advantage of allowing a comparison between results of equally strong SWBLI's. However, it will hinder a direct equivalence with experimental data, which will be acquired by moving the shock instead of the indentation. Furthermore, only smaller relative displacements could be achieved in the simulations, for the indentation geometry position was constrained within the limits of the circular test section. Here, $x_s = 0$mm corresponds to the dimple trailing edge located at x = 760mm.

A simulation matrix with the degrees of freedom analysed can be seen in Table C.1. Simulations 2 & 3 evaluate the influence of deflection angle, 4 & 5 the dimple size and 6 & 7 the relative shock location. The geometries that correspond to the respective ID numbers are presented in Figure C.5. The following pages display the results of the computational analysis of the dimple geometric parameters.

ID	Geometry ID	D (mm)	d (mm)	x_S (mm)	θ_1
1	D40d10 - x0	40	1.0	0	5.7°
2	D40d05 - x0	40	0.5	0	2.9°
3	D40d125 - x0	40	1.25	0	7.2°
4	D30d075x0 - x0	30	0.75	0	5.7°
5	D50d125x0 - x0	50	1.25	0	5.7°
6	D40d10 - x-10	40	1.0	-10	5.7°
7	D40d10 - x+10	40	1.0	+10	5.7°

Table C.1: Simulation matrix with the tested dimple parameters.

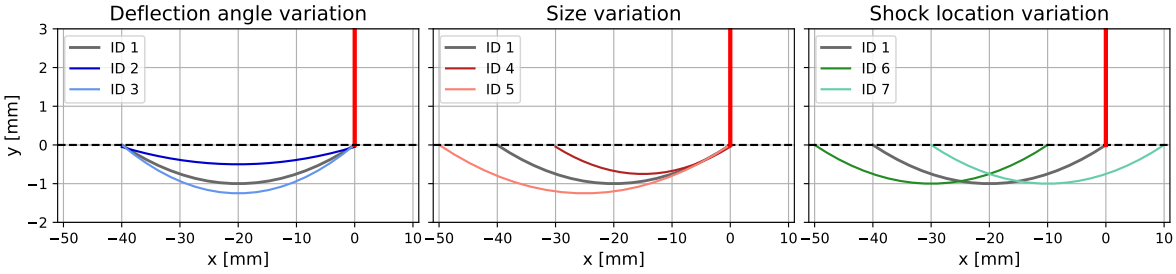

Figure C.5: Dimple geometries considered in the preliminary simulations. Red vertical line represents the shock location.

Deflection angle analysis

This subsection compares the simulation results of dimples with varying deflection angle (ID 2 and 3). This was obtained by maintaining the diameter D and changing the depth d. Dimple geometries correspond to entries ID 2, 1 and 3 from Table C.1, in order of increasing deflection angle.

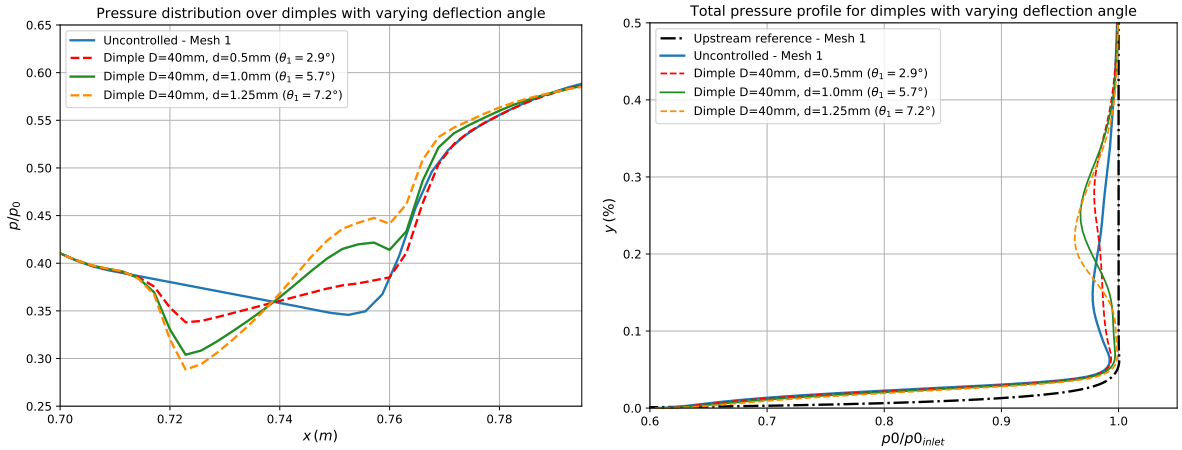

(a) Relative pressure p/p_0

(b) Total pressure profile $p_t/(p_0)_{\text{inlet}}$

Figure C.6: Relative pressure distribution and total pressure profile for dimples with varying deflection angle.

(a) θ_1 = 2.9°

(b) θ_1 = 5.7°

(c) θ_1 = 7.2°

Figure C.7: Qualitative density gradient distribution for dimples with varying deflection angle.

- Strength of expansion fan at leading edge as well as flow compression inside indentation increases with deflection angle.
- Shock structure becomes more curved with increasing deflection angle due to interaction with stronger leading edge expansion fan.
- For larger deflection angles, total pressure recovery saturates close to the wall (does not further improve) while deficit profile away from it continuously increases in magnitude and breadth.
- For dimple with a small deflection angle, both benefits and detriments of its influence are smaller, leading to a somewhat constant p_0 profile.
- In summary, the deflection angle is indeed a major parameter for the interaction. The deflection angle of the reference dimple geometry (θ_1 = 5.7°) seems however to be an upper limit, whereas smaller angles can be further explored.

Size variation analysis

This subsection compares the simulation results of dimples with varying size (ID 4 and 5). This was obtained by changing the diameter D and depth d while maintaining the d/D ratio constant. Dimple geometries correspond to entries ID 4, 1 and 5 from Table C.1, in order of increasing size.

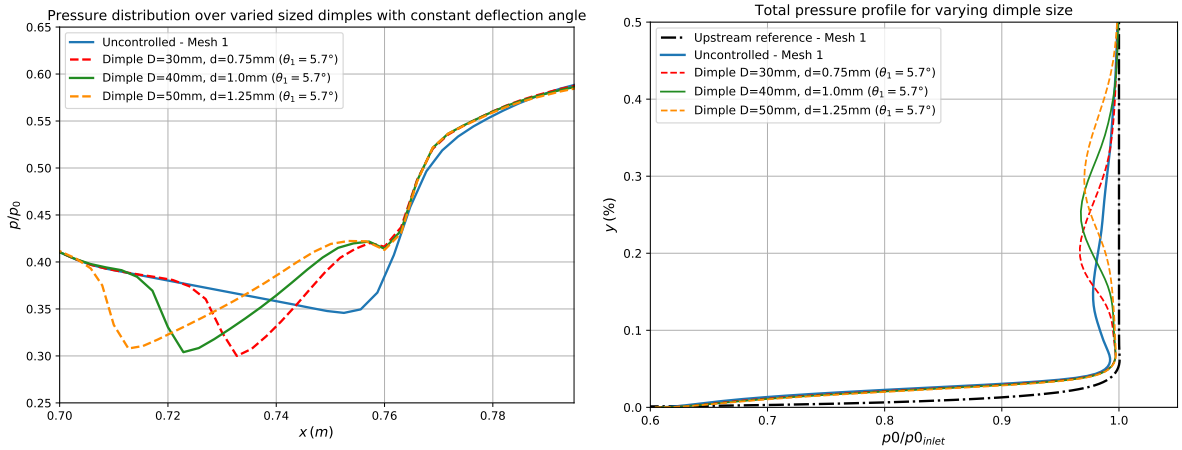

(a) Relative pressure p/p_0

(b) Total pressure profile $p_t/(p_0)_{\text{inlet}}$

Figure C.8: Relative pressure distribution and total pressure profile for dimples with varying size.

(a) D=30mm, d = 0.75mm

(b) D=40mm, d = 1.0mm

(c) D=50mm, d = 1.25mm

Figure C.9: Qualitative density gradient distribution for dimples with varying size.

- Strength of expansion fan at leading edge similar for all analysed cases due to constant deflection angle.
- Larger dimple size results in a smoother pressure gradient upstream of normal shock leg and influences a larger portion of the interaction structure.
- Total pressure minimum moves upwards with increasing dimple size and minimum freestream p_0 value is decreased, but breadth of deficit is enlarged.
- For larger dimples, pressure loss is smeared over a larger region further away from the wall.
- In summary, for a given deflection angle, a larger dimple size ensures that a bigger portion of the flowfield is affected by the dimple. However, there is no direct evidence that dimple effectiveness itself is improved.

Position variation analysis

This subsection compares the simulation results of dimples with varying relative position with the shock (ID 6 and 7). This was obtained by moving the indentation location within the circular section region. Displacements of $\pm$10mm were performed. Dimple geometries correspond to entries ID 6, 1 and 7 from Table C.1, in order of increasing downstream displacement.

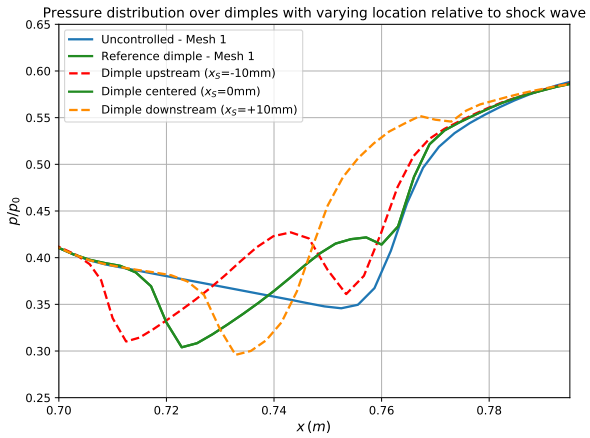

(a) Relative pressure p/p_0

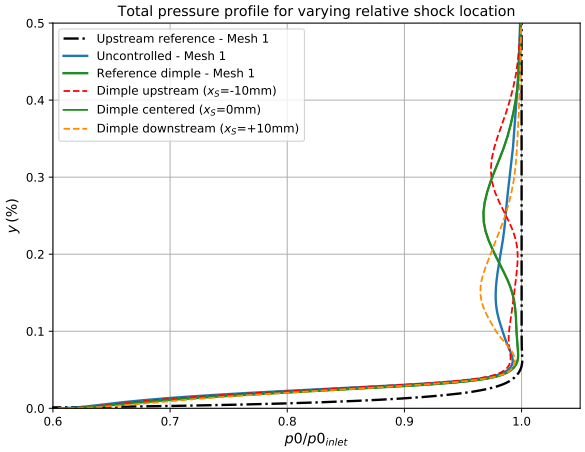

(b) Total pressure profile $p_t/(p_t)_{\text{inlet}}$

Figure C.10: Relative density distribution and total pressure profile for dimples with varying relative distance to the shock.

(a) $x_S = -10$

(b) $x_S = 0$

(c) $x_S = +10$

Figure C.11: Total pressure and boundary layer profiles upstream and downstream of the SWBLI for dimples with varying relative distance to the shock.

- A more upstream placed dimple produces a second expansion fan at the trailing edge . As a result, pressure drop at the normal shock leg suffered close to the wall is similar to the uncontrolled case. Nonetheless, it is not translated to the total pressure profile, which displays a larger recovery region, characterised by a reduced and upwards shifted loss area.
- For the downstream dimple, the preliminary compression merges with the pressure rise across the normal shock leg. Nonetheless, losses are still perceived close to the wall and are much stronger than those recorded for the uncontrolled case.
- The shock structure with the upstream dimple displays an upstream curvature close to the wall due to the interaction with the secondary expansion fan at the dimple trailing edge. For the downstream case it mingles with the compression waves inside the indentation.

C.2.3. Mass-averaged total pressure recovery

Finally, the mass-averaged total pressure $\overline{p_0}$ was computed from the total pressure profiles. The total pressure recovery ratio $\overline{p_{02}}/\overline{p_{01}}$ between downstream and upstream of the interaction was used as an indicator of the dimple influence on wave drag. As could be seen in previous total pressure profile plots, shock extended only until a limited height of the nozzle, and no pressure loss would be perceived above mid-channel height. Therefore, pressure ratio was calculated only until 50% of channel height to provide a higher sensitivity to the final results. The pressure recovery ratio for the dimple geometries simulated in this workstream is presented below, in Figure C.12.

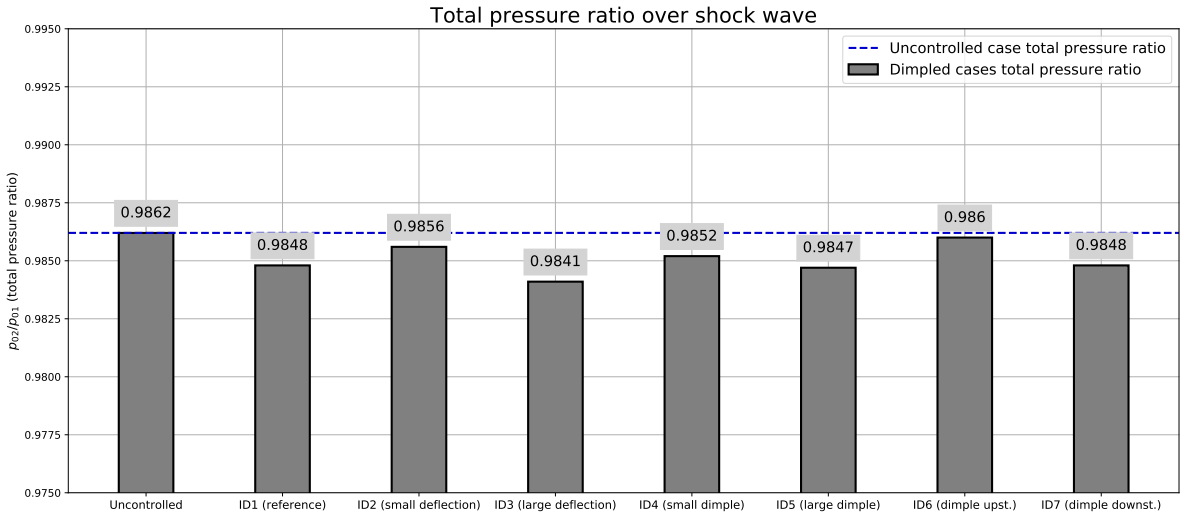

Figure C.12: Pressure recovery ratio for all the tested dimple geometries, against the value for the uncontrolled interaction.

As it can be seen from the results, no dimple geometry was able to increase the total pressure recovery over the shock computed for the uncontrolled case. The most notable improvement was obtained by displacing the dimple 10mm upstream of the original location, what produced a shock structure that can be deemed equivalent to the uncontrolled one in terms of pressure recovery. Other improvements from the reference case were observed in the ID2 and ID4 simulations. However, this result might be simply explained by a reduced influence on the SWBLI, given that their shape is characterised by a smaller deformation which converges towards the uncontrolled case geometry.

This preliminary analysis provided a first indication that dimples might not be able to reduce wave drag. It confirms the presence of antagonist mechanisms in the interaction over the dimple which ultimately lead to a slight deterioration of the pressure recovery across the shock. Nonetheless, these simulations only considered very simple 2D geometries, and three-dimensional effects are still to be evaluated in the experimental analysis. In conclusion, they provided a deeper prediction of the flow mechanics to be reproduced and measured in the wind tunnel. Given that no geometry yielded a larger recovery over the shock, the geometry from ID1 simulation was kept as a reference for the test plates to be manufactured.

D

Oil flow visualisation

To support the validation of the uncontrolled flow field, oil flow visualisation was performed over the smooth reference plate. The results are displayed in Figure D.1.

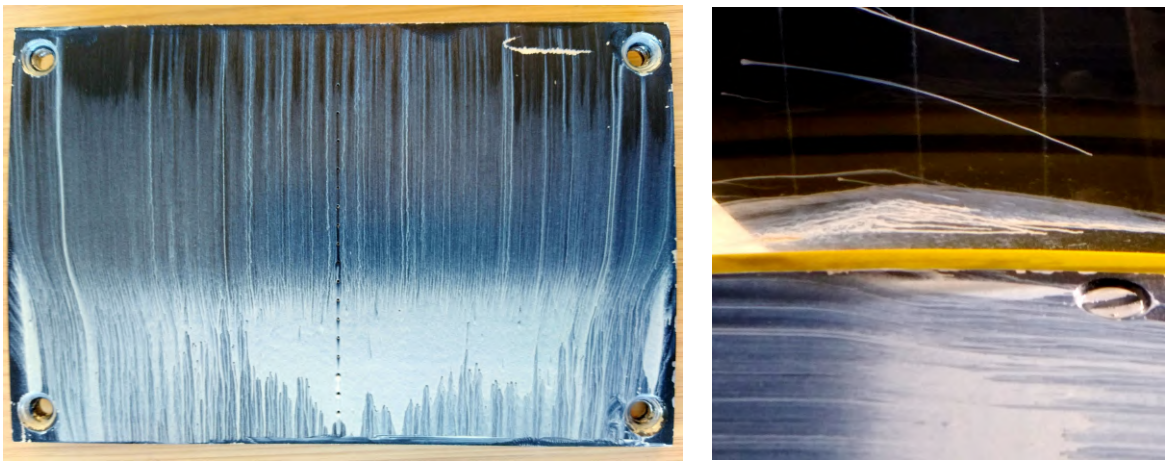

(a) Top view

(b) Detail close to the wall

Figure D.1: Oil flow visualisation over the smooth reference test plate and detail of vortical structure close to the wall. Flow goes from top to bottom in the top view, left to right on the right view.

It can be seen that around the plate symmetry, incoming flow is two-dimensional and the streamlines travel parallel to each other in the streamwise direction. The shock was placed slightly after the middle of the plate, being identified in the image by the sudden increase of oil concentration, as a result of the reduced shear caused by flow deceleration. Near the shock, streamlines further away from the symmetry display a converging behaviour due to compression. Additionally, close to the side wall, vortical structures are formed due to the separation of the corner boundary layer (Figure D.1b).

E

Post-processing of PIV results

In this appendix, the post-processing routine applied to all PIV data will be presented.

E.1. Shock instability

The acquisition of velocimetry data for each flow case followed always the same steps. First, a short run was performed with Schlieren visualisation in order to determine the voltage input for the choke system that placed the shock in the desired location. Then, PIV measurements were conducted by applying always the same voltage. Image pairs were acquired at a frequency of 15Hz during 20 seconds, thus yielding 300 pairs at each PIV run. In order to have a statistically meaningful data set, each flow case was measured 3 times, thus yielding a total of 900 image pairs. By deploying the cross-correlation procedure described in Chapter 7, 900 velocity distributions were obtained, from which the average and standard deviation of the velocity field vectors was computed.

Measurements were first performed for all plates over Plane 1, at the symmetry of the channel, and then 3D dimples were also measured over Plane 2 (at the dimple centreline). When processing the data, it was identified that the shock oscillated considerably more in measurements performed over Plane 2 than over Plane 1. This was confirmed by much larger standard deviation values around the shock, and also by a smeared mean velocity distribution in this region, where a sharp velocity change would be expected. In order to investigate this more closely, the shock location was computed for each individual velocity distribution, by identifying the x-coordinate where the smallest derivative of the U-component in the streamwise direction could be found.

Results of this analysis can be seen in Figure E.1, which displays the data points of the three PIV runs for the 3D dimpled plates, over both planes. For Plane 1 measurements of the D20d10-3D dimple, there is a small spread of the shock locations (with a standard deviation σ_x of 2.3mm), and the average computed shock location $\overline{x}_s$ is very close to the desired one, at x=760mm. On the other hand, measurements over Plane 2 display a much larger deviation (σ_x=4.4mm), and a mean shock location further away from the desired value. A similar trend was observed for the other three-dimensional plates, with the R10D40d10-3D displaying a major shift of the mean shock location between the first (data points 1-300) and the last two runs (301-600 and 601-900 respectively).

Measurements over both planes were conducted following the same procedure, with the same apparatus, and using the same mirror probe, mounted at the back of the test section. The only difference between them was the probe position, shifted sideways to generate the laser sheet over the dimple centreline. Therefore, an explanation for the higher shock instability over the Plane 2 measurements is the closer proximity between the probe and the wind tunnel side wall in this configuration, which presumably triggers unsteady flow structures that change the back pressure of the test section, resulting in a stark shock oscillation.

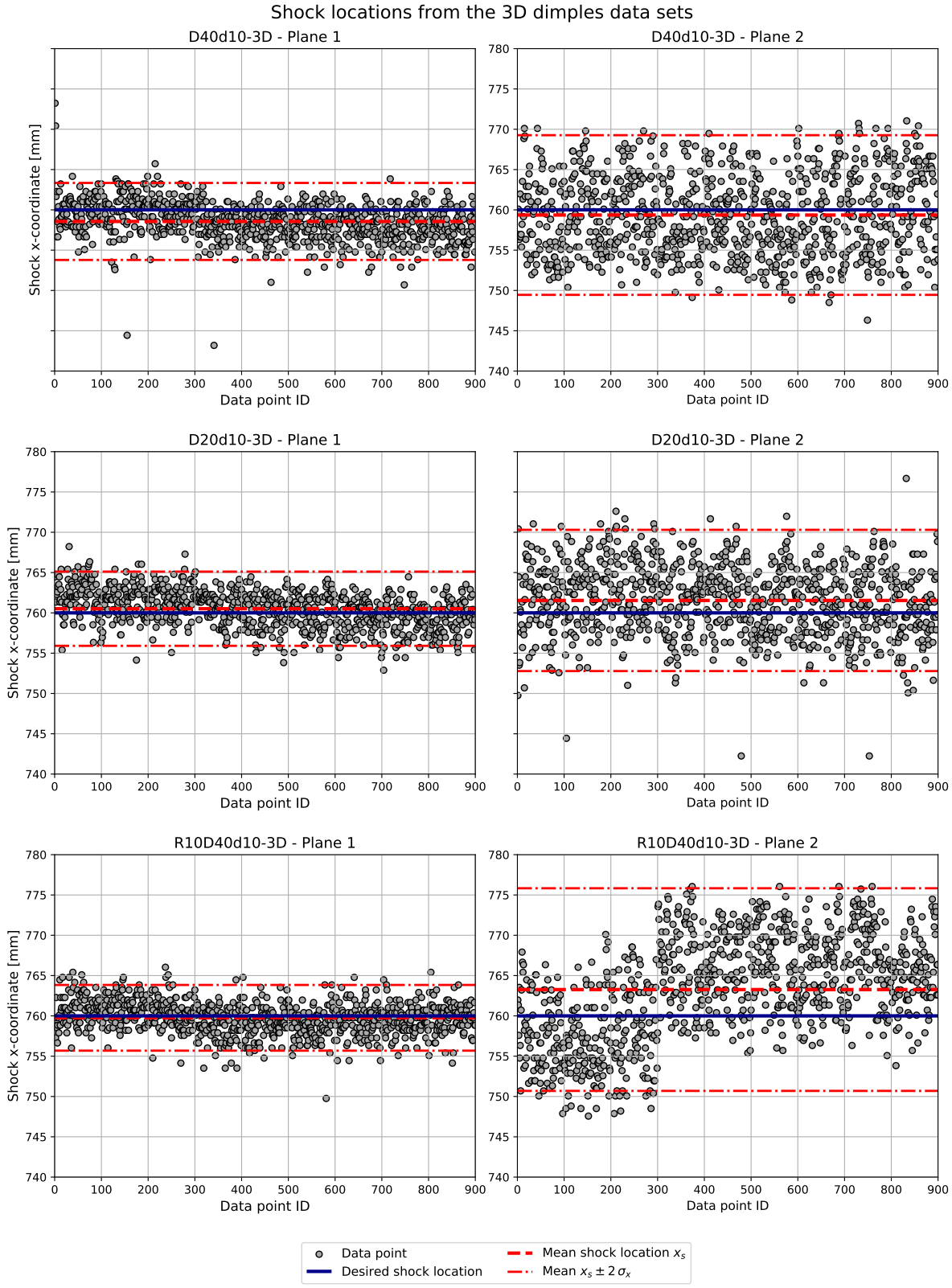

Figure E.1: Shock location of all data points acquired for the three-dimensional dimples plates over planes 1 and 2. Data points from 1-300, 301-600 and 601-900 correspond to the first, second and third PIV runs of each flow case respectively.

E.2. Post-processing routine

In light of the issue identified, the raw data acquired over Plane 2 could not be directly used to compute a mean flow field, which would be later compared with the other flow cases. Given the stark oscillation, the average would not be representative of a specific shock location, but the smeared mean result over an excessively wide range of positions. Hence, a two-step post-processing routine was adopted.

The first step consisted of filtering data points based on shock position, and aimed at minimising oscillation effects. The shock x-coordinate was identified in each individual velocity distribution by searching for the minimum value of the derivative of the U-component in the streamwise direction. The range of accepted shock locations was centered at x=760mm, the desired shock location, and had a spread of $2\,\sigma_x$, where σ_x was always 2mm, identified from the Plane 1 raw data as being a characteristic shock location deviation. The data points whose shock was positioned outside this range would not be considered in the mean flow field computations. This approach is supported by the assumption that data acquired at every instant represents a steady state velocity field, and unsteady flow phenomena can be neglected.

This procedure was applied to all nine flow cases, and resulted in a reduction of the number of data points available for the mean flow field computation. Given that the deviation value was taken from Plane 1 measurements, data sets originally acquired over this plane were less affected, and there is barely no difference between the raw data average and the one computed after filtering the shock location (Figure E.2). On the other hand, Plane 2 data sets were considerably diminished, but the remaining points were more coherent, yielding palpable improvements in the average distribution (Figure E.3). Table E.1 presents an overview of the mean and standard deviation values of the shock location before and after the shock location filtering, as well as the number of individual velocity fields available after the procedure, for every flow case.

The mean and standard deviation values of the resulting velocity field vectors were computed and used as a reference for the second post-processing step. The second step consisted of recomputing the mean velocity by including only vectors within a range defined by three-times the reference U-component standard deviation value ($3\,\sigma$) at each point where a vector was defined. Therefore, all velocity fields filtered from the shock location procedure were used, however the individual vectors were filtered based on the reference deviation at every location.

This second step influenced the final mean flow field of Plane 1 and 2 measurements alike. It prevented poorly correlated vectors from individual data points from modifying the final mean distribution. These could be caused during measurements by reflections from the optical access window and by sparsely seeded portions of the flow. These final mean and standard deviation distributions were effectively used in the results presentation and discussion from Chapters 7 and 8.

	Raw data		After shock loc. filter		
Plate ID	$\overline{x}_s$ (mm)	σ_x (mm)	$\overline{x}_s$ (mm)	σ_x (mm)	No. of data points
Smooth reference plane 1	758.4	2.4	759.0	1.9	761
D40d10-2D plane 1	757.0	2.2	757.4	1.8	812
D20d10-2D plane 1	761.9	2.3	761.2	1.8	736
D40d10-3D plane 1	758.6	2.4	759.0	1.7	791
D40d10-3D plane 2	759.4	5.0	759.7	2.4	453
D20d10-3D plane 1	760.5	2.3	760.4	1.9	827
D20d10-3D plane 2	761.5	4.4	760.2	2.3	543
R10D40d10-3D plane 1	759.8	2.0	759.8	1.8	862
R10D40d10-3D plane 2	763.3	6.3	760.5	2.4	345

Table E.1: Overview of geometrical parameters of tested dimpled plates.

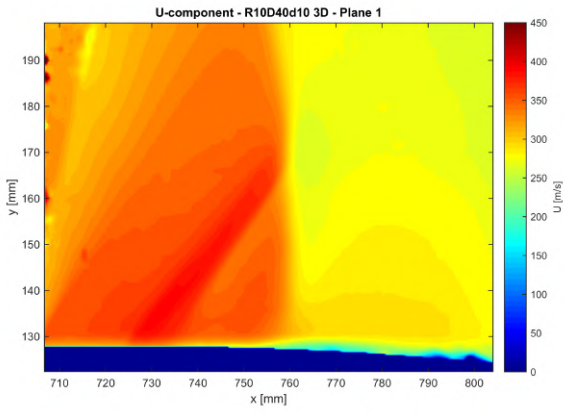

(a) U-component mean, raw data

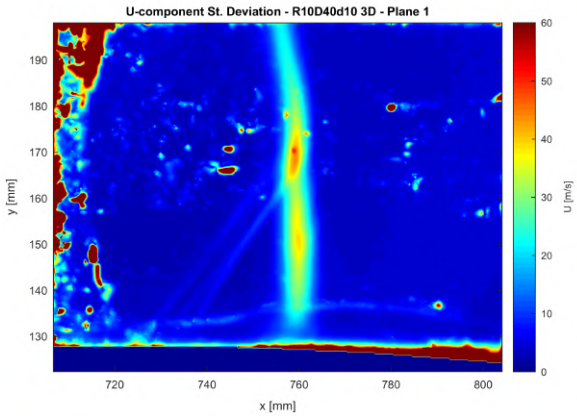

(b) U standard deviation, raw data

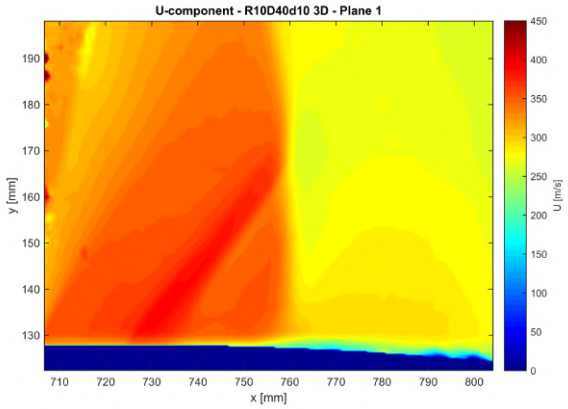

(c) U-component, $2\sigma_x$ shock location

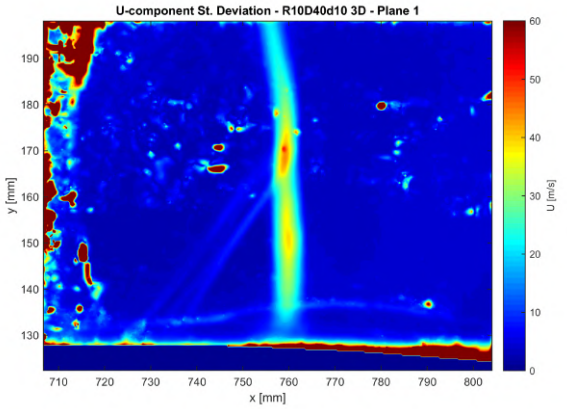

(d) U standard deviation, $2\sigma_x$ shock location

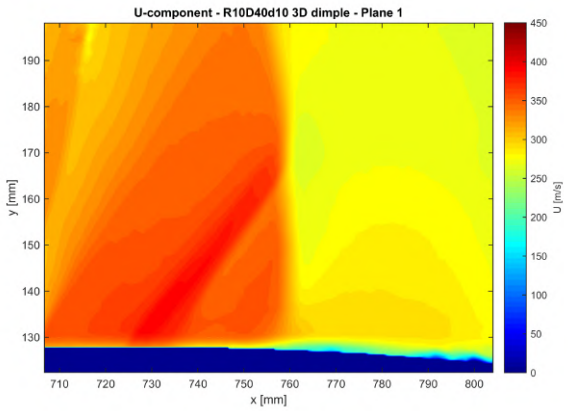

(e) U-component, $2\sigma_x$ shock location, 3σ vector deviation

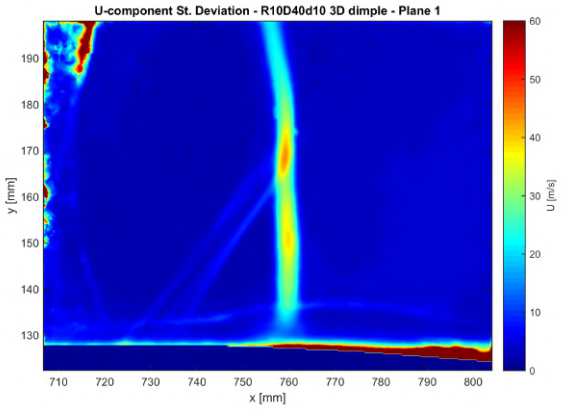

(f) U-component st. deviation, $2\sigma_x$ shock location, 3σ vector deviation

Figure E.2: Mean and standard deviation U-component distribution after each post-processing steps. Velocimetry data acquired over Plane 1 for the R10d10d10 3D dimpled plate.

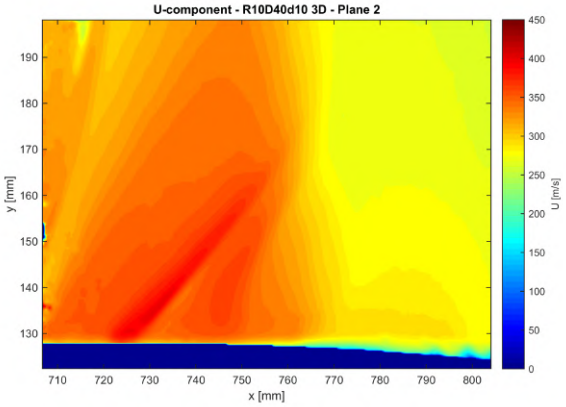

(a) U-component mean, raw data

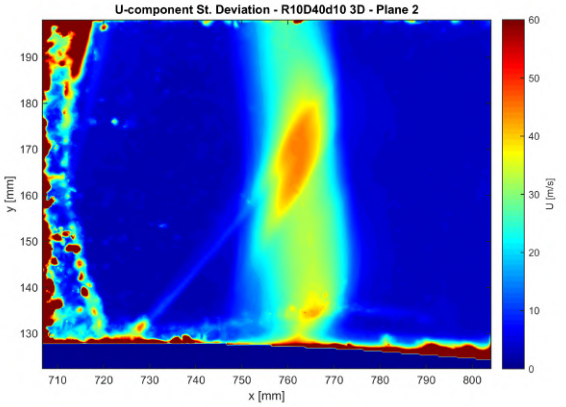

(b) U standard deviation, raw data

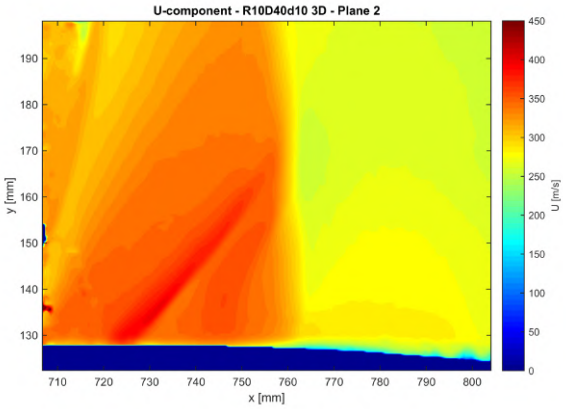

(c) U-component mean, 2σ shock location, 3σ vector deviation

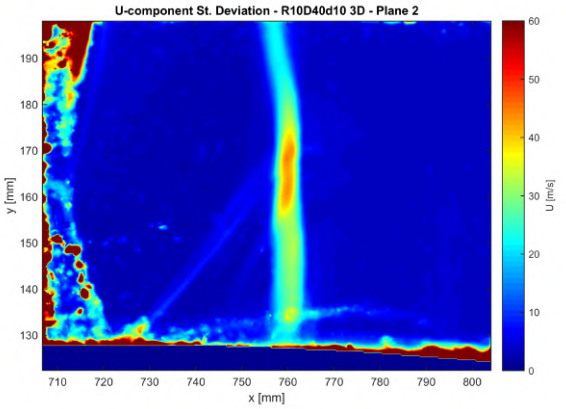

(d) U-component st. deviation, 2σ shock location, 3σ vector deviation

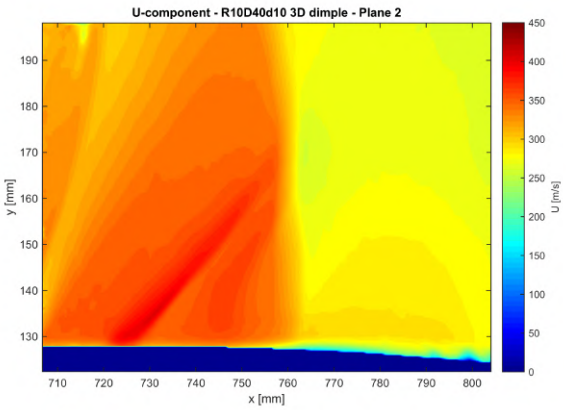

(e) U-component, 2σ shock, 3σ deviation

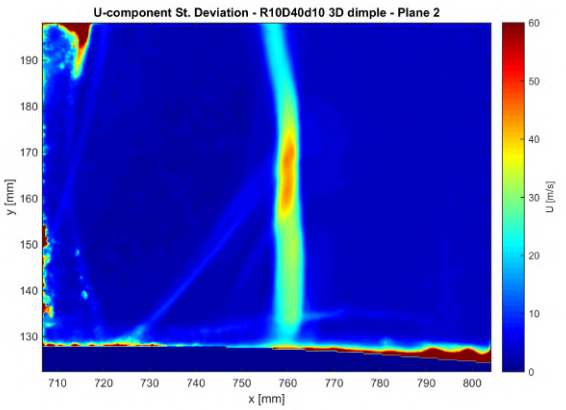

(f) U standard deviation, 2σ shock, 3σ deviation

Figure E.3: Mean and standard deviation U-component distribution after each post-processing steps. Velocimetry data acquired over Plane 2 for the R10d10d10 3D dimpled plate.

F Overflow measurement results

In order to keep the discussion on the measurement outcomes objective and concise, not all result were presented in the main chapters of this thesis. Nonetheless, the plots that were kept out still hold valuable information that may serve to gain additional understanding of the phenomenon currently investigated and to support further work. The overflow results are therefore consolidated in this chapter. The first section contains PIV results, whereas the second holds additional surface pressure distributions.

F.1. PIV overflow results

Throughout the main part of the report, different distributions were used to interpret velocimetry data acquired over the SWBLI. This section includes the plots from all of these analysis that were not displayed in previous chapters. These are distributions of mean velocity, U-component standard deviation over Plane 1 (for shock instability interpretation purposes), streamwise velocity gradient and flow direction angle. To conclude, the total density ratio profile for the R10D40d10 3D plate is presented.

F.1.1. Mean velocity distributions

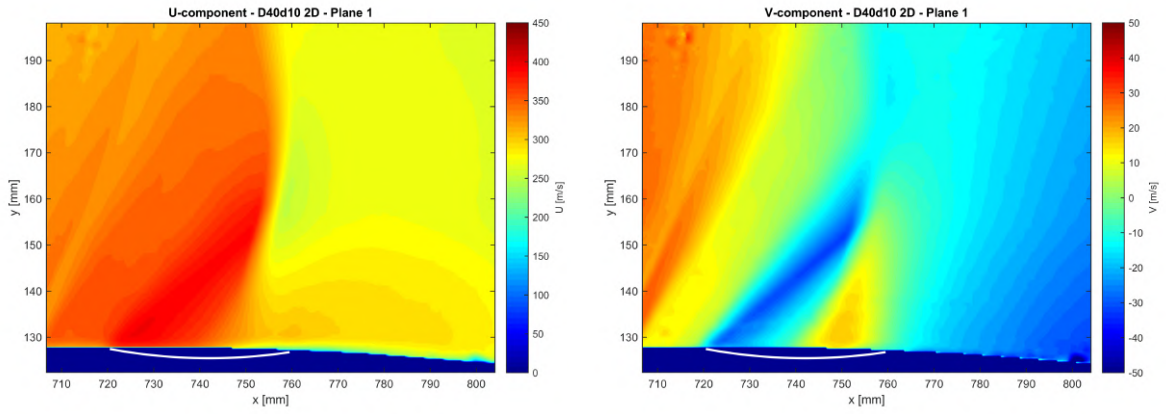

(a) U-component

(b) V-component

Figure F.1: Distributions of the mean U and V velocity components for the D40d10-2D dimpled plate over Plane 1.

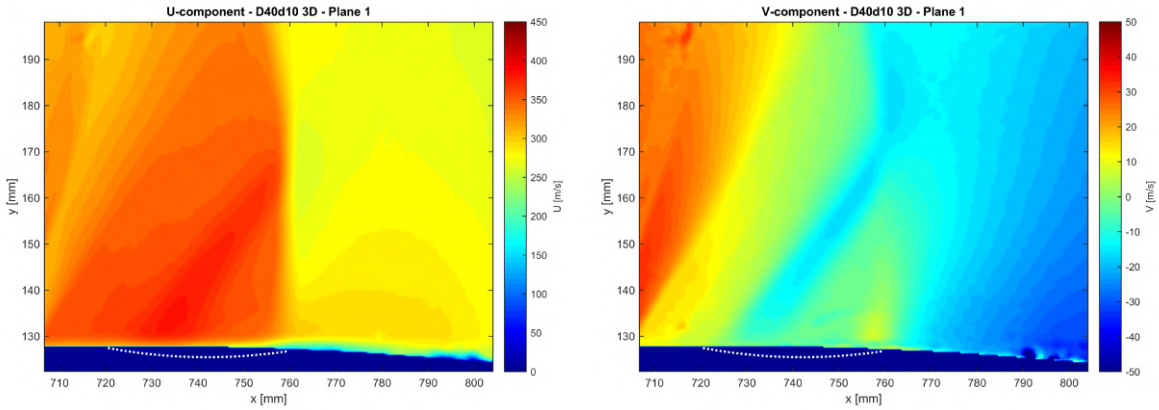

(a) U-component (b) V-component

Figure F.2: Distributions of the mean U and V velocity components for the D40d10-3D dimpled plate over Plane 1.

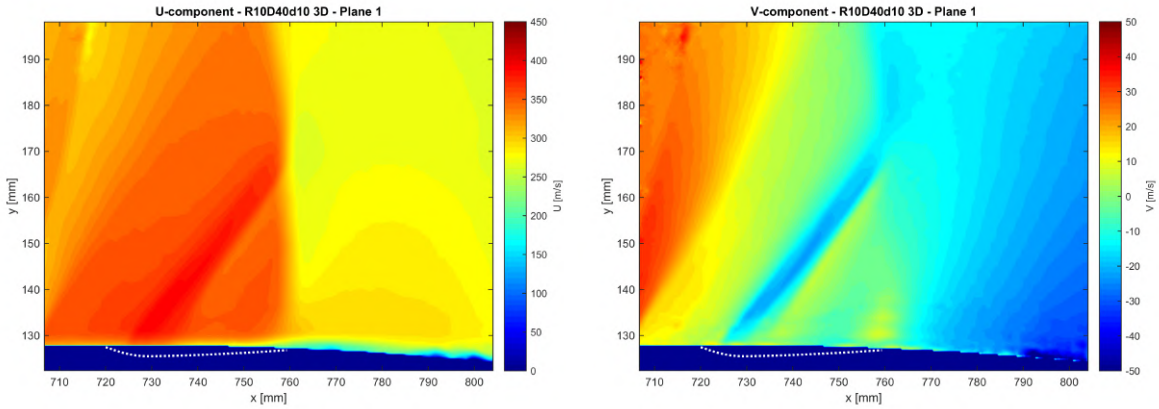

(a) U-component (b) V-component

Figure F.3: Distributions of the mean U and V velocity components for the R10D40d10-3D dimpled plate over Plane 1.

F.1.2. U-component standard deviation

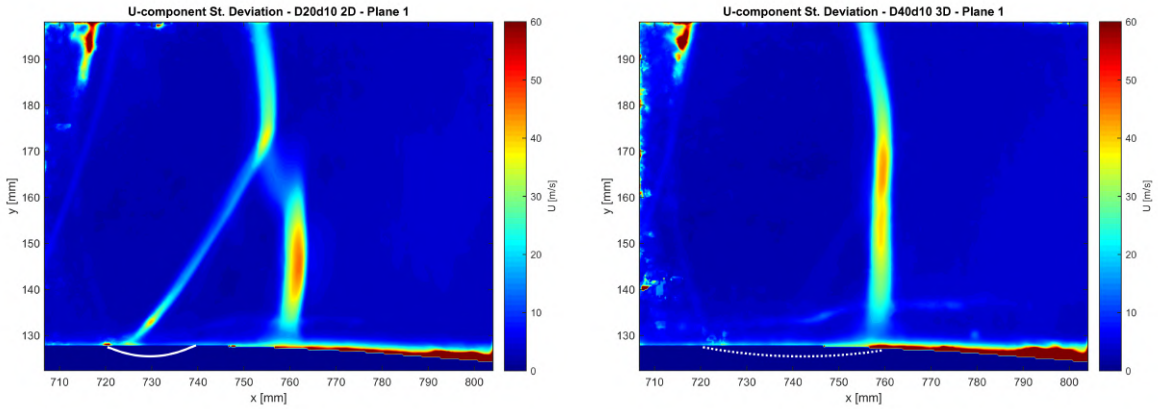

(a) D20d10 2D (b) D40d10-2D dimple

Figure F.4: Distributions of the U-component standard deviation over Plane 1 for different test plates.

F.1.3. U-component streamwise gradient

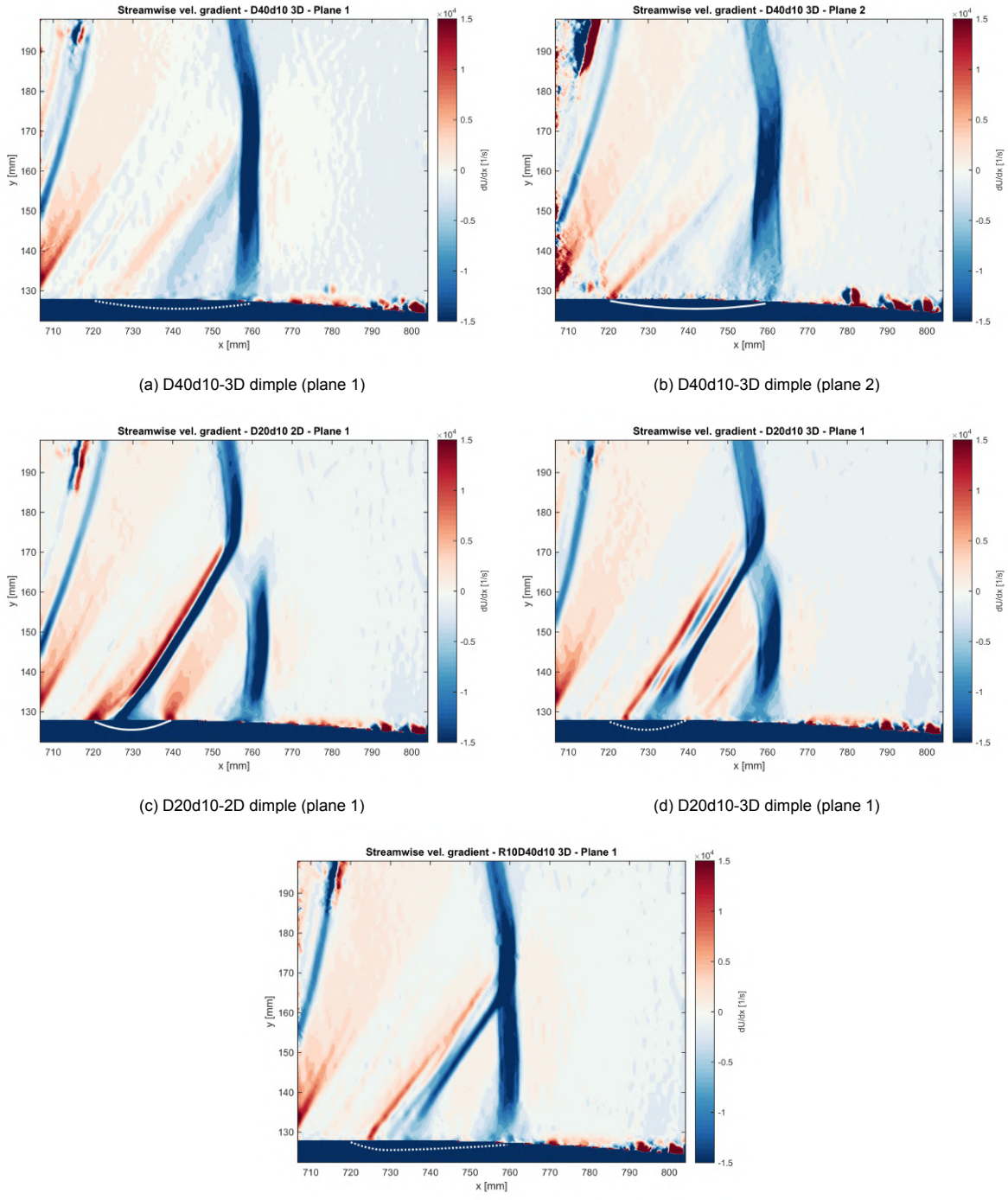

(a) D40d10-3D dimple (plane 1)

(b) D40d10-3D dimple (plane 2)

(c) D20d10-2D dimple (plane 1)

(d) D20d10-3D dimple (plane 1)

(e) R10D40d10-3D dimple (plane 1)

Figure F.5: Distributions of the U-component gradient in the streamwise direction for different test plates.

F.1.4. Flow direction angle

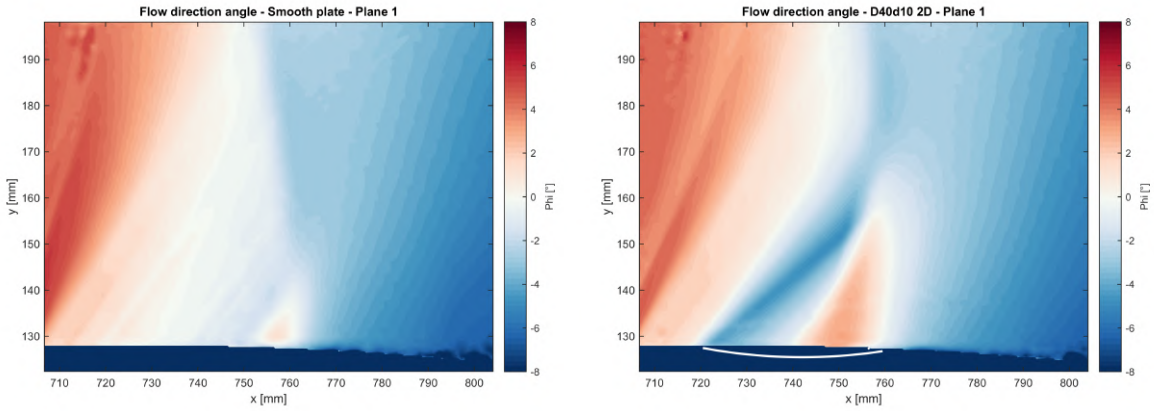

(a) Smooth plate

(b) D40d10 2D

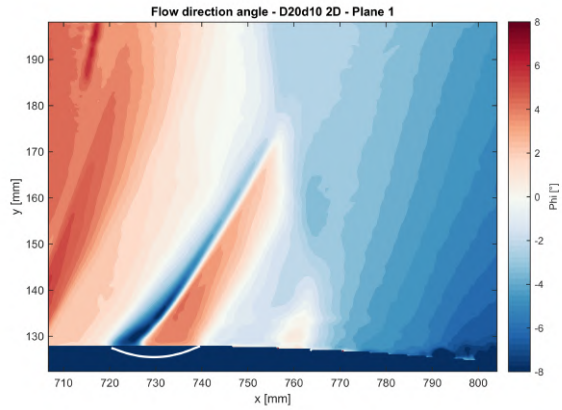

(c) D20d10 2D

Figure F.6: Flow direction distribution for the two-dimensional plates. Angle computed relative to the horizontal line.

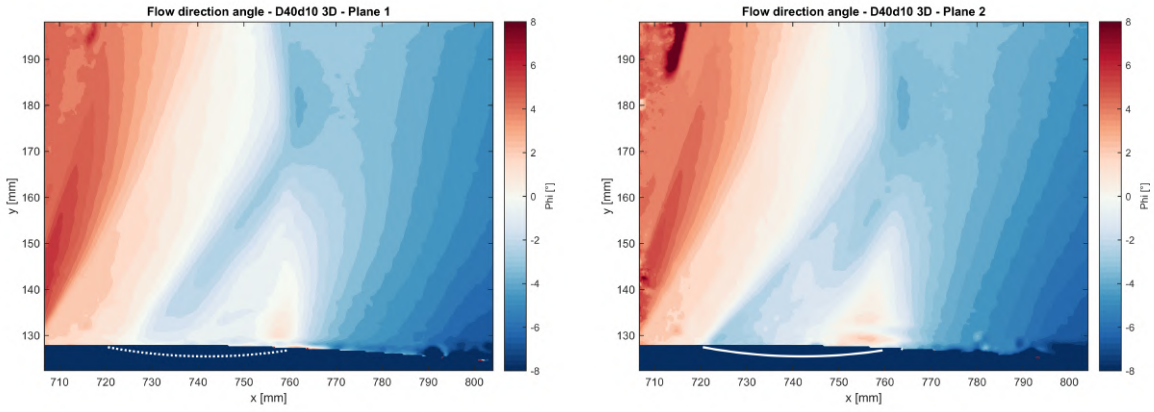

(a) Plane 1

(b) Plane 2

Figure F.7: Flow direction distribution for the D40d10 3D plate. Angle computed relative to the horizontal line.

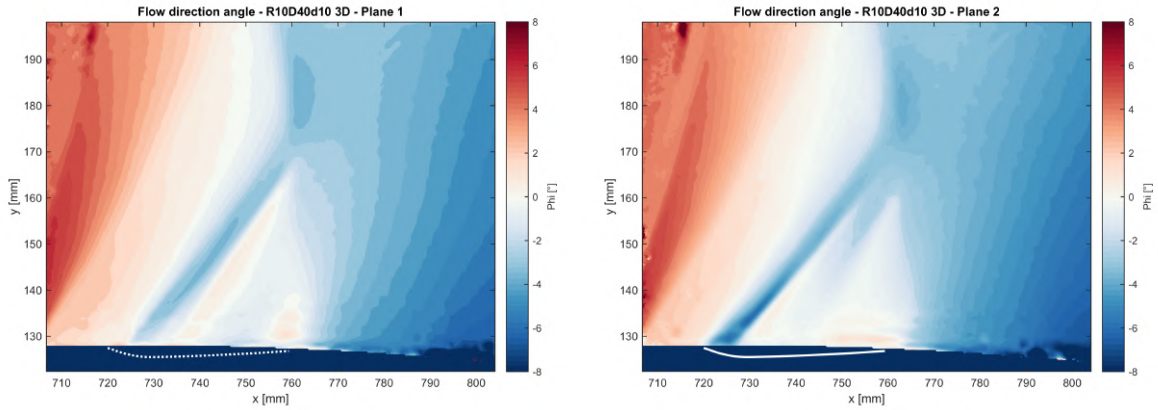

(a) Plane 1 (b) Plane 2

Figure F.8: Flow direction distribution for the R10D40d10 3D plate. Angle computed relative to the horizontal line.

F.1.5. Total density losses

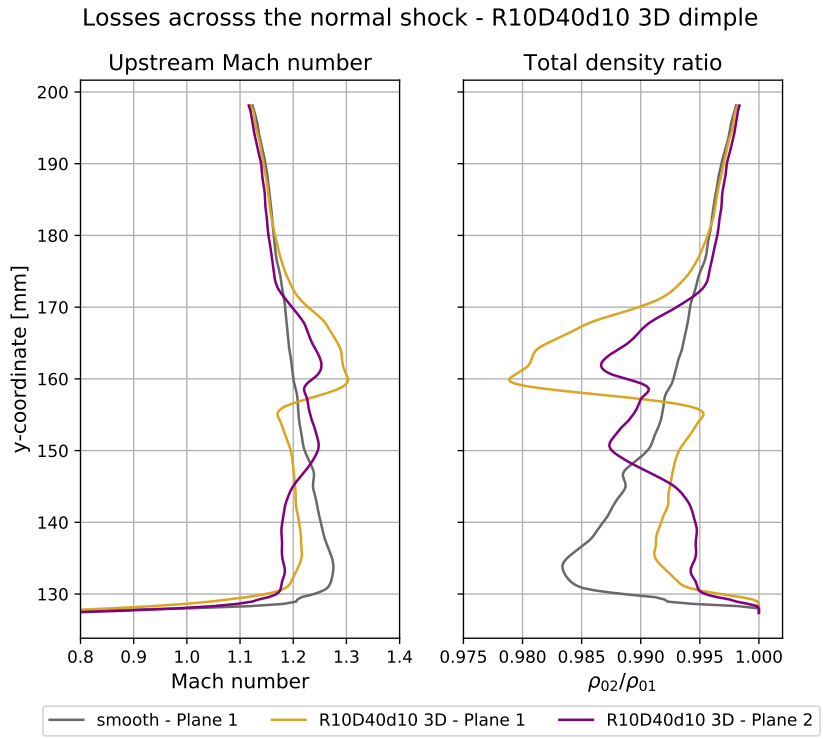

Figure F.9: Upstream mach number and total density ratio profiles using normal shock relations for the R10D40d10 3D plate

F.2. Surface pressure measurements overflow results

When the surface pressure distributions for the 3D plates were presented in Chapter 6, only results obtained with the shock moving in the downstream direction were displayed (ie. Run 1 results). The same kind of plots are shown below but now for the upstream-moving shock wave (Run 2).

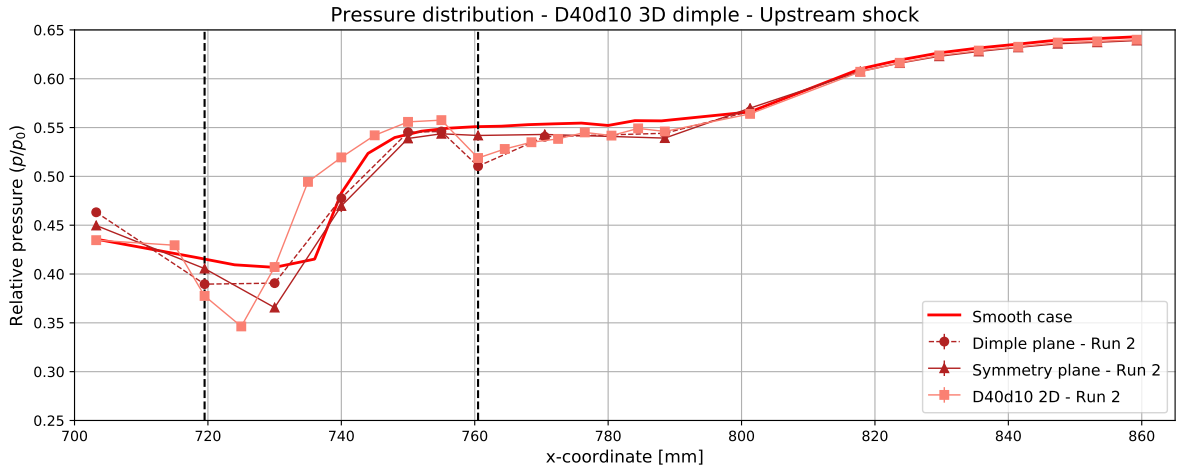

(a) Upstream shock location.

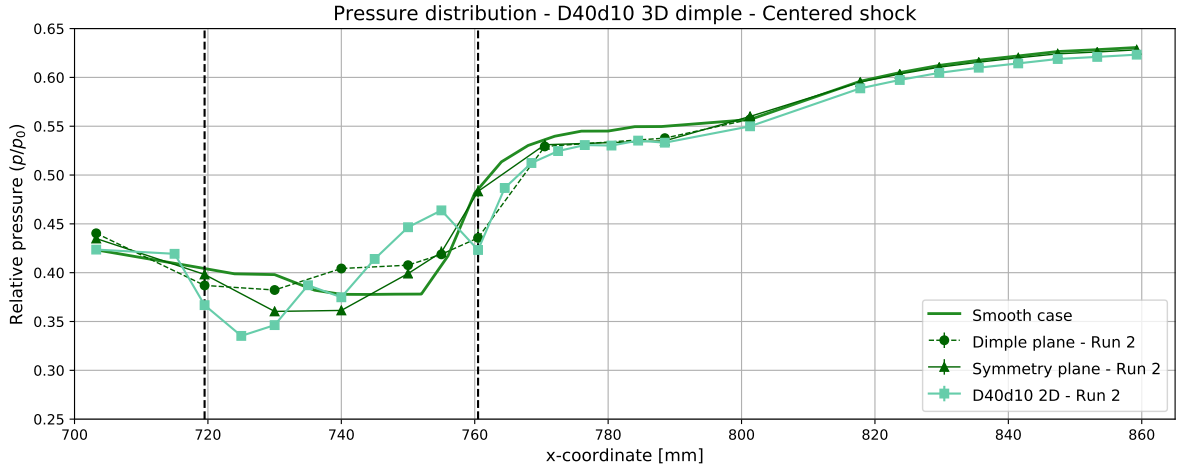

(b) Centered shock location.

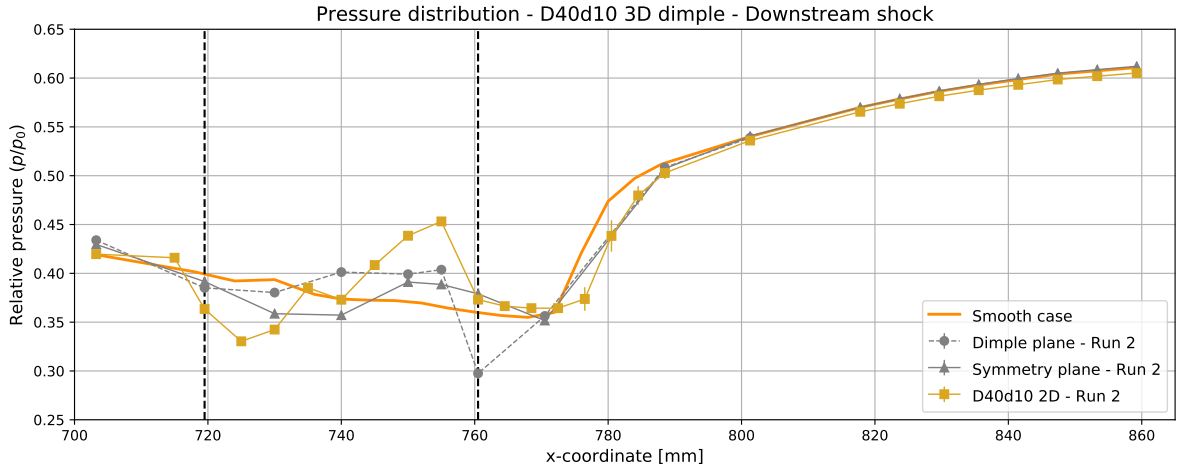

(c) Downstream shock location.

Figure F.10: Relative pressure distribution over the plate symmetry and dimple centreline for the D40d10 - 3D dimpled plate.

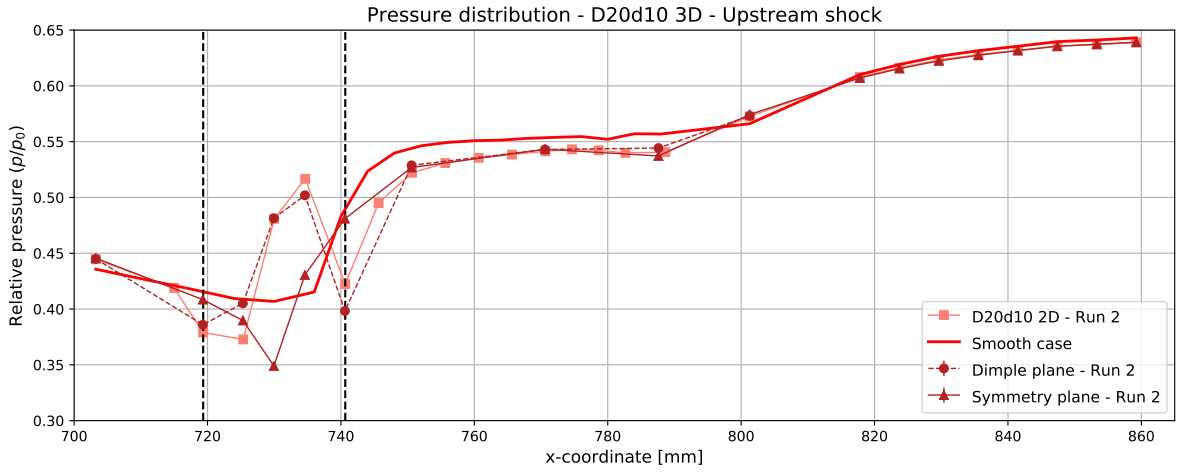

(a) Upstream shock location.

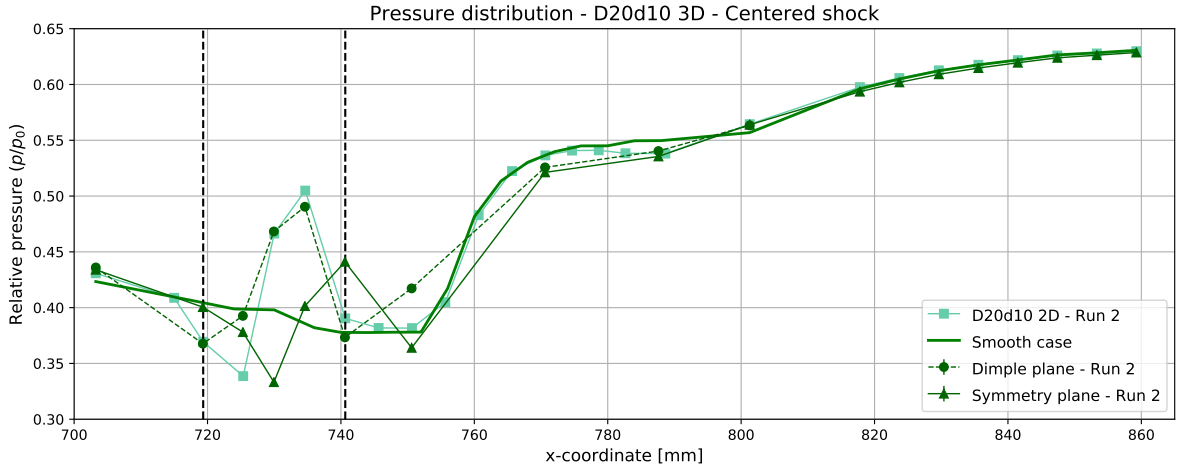

(b) Centered shock location.

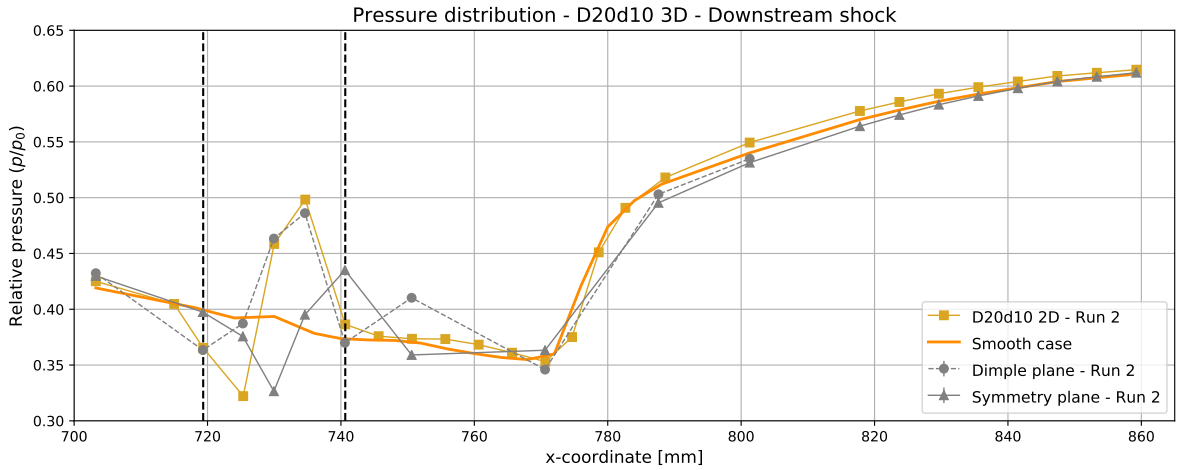

(c) Downstream shock location.

Figure F.11: Relative pressure distribution over the plate symmetry and dimple centreline for the D20d10 - 3D dimpled plate.

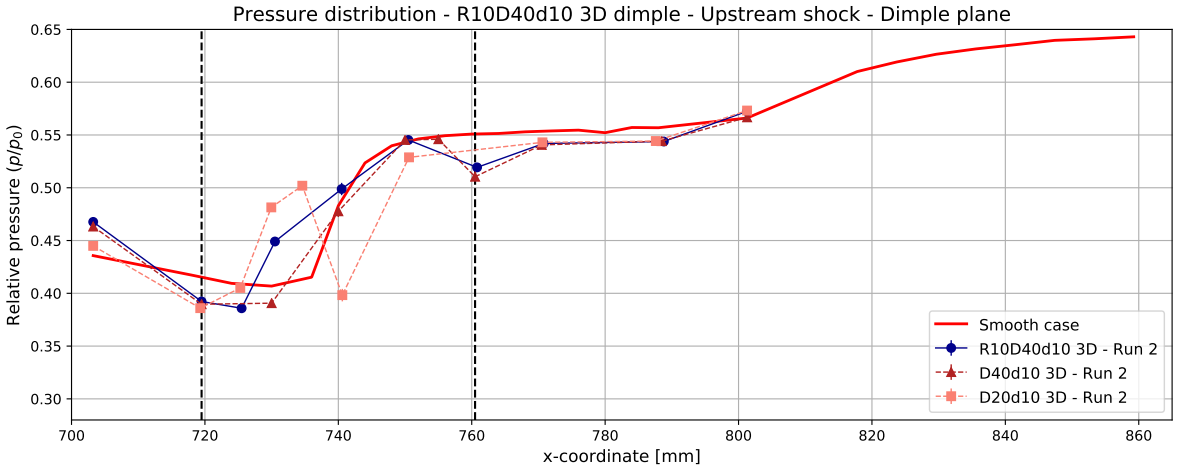

(a) Upstream shock location.

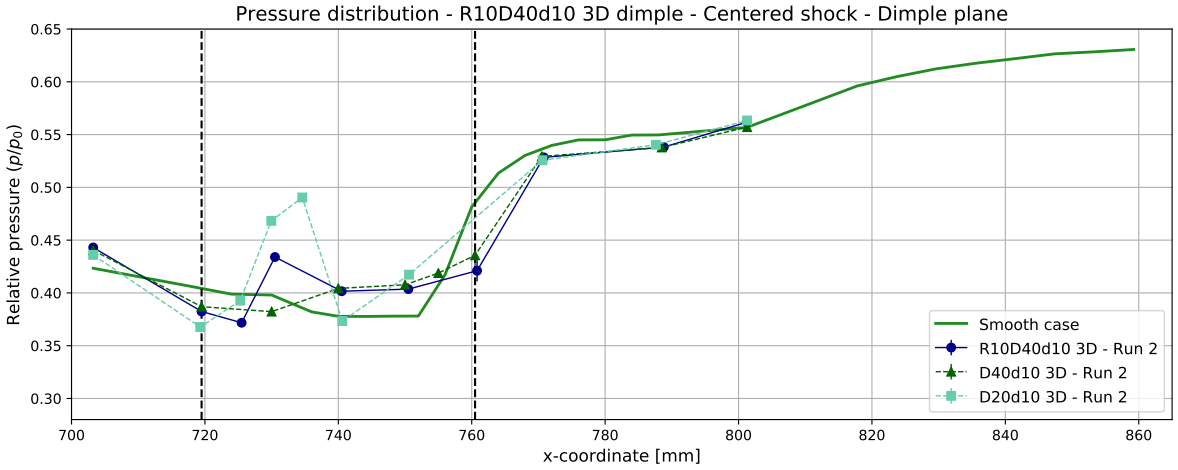

(b) Centered shock location.

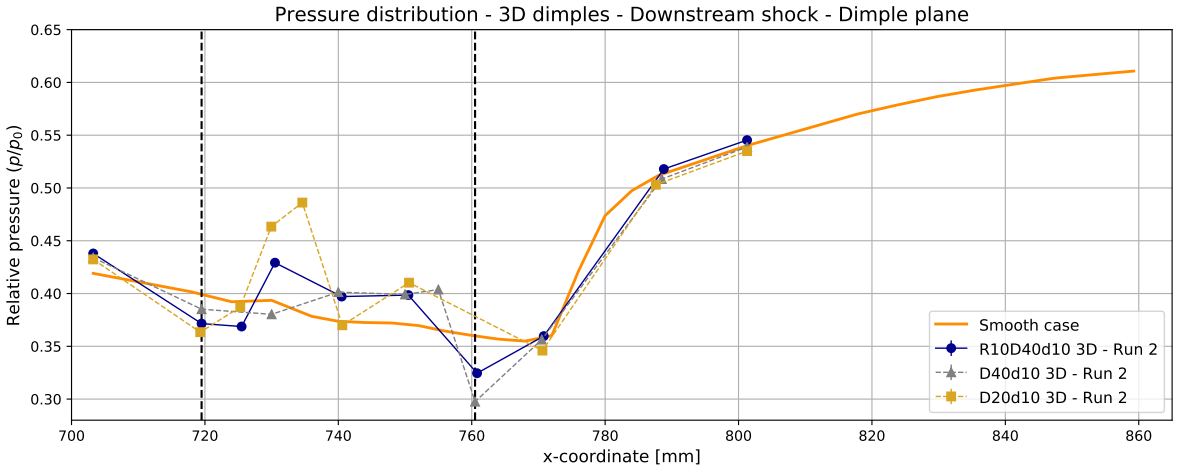

(c) Downstream shock location.

Figure F.12: Relative pressure distribution over the dimple centreline for the R10D40d10 - 3D dimpled plate.

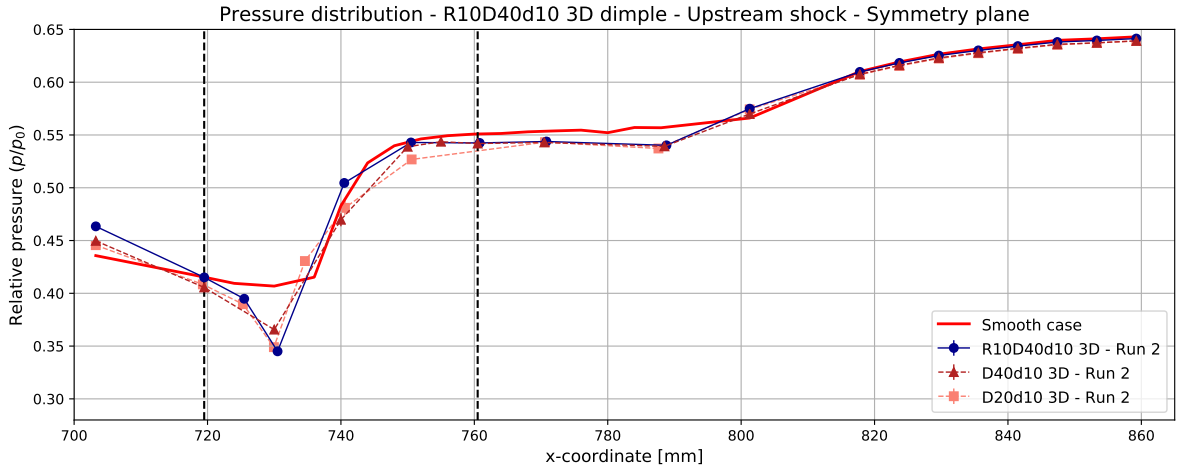

(a) Upstream shock location.

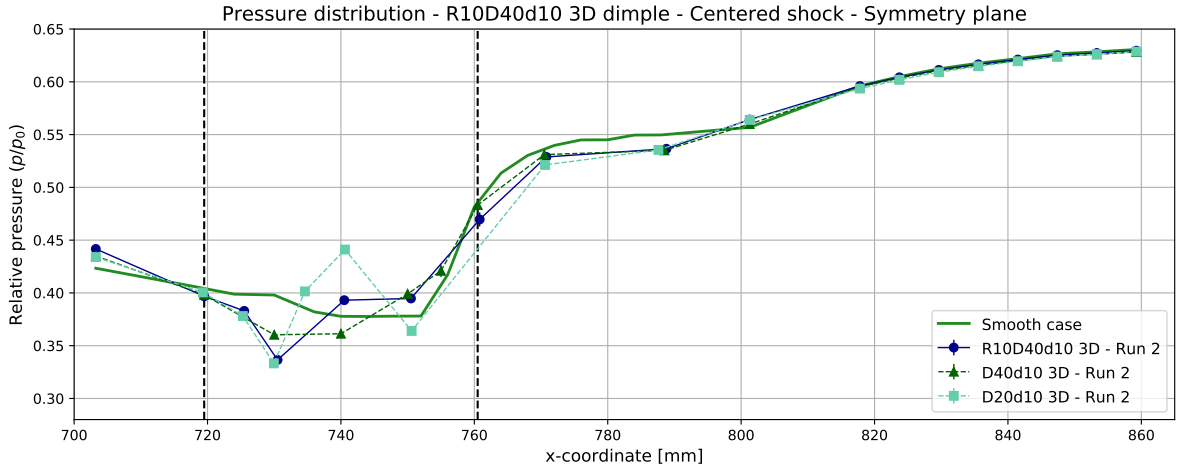

(b) Centered shock location.

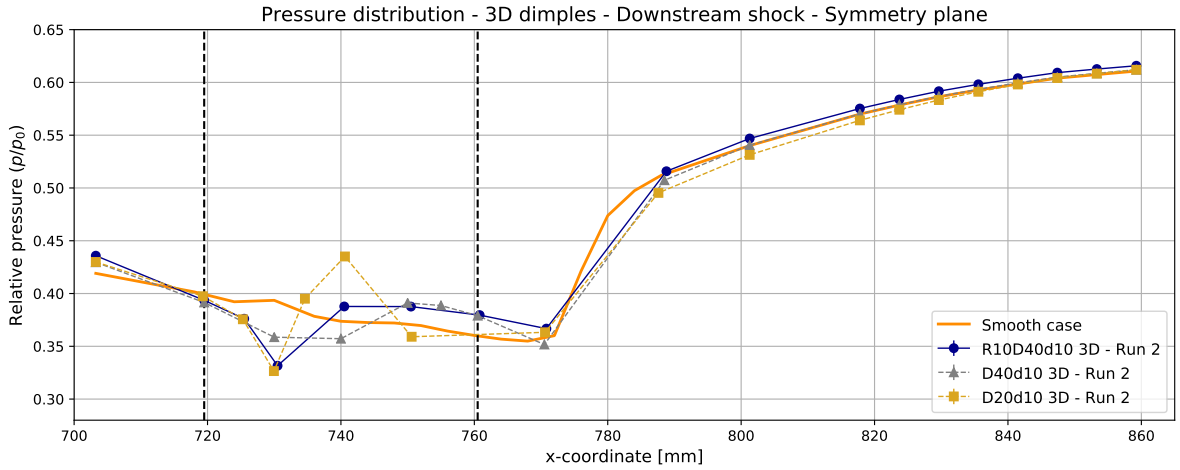

(c) Downstream shock location.

Figure F.13: Relative pressure distribution over the plate symmetry for the R10D40d10 - 3D dimpled plate.

Bibliography

[1] Flying v - flying long distances energy-efficiently. *TU Delft website*. https://www.tudelft.nl/en/ae/flying-v/.

[2] *Lilium website*. https://lilium.com/.

[3] Cleaner and quieter flights. *Schiphol Airport*. https://www.schiphol.nl/en/schiphol-as-a-neighbour/page/fleet-renewal/.

[4] The world of air transport in 2018. *ICAO Annual Report*, 2018. https://www.icao.int/annual-report-2018/Pages/the-world-of-air-transport-in-2018.aspx.

[5] Airbus reveals new zero-emission concept aircraft. *Airbus press*, (09), 2020. https://www.airbus.com/newsroom/press-releases/en/2020/09/airbus-reveals-new-zeroemission-concept-aircraft.html/.

[6] What if aviation doesn't recover from covid-19? *The Economist*, (07), 2020. https://www.economist.com/the-world-if/2020/07/04/what-if-aviation-doesnt-recover-from-covid-19/.

[7] Is the time now ripe for planes to run on hydrogen? *The Economist*, (12), 2020. https://www.economist.com/science-and-technology/2020/12/08/is-the-time-now-ripe-for-planes-to-run-on-hydrogen?itm_source=parsely-api&tg=a/.

[8] Effects of novel coronavirus (covid-19) on civil aviation: Economic impact analysis. *ICAO*, 2020. https://www.icao.int/sustainability/.

[9] J. Fulker A. Smith, H. Babinsky and P. Ashill. Normal shock wave-turbulent boundary-layer interactions in the presence of streamwise slots and grooves. *The Aeronautical Journal*, 106: 493–500, 2002. doi: 10.1017/S0001924000092344.

[10] J. L. Fulker A. Smith, H. Babinsky and P. Ashill. Shock-wave/boundary-layer interaction control using streamwise slots in transonic flows. *Journal of Aircraft*, 41:540–546, 2004. doi: 10.2514/1.11479.

[11] T. Lutz A. Sommerer and S. Wagner. Design of adaptive transonic airfoils by means of numerical optimisation. *European Congress on Computational Methods in Applied Sciences and Engineering*, 2000.

[12] R. J. Adrian, M. Gharib, and W. Merzkirch. *Schlieren and Shadowgraph Techniques : Visualizing Phenomena in Transparent Media*. Springer Verlag, 2001. ISBN 9783642566400.

[13] J. D. Anderson. The airplane: a history of its technology. *AIAA, Reston, Virginia*, 2002. doi: 10.2514/4.102998.

[14] M. Ostieri B. Mele and R. Tognaccini. Aircraft lift and drag decomposition in transonic flows. *Journal of Aircraft*, 54, 09 2017. doi: 10.2514/1.C034288.

[15] J. Benad. The flying v - a new aircraft configuration for commercial passenger transport. 11 2015.

[16] E. Breitbach and T. Bein. Design aspects of the adaptive wing - the elastic trailing edge and the local spoiler bump. *Aeronautical Journal*, Volume 104:89–95, 02 2000.

[17] B. Brelje and J. Martins. Electric, hybrid, and turboelectric fixed-wing aircraft: A review of concepts, models, and design approaches. *Progress in Aerospace Sciences*, 104:1–19, 01 2019. doi: 10.1016/j.paerosci.2018.06.004.

[18] P. J. K. Bruce and H. Babinsky. Experimental study into the flow physics of three-dimensional shock control bumps. *Journal of Aircraft*, 49:1222–1233, 5 2012. doi: 10.2514/1.C031341.

[19] P. J. K. Bruce and S. P. Colliss. Review of research into shock control bumps. *Shock Waves*, 25:451—471, 2015. doi: 10.1007/s00193-014-0533-4.

[20] B. C. Khoo C. M. Tay, Y. T. Chew and J. B. Zhao. Development of flow structures over dimples. *Experimental Thermal and Fluid Science*, pages 278–287, 2014. doi: 10.1016/j.expthermflusci.2013.10.001.

[21] N. Caballero. 2d numerical investigations of shock and boundary layer control techniques. *Drag Reduction by Shock and Boundary Layer Control - Results of the Project EUROSHOCK II*, pages 255–284, 2002. doi: doi.org/10.1007/978-3-540-45856-2_8.

[22] N. Catino and N. Ceresola. Drag reduction and buffet damping by a contour bump control device and regional-jet application. *Drag Reduction by Shock and Boundary Layer Control - Results of the Project EUROSHOCK II*, pages 417–431, 2002. doi: 10.1007/978-3-540-45856-2_15.

[23] A. L. Coimbra. *Mecânica dos Fluidos*. Editora e-papers, 2015. ISBN 978-85-7650-479-5.

[24] C. Dima and P. De Matteis. Numerical investigation of active shock wave and boundary-layer control on airfoils and sheared wings. *Drag Reduction by Shock and Boundary Layer Control - Results of the Project EUROSHOCK II*, 2002.

[25] E. C. Dittrich. Drag reduction by means of dimpled surfaces in transonic flow. *Literature Study & Research Plan, Delft University of Technology*, 2020.

[26] D. S. Dolling. Fifty years of shock-wave/boundary-layer interaction research: What next? *AIAA Journal*, 39:1517–1531, 2001. doi: 10.2514/2.1476.

[27] J. Domone. The challenges and benefits of the electrification of aircraft. *Atkins (SNC-Lavalin Group)*, 06 2018.

[28] J. Délery. Shock wave/turbulent boundary layer interaction and its control. *Progress in Aerospace Sciences*, 22:209–280, 1985. doi: 10.1016/0376-0421(85)90001-6.

[29] J. Délery and R. Bur. The physics of shock wave/boundary layer interaction: Last lessons learned. *European Congress on Computational Methods in Applied Sciences and Engineering*, 2000. doi: 10.13140/2.1.4478.8169.

[30] J. Fulker E. Stanewsky, J. Délery and W. Geißler. *EUROSHOCK - Drag Reduction by Passive Shock Control*. Springer Verlag, 1997. ISBN 978-94-010-5826-1.

[31] J. Fulker E. Stanewsky, J. Délery and editors P. de Matteis. *Drag Reduction by Shock and Boundary Layer Control—Results of the Project EUROSHOCK II*. Notes on Numerical Fluid Mechanics and Multidisciplinary Design. Springer, Berlin, 2002. ISBN 978-3-540-45856-2.

[32] J. P. Eastwood and J. P. Jarrett. Toward designing with three-dimensional bumps for lift/drag improvement and buffet alleviation. *AIAA Journal*, 50, 12 2012. doi: 10.2514/1.J051740.

[33] M. Gad el Hak. *Flow control : passive, active, and reactive flow management*. (Cambridge University Press, 2006.

[34] S. El-Takriti, N. Pavlenko, and S. Searle. Mitigating international aviation emissions - risks and opportunities for alternative jet fuels. *The International Council on Clean Transportation*, 03 2017.

[35] M. Baan F. Faggiano, R. Vos and R. Dijk. Aerodynamic design of a flying v aircraft. 06 2017. doi: 10.2514/6.2017-3589.

[36] A. Fage and R. F. Sargent. Shock wave and boundary layer phenomena near a flat surface. *Proceedings of the Royal Society of London, Series A: Mathematical and Physical Sciences*, 190, 1947. doi: https://doi.org/10.1098/rspa.1947.0058.

[37] A. Ferri. Experimental results with airfoils tested in the high speed tunnel at guidonia. *Washington, D.C: National Advisory Commitee for Aeronautics*, 946, 1940.

[38] A. Flinkerbusch. Oblique shock wave-boundary layer interactions over porous plates. *MSc. Thesis, Delft University of Technology*, 2018.

[39] O. Igra G. Ben-Dor and T. Elperin. *Handbook of Shock Waves*. Volume 1. Academic Press, 2000. ISBN 978-00-805-3372-8.

[40] Y. K. Krasnov G. I. Kiknadze and Y. V. Chushkin. Investigation of the enhancement of heat transfer due to self-organization of ordered dynamic twisted heat-carrier structures on a heat-transfer surface. *Report - I. V. Kurchatov Institute of Atomic Energy*, 1984.

[41] B. Gölling G. Schrauf and N. Wood. Katnet-key aerodynamic technologies for aircraft performance improvement. *Fifth Community Aeronautical Days, Vienna, Austria - Airbus Deutschland GmbH*, 2006. https://trimis.ec.europa.eu/sites/default/files/project/documents/20121105_140611_34998_2006_aerodays_KATnet.pdf.

[42] C. D. Harris. Nasa supercritical airfoils: A matrix of family-related airfoils. *NASA Technical Paper*, 2969, 1990.

[43] W. P. Henderson and B. J. Holmes. Induced drag - historical perspective. *Society of Automotive Engineers (SAE)*, 54, 09 1989. ISSN 0148-7191.

[44] S. F. Hoerner. *Fluid-Dynamic Drag - Practical Information on Aerodynamic Drag and Hydrodynamic Resistance*. 1965.

[45] H. A. Holden and H. Babinsky. Shock/boundary layer interaction control using 3d devices. *41st Aerospace Sciences Meeting and Exhibit*, 2003. doi: 10.2514/6.2003-447.

[46] IATA. Iata technology roadmap. *Report*, 2013.

[47] F. Feldmann J. Ackeret and N. Rott. Investigations of compression shocks and boundary layers in gases moving at high speed. *NACA TM*, 1113, 1947.

[48] H. Rosemann J. Birkemeyer and E. Stanewsky. Shock control on a swept wing. *Aerospace Science and Technology*, 4:147—156, 2000.

[49] P. Girodroux-Lavigne J. C. Le Balleur and H. Gassot. Prediction of transonic airfoil/wing flow and buffet with control using a time-accurate viscous-inviscid interaction approach. *Drag Reduction by Shock and Boundary Layer Control - Results of the Project EUROSHOCK II*, pages 285–314, 2002. doi: 10.1007/978-3-540-45856-2_9.

[50] W. P. Jeon J. Choi and H. Choi. Mechanism of drag reduction by dimples on a sphere. *Physics of Fluids*, 18:041702, 2006. doi: 10.1063/1.2191848.

[51] H. Zare-Behtash K. Kontis, C. Lada. Effect of dimples on glancing shock wave turbulent boundary layer interactions. *42nd AIAA Aerospace Sciences Meeting and Exhibit*, pages 323–335, 2007. doi: 10.2514/6.2004-1058.

[52] G. I. Kiknadze and I. A. Gachechiladze. Method of forming a current that generates tornado like jets (tlj) embedded into the flow, and the surface for its implementation. *patent*, 2009.

[53] G. I. Kiknadze and I. A. Gachechiladze. The mechanisms of the phenomenon of tornado-like jets self-organization in the flow along the dimples on the initially flat surface. *ASME 2012 International Mechanical Engineering Congress and Exposition*, 2012. doi: 10.1115/IMECE2012-93581.

[54] J. Kompenhans, A. Arnott, J. Agocs, G. Anne, and J.-C. Monnier. *Application of Particle Image Velocimetry for the Investigation of High Speed Flow Fields*. 01 2003. ISBN 84-95999-18-8.

[55] L. Kral. Active flow control technology. *ASME Fluids Engineering Division Newsletter*, pages 3–6, 1999.

[56] K. Kyprianidis. *Future Aero Engine Designs: An Evolving Vision*, pages 3–24. 11 2011. ISBN 978-953-307-611-9. doi: 10.5772/19689.

[57] B. König, M. Pätzold, T. Lutz, and E. Krämer. Numerical and experimental validation of three-dimensional shock control bumps. *Journal of Aircraft*, 46:675–682, 2008. doi: 10.2514/1.41441.

[58] J. M. Ross L. Bahi and H. T. Nagamatsu. Passive shock wave/boundary layer control for transonic airfoil drag reduction. *AIAA 21st Aerospace Sciences Meeting*, 1983. doi: 10.2514/6.1983-137.

[59] G. Dargel L. Gildemeister and H. Hansen. Theoretische grundsatzuntersuchungen zum thema 'adaptive hautstrukturen im verdichtungsstoßbereich. *DGLR Fachausschußtagung T 2.2 'Experimentelle Aerodynamik'*, 1996.

[60] D. Monet N. Qin and S. T. Shaw. 3d bumps for transonic wing shock control and drag reduction. *CEAS Aerospace Aerodynamics Research Conference*, 2002.

[61] S. Wong N. Qin and A. Moigne. Three-dimensional contour bumps for transonic wing drag reduction. *Proceedings of The Institution of Mechanical Engineers Part G-journal of Aerospace Engineering - PROC INST MECH ENG G-J A E*, 222:619–629, 08 2008. doi: 10.1243/09544100JAERO333.

[62] C. Nebbeling. A curved test section for research on transonic shock wave-boundary layer interaction. *Report LR-414, Department of Aerospace Engineering, Delft University of Technology*, 1984.

[63] C. Nebbeling. An experimental investigation of the interaction between a shock wave and a turbulent boundary layer on a convex wall. *Report LR-428, Department of Aerospace Engineering, Delft University of Technology*, 1984.

[64] M. Santer O. Rhodes. Structural optimization of a morphing shock control bump. *52nd AIAA/ASME/ASCE/AHS/ASC Structures, Structural Dynamics and Materials Conference*, 2011. doi: 10.2514/6.2011-2129.

[65] H. Ogawa and H. Babinsky. Wind-tunnel setup for investigations of normal shock wave/boundary-layer interaction control. *AIAA Journal*, 44, 2006. doi: 10.2514/1.24370.

[66] H. Ogawa, H. Babinsky, M. Pätzold, and T. Lutz. Shock-wave/boundary-layer interaction control using three-dimensional bumps for transonic wings. *AIAA Journal*, 46:1442–1452, 2008. doi: 10.2514/1.32049.

[67] M. Orphanides, E. Hafenrichter, Y. Lee, J. Dutton, E. Loth, and S. McIlwain. Shock-position sensitivity and performance of sbli passive-control methods. *19th AIAA Applied Aerodynamics Conference*, 2001. doi: 10.2514/6.2001-2439.

[68] J. L. Fulker P. R. Ashill and A. Shires. A novel technique for controlling shock strength of laminar-flow aerofoil sections. *DGLR Bericht*, 6:175—183, 1992.

[69] T. Pallini. More iconic planes are disappearing from the sky as the coronavirus continues to wreak airline havoc. *Business Insider*, 2020. https://www.businessinsider.com/coronavirus-havoc-forces-airlines-to-retire-iconic-planes-sooner-2020-3/.

[70] B. Corbel R. Bur and J. Délery. Study of passive control in a transonic shock wave/boundary-layer interaction. *AIAA Journal*, 36:394–400, 1998. doi: 10.2514/2.376.

[71] J F Palacin R Martinez-Val and E Perez. The evolution of jet airliners explained through the range equation. *Proceedings of the Institution of Mechanical Engineers, Part G: Journal of Aerospace Engineering*, 222(6):915–919, 2008. doi: 10.1243/09544100JAERO338.

[72] J. Puertas R. Martinez-Val, E. Perez and J. Roa. Optimization of planform and cruise conditions of a transport flying wing. *Proceedings of The Institution of Mechanical Engineers Part G-journal of Aerospace Engineering - PROC INST MECH ENG G-J A E*, 1:1–9, 12 2010. doi: 10.1243/09544100JAERO812.

[73] M. Raffel, C. E. Willert, F. Scarano, C. J. Kähler, S. T. Wereley, and J. Kompenhans. *Particle Image Velocimetry - A Practical Guide, 3rd Edition*. Springer Verlag, 2007. ISBN 978-3-319-68851-0.

[74] K. Nübler S. P. Colliss, H. Babinsky and T. Lutz. Joint experimental and numerical approach to three-dimensional shock control bump research. *AIAA Journal*, 52:436–446, 2 2014. doi: 10.2514/1.J052582.

[75] K. Nübler S. P. Colliss, H. Babinsky and T. Lutz. Vortical structures on three-dimensional shock control bumps. *AIAA Journal*, 54, 08 2016. doi: 10.2514/1.J054669.

[76] F. Scarano. *Overview of PIV in Supersonic Flows*, volume 112, pages 445–463. 01 2008. doi: 10.1007/978-3-540-73528-1_24.

[77] F Scarano. Tomographic PIV: principles and practice. 24(1), 10 2012. doi: 10.1088/0957-0233/24/1/012001.

[78] J. Seddon. The flow produced by interaction of a turbulent boundary layer with a normal shock of strength sufficient to cause separation. *Aeronautical Research Council (ARC) R&M*, 1960.

[79] P. Spalart and J. McLean. Drag reduction: Enticing turbulence, and then an industry. *Philosophical transactions. Series A, Mathematical, physical, and engineering sciences*, 369:1556–69, 04 2011. doi: 10.1098/rsta.2010.0369.

[80] P. Spalart, M. Shur, M. Strelets, A. Travin, K.B. Paschal, and S.P. Wilkinson. Experimental and numerical study of the turbulent boundary layer over shallow dimples. *International Journal of Heat and Fluid Flow*, 78:108438, 08 2019. doi: 10.1016/j.ijheatfluidflow.2019.108438.

[81] E. Stanewsky. Aerodynamic benefits of adaptive wing technology. *Aerospace Science and Technology*, 4(7):439 – 452, 2000. ISSN 1270-9638. doi: 10.1016/S1270-9638(00)01069-5.

[82] K. I. Swartz. Charging forward: New evtol concepts advance. *Vertiflite*, pages 24–29, 07 2017.

[83] R. M. Hicks T. C. Tai, G. G. Huson and G. M. Gregorek. Transonic characteristics of a humped airfoil. *Journal of Aircraft*, 25, 1988. doi: 10.2514/3.45642.

[84] H. Babinsky T. Gibson and L. C. Squire. Passive control of shock wave-boundary-layer interactions. *Aeronautical Journal*, 104:129–140, 2000. doi: 10.1017/S000192400002532X.

[85] T. C. Tai. Theoretical aspects of dromedaryfoil, report 77–0104. *Technical report, David W. Taylor Naval Ship Research and Development Center*, 1977.

[86] C. M. Tay. Determining the effect of dimples on drag in a turbulent channel flow. *49th AIAA Aerospace Sciences Meeting including the New Horizons Forum and Aerospace Exposition*, 2011. doi: 10.2514/6.2011-682.

[87] C. M. Tay, B. C. Khoo, and Y. T. Chew. Mechanics of drag reduction by shallow dimples in channel flow. *Physics of Fluids*, 27, 2015. doi: 10.1063/1.4915069.

[88] V. I. Terekhov, S. V. Kalinina, and Yu. M. Mshvidobadze. Pressure field and resistance of a single cavity with sharp and rounded edges. *Journal of Applied Mechanics and Technical Physics*, 34: 331–338, 1993. doi: 10.1007/BF00864784.

[89] E. Torenbeek. Blended wing body and all-wing airliners. *European Workshop on Aircraft Design Education (EWADE)*, 2007.

[90] O. W. G. van Campenhout. Drag reduction in turbulent flows due to dimpled surfaces. *Literature Study & Research Plan, Delft University of Technology*, 2016.

[91] O. W. G. van Campenhout. Going against the flow - an experimental investigation into the w mechanics of dimpled surfaces in turbulent boundary layers. *MSc. Thesis, Delft University of Technology*, 2016.

[92] O. W. G. van Campenhout, M. van Nesselrooij, L. L. M. Veldhuis, B. W. van Oudheusden, and F. F. J. Schrijer. An experimental investigation into the flow mechanics of dimpled surfaces in turbulent boundary layers. *AIAA SciTech Forum*, 2016. doi: 0.2514/6.2018-2062.

[93] M. van Nesselrooij. On the drag reduction of dimpled surfaces in turbulent boundary layers - proof of concept and identification of flow structure. *MSc. Thesis, Delft University of Technology*, 2015.

[94] B. W. van Oudheusden. Piv-based pressure measurement. *Measurement Science and Technology*, 2013. doi: 10.1088/0957-0233/24/3/032001.

[95] B. W. van Oudheusden, A. Flinkerbusch, and F. Schrijer. Velocity and pressure fields of swblis on porous plates. *13th International Symposium on Particle Image Velocimetry – ISPIV 2019*, 06 2019.

[96] L. L. M. Veldhuis and E. Vervoort. Drag effect of a dented surface in a turbulent flow. *27th AIAA Applied Aerodynamics Conference*, 2009. doi: 10.2514/6.2009-3950.

[97] E. Vervoort. Drag effect of dented surfaces in turbulent flows. *MSc. Thesis, Delft University of Technology*, 2007.

[98] N. Vida. Three dimensional surface structure for reduced friction resistance and improved heat exchange. *patent*, 2004.

[99] R. Vos and S. Farokhi. *Introduction to Transonic Aerodynamics*. Fluid Mechanics and its Applications. Springer Verlag, 2015. ISBN 978-94-017-9746-7.

[100] L Owens W Milholen. On the application of contour bumps for transonic drag reduction. *43rd AIAA Aerospace Sciences Meeting and Exhibit*, 2005. doi: 10.2514/6.2005-462.

[101] Y. H. J. Weersch. On the turbulent drag reduction of a dimpled surface under a pressure gradient. *MSc. Thesis, Delft University of Technology*, 2017.

[102] F. M. White. *Viscous Fluid Flow*. F. M. White, 2006. ISBN 978-00-724-0231-5.

[103] W. Wong, N. Qin, and N. Sellars. A numerical study of transonic flow in a wind tunnel over 3d bumps. 01 2005. ISBN 978-1-62410-064-2. doi: 10.2514/6.2005-1057.

[104] W. S. Wong, N. Qin, N. Sellars, H. Holden, and H. Babinsky. A combined experimental and numerical study of flow structures over three-dimensional shock control bumps. *Aerospace Science and Technology*, 12, 2008. doi: 10.1016/j.ast.2007.10.011.

[105] C. Wüst. Dellen im dach. *Der Spiegel*, 14, 2004.

[106] Y. T. Chew Y. Chen and B. C. Khoo. Enhancement of heat transfer in turbulent channel flow over dimpled surface. *International Journal of Heat and Mass Transfer*, 55:8100–8121, 2012.